NTNU
Norwegian University of
Science and Technology

Master's thesis
2019
Mona Haukali

Master's thesis

NTNU
Norwegian University of
Science and Technology
Faculty of Natural Sciences
Department of Materials Science and Engineering

Mona Haukali

In situ EBSD Investigations of the Nucleation and Growth of Intermetallic Phases in a SDSS

June 2019

NTNU
Norwegian University of
Science and Technology

NTNU
Norwegian University of
Science and Technology

In situ EBSD Investigations of the Nucleation and Growth of Intermetallic Phases in a SDSS

Mona Haukali

Materials Science and Engineering
Submission date: June 2019
Supervisor: Jarle Hjelen, IMA
Co-supervisor: Ida Westermann, IMA
Morten Karlsen, IMA

Norwegian University of Science and Technology
Department of Materials Science and Engineering

Preface

The present thesis and experimental work are submitted to the Norwegian University of Science and Technology (NTNU), Department of Materials Science and Engineering spring 2019 and is a part of TMT4905 Materials Technology, Master's Thesis. This thesis is a direct continuation of a project done in Fall 2018, and some parts have been reused. The thesis is conducted according to the regulations for the completion of a Master's thesis at NTNU. The author hopes that the work presented will contribute to the field of materials science.

I wish to thank my supervisor Professor Jarle Hjelen for extremely good help and guidance through this work. I would also like to thank my co-supervisors Associate Professor Ida Westermann and Professor II Morten Karlsen for guidance and motivation throughout this work. For especially great help with the in situ experiments, I express my gratitude to senior engineer Sergey Khromov. I am grateful for help from Yingda Yu in answering questions about analysis of the EBSD data, as well as application specialist at EDAX, the Netherlands, Dr. Rene de Kloe for help with optimizing results after the EBSD acquisition. I would also like to thank my fellow co-students for the great support during this period.

June 10, 2019
Trondheim, Norway

Mona Haukali

Abstract

Super duplex stainless steel (SDSS) is used in wells with high temperature and high pressure in the oil and gas industry due to the good combination of high corrosion resistance and excellent mechanical properties. But SDSS are susceptible to the formation of brittle intermetallic phases like sigma(σ)- and chi(χ)-phase at high temperatures which gives a significant decrease in the mechanical properties of the steel. Such high temperatures can be caused during hot forming, heat treatments, and welding. The χ-phase precipitates on ferrite/ferrite grain boundaries and occurs before the σ-phase. It is a metastable phase which is consumed during σ-phase precipitation. The σ-phase is typically formed at austenite-ferrite grain boundaries but can also form on ferrite-ferrite grain boundaries.

The SDSS material was investigated in situ with a Zeiss Ultra 55 FESEM using a NORDIF UF-1100 EBSD detector system to acquire the EBSD patterns, and TSL/OIM to analyze these patterns. The material was heated to temperatures between 625°C and 700°C using the software HT Traction and a heating stage created by Rémi Chiron, CNRF. To improve the pattern quality image averaging was applied during pattern acquisition. The SDSS material with varying amounts of intermetallic phases was also tensile tested with a 100 kN MTS 810 machine after being heat treated at 300°C for four weeks.

The main objective of this work is to investigate the nucleation and formation of σ- and χ-phase in the SDSS. This work investigates where these phases nucleate as well as the rate of the propagation. In addition to this, the effect of long term heat treatment on the tensile properties of the material was investigated.

Samandrag

Super dupleks rustfritt stål (SDSS) blir brukt i brønnar med høg temperatur og høgt trykk i olje- og gassindustrien på grunn av den gode kombinasjonen av høg korrosjonsmotstand og gode mekaniske eigenskapar. Men SDSS er mottakeleg for danninga av sprø intermetalliske fasar som sigma (σ) - og chi (χ) - fase ved høge temperaturar som gir en betydeleg reduksjon i stålet sine mekaniske eigenskapar. Slike høge temperaturar kan bli forårsaka under varmebehandling og sveising. Chi(χ)-fasen blir presipitert på ferritt-ferritkorngrenser og kjem før σ-fasen. χ-fasen er en metastabil fase som blir forbrukt når σ blir presipitert. Sigma (σ)-fasen er vanlegvis danna på austenitt-ferrittkorngrenser, men kan også bli danna på ferritt-ferrittkorngrenser.

SDSS-materialet blei undersøkt in situ med Zeiss Ultra 55 FESEM ved hjelp av eit NORDIF UF-1100 EBSD-detektorsystem for å ta opp EBSD-mønstrene, og TSL/OIM for å analysere desse mønstra. Materialet blei varma opp til temperaturar mellom 625°C og 700°C ved å bruke programvare HT Traction og eit varmebord laga av Rémi Chiron, CNRF. For å forbetre mønsterkvalitetsbilete ble averaging brukt når mønstra blei tatt opp. SDSS-materialet med varierande mengder intermetalliske faser blei også strekkprøva med ein 100 kN MTS 810-maskin etter å ha vore behandla ved 300 ° C i fire veker.

Hovedformålet med dette arbeidet er å undersøke kimdanninga og veksten av σ - og χ-fasen i SDSS. Dette arbeidet undersøkjar kvar desse fasane kjem, i tillegg til veksten av desse fasane. I tillegg blei effekten av langtidsvarmebehandling på strekkeigenskapane undersøkt.

Abbreviations

Abbreviation	Explanation
A_0	Initial cross-sectional area
BCC	Body Centered Cubic cell
CI	Confidence Index
DSS	Duplex Stainless Steel
e	Engineering strain
EBSD	Electron Backscatter Diffraction
FCC	Face Centered Cubic cell
E	Elastic Modulus/ Youngs Modulus
F	Force
fps	Frames per second
JMAK	Johnson-Mehl-Avrami- Kolmogorov
IPF	Inverse Pole Figure
IQ	Image Quality
L_0	Initial gage length
PREN	Pitting Resistance Equivalent Number
px	Pixels
ROI	Region of Interest
rpm	Rounds per minute
s	Engineering stress
SDSS	Super Duplex Stainless Steel
SEM	Scanning Electron Microscope
TCP	Topologically Close-Packed
TTT	Time Temperature Transformation (diagram)
UTS	Ultimate Tensile Strength
YS	Yield Tensile Strength

Symbols

Symbols	Explanation
α	Ferrite
α'	Cr-rich ferrite
δ	Dirac function used in Radon transform
δL	Change in gage length
ΔG	Gibbs free energy
γ	Austenite
γ_{new}	Secondary austenite
χ	Chi-phase
σ	Sigma-phase
θ	Point in the Hough-space
θ_b	Bragg's angle
θ_i^c	Actual angle between crystal planes
θ_ϵ	Degree of fit
θ_i^m	measured angle between Kikuchi bands
ρ	Point in the Hough-space
λ	Electron wavelength

Contents

1 Introduction

Super duplex stainless steel (SDSS) is used in industries like oil and gas, hydropower, pressure vessels, and chemical tankers because of its resistance to a wide variety of corrosive chemicals [1]. SDSS possesses a good combination of corrosion properties together with high mechanical strength. These properties are due to high alloying content, especially the content of Cr which gives the good corrosion resistance.

But intermetallic phases like σ(sigma)- and χ(chi)-phase in the SDSS can develop if the heat treatment is wrong. This can lead to embrittlement and catastrophic service failure of the component. This can happen during fabrication, welding processes and prolonged exposure to high temperatures during their service lives. An example of a process safety incident was at Sarawak Shell Bhd.[2]. Here a duplex stainless steel gas flowline flange fractured and parted eleven hours after being installed and put in service. The failure investigations done by DNV GL Singapore Pte. Ld. explained that the failure was because of embrittlement caused by the formation of σ-phase and that the σ was formed during the fabrication process [3, 4]. The nucleation of σ is studied mostly due to the effect it has on the mechanical properties of the steel.

One method to investigate the intermetallic phases σ and χ is with EBSD (electron backscatter diffraction) with SEM (scanning electron microscope). EBSD can give quantitative microstructural information about many different materials, and it can reveal grain size, grain boundary character, grain orientation, texture, and phase identity of the sample. This thesis aims to investigate a super duplex stainless steel alloy in situ, UNS S37260, during heat treatment between 625°C-700°C to look at nucleation and growth of the intermetallic phases σ and χ. It also investigates the effects of heat treatment at 300°C for four weeks has on the same alloy with varying degrees of intermetallic phases. The master thesis is done together with Equinor ASA.

2 Theory

In this chapter, the relevant theory is presented. Theory about duplex stainless steel (DSS), its microstructure and the intermetallic phases that can form during specific heat treatments, with focus on sigma(σ)- and chi(χ)-phase, will be presented. Also spinodal decomposition, that can happen at lower temperatures will be presented. Theory about the characterization methods with scanning electron microscopy (SEM) and electron backscatter diffraction (EBSD) with the belonging indexing will also be introduced. The testing of mechanical properties will also be presented with tensile testing.

2.1 Duplex Stainless Steel (DSS)

Steels that have a higher Cr-content than 10.5wt.% are defined as stainless steel [5]. The reason for this is that this level is needed to passivate the steel. Stainless steel can be divided into four groups according to their composition and crystal structure: Ferritic, austenitic, martensitic and duplex stainless steels. Duplex stainless steel is a dual-phase steel composed of almost equal volume fraction of ferrite (α) and austenite (γ), with at least 30% of the smallest phase, that gives a good combination of mechanical and corrosion resistance properties in a temperature range from $-50\,°C$ to $250\,°C$ [6, 7]. These properties are achieved with combining various phase stabilizing elements to get a γ-α matrix [1, 8]. The α-phase provides high strength and corrosion resistance, while the γ-phase gives ductility and resistance to uniform corrosion [9].

2.1.1 Microstructure

Duplex stainless steel is composed of both α and γ. The amount of γ versus α depends on the chemical composition of the steel as well as thermal history. γ has a face-centered cubic (FCC) crystal structure, shown in Figure 2.1a while α has a body-centered cubic (BCC) crystal microstructure, shown in Figure 2.1b. To get the optimum mechanical and corrosion properties the balance between the amount of γ and α is important.

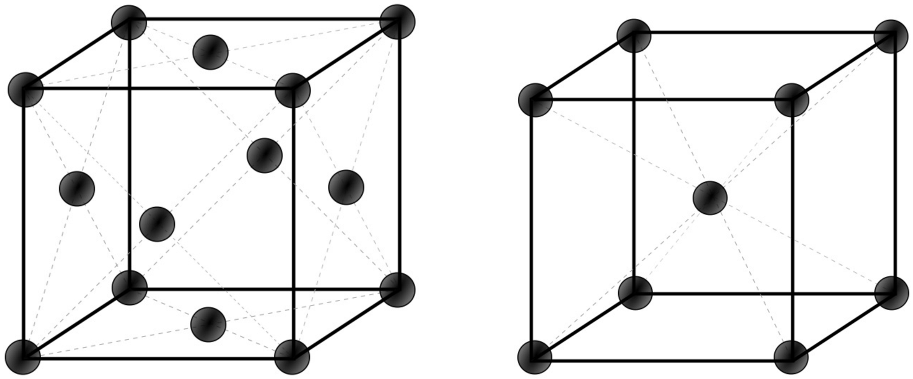

(a) Face-centred cubic (FCC) microstructure

(b) Body-centred cubic (BCC) microstructure

Figure 2.1: a) FCC (for austenite) and b) BCC (for ferrite) microstructure [10]

The duplex steel is formed with δ-ferrite starting to partially decompose into austenite from melting temperature. The austenite firstly grows at the grain boundaries of ferrite and follows the favorable crystallographic orientations inside of the grains. At smaller temperatures, the ferritic content decreases as the austenite increases and carbides and several intermetallic phases may be present [1]. The amount of alloying elements present and the cooling rate decides the amount of austenite and intermetallic phases precipitated. Additional austenite forms by a solid-phase transformation during subsequent annealing [11]. To achieve a phase composition with high strength and corrosion resistance, the steel needs to be annealed and quenched. Normal annealing temperatures is at 1050-1150°C [10].

The rate of the phase transformation is governed by the rate of nucleation and growth, but also the density and distribution of nucleation sites. The fraction transformed for an isothermal hold time follows the Johnson-Mehl-Avrami- Kolmogorov (JMAK) equation:

$$f = \frac{V}{V_e} = 1 - exp(-kt^n) \tag{1}$$

where f is fraction transformed, k is a reaction constant in min^{-n} which is sensitive to temperature, and exponent n is a dimensionless constant that depends on combination of nucleation and growth mechanisms. V_e is the equilibrium volume percent at temperature of interest [1].

2.1.2 Alloying elements

Cr and Mo are effective stabilizers for ferrite because it gives a wide ferritic field and restricts the formation of austenite, shown in the phase diagram for Fe-Cr in Figure 2.2. Stainless steel has excellent corrosion resistance predominantly due to the high solubility of Cr in ferrite. Typical Cr-content in SDSS ranges from 21.00 to 26.00%. The corrosion resistance tends to improve with higher Cr content [12]. The upper limit of Cr comes from risk of formation of chromium carbides. Mo is mainly added to improve corrosion resistance and duplex stainless steel can contain up to 4.50% Mo [12].

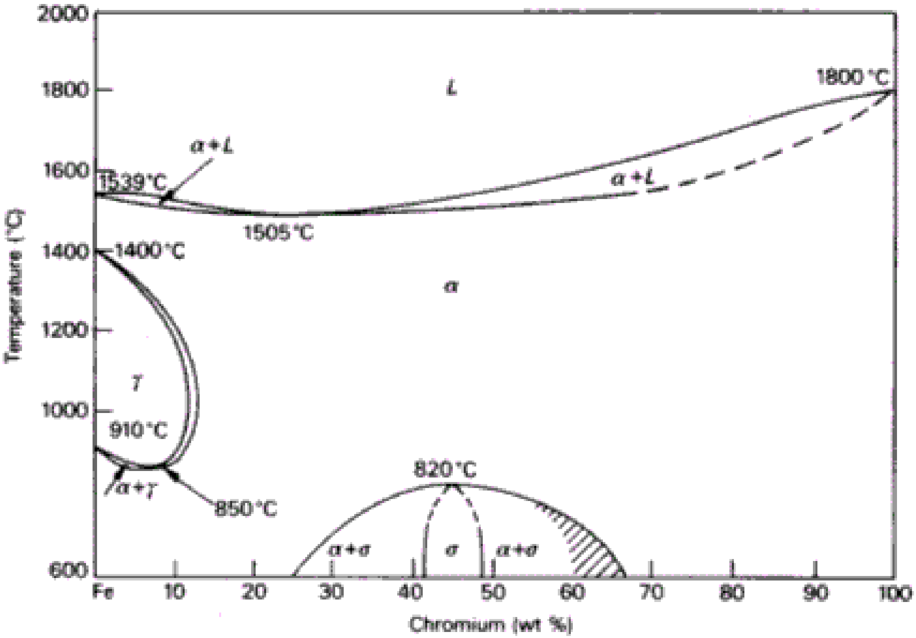

Figure 2.2: Phase diagram for Fe-Cr [13]

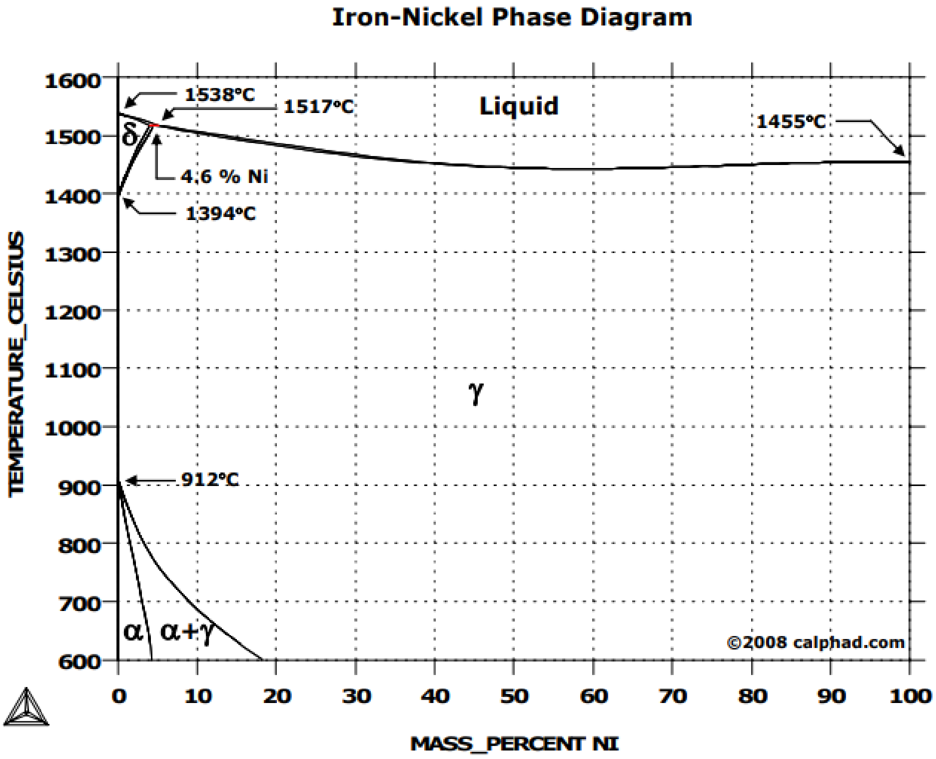

Figure 2.3: Phase diagram for Fe-Ni [14]

Austenitic stabilizing elements like Ni and N are known to increase mechanical properties. The effect of Ni as a stabilizing element can be seen in Figure 2.3. As can be seen from the phase diagram Ni dissolves preferentially in γ-Fe and its solubility in α- and δ-Fe is restricted. The Ni-content in SDSS varies from 3.50 to 8.00% [12]. N is often used as a cheap Ni substitute in austenitic and duplex stainless steels. N also adds strength by causing interstitial solid solution hardening and increase the pitting resistance. Mn is important in duplex stainless steels as an oxygen and sulphur scavenger but should be added with consideration because of the tendency to form MnS which are favourable sites for pit initiation. But if N and Mo are added combined it can override this effect [15]. C is also an austenite stabilizer and increases the maximum solubility of Cr in austenite. It also widens the α+γ phase field up to 0.3% C. The C-content is kept very low (C<0.03%) in SDSS due to the risk of precipitation of chromium carbides which results in lower corrosion resistance and risk of intergranular corrosion.

To see the combined effect of the austenite- and ferrite stabilizing elements, a Schaeffler diagram can be used. A Schaeffler diagram shows the compositional limits at room temperature for martensite, austenite, and ferrite as a function of Ni and Cr equivalents. It shows the regions where the three phases will exist with the different content of Ni and Cr equivalents. The equations for Cr- and Ni-equivalents are empirically determined and is given in Equation 2 and 3 respectively. The equation contains austenite- and ferrite forming elements. The Schaeffler diagram is a very good method to show the effect of various elements in the basic structure of Cr-Ni stainless steels, however, it does not consider the influence of cooling rate and aging treatments [16]. The Schaeffler diagram for stainless steel is shown in Figure 2.4, where austenite is A, ferrite is F and martensite is M.

$$Cr - equivalent = Cr + 2Si + 1.5Mo + 5V + 5.5Al + 1.75Nb + 1.5Ti + 0.75W \quad (2)$$

$$Ni - equivalent = Ni + Co + 0.5Mn + 0.3Cu + 25N + 30C \quad (3)$$

with all the fractions being in weight percentage. UNS S32760 is well defined in the austenitic-ferritic area.

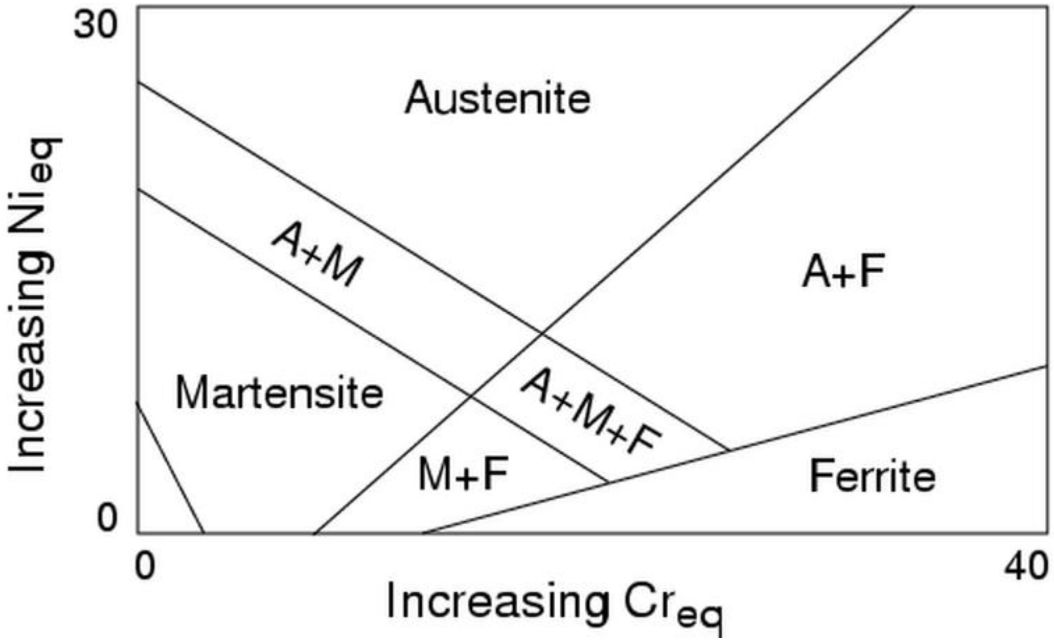

Figure 2.4: Schaeffler diagram. Effect of alloying elements on the basic structure of Cr- Ni stainless steels [17]

Therefore, a structure which combines Cr, Mo, Ni, and N produces a good combination of mechanical properties and high corrosion resistance. SDSS contains an increased amount of these elements which gives these steels higher strength than standard duplex alloys.

2.1.3 Corrosion Resistance of SDSS

The corrosion resistance is one of the key properties of SDSS. The high Cr-content combined with the content of Mo, Ni, and N in the steel gives an excellent corrosion resistance [4]. The Cr content needs to be at least 10.5% to be called stainless, however, to obtain the duplex structure, that means to include both α and γ in the structure, the Cr content needs to be above 20 wt.%, see Figure 2.4. The corrosion resistance comes from a Cr passive layer that is formed on the surface of the material. The Cr-layer is quite thin, about 1.0-2.0 nm, and it shields the metal substrate from uniform and localized corrosion attacks because it prevents diffusion. Mo improves the stability of the film against pitting corrosion while N increases the general pitting resistance, described by the pitting resistance equivalent number(PREN) [18]:

$$PREN = wt\%Cr + 3.3wt\%Mo + xwt\%N \tag{4}$$

where x ranges from 16 to 30. x is usually said to be 16 by the industry [9, 19]. PREN can be used to classify different DSS; lean duplex (PREN = 25-26), standard duplex (PREN = 35-36), super duplex (PREN = 40-42) and hyper duplex (PREN $>$ 45) [6]. A high pitting resistance is given by a high PREN.

2.1.4 Orientation and Misorientation

The orientation of a crystal lattice refers to a coordinate system fixed in the sample and can be represented in many different ways. A common way of representing it is with ideal orientation nomenclature (hkl) [uvw], where (hkl) is the normal to the crystal plane and [uvw] is the crystal direction [20].

The misorientation is the rotation required to rotate one set of crystal axes into coincidence with the other crystal. It is defined by an angle θ through which one lattice is rotated about an axis of misorientation r which is common to both lattices. These parameters are known as the "angle/axis pair" [21].

2.1.5 Spinodal Decomposition

If an Fe-alloy containing between 15 and 75% Cr is heat treated or used at temperatures between 250 °C and 550 °C, spinodal decomposition occurs in the ferrite matrix from α into α and α'. The spinodal decomposition can lead to phases with very different chemical compositions and physical properties. For steel, applications between 250 °C and 500 °C leads to an embrittlement which is often called the "475 °C-embrittlement", and one of the factors that leads to this is the spinodal decomposition into Fe-rich α and Cr-rich α' [22]. The spinodal decomposition of the matrix occurs firstly, and consequently, the α'-phase is formed coherent to the matrix. Next, the cohesion with the matrix is lost and the α'-phase grows. The γ-phase does not have any transformation change with this temperature range [23, 24]. Service in this temperature interval can lead to hardening and embrittlement, which is caused by the ferritic phase. This will lead to a loss of ductility and toughness. The reason for the spinodal decomposition is due to the miscibility gap in the Fe-Cr phase diagram, which can be seen in Figure 2.2, and is reversible by reheating to a region of 600°C where the α' dissolves.

2.2 Intermetallic phases

Intermetallic phases like σ-phase and χ-phase can be precipitated in SDSS if it is exposed to temperatures between 600 °C and 1000 °C [25, 26]. These temperatures can occur with processing, improper heat treatment and long exposure to high temperature during their life time. The intermetallic phases can lead to catastrophic service failure of components [3].

Time-temperature-transformation (TTT) diagram, also called isothermal transformation (IT) diagram, predicts the transformed fraction of a phase with respect to time at a fixed temperature with certain cooling rates. A TTT-diagram for intermetallic phases in a UNS S32760 is shown in Figure 2.5. Because of precipitation of intermetallic phases Cr and Mo diffuse from the ferritic phase and the ferrite transforms into secondary austenite as a result of losing ferritic-promoting elements [9]. Both σ and χ is topologically close-packed (TCP) phases. These kind of phases are characterized by close-packed layers of atoms separated by relatively large interatomic distances. The layers of close-packed atoms are displaced from one to the other by sandwiched large atoms.

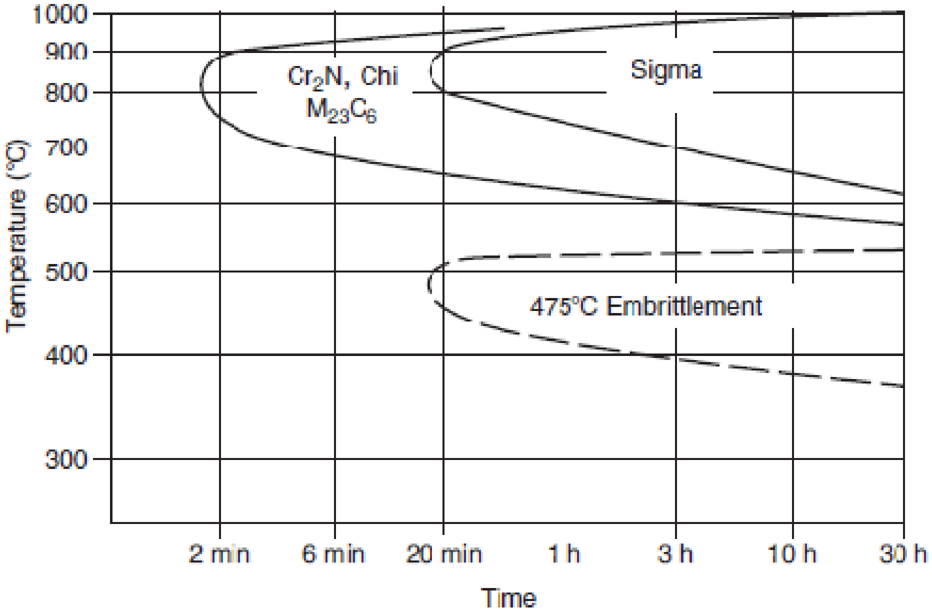

Figure 2.5: TTT-diagram of UNS32760 [16]

The intermetallic phases σ and χ usually appear on grain boundaries, incoherent twin boundaries and dislocations [27]. The precipitations increase the hardness and decrease ductility and toughness. Compared to austenitic and ferritic stainless steels, the precipitation of σ occurs at shorter times, at higher temperatures and larger volumes fractions may be formed in SDSS. SDSS has a high tendency to precipitate intermetallic phases due to high Cr and Mo contents and high diffusion rates in the ferrite phase, compared to other duplex and austenitic stainless steels [23].

2.2.1 Sigma-phase (σ)

The σ-phase is usually formed at temperatures between 600 °C and 950 °C at the α-γ and α-α boundaries [11, 28]. It has a tetragonal crystallographic structure with 32 atoms per unit cell, chemical composition about 30%Cr, 4%Ni and 7%Mo and unit parameters $a = b = 8.80\,\text{Å}$ and $c = 4.56\,\text{Å}$ [28, 29, 30]. The σ-phase increases hardness and reduces toughness, ductility and corrosion resistance [3]. The content of Cr, Mo, and Si promotes formation of σ-phase precipitation, which causes the region to be depleted for these elements which again can result in intergranular corrosion and pitting corrosion [6, 28].

The σ-phase can be precipitated with three different mechanisms: Nucleation and growth from the original ferrite, eutectoid type reaction of ferrite giving σ-phase and austenite as follows: $\delta \rightarrow \sigma + \gamma_{new}$ where γ_{new} is known as the *new austenite*, and growth from austenite after total consumption of original ferrite [31, 32]. The austenite formed can either be intergranular or intragranular secondary austenite. The intergranular secondary austenite nucleates at the α/γ grain boundaries and the intragranular is nucleated in the ferritic phase and is diffusion controlled [33].

The morphology of the σ-phase will vary with different heating temperatures. The diffusion velocity will be lower at lower temperatures causing more single σ nuclei at the beginning of precipitation. This will give a a coral-like structure. At higher temperatures the diffusion velocity will be higher and this causes the σ-phase to be bigger and more compact [34].

The elements that work as ferrite stabilizers are the ones that increase the tendency of the material to form σ-phase. The effect of Cr on the thermodynamic driving force for intermetallic phase formation can be seen in Figure 2.6. It can be seen that for higher Cr-content ΔG is lower, which implies that σ is easier formed at higher Cr content. Mo is the element that promotes the σ-phase the most, more than Cr, especially at higher temperatures. γ-forming elements like Ni and N can also accelerate the nucleation and growth of the σ-phase but might decrease the total amount formed.

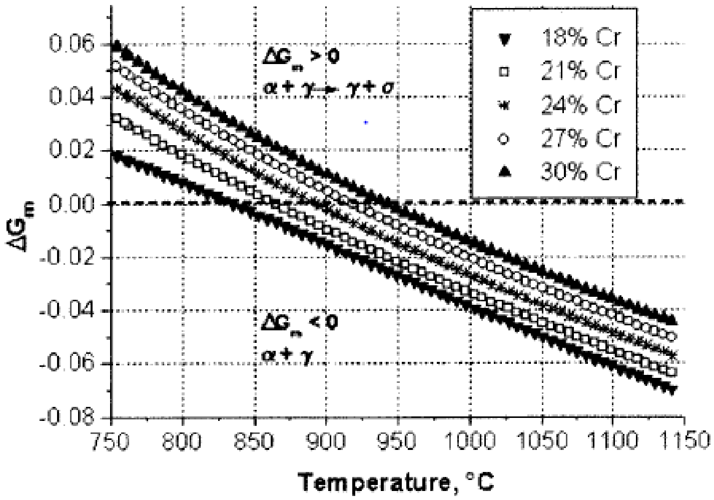

Figure 2.6: Influence of Cr content on the driving force ΔG_m for precipitation of σ phase [35]

2.2.2 Chi-phase (χ)

The χ-phase is said to have a BCC [4, 36] unit cell with unit parameter $a = b = c = 8.92\,\text{Å}$ and is precipitated as a ternary compound of Fe, Cr and Mo [26, 37]. According to Chan and Tjong [4] the χ-phase contains about 25% Cr, 14% Mo and 3% Ni. Kasper [38] synthesized the χ-phase with a composition $Fe_{36}Cr_{12}Mo_{10}$ in a Cr-Ni-Mo steel. The χ-phase nucleates before the σ because of low interfacial energy at the χ/α interface with a characteristic of cubic-to-cubic orientation relationship due to the BCC structure of both the phases. χ usually nucleates at α-α grain boundaries, but may also nucleate at α-γ grain boundaries. After prolonged aging, the χ-phase transforms to σ [4, 31].

The biggest difference between the σ- and χ-phase is that the χ-phase contains less Cr and more Mo. C can also be dissolved in the χ-phase and not in σ. Another difference is that the χ-phase precipitates at lower temperatures and in smaller amounts than σ [9, 31].

2.3 Scanning Electron Microscopy (SEM)

SEM can be used to characterize many different materials, amongst them metals and ceramics, on microscale by using electrons. When the thin beam of electrons hits the surface of the sample, it gives rise to a majority of signals shown in Figure 2.7 that can be detected, for example, secondary electrons, backscattered electrons, and characteristic X-rays. These signals can give information about chemical composition or topographical information about the sample [39].

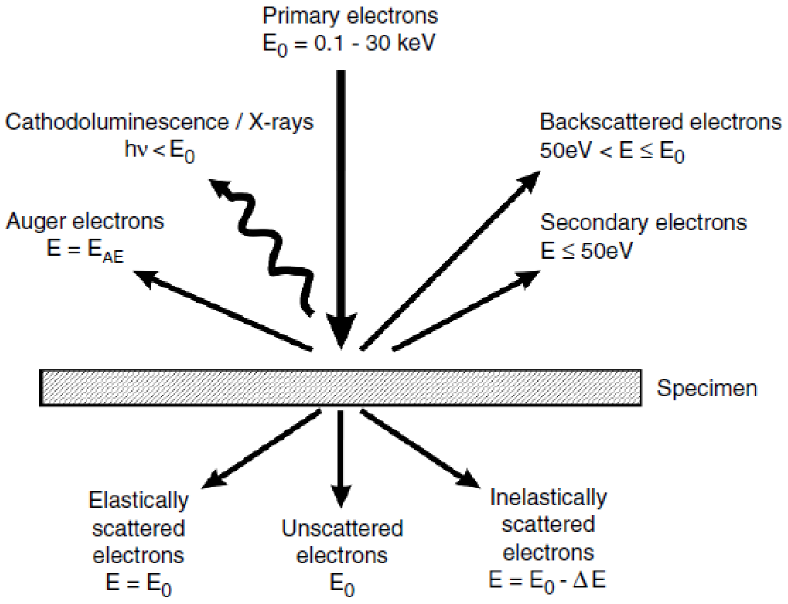

Figure 2.7: Different signals in the SEM

Using the signal from secondary electrons is the most common way to image the surface of a specimen because they come from a small emission volume. Secondary electrons occur due to inelastic interactions between the primary beam and the sample and the images taken with secondary electrons can describe the topography of the sample surface, as well as having contrast from atomic elements [40]. Another way is to use the signal from the backscattered electrons, which can show a channelling contrast as well as atomic number contrast. The backscattered electrons are high energy electrons that are scattered back from the emission volume by elastic interactions. Channelling contrast depends on the direction of the primary beam relative to the lattice. With atomic contrast or Z-contrast, the heavier elements will appear brighter because more signal will come from these phases [41].

2.4 Electron Backscatter Diffraction (EBSD)

EBSD can be used for crystallographic analysis like the determination of the orientation of individual crystallites, phase identification, and characterization of grain boundaries. The signals are obtained from a small volume. To detect the signals, it is very important to have the surface deformation free, because the patterns come from the upper 40 nm layer of the material. A schematic of the EBSD system is shown in Figure 2.8. Normal parameters for EBSD used in SEM is acceleration voltage 10-30 kV and a working distance between 20-25 mm [42].

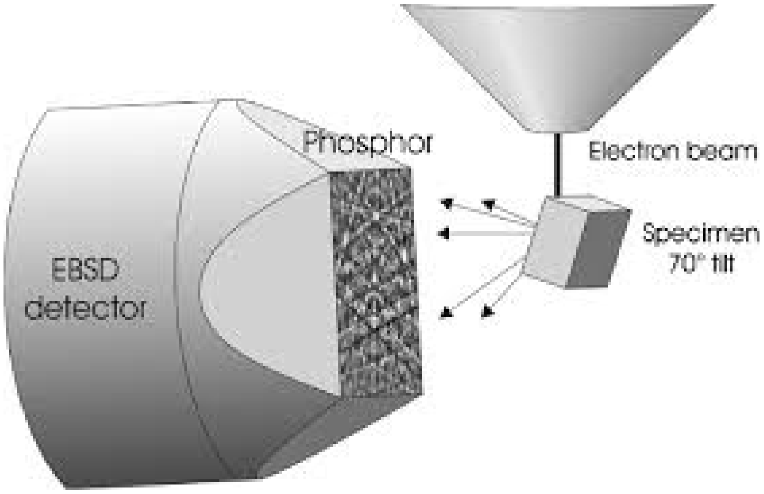

Figure 2.8: Schematic of EBSD setup [42]

The electrons are diffracted in the lattice planes according to Bragg's law given as:

$$2d \sin \theta_b = n\lambda \tag{5}$$

where d is the lattice plane spacing, θ is Bragg's angle, λ is the electron wavelength and n is an integer. A requirement for the incident and emergent angles is that they should be equal θ. To have the best results possible, the sample is tilted to an angle of 70°relative to the electron beam, which leads to a bigger fraction of backscatter electrons hitting the phosphorus screen [42]. The focused probe of electrons is moved point by point across a grid of positions. In every point, some backscattered electrons are collected by the detector which consists of a scintillator screen (phosphorus screen) typically coupled with a lens, but also sometimes a fibre optic bundle to a photon sensitive imaging detector. On the phosphorus screen, a pattern is created. Each pattern consists of many bands of raised intensity that span across the screen, see Figure 2.9. These patterns represent the lattice planes in the crystal. The Kikuchi bands are formed by diffusively scattered electrons of individual crystals of a specimen. The bandwidths are proportional to the inverse interplanar spacing, see Equation 5. The reason that we can identify different phases is that the different crystals have different bands represented. In an FCC, the *hkl* indices must be all odd or all even. For the BCC-system the system of the *hkl* indices must be even ($h + k + l = 2n$). The patterns are transferred from the camera to the computer for indexing and determining the crystal orientation. The Hough transformation converts the nearly straight Kikuchi bands from lines to points which can be more easily located [43].

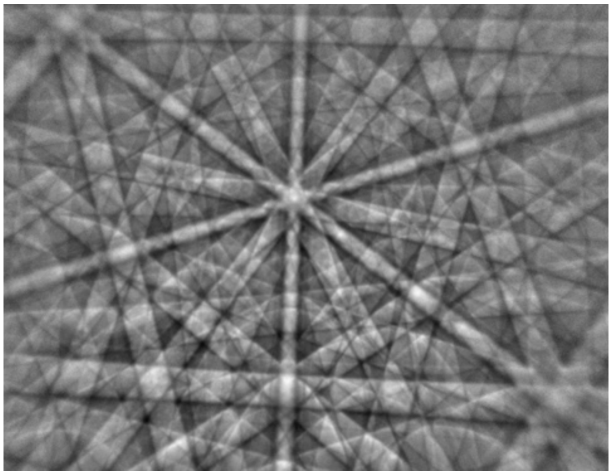

Figure 2.9: Kikuchi band for a cubic crystal

2.4.1 Hough Transformation Parameters

The patterns that are detected with EBSD contains many Kikuchi bands at different angles and positions. The geometry of a Kikuchi pattern is unique for a particular crystal structure and crystal lattice orientation. To index the pattern, it is necessary to detect the band positions and angles with the help of a mathematical approach that is accomplished with a computer algorithm. The Hough transform is a special case of the more general Radon transform, which is a well-established technique for recognition of geometrical features in a binary image. The Hough transform provides a good method to derive the parameters of a straight line and band positions in the pattern formed by the EBSD. The mathematical definition of the Radon transformation of $f(x,y)$ for projections along straight lines is given in Equation 6.

$$R(\rho,\theta) = \int_{-\infty}^{\infty}\int_{-\infty}^{\infty} f(x,y) * \delta(\rho - x * \cos\theta - y * \sin\theta)dxdy \tag{6}$$

$f(x,y)$ stands for the intensity distribution along the line, δ denotes the Dirac function, ρ is the perpendicular distance of the line from the origin, θ is the angle between the x-axis and the normal from the origin to the line. Every point (ρ, θ) in the Radon space thus corresponds to the sum of intensity values along a certain straight line in the image space.

The task of locating lines or bands in the diffraction pattern is reduced by this equation to the simpler task of locating isolated peaks in Radon space [42]. The polar equation of a straight line in the Hough space is:

$$r = x * \cos\theta + y * \sin\theta \tag{7}$$

where r is the distance of the line from the origin, and θ the angle between the x-axis and the normal from the origin to the line. The conversion from the Cartesian grid to the Hough space is shown in Figure 2.10. For each pixel all possible ρ values are calculated for angles θ's ranging in values from 0°to 180°using Equation 7. This means that the Hough transformation maps each pixel (x_r, y_s) separately from the image onto a sinusoidal curve of constant intensity in Hough space that represents all possible lines through this pixel. This produces sinusoidal curves which intersect at a point at a ρ, θ coordinate corresponding to the angle of the line (θ) and its position relative to the origin (ρ). This is how the line in image space transforms to a point in the Hough space [42, 44, 45].

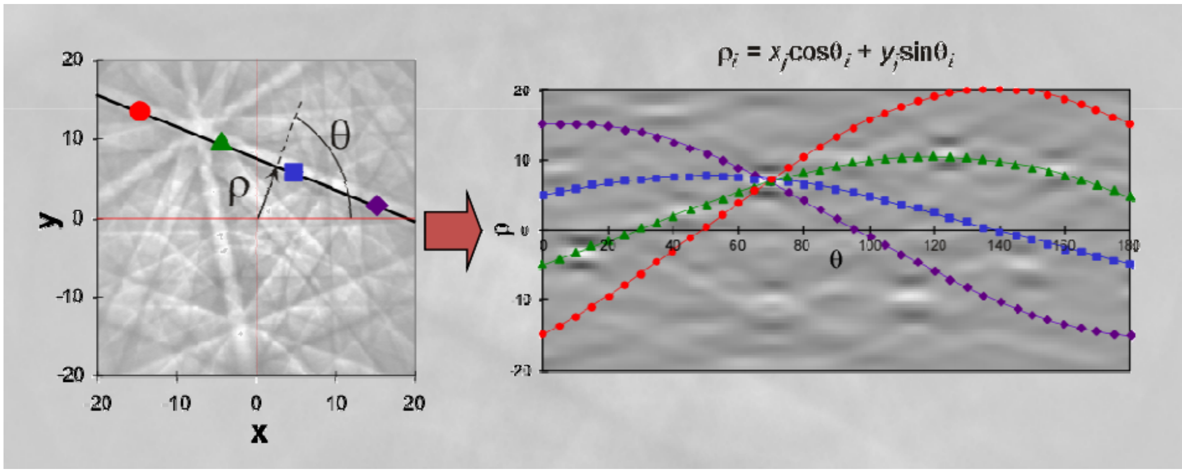

Figure 2.10: Hough transformation [44]

2.4.2 Confidence Index (CI)

The confidence index (CI) is a measure of the probability that a correct solution has been found. It can be defined as the maximum number of indexed bands versus the number of bands that have been considered for indexing a pattern [42]:

$$CI = \frac{S1 - S2}{number of band triplets} \tag{8}$$

where S1 is the number of votes for the best solution and S2 is the number of votes for the second-best solution. The number of band triplets is the total possible number of band triplets possible. The closer the CI is to unity, the more probable it is that the characterization is done correctly [44]. Experiments on FCC materials have shown that patterns indexed with CI larger than 0.1 are correctly indexed 95% of the time [46].

2.4.3 Image Quality (IQ)

By measuring the sharpness of some band edges or the height of the peaks in the Hough space the image quality (IQ) value can be obtained [42]. This is simply the average grayscale value of detected Hough peaks [47]. The IQ map can reveal grain boundaries and precipitates, and the gradients in IQ can even imply dislocation structures.

The quality of the diffraction patterns depends mostly on the perfection of the crystal lattice in the diffracting volume. Any distortions of the crystal lattice within the diffracting volume lower the quality of diffraction patterns (more diffuse). The IQ can also be improved by changing conditions in the microscope or simply adjusting brightness and contrast in video processing [47].

2.4.4 Fit Parameter

The fit parameter describes the average angular deviation between recalculated and detected bands. For each orientation measurement a residual angle θ_E can be calculated:

$$\theta_E = \sqrt{\sum_{i=1-n} (\theta^m - \theta_i^c)^2} \tag{9}$$

where θ_i^m is the measured angle between the i^{th} pair of Kikuchi bands, θ_i^c is the actual angle between the corresponding crystal planes and n is the number of Kikuchi band pairs. θ_ϵ is a measure of the degree of fit of a solution to the diffraction pattern and is used to rank possible solutions [20].

2.5 Tensile Testing

Tensile testing is frequently used to determine the tensile properties of a material. Both the strength and ductility of a material can be determined from tensile testing. The strength can be measured as the stress necessary to cause appreciable plastic deformation (yield tensile strength (YS)) or the maximum stress that a material can withstand (ultimate tensile strength (UTS)). Figure 2.11 shows an example of an engineering stress-strain curve for a typical engineering alloy. In this figure, the YS can be seen as $\sigma_{2\%ys}$ and the UTS as σ_{uts}. E is the elastic modulus and is calculated from the slope of the elastic part of the curve. Low ductility is given by low resistance to fracture after maximum loading. Ductility is typically measured in percent elongation or reduction in area.

The shape and magnitude of the stress-strain curve depend on the composition of the material, heat treatment, prior history of plastic deformation and strain rate, temperature and state of stress imposed during testing [48].

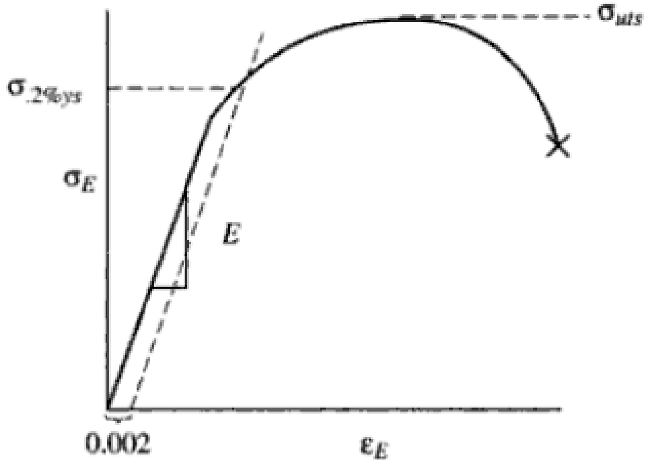

Figure 2.11: An example of a stress-strain curve for a typical engineering alloy with σ_E being engineering stress and ϵ_E being engineering strain

In a tensile test, the sample is mounted in a machine, and the tensile force is recorded as a function of the increase in the gage length. Engineering stress s and strain e is defined as:

$$s = \frac{F}{A_0} \tag{10}$$

$$e = \frac{\delta L}{L_0} \tag{11}$$

where F is the tensile force, A_0 is the initial cross-sectional area, L_0 is the initial gage length and δL is the change in gage length. The first part of the stress-strain curve, Figure 2.11, corresponds to elastic deformation. Here the bonds between the atoms are stretched such a way that when the stress is removed, the bonds relax and the material returns to its natural shape. The other type of deformation is plastic deformation, which is the part of the curve after the elastic portion. Here the planes of atoms slide over one another and the deformation is not removed when removing the stress [49].

3 Experimental

3.1 Material

The SDSS-alloy UNS S32760 (Zeron 100) was used in the experiments in this thesis. The chemical composition is given in Table 1 and the material was provided by Equinor ASA.

Table 1: Chemical composition of UNS S32760 (wt%)[50]

Alloy element	**Cr**	**Ni**	**Mo**	**Cu**	**Mn**	**W**	**Si**	**N**	**C**	**P**	**S**
wt%	25.55	8.28	3.46	0.72	0.52	0.52	0.42	0.2-0.3	0.018	0.017	0.001

The material was investigated in situ during heat treatment at high temperatures which caused a phase transformation that lead to the intermetallic phases σ and χ. Tensile testing of the material heat treated for four weeks at 300°C was also carried out.

3.2 Sample Preparation

The sample preparation was done with a sample holder of stainless steel with a diameter of 25 mm shown in Figure 3.1. First, the samples were grinded with the machine ATM Saphir 330 with 150 rpm and with water as a lubricant. Used together with this machine was SiC paper with grit 500, 800, 1200, 2400 and 4000. After the grinding, the samples were polished with Struers Tegramin-30 with force 20 N and 150 rpm with belonging polishing disk, diamond suspension with particle size 3.0 μm and 1.0 μm and with ethanol-based lubricant for 15 minutes. To eliminate the deformation formed by the polishing, vibration polishing was used. The samples were vibration polished for 24 hours with Buehler Vibromet 2. An amplitude of 70% was used for vibration polishing and a weight of 200 grams. After all the grinding steps, both the polishing steps, and the vibration polishing, the samples were cleaned with ethanol and washed in VWR ultrasonic bath, and then finally dried in hot air. The final cleaning stage was to plasma clean the samples for five minutes with Fischione Model 1020.

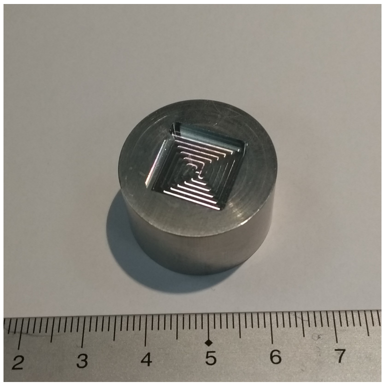

Figure 3.1: Sample holder for sample preparation with diameter 25 mm

3.3 Scanning Electron Microscope (SEM)

The SEM used to study the material and acquire the EBSD data was Zeiss Ultra 55 FESEM. The parameters used for EBSD is shown in Table 2. The magnification and the working distance varied a little between the different experiments and is shown in Table 3.

Table 2: Parameters used in SEM for the characterization with EBSD

Parameter	**Value**
Accelerating voltage	20kV
Aperture	300 µm
Angle	70°
High current mode	ON
Dynamical focus	6-15 %

Table 3: Magnification and working distances in the different experiments

Experiment	*1*	*2*	*3*	*4*	*5*	*6*	*7*
Magnification	200X	200X	300X	300X	300X	300X	300X
Working distance [mm]	24.7	24.5	24.3	24.1	24.4	24.5	25.1

3.4 Electron Backscatter Diffraction (EBSD)

EBSD analyses were done on all the samples. The NORDIF UF-1100 EBSD detector together with the software NORDIF 3.1 was used to acquire the patterns. The scan mode was set as "Timed" and the electron and background images were set as "Manual" in the NORDIF software, see Appendix B for manual on software. The acquisitions were done with the parameters shown in Table 4 in every experiment. The calibration settings are also shown in Table 4. To acquire a scan before the start of the heat treatment, averaging 1 and step size 0.5 μm were used in every experiment. This was done to be able to scan a bigger area without the expense of time to choose a wanted area.

Table 4: Parameters used in NORDIF 3.1 Software in the acquisitions

Parameter	**Acquisition**	**Calibration**
Averaging	5	5
Speed	400 fps	140 fps
Resolution	120x120 px	160x160 px
Exposion time	2450μs	7092 μs
Gain	4	1

Figure 3.2 shows how a period was split in scan time and pause. The period was chosen to be 30 minutes and the scan time varied a little, from 21 to 26 minutes all which is shown in Table 5. The first scan was done 10 minutes after heating to avoid thermal expansion during the scan. The area scanned was in most of the experiments 85x85 μm, all of the areas can be seen in Table 7. In between the scan times, the region of interest (ROI) had to be adjusted to correct for thermal expansion of the steel as well as drifting.

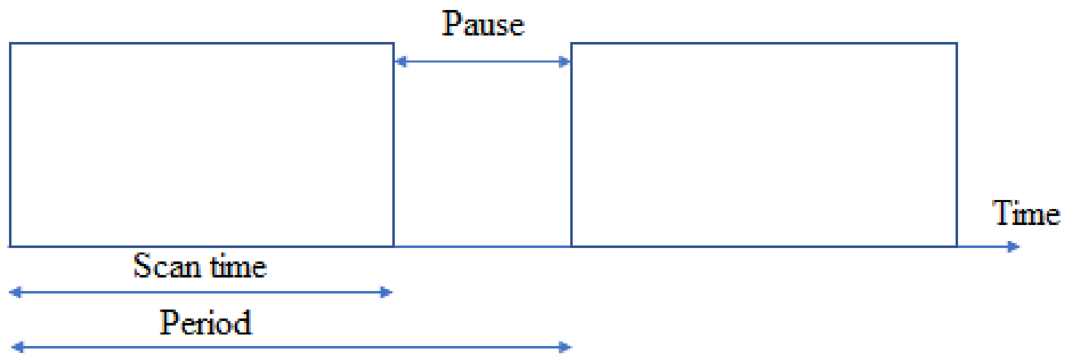

Figure 3.2: The heating intervals

Table 5: Time intervals, areas and step sizes for the in situ observations

Experiment	*1*	*2*	*3*	*4*	*5*	*6*	*7*
Area [µmxµm]	80x80	68x68	85x85	85x85	85x85	85x85	85x85
Step Size [µm]	0.25	0.20	0.25	0.25	0.25	0.25	0.25
Scan time [mm:ss]	21:04	23:56	24:22	24:22	24:22	24:22	24:22
Scan pause [mm:ss]	08:56	06:04	05:38	05:38	05:38	05:38	05:38
Scan period [mm:ss]	30:00	30:00	30:00	30:00	30:00	30:00	30:00

For every measurement five calibration patterns were collected, one in each corner and one in the middle of the area. A background picture was acquired before the start of acquiring the patterns. This was done to get a better signal and avoid background noise.

3.4.1 Indexing and Analysis of EBSD Data

The data was indexed with default bmt material files for γ and α and bmt material files for intermetallic phases σ and χ provided by Rene de Kloe, EDAX, in TSL OIM Data Collection version 7.3.b. The parameters used for the Hough transform is shown in Table 6.

The data from the EBSD was characterized with TSL OIM Analysis version 7.3.b. This software was mainly used to acquire IQ-, IPF- and phase maps as well as check CI- and fit values for different areas. The misorientation between different grains

Table 6: OIM Data Analysis Hough Parameters

Parameter	Value
Binned Pattern Size	96
Theta Step Size	0.5°
Rho Fraction	88
Max Peak Count	10
Min Peak Count	3
Hough Type	Classic
Hough Resolution	Low
Convolution Mask	7x7
Min Peak Magnitude	1
Max Peak Magnitude	10
Peak Symmetry	0.70
Vertical Bias	0%

was also acquired in this software.

3.4.2 In Situ Heating

To assemble the heating stage the manual made by Enstad et. al. [51] was used. The setup in the SEM is shown in Figure 3.3a where the sample, heating stage and the heating element is marked. For a more detailed image of the stage, see Figure 3.5. The strain relief was used to fasten the heating element and the thermocouples for the sample and the oven so that these would not break during installation. The heating in the setup is controlled by an external computer shown in Figure 3.3b where the in situ stage controller is marked. This computer registers the temperature in the sample and the oven with the help of the thermocouples. The tools are developed by Rémy Chiron at CNRS in France. The thermocouples used to measure the temperature in the oven and in the sample is type K thermocouples with Inconel 600-mantle and diameter 0.5 cm.

Gloves were used during the entire installation. The stage was assembled with caution, because the equipment is quite fragile. In the first experiments the stage was assembled by an engineer at the lab, and in the last experiments the assembling was done by the author.

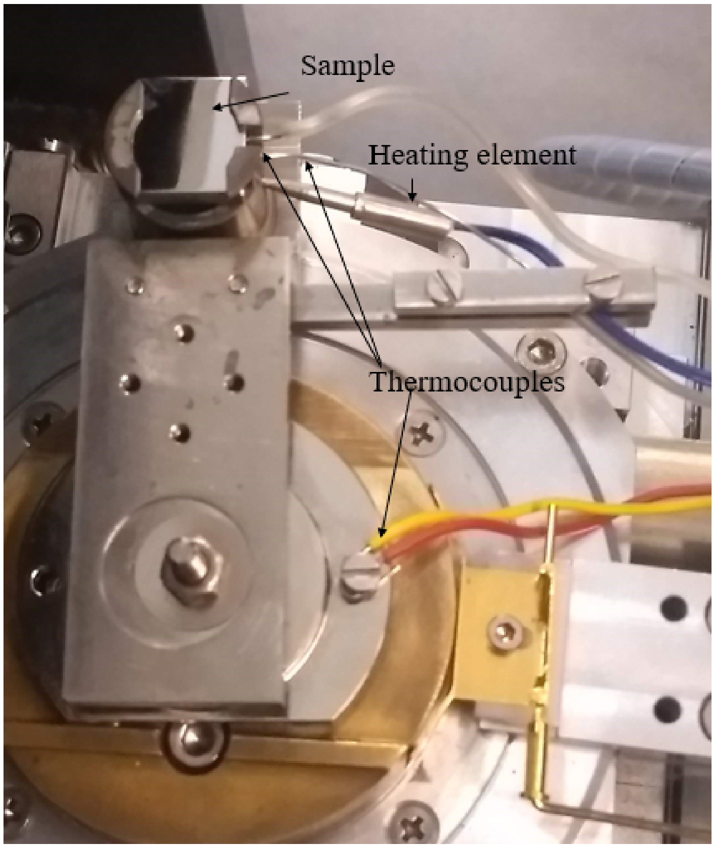

(a) Stage with the sample inserted

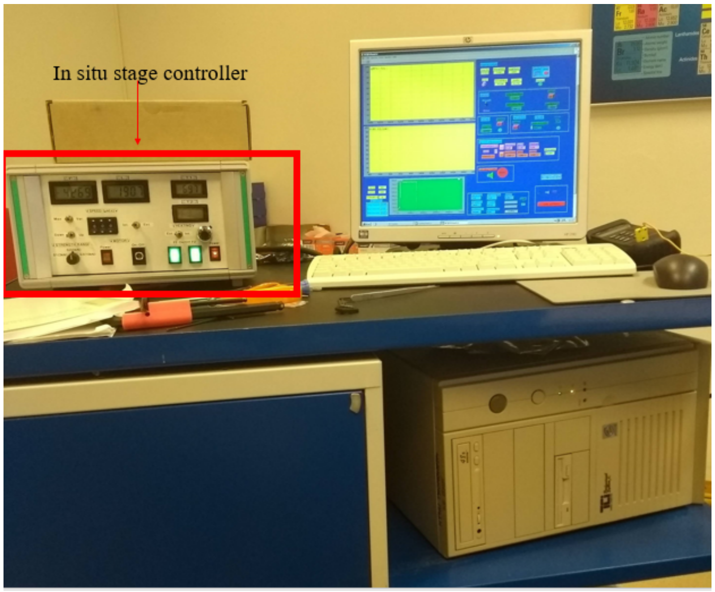

(b) The computer used for adjusting temperature in the oven

Figure 3.3: The stage and the computer used for the experiments

The dimensions of the samples used are given in Figure 3.4. The width of the sample is not critical and can be larger than 11 mm. Height should be 3 mm ±0.5 mm. The hole in the sample is to plug in the thermocouple. The hole should have a diameter of 0.55 mm and be about 2-3 mm deep. The hole was placed in the center of the sample.

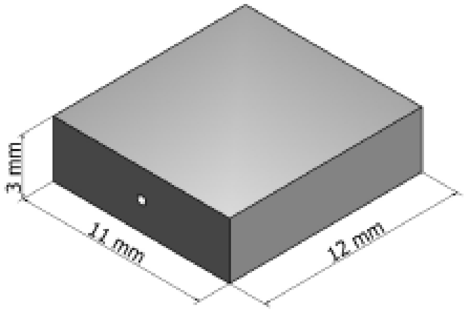

Figure 3.4: Dimensions for sample used for in situ heating in SEM [51]

A thermocouple was also attached to the stage of the SEM to make sure that the temperature inside the SEM was not too high. Unfortunately, this thermocouple did not work properly, it showed negative values. Preferably the temperature on the stage should not be higher than 47 °C.

Before placing the heating stage in the chamber, all of the wires were fastened with the strain relief and the different parts of the heating stage were fastened to each other. The sample was placed above the oven and fastened with a screw which was located underneath the oven. The heating element as well as the thermocouples for the oven and sample was fastened to a part marked ″Heating″, while the thermocouple for the stage was fastened to a part marked ″Traction″. The equipment is marked this way because it can be used both for traction and heating.

The stage was tilted up to 50° before the thermocouples for the oven and the sample was fastened. The reason to tilt it to only 50°was that the stage would crash into the lens at higher angles. The thermocouples were fastened, then the stage were pushed further into the chamber and tilted to 70°. Through this process the chamber was

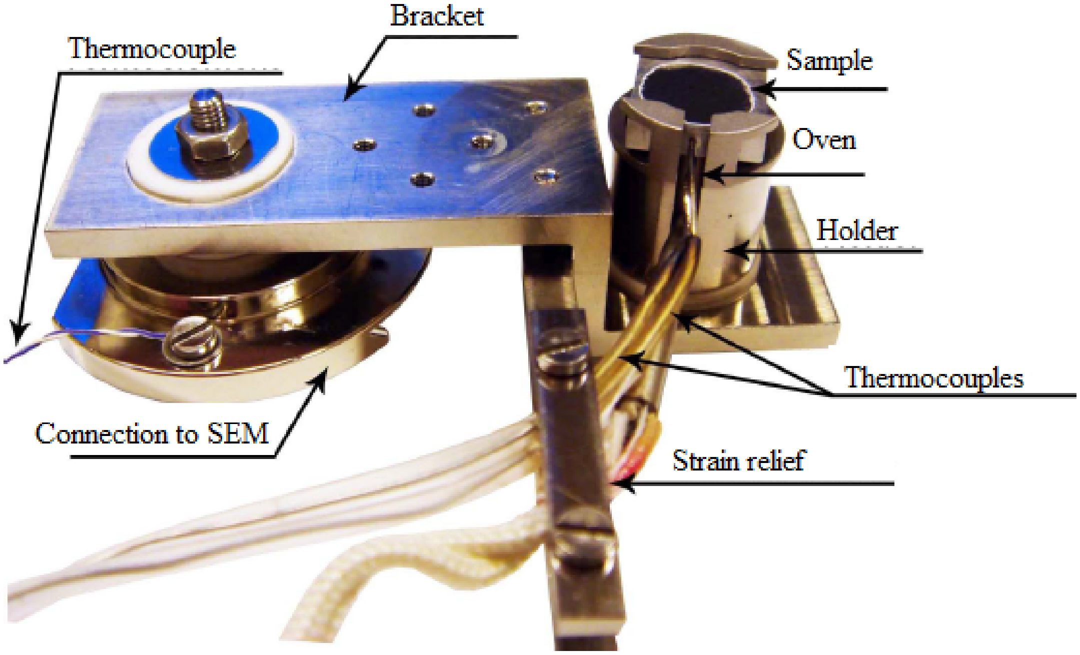

Figure 3.5: The heating stage [51]

open, and before the chamber was closed the thermocouples were checked to see if they still were injected into the oven and sample.

In total, seven heating experiments were done. The parameters for the different measurements is shown in Table 7. The heating rate was 1°C/s. As can be seen the temperature difference between the sample and oven varies in the experiments. HT Traction Software was used to heat and track the heating of the samples. The parameters L1 = 18, *H1 = 14* and *Strength Range* was set as *S2 (4500 N)* in the HT Traction software to only use the heating part of it. The program is programmed in a way that the temperature measured in the oven is the value set by the operator.

Table 7: Temperatures measured in the different thermocouples for the in situ observations

Experiment	*1*	*2*	*3*	*4*	*5*	*6*	*7*
Temperature oven [°C]	700	675	650	650	640	625	750
Temperature attached box [°C]	715	690	664	666	655	640	766
Temperature sample [°C]	610	595	685	540	590	556	680
Number of scans	15	10	15	11	15	15	14
Total time [min]	460	310	460	240	460	460	430

3.4.3 JMAK (Johnson-Mehl-Avrami- Kolmogorov)-Equation

The curves for the phase fraction per time for the sigma phase was plotted in Excel. This was done by taking the time after heating the scans were acquired and the phase fraction in each scan. These curves were then approximated to the JMAK-equation using Solver with variables n and k and the least square method. To be able to do this the equation was modified to:

$$ln(1-f) = -kt^n \tag{12}$$

where f is fraction transformed, k is a reaction constant in min^{-n} which is sensitive to temperature, and exponent n is a dimensionless constant that depends on combination of nucleation and growth mechanisms [1].

The JMAK equation was calculated for the six first experiments. The reason for not calculating the last one was due to large amounts of obvious wrong indexing in this experiment, see Appendix E.8.

3.5 Tensile Testing

Tensile specimens were made from the bolts shown in Figures 3.6 and 3.7. In each layer of the bolt shown in Figure 3.6, three tensile specimens were cut as shown in Figure 3.8. This was supposed to be done in five layers, but due to difficulties with cutting the material, only eleven samples were cut instead of 15, the sample dimensions given in Table 8. The seven last samples shown in Table 9 was made at a later point, and had a bigger width to make them easier to cut. The heat treatments done on the samples is shown in Table 10. The tensile testing was done in a 100 kN MTS 810 with an extensometer of 25 mm and a strain rate of 2 mm per second.

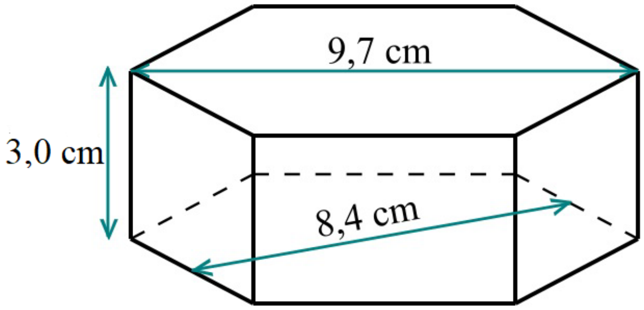

Figure 3.6: The dimension of the bolt used to make the first tensile specimens

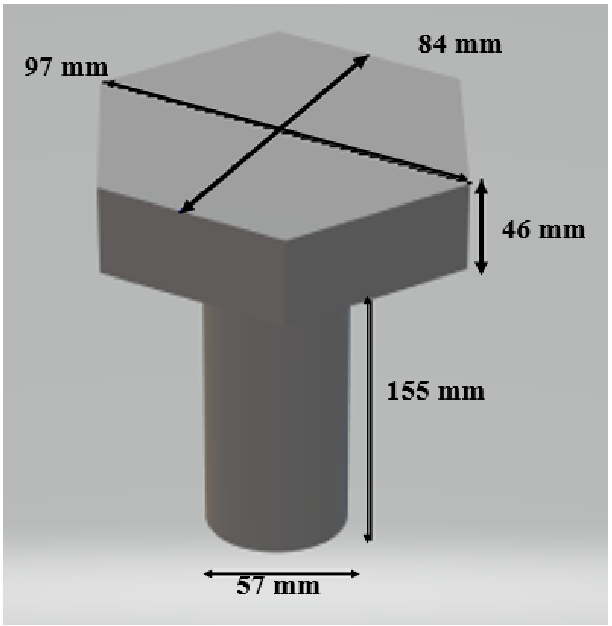

Figure 3.7: The dimension of the bolt used to make the second tensile specimens

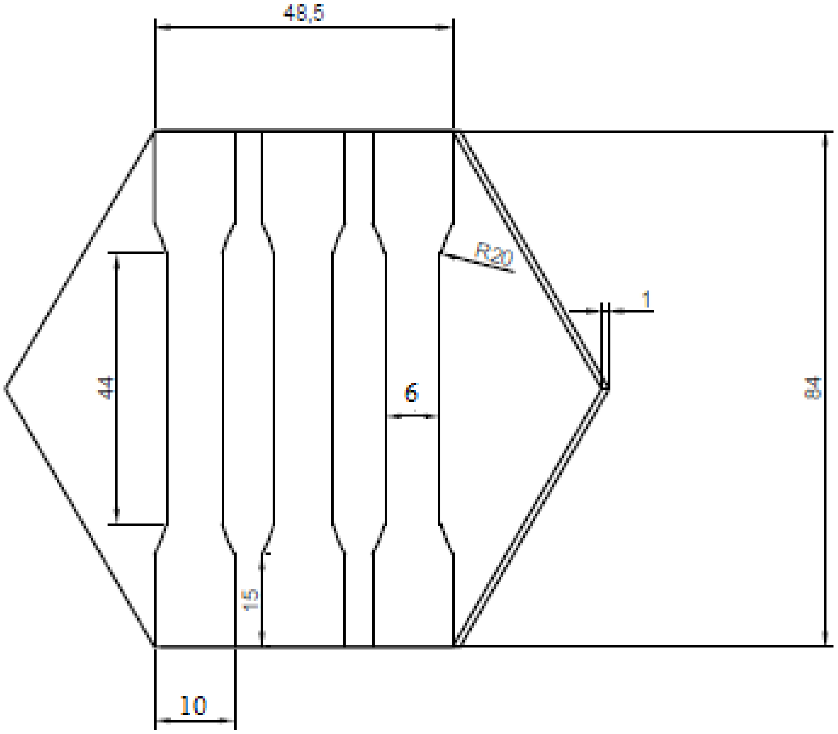

Figure 3.8: Schematic of how to cut the tensile specimens

Table 8: Cross sectional area of the tensile samples made from bolt in Figure 3.6

Sample	*1*	*2*	*3*	*4*	*5*	*6*	*7*	*8*	*9*	*10*	*11*
Width [mm]	0.98	1.00	1.03	1.06	1.05	1.06	1.02	1.00	0.97	1.05	1.03
Length [mm]	6.09	6.01	6.01	6.06	6.08	6.03	5.99	5.97	6.02	6.05	6.07

Table 9: Cross sectional area of the tensile samples made from bolt in Figure 3.7

Sample	*12*	*13*	*14*	*15*	*16*	*17*	*18*
Width [mm]	2.01	2.13	2.05	2.09	2.18	2.11	1.99
Length [mm]	6.07	6.07	6.04	6.07	6.05	6.06	6.06

3.5.1 Heat Treatment of Tensile Specimens

Some of the tensile specimens were heat treated with the furnace Nabertherm N17/HR, the heat treatments done in this oven were above 750 °C and are shown in Table 10. After these heat treatments the samples were quenched in water and some of the samples were further heat treated. These heat treatments were done at 300 °C for 4 weeks in salt bath furnace and was done to simulate the use in the oil industry of SDSS-pipes used at temperatures up to 250 °C. Steel wire was used to be able to get the samples in and out of the bath. After this heat treatment, the samples were cooled in air.

Table 10: Heat treatments for the different tensile specimens

Sample	Heat Treatment
1	900 °C for 8 minutes
2	900 °C for 8 minutes
3	900 °C for 8 minutes
4	900 °C for 8 minutes + 300 °C for 4 weeks
5	900 °C for 8 minutes + 300 °C for 4 weeks
6	900 °C for 8 minutes + 300 °C for 4 weeks
7	750 °C for 4 hours
8	750 °C for 4 hours
9	750 °C for 4 hours + 300 °C for 4 weeks
10	750 °C for 4 hours + 300 °C for 4 weeks
11	As-received
12	750 °C for 4 hours + 300 °C for 4 weeks
13	750 °C for 4 hours + 300 °C for 4 weeks
14	750 °C for 4 hours
15	750 °C for 4 hours
16	As-received
17	300 °C for 4 weeks
18	300 °C for 4 weeks

4 Results

In this section tensile testing of samples as received and heat treated will be presented. The results from the in situ heat treatment will be presented with IQ-, IPF- and phase maps of two experiments. Misorientation between some grains, phase fraction in the different scans, and CI and fit values will also be presented. The rest of the results from the in situ experiments will be found in Appendix E.

4.1 Tensile Testing

In this section the results from the tensile testing will be presented. The stress versus strain curves, in addition to tables with yield strength, ultimate tensile strength and elongation will be given for the materials with varying degree of σ.

4.1.1 Material containing no σ

Samples of the as-received material was tested before and after a heat treatment at 300°C for four weeks. This material was found to contain no σ in previous work done by the author. The stress-strain curves for the as-received material before and after the heat treatment at 300°C is given in Figure 4.1. The blue curves represents the tensile samples as received and the red represents the tensile samples heat treated at 300°C for four weeks. The mechanical properties for the material containing no σ is given in Table 11, where the values for the property is given and the standard deviation.

4.1.2 Material with 5% σ

The material heat treated at 900°C for eight minutes contains around 5% σ. This has been proven by previous work done by the author. Some of the tensile specimens

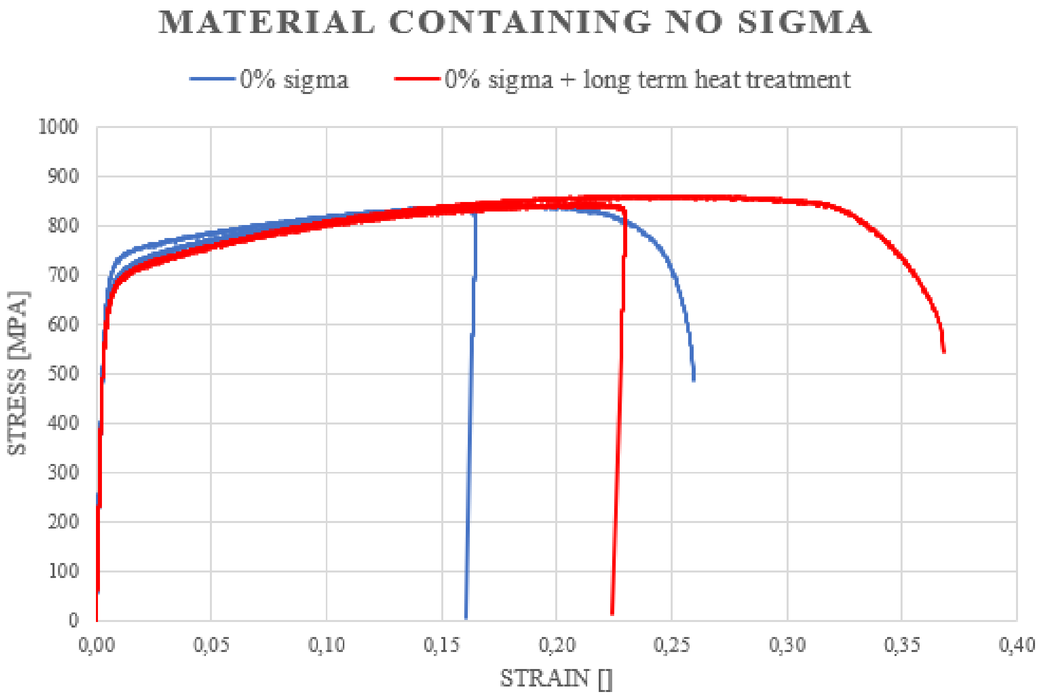

Figure 4.1: Stress-strain curve for material with no σ

Table 11: Mechanical properties for the material containing no σ

Property	*Before*	*After*
Elastic Modulus [GPa]	185.5 ±2.3	189.6 ±1.0
Yield Tensile Strength [MPa]	655.4 ±4.1	624.5 ±6.5
Ultimate Tensile Strength[MPa]	838.9 ±3.7	851.7 ±12.0
Elongation [%]	21.2 ±6.7	29.9 ±9.8

were heat treated at 300°C for four weeks. The stress-strain curves for the tensile specimens before and after this heat treatment is shown in Figure 4.2. The stress-strain curves for the tensile specimens not heat treated at 300°C is shown as the blue curves and the ones heat treated at 300°C are shown in red. The mechanical properties for the material containing around 5% σ is shown in Table 12, where the value for the property as well as the standard deviation is given.

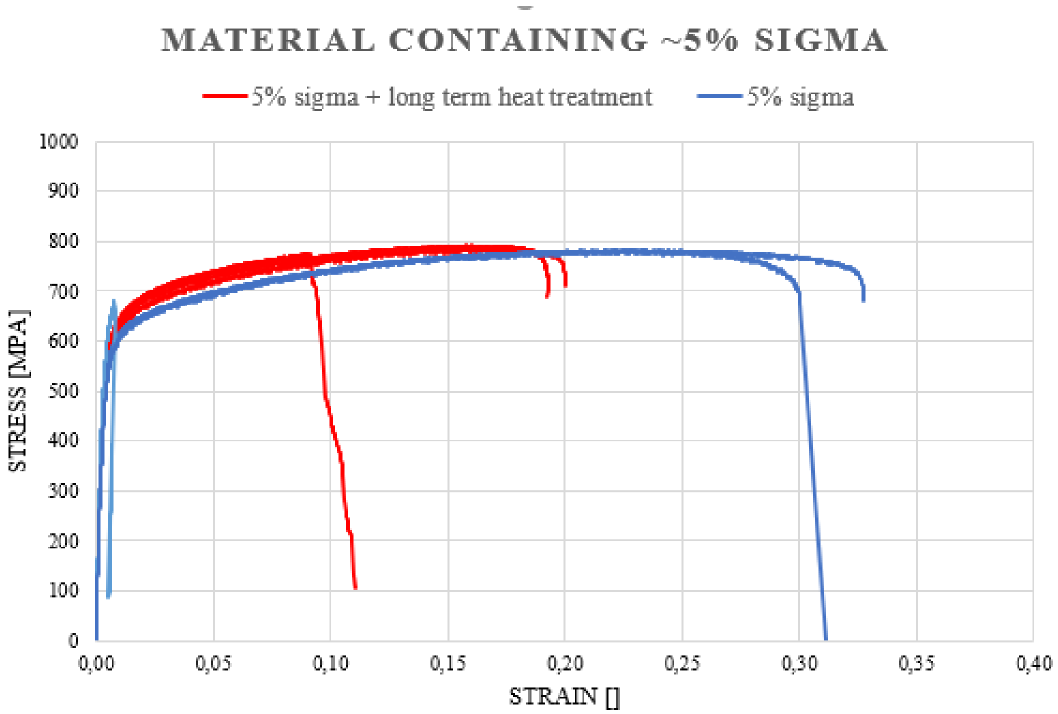

Figure 4.2: Stress-strain curve for material containing 5% σ

Table 12: Mechanical properties for the material containing around 5% σ

Property	*Before*	*After*
Elastic Modulus [GPa]	167.5 ±24.1	165.2 ±6.2
Yield Tensile Strength [MPa]	577.9 ±38.9	567.6 ±12.6
Ultimate Tensile Strength[MPa]	748.5 ±58.2	784.5 ±8.15
Elongation [%]	31.4 ±1.9	16.3 ±5.8

4.1.3 Material with 35% Intermetallic Phases

The material heat treated at 750°C for four hours contains around 35% intermetallic phases. This has been proven by previous work done by the author. Some of the tensile specimens were heat treated at 300°C for four weeks. The stress-strain curves for the tensile specimens before and after this heat treatment is shown in Figure 4.3. The stress-strain curves for the tensile specimens not heat treated at 300°C are shown as the blue curves and the ones heat treated at 300°C are shown in red. The mechanical properties for the material containing around 35% intermetallic phases are shown in Table 12, where the value for the property as well as the standard deviation is given. Notice the large standard deviation for the elongation in both cases.

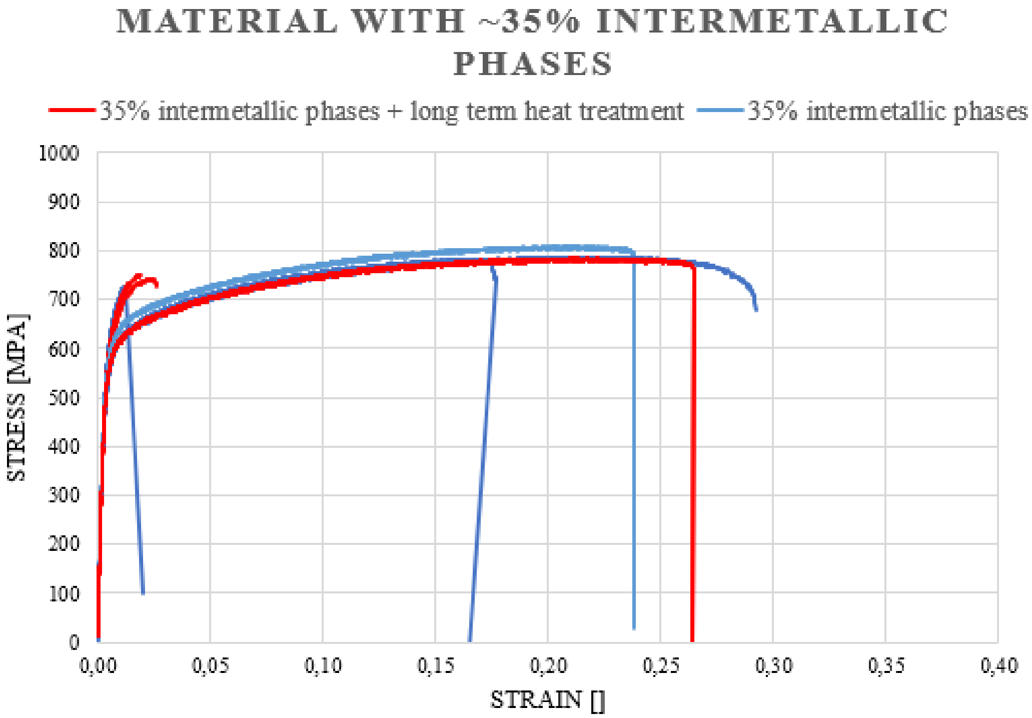

Figure 4.3: Stress-strain curve for material containing 35% intermetallic phases

Table 13: Mechanical properties for the material containing 35% intermetallic phases

Property	*Before*	*After*
Elastic Modulus [GPa]	167.0 ±13.6	164.2 ±5.1
Yield Tensile Strength [MPa]	578.8 ±30.9	587.45 ±21.6
Ultimate Tensile Strength[MPa]	776.3 ±35.6	767.6 ±23.9
Elongation [%]	18.0 ±12.1	11.2 ±11.5

4.2 In situ Heating

In this section some results from Experiments 3 and 6 from the in situ heat treatment will be presented. The other results from the other experiments will be given in Appendix E. EBSD analyses were done, and the results will be presented in the form of IQ-, IPF- and phase maps, as well as CI- and fit values for the different phases in

Experiments 3 and 6. The misorientation between specific grains will also be given. The colours indicating different orientation is shown in Figure 4.4a and the colours of the different phases is shown in Figure 4.4b. There were also obtained electron images of the area scanned for each time interval, and these will also be shown.

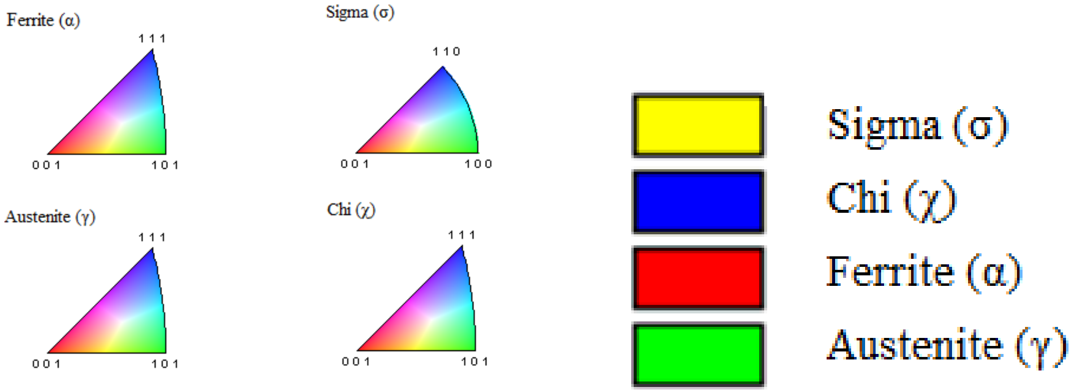

(a) Colours used in IPF maps (b) Colours used in phase maps

Figure 4.4: Colours used to describe a) IPF maps and b) Phase maps

4.2.1 Experiment 3 done at 650°C

The electron images of the area scanned in Experiment 3 are shown in Figure 4.5. Figure 4.5a shows the electron image of the area after 10 minutes of heating, and Figure 4.5b shows the electron image for the area after 430 minutes of heating. The blue line represents 100μm in the image. The contrast and brightness used differs a little from the first to the last. Notice the difference in contrast for the different phases in the two images. The red square in the images indicates the region of interest (ROI).

Four of the IQ maps from Experiment 3 are shown in Figure 4.6. The area of measurement is 85μmx85μm and step size used was 0.25μm. The grain boundaries appear clear, in focus and are dark in all the maps. No topography can be observed on the sample surface. Polishing marks can be observed in some of the grains in the middle of the map. The quality of focus can also be deducted from these maps and is decent in all the four scans. The grey tone indicates the quality of the pattern from

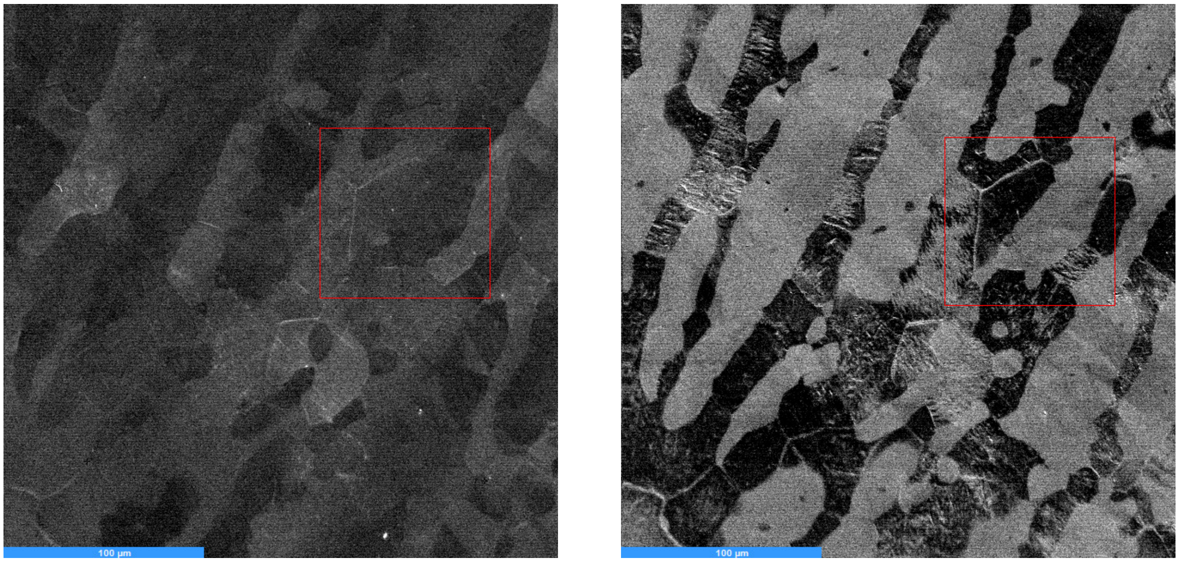

(a) Electron image taken 10 minutes after heating

(b) Electron image taken 430 minutes after heating

Figure 4.5: Electron images from Experiment 3, 10 and 430 minutes after heating respectively

that point in the sample. It can be observed that there is a difference in grey tone in the different grains inside one map as well as difference in grey tone between the different maps. It can be seen that the map in Figure 4.6d is clearly darker than the map in 4.6a, especially in some regions. There can also be observed some spots that appears in some of the grains in the later IQ maps. The black spots, the areas where the quality of the patterns are poor, grows from Figure 4.6a to Figure 4.6d. It can also be observed some movement from one IQ-map to the other, due to slightly different ROI (region of interest) in the scans.

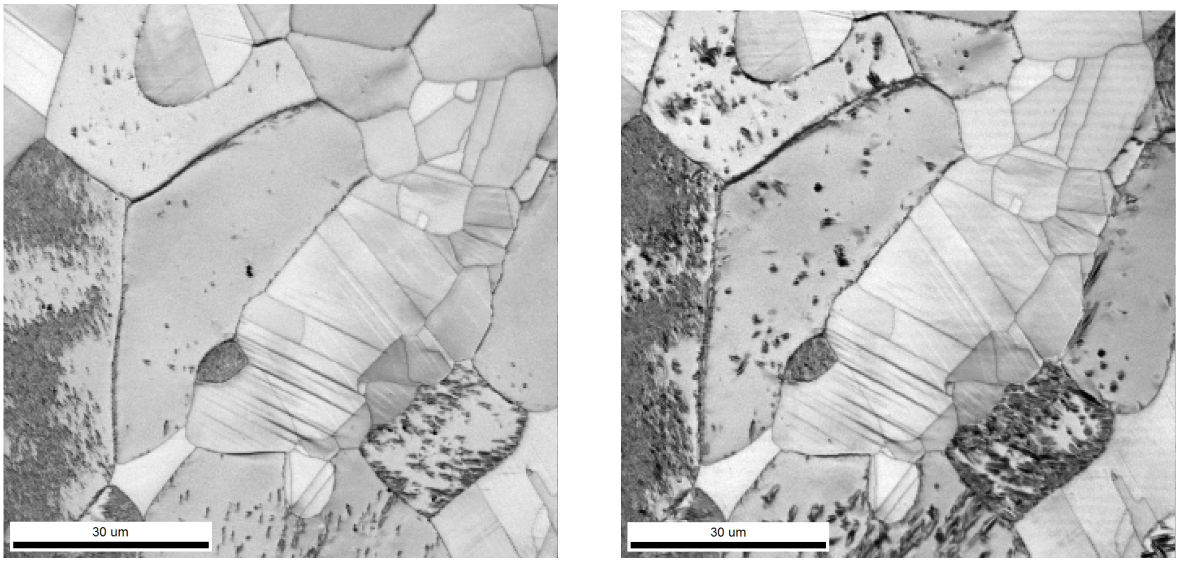

(a) IQ-map acquired 10 min after heating (b) IQ-map acquired 160 min after heating

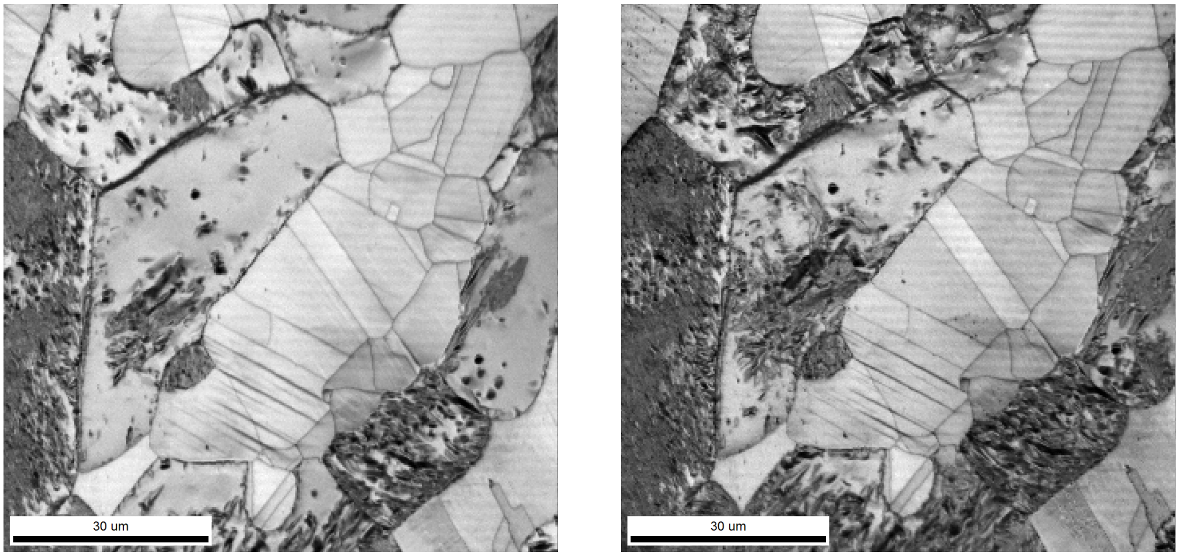

(c) IQ-map acquired 250 min after heating (d) IQ-map acquired 400 min after heating

Figure 4.6: IQ maps from Experiment 3: Temperature set at 650 °C in oven

Four of the IPF maps from Experiment 3 is shown in Figure 4.7, using the same patterns as the IQ maps in Figure 4.6 as well as the phase maps in Figure 4.8. The colour of the orientation is given by Figure 4.4a. It can be seen that the grains do not have a preferred orientation and that the nucleation of phases with new orientation starts in some grains before others and some of the new phase has a clear orientation.

Some twin boundaries are observed, and the grain sizes vary.

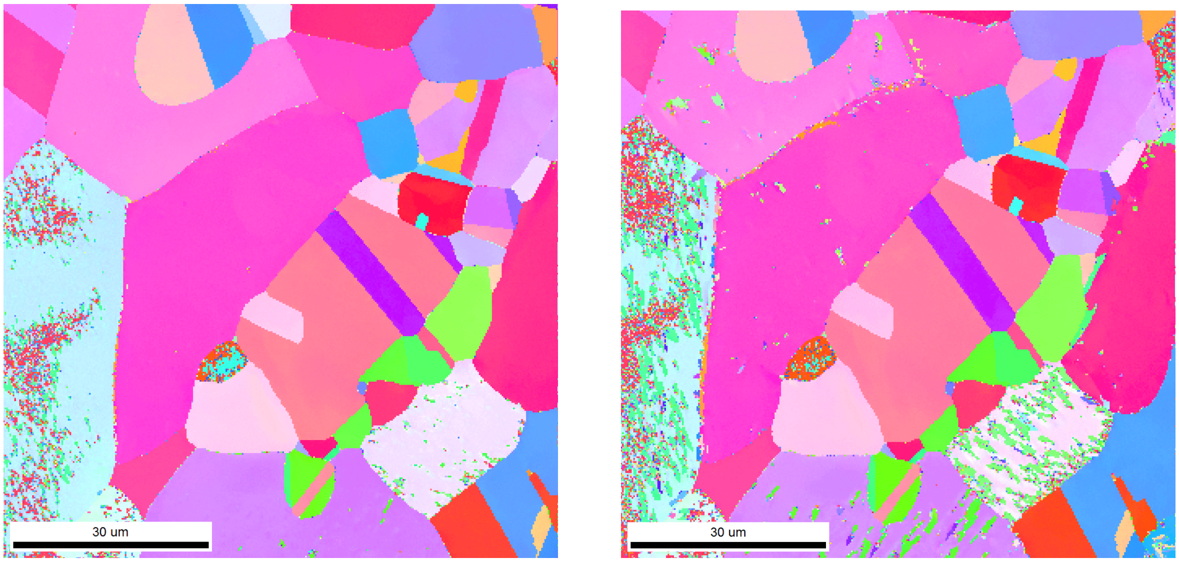

(a) IPF-map acquired 10 min after heating (b) IPF-map acquired 160 min after heating

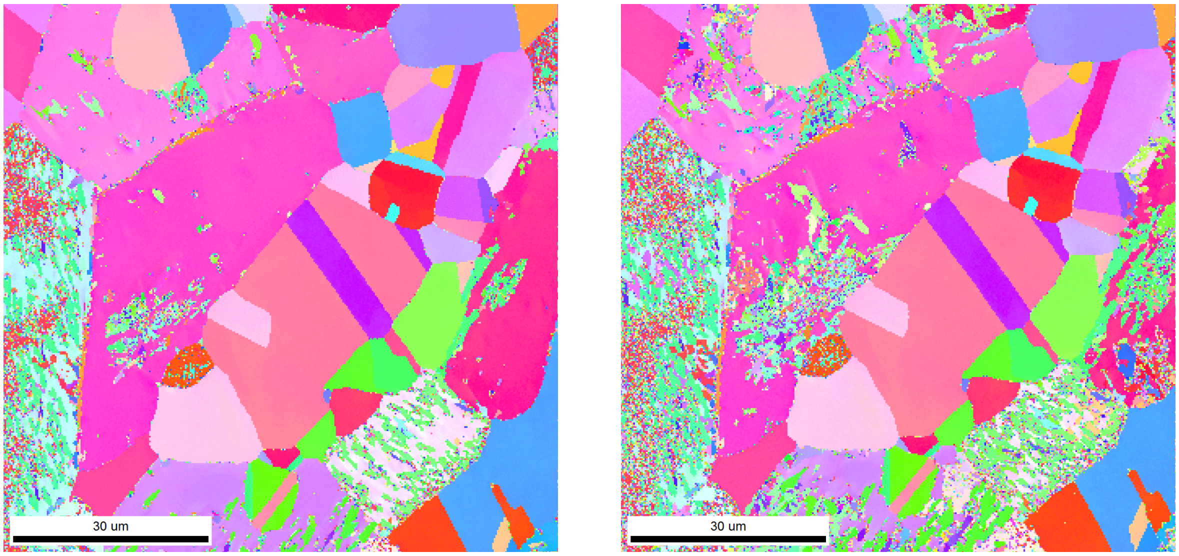

(c) IPF-map acquired 250 min after heating (d) IPF-map acquired 400 min after heating

Figure 4.7: IPF maps from Experiment 3: Temperature set at 650 °C in oven

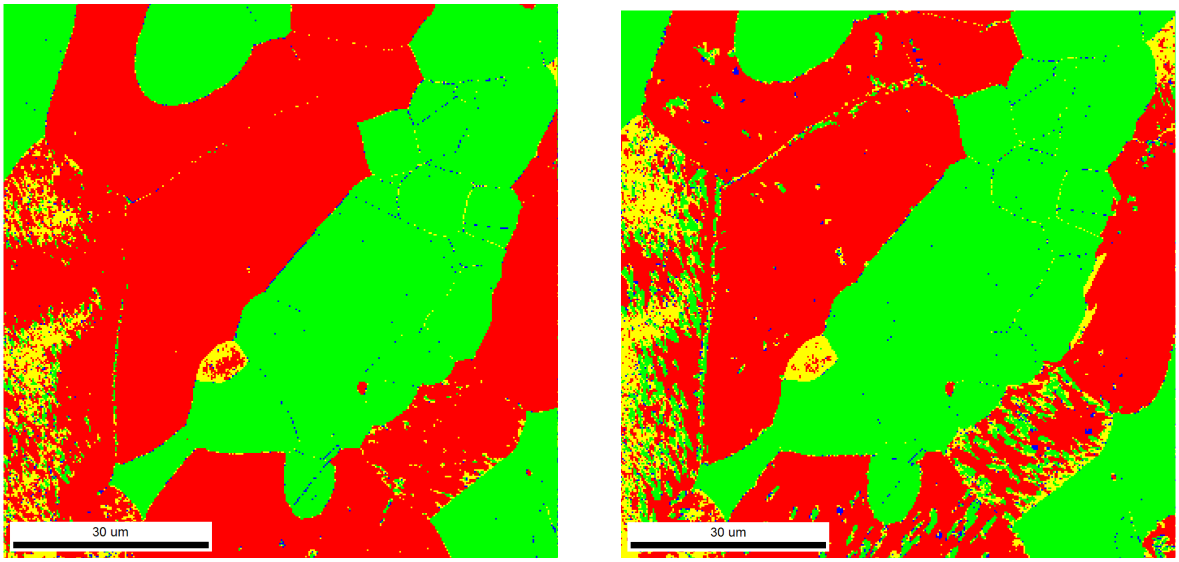

(a) Phase-map acquired 10 min after heating

(b) Phase-map acquired 160 min after heating

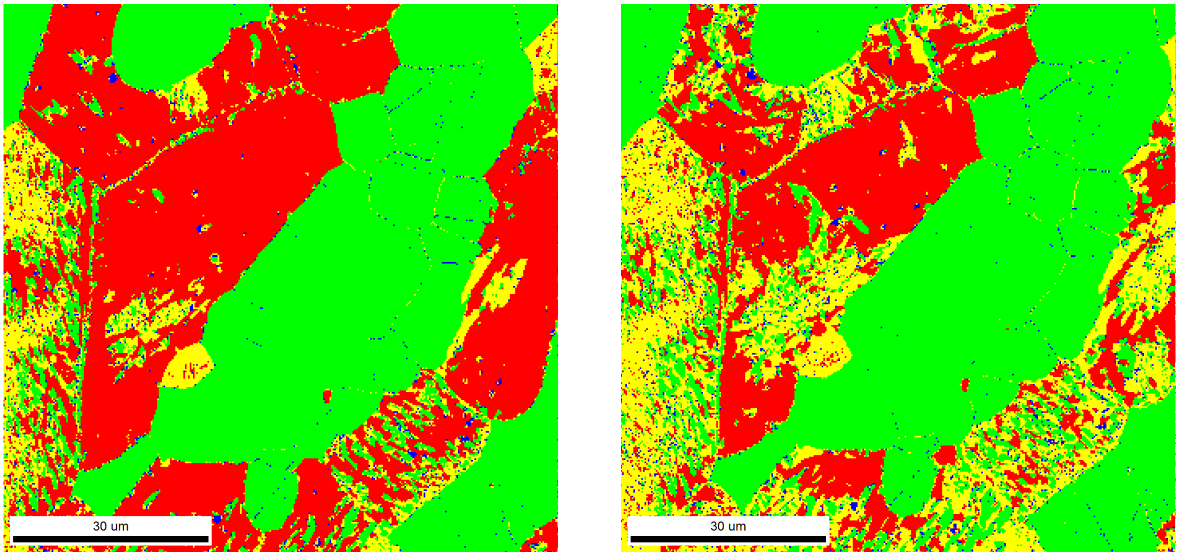

(c) Phase-map acquired 250 min after heating

(d) Phase-map acquired 400 min after heating

Figure 4.8: Phase maps from Experiment 3: Temperature set at 650 °C in oven

The phase maps from Experiment 3 are shown in Figure 4.8. The colour of the phases is given by Figure 4.4b, where the α is shown as red, γ shown as green, σ as yellow and χ as blue. In the first phase map, Figure 4.8a, all of the four phases can be seen. Notice grain boundaries in the γ indexed as χ (blue) and σ (yellow). Also notice the two intermetallic phases (σ and χ) inside the ferritic grains. Especially notice the growth of the σ-phase in grains 4 and 6, and the χ-formation in grains 1 and 6, the grain numbers given in Figure 4.9. Table 14 gives the increase and decrease of the four phases during the time interval. Table 15 shows the CI and Fit values for σ and χ in the different scans.

Table 14: Phase fraction in the different phase maps in Figure 4.8

Time after Heating	α	γ	σ	χ
10 min	0.502	0.432	0.059	0.008
160 min	0.475	0.442	0.073	0.011
250 min	0.424	0.462	0.100	0.014
400 min	0.249	0.497	0.232	0.022

Table 15: CI and Fit for the average, σ and χ phase in Experiment 3

	CI			Fit		
Time after Heating	Average	σ	χ	Average	σ	χ
10 min	0.63	0.03	0.03	0.78	1.93	1.63
160 min	0.56	0.04	0.05	0.87	1.95	1.69
250 min	0.51	0.04	0.05	0.94	1.91	1.71
400 min	0.39	0.07	0.04	1.14	1.80	1.77

Figure 4.9 shows the IPF map acquired after 10 minutes of heating. The numbers indicate the different grains inside of the sample, which is used in Tables 16 and 17 to indicate where the measurements has been done. The ferritic grains are marked with black numbers, while the γ is marked with red or blue.

Table 16 shows the misorientation of the developed phase in reference to their parent phase. The grain number in this table refers to Figure 4.9. The points where it was measured is chosen randomly for the three different phases. The mean value of the angles are 44.2°, 36.7° and 37.2 ° for γ, σ and χ respectively. The standard deviation

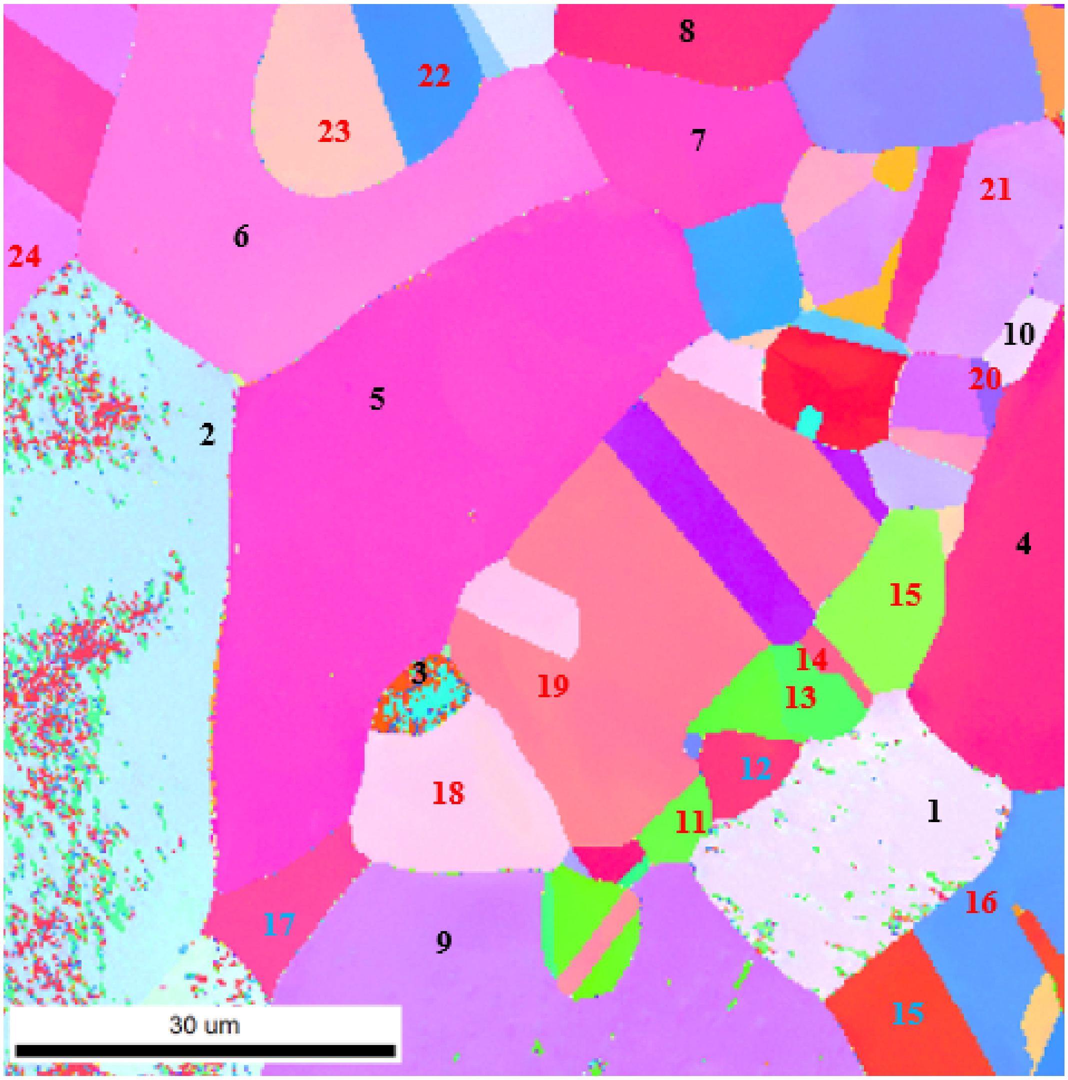

Figure 4.9: The IPF-map for the area from Experiment 3 with the numbers indicating the different grains, α marked with black numbers, γ marked with coloured

of the angles are 0.4, 12.7 and 28.9 for γ, σ and χ respectively.

Table 16: Misorientation between the different phases inside one grain given with angle/axis pair, measurements done in phase map from Figure 4.8c

In Grain	Between	Angle	Axis
1	γ/α	44.2	[-2 13 -2]
2	γ/α	44.7	[3 2 19]
4	γ/α	44.3	[23 4 -3]
5	γ/α	44.6	[-5 -28 -4]
6	γ/α	43.6	[-2 -2 13]
7	γ/α	43.8	[3 -4 20]
1	σ/α	51.7	[4 11 21]
2	σ/α	46.8	[-23 5 -18]
3	σ/α	44.2	[-2 13 -2]
4	σ/α	16.7	[-12 -1 -3]
5	σ/α	23.0	[27 8 -6]
6	σ/α	38.7	[-9 -12 5]
1	χ/α	1.2	[-11 -4 -23]
4	χ/α	59.9	[-1 -1 -1]
5	χ/α	59.7	[-1 -1 1]
6	χ/α	0.7	[17 10 -23]
7	χ/α	42.4	[-7 -4 28]
9	χ/α	59.5	[1 1 -1]

Table 17: Misorientation between the different grains where σ nucleates, measurements done in phase map from Figure 4.8c

Between grains	Phases	Angle	Axis	When
5/3	α/α	56.2	[10 -16 17]	Early
9/1	α/α	41.9	[21 2 5]	Early
6/2	α/α	57.1	[-6 8 5]	Early
5/2	α/α	43.8	[12 -19 18]	Medium
5/6	α/α	50.0	[9 2 -12]	Late
18/3	γ/α	34.4	[-9 5 28]	Early
19/3	γ/α	48.6	[11 -17 9]	Early
11/1	γ/α	60.3	[21 17 14]	Early
15/1	γ/α	32.0	[-3 13 18]	Medium
17/2	γ/α	29.9	[26 11 5]	Medium
23/6	γ/α	42.7	[-3 -9 8]	Medium
22/6	γ/α	26.2	[-8 -19 2]	Late
20/10	γ/α	53.8	[17 -6 15]	Late
21/10	γ/α	31.1	[-23 1 3]	Late

To know something about the reliability of data, CI can be used. Figures 4.10 and 4.11 shows the phase maps before and after removing all patterns that have a CI value lower than 0.1 for a ferritic grain and γ-γ grain boundaries respectively. These phase maps were acquired 250 minutes after start of heating and are cropped versions of Figure 4.8c. Notice that almost all of the points removed was indexed as intermetallic phases. Also notice the patterns indexed as intermetallic phases that remains after the removing of points.

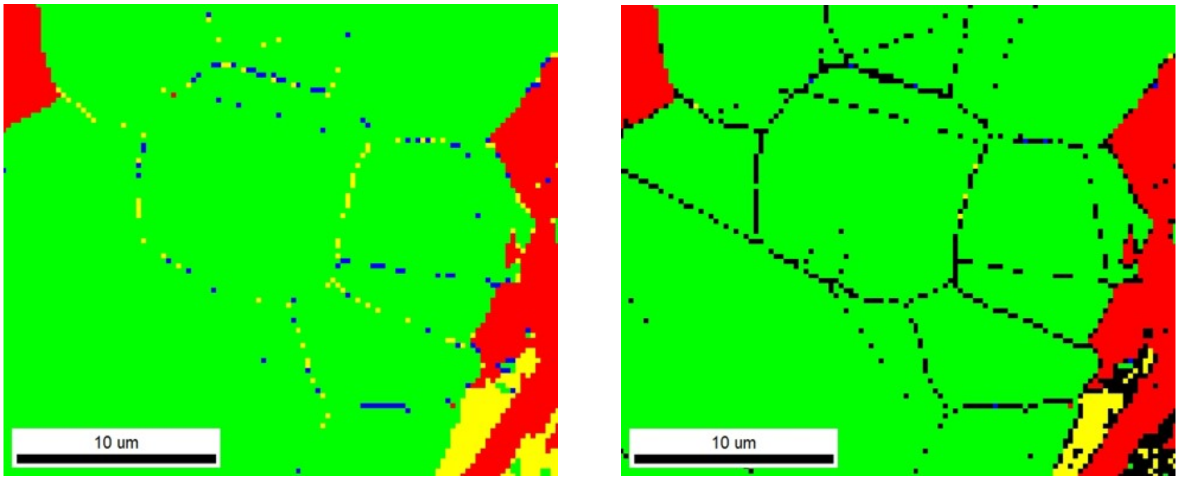

(a) Phase-map acquired 250 min after heating, no removing of points

(b) Phase-map acquired 250 min after heating, removing of all points with CI<0.1

Figure 4.10: Phase maps of γ-γ grain boundaries after 250 minutes from Experiment 3 with different degree of removing. Temperature set at 650 °C in oven

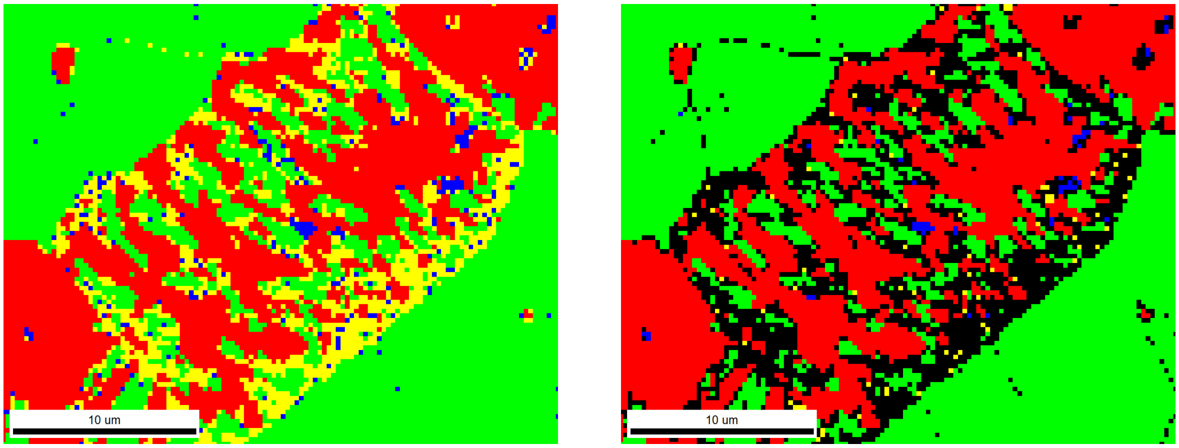

(a) Phase-map acquired 250 min after heating, no removing of points

(b) Phase-map acquired 250 min after heating, removing of all points with CI<0.1

Figure 4.11: Phase maps after 250 minutes from Experiment 3 with different degree of removing. Temperature set at 650 °C in oven

4.2.2 Experiment 6 done at 625°C

The electron images of the area scanned in Experiment 6 is shown in Figure 4.12. Figure 4.12a shows the electron image acquired 10 minutes after heating, and Figure 4.12b shows the electron image for the area after 430 minutes of heating. The blue line represents 100μm in the image. The contrast and brightness used differs from the first to the last. Notice the difference in contrast for the different phases in the first and the last image. The red square in the electron images indicates the region of interest (ROI).

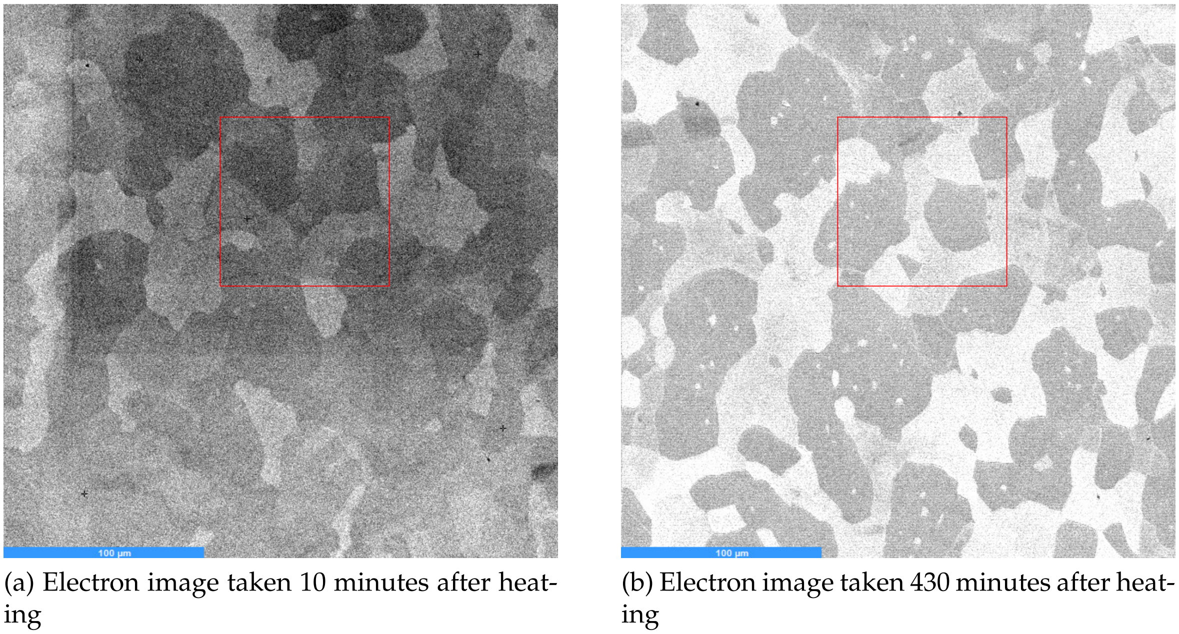

(a) Electron image taken 10 minutes after heating

(b) Electron image taken 430 minutes after heating

Figure 4.12: Electron images from Experiment 6, 10 and 430 minutes after heating respectively

Four of the IQ maps from Experiment 6 are shown in Figure 4.13. The area of measurement is 85μmx85μm and step size used was 0.25μm. The grain boundaries appear clear, in focus and are dark in all of the maps. No topography can be observed on the sample surface. The quality of focus can also be deducted from these maps, which can particularly be seen from the grain boundaries. The gray tone indicate how good the pattern from the points in the sample is. Some black lines in the lower right of the map can be observed in Figure 4.13a, as well as some patterns with worse quality in the grain in the lower middle. It can be observed that there is a difference in gray tone in the different grains inside one map as well as difference in gray tone between the different maps. It can be seen that the map in Figure 4.13d is clearly darker than the map in 4.13a in some regions or grains. In the later IQ maps, Figures

4.13b-4.13d, some black spots can also be seen in some of the grains. It can be observed some movement from one IQ-map to the other, due to slightly different ROI in the scans.

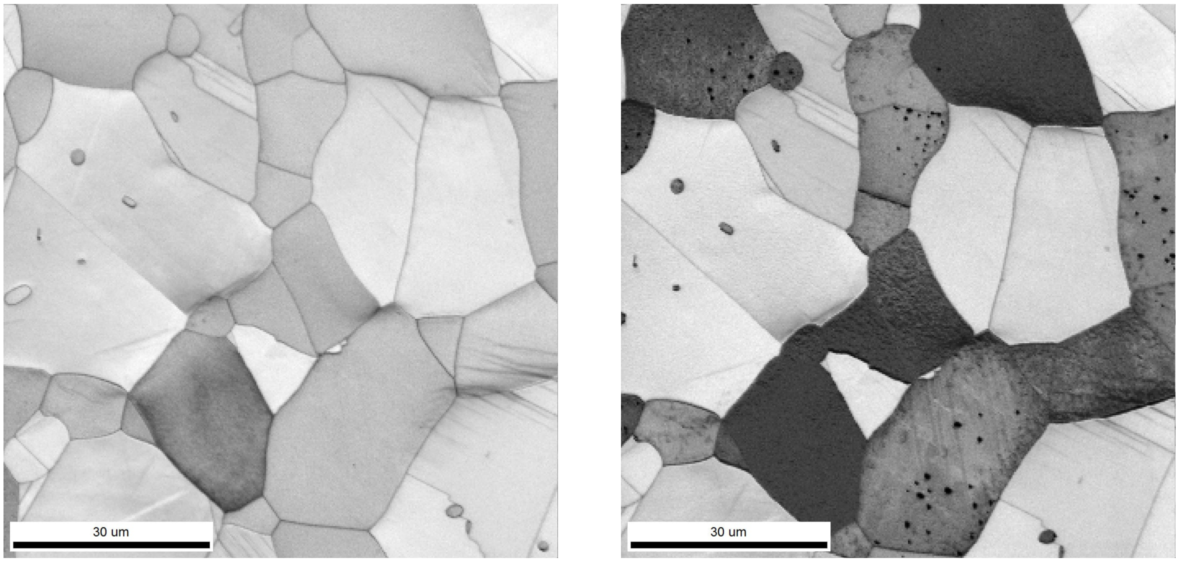

(a) IQ-map acquired 10 min after heating (b) IQ-map acquired 160 min after heating

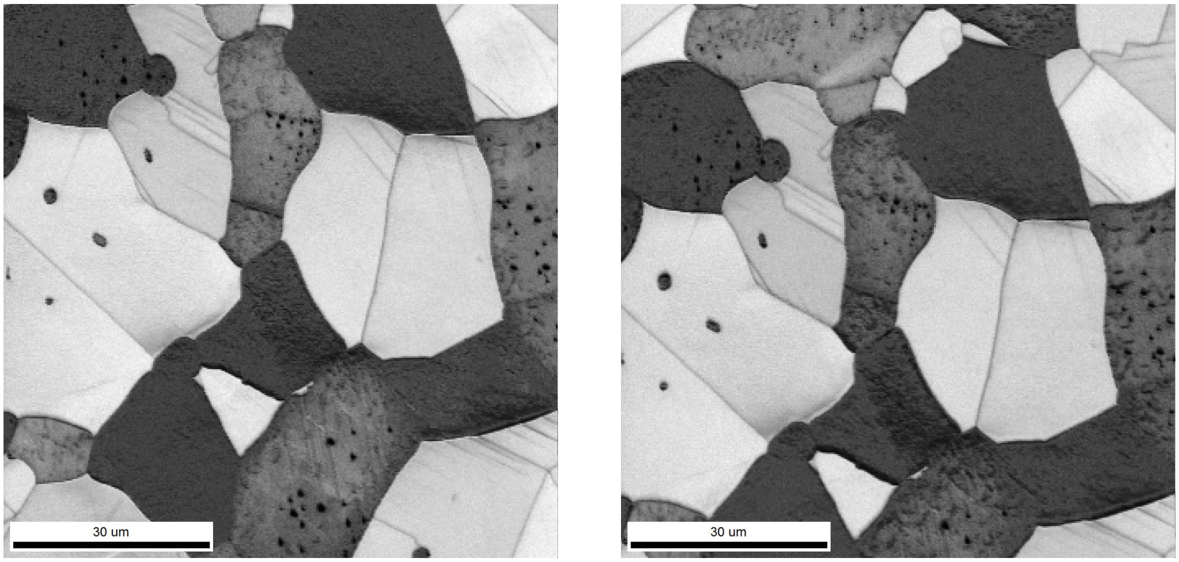

(c) IQ-map acquired 250 min after heating (d) IQ-map acquired 400 min after heating

Figure 4.13: IQ maps from Experiment 6: Temperature set at 625 °C in oven

The IPF maps from Experiment 6 is shown in Figure 4.14, using the same patterns as the IQ maps in Figure 4.13 as well as the phase maps in Figure 4.15. The colours of the orientation is given in Figure 4.4a. It can be seen that the grains in Figure 4.14a do not have a preferred orientation. It can be seen that the development of the new phases starts in some grains before others and that the new phase has random orientation. It can be seen that there are some big and some small grains and some twins can be observed.

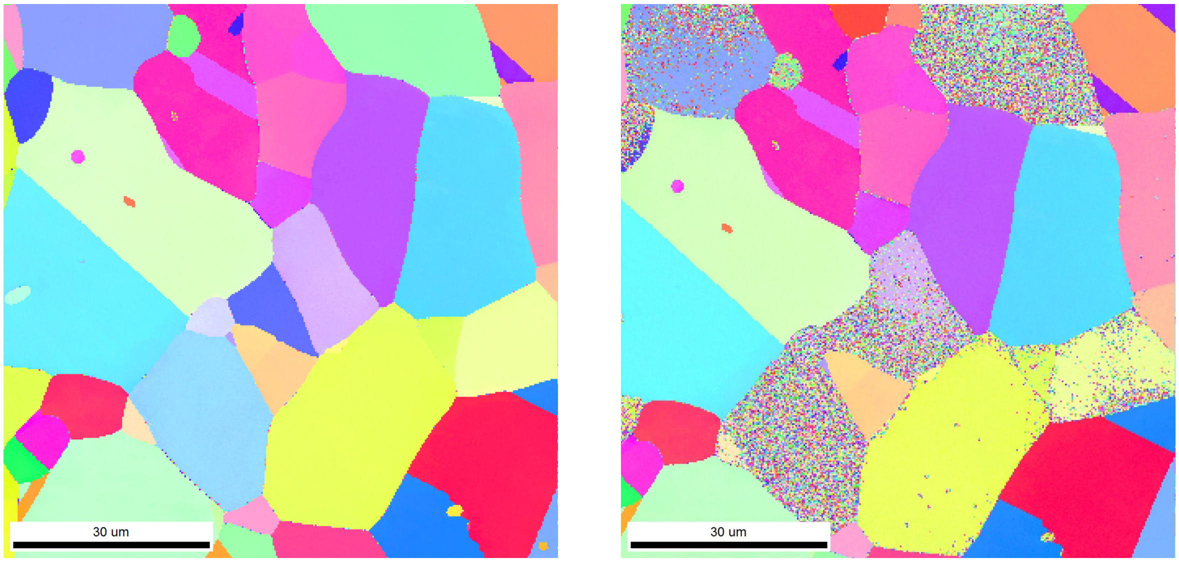

(a) IPF-map acquired 10 min after heating (b) IPF-map acquired 160 min after heating

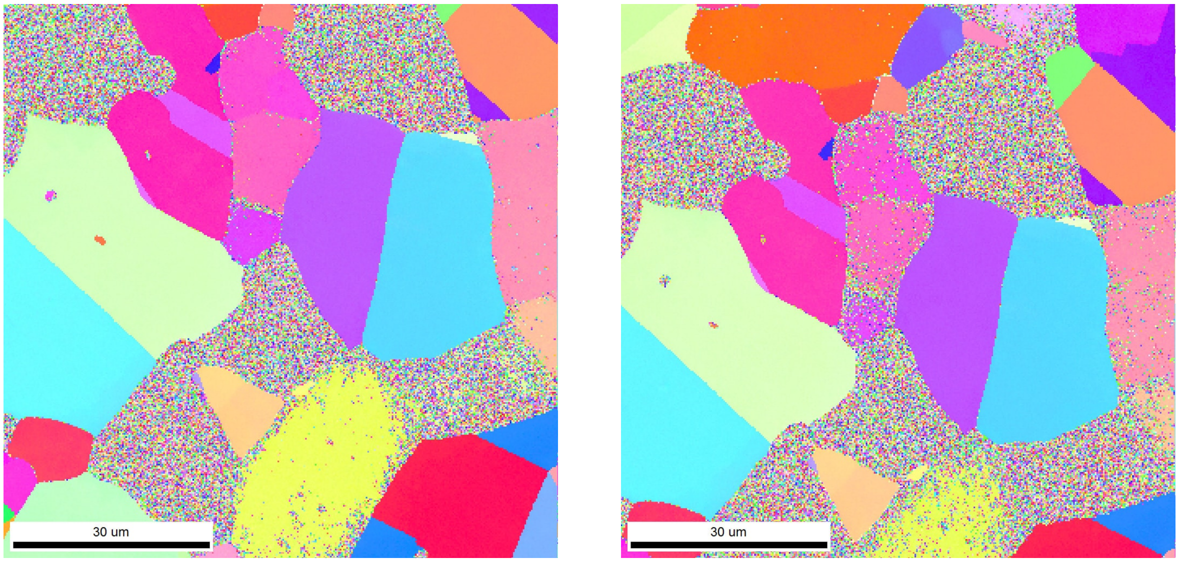

(c) IPF-map acquired 250 min after heating (d) IPF-map acquired 400 min after heating

Figure 4.14: IPF maps from Experiment 6: Temperature set at 625 °C in oven

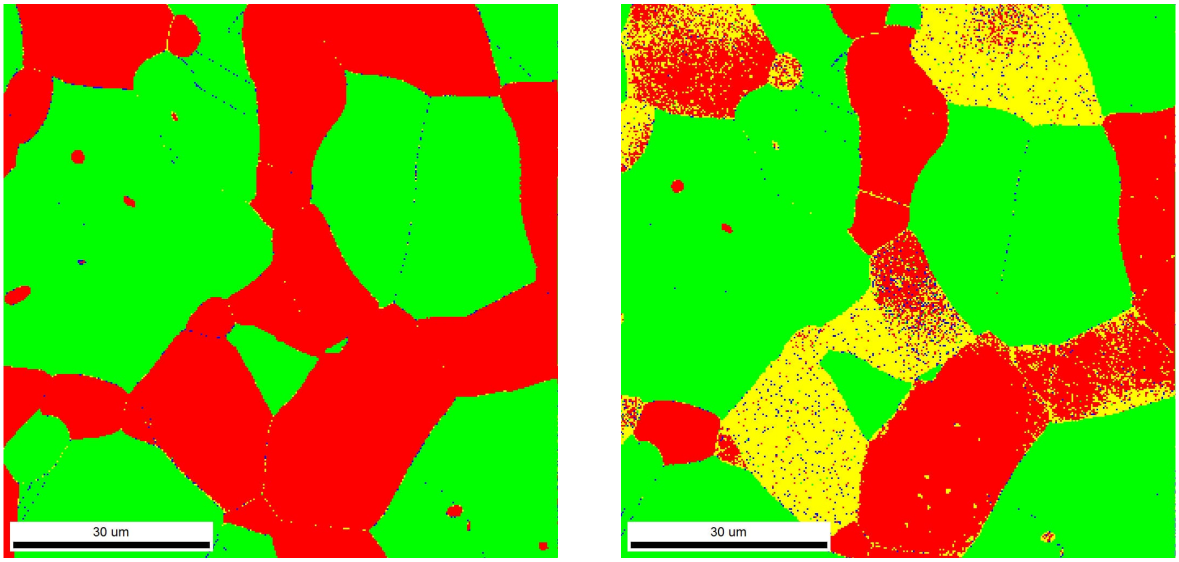

(a) Phase-map acquired 10 min after heating

(b) Phase-map acquired 160 min after heating

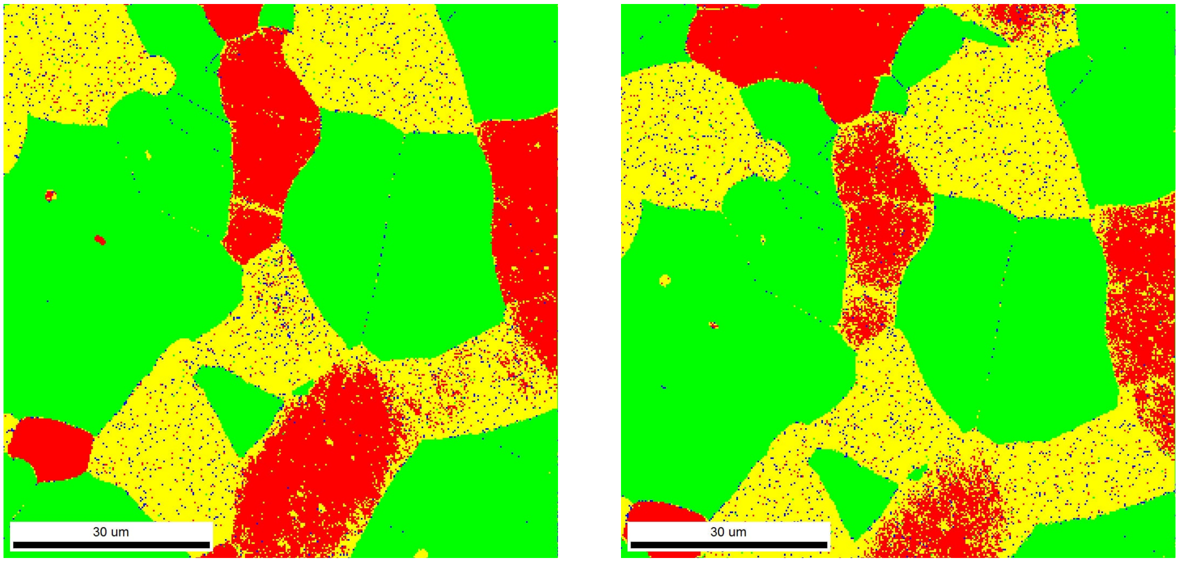

(c) Phase-map acquired 250 min after heating

(d) Phase-map acquired 400 min after heating

Figure 4.15: Phase maps from Experiment 6: Temperature set at 625 °C in oven

The phase maps from Experiment 6 is shown in Figure 4.15. The colour of the phases is given in Figure 4.4b, where α is red, γ is green, σ is yellow and χ is blue. From the start, the structure is clearly consisting of γ and α, as well as some single points being indexed as χ and σ. Notice both the γ-γ- and the α-γ grain boundaries being indexed as σ and χ. Notice in later phase maps that the σ-phase appears in some grains before others. The phase fractions in the different phase maps is given in Table 18, and the CI and Fit values for the average, σ and χ is given in Table 19.

Table 18: Phase fraction in the different phase maps in Figure 4.8

Time after Heating	α	γ	σ	χ
10 min	0.436	0.559	0.003	0.003
160 min	0.275	0.541	0.174	0.010
250 min	0.188	0.529	0.270	0.012
400 min	0.172	0.499	0.314	0.015

Table 19: CI and Fit for the σ and χ phase in Experiment 6

	CI			Fit		
Time after Heating	Average	σ	χ	Average	σ	χ
1	0.68	0.02	0.02	0.72	1.91	1.53
6	0.46	0.02	0.02	1.09	2.11	2.02
9	0.40	0.02	0.02	1.22	2.12	2.08
14	0.36	0.02	0.02	1.28	2.13	2.09

Figure 4.16 shows the IPF map acquired after 10 minutes of heating in Experiment 6. The numbers indicate the different grains inside of the sample, which is used in Table 20 to indicate where the measurements has been done. The ferritic grains are marked with black numbers, while the γ is marked with red or blue.

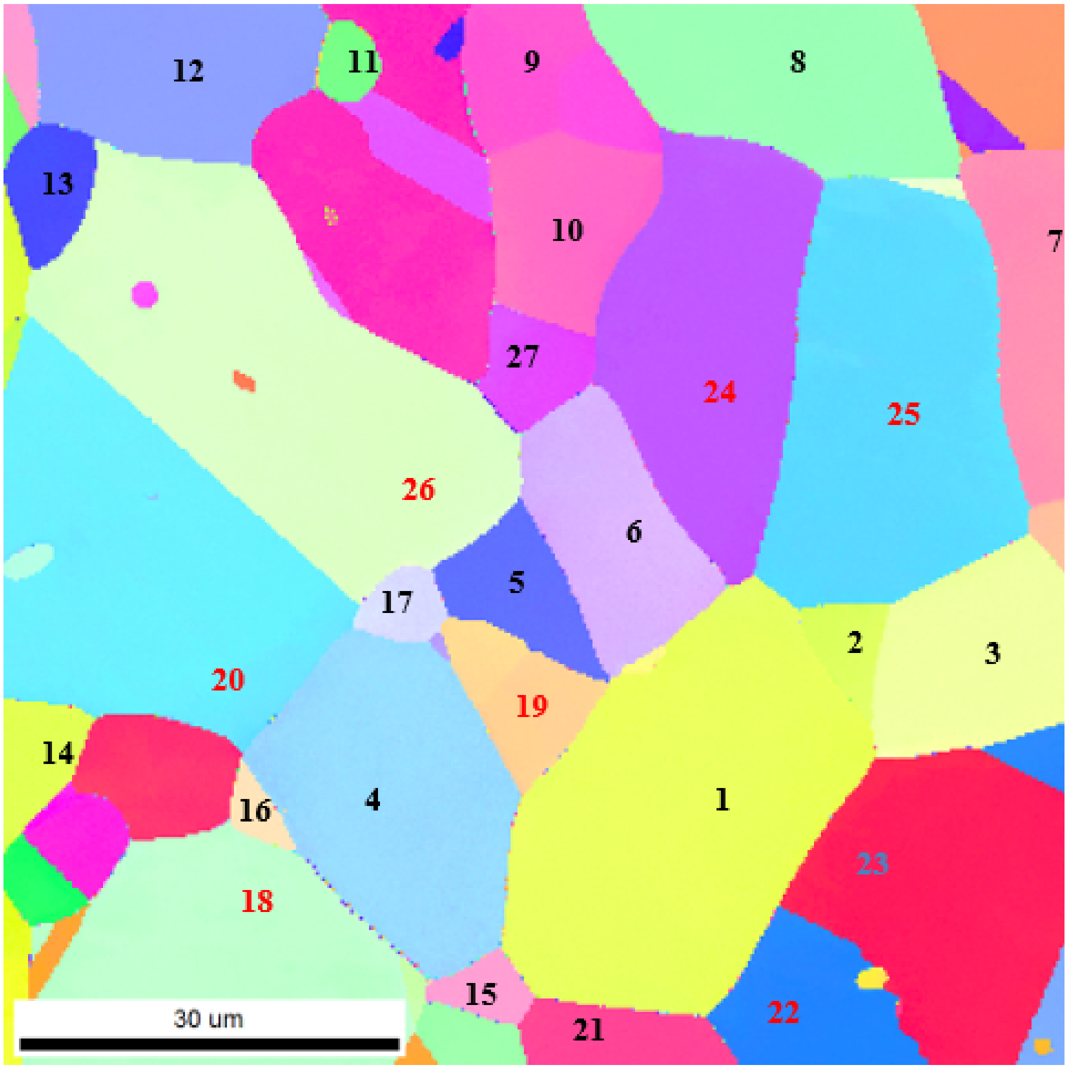

Figure 4.16: The IPF-map for the area from Experiment 6, with black numbers indicating ferritic grains and coloured austenitic

Table 20: Misorientation between the different grains, measurements done in phase map from Figure 4.15c

Between grains	Phases	Angle	Axis	When
18/4	γ/α	39.2	[23 18 -8]	Early
19/4	γ/α	45.4	[27 -6 1]	Early
20/4	γ/α	58.5	[-8 9 -6]	Early
22/1	γ/α	38.1	[-29 7 3]	Medium
23/1	γ/α	39.6	[10 1 -17]	Medium
24/1	γ/α	43.9	[11 -21 1]	Medium
25/1	γ/α	58.8	[-19 17 10]	Medium
19/1	γ/α	28.0	[14 -3 14]	Medium
26/5	γ/α	20.6	[1 -28 7]	Medium
19/5	γ/α	44.1	[-30 1 -3]	Medium
24/6	γ/α	38.0	[18 1 -8]	Medium
26/6	γ/α	27.2	[27 7 5]	Medium
16/4	α/α	22.7	[18 -1 -15]	Early
15/4	α/α	20.8	[-17 -12 2]	Early
17/4	α/α	15.0	[15 -7 -12]	Early
1/4	α/α	30.7	[-9 1 14]	Early
15/1	α/α	43.0	[-25 3 5]	Early
21/1	α/α	38.7	[27 -5 0]	Late
2/1	α/α	6.1	[-29 5 -5]	Medium
6/1	α/α	47.6	[16 8 13]	Medium
6/5	α/α	37.1	[-16 18 3]	Early
17/5	α/α	14.4	[17 17 -16]	Early
27/6	α/α	56.8	[0 13 -11]	Late

To know something about the reliablity of data CI can be used. In Figure 4.17 Grain 1 from Experiment 6 is shown. Figure 4.17a includes all of the points from the analysis, while Figure 4.17b includes all patterns that have a CI higher than 0.1. Notice that most of the points removed are intermetallic phases, but still there is some points indexed as intermetallic phases remaining.

Figure 4.18 shows the phase maps before and after removing all patterns that have a CI value lower than 0.1 for the γ-γ grain boundaries. Notice that almost all of the points removed was indexed as intermetallic phases. Also notice the patterns indexed as intermetallic phases that remains.

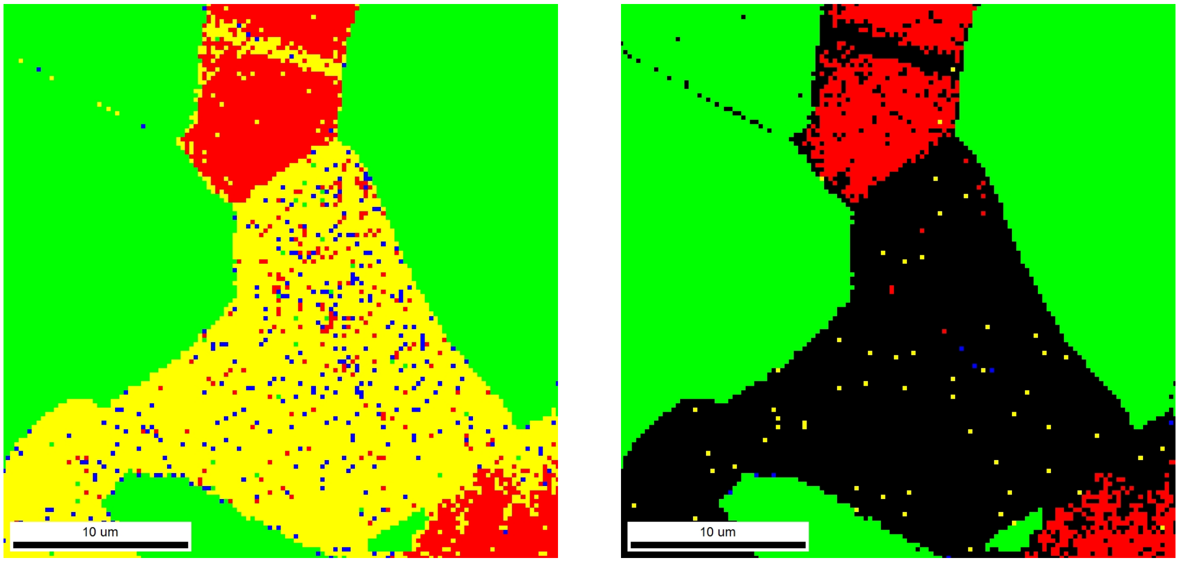

(a) Phase-map acquired 250 min after heating, no removing of points

(b) Phase-map acquired 250 min after heating, removing of all points with CI<0.1

Figure 4.17: Phase maps after 250 minutes from Experiment 6 with different degree of removing of points: Temperature set at 625 °C in oven

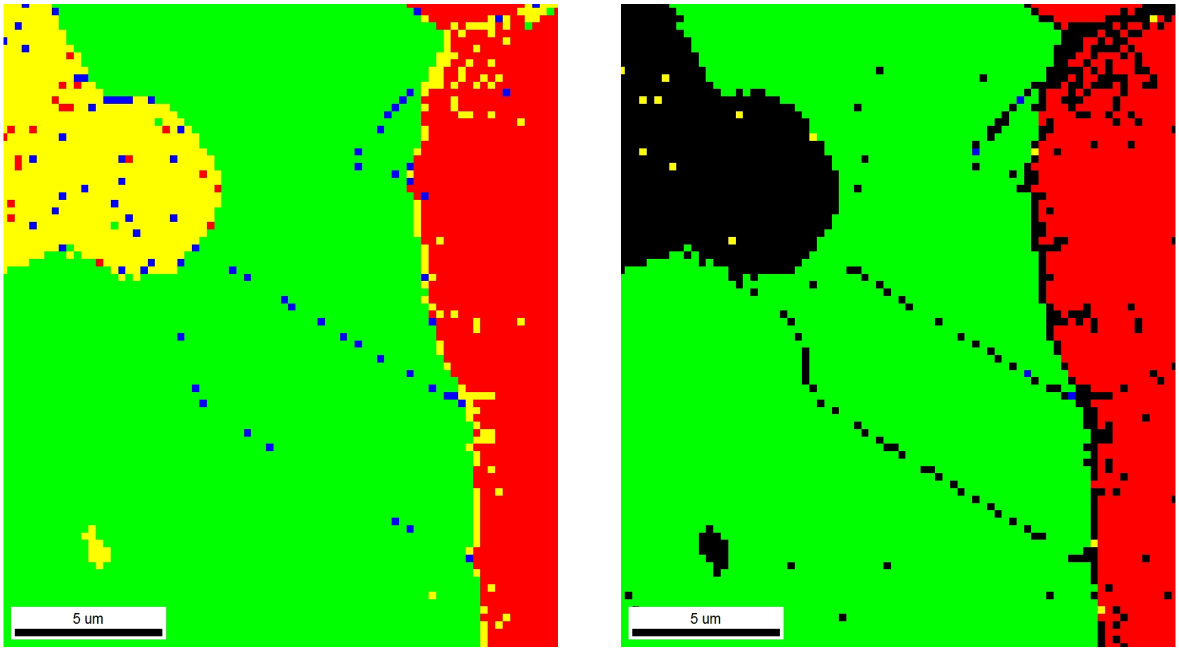

(a) Phase-map acquired 250 min after heating, no removement of points

(b) Phase-map acquired 250 min after heating, removement of all points with CI<0.1

Figure 4.18: Phase maps after 250 minutes from Experiment 6 with different degree of removement of points. Temperature set at 625 °C in oven

4.3 JMAK Constants and Curves

The JMAK equation was calculated for the six first experiments, shown in Figure 4.19. The curves show fraction σ-phase versus the time in minutes it takes to form that fraction. The calculated parameters n and k for each of the experiments can be found in Table 21. The different experiments are shown with different colours indicated in the figure. Experiment 7 was not calculated due to large amounts of poor indexing.

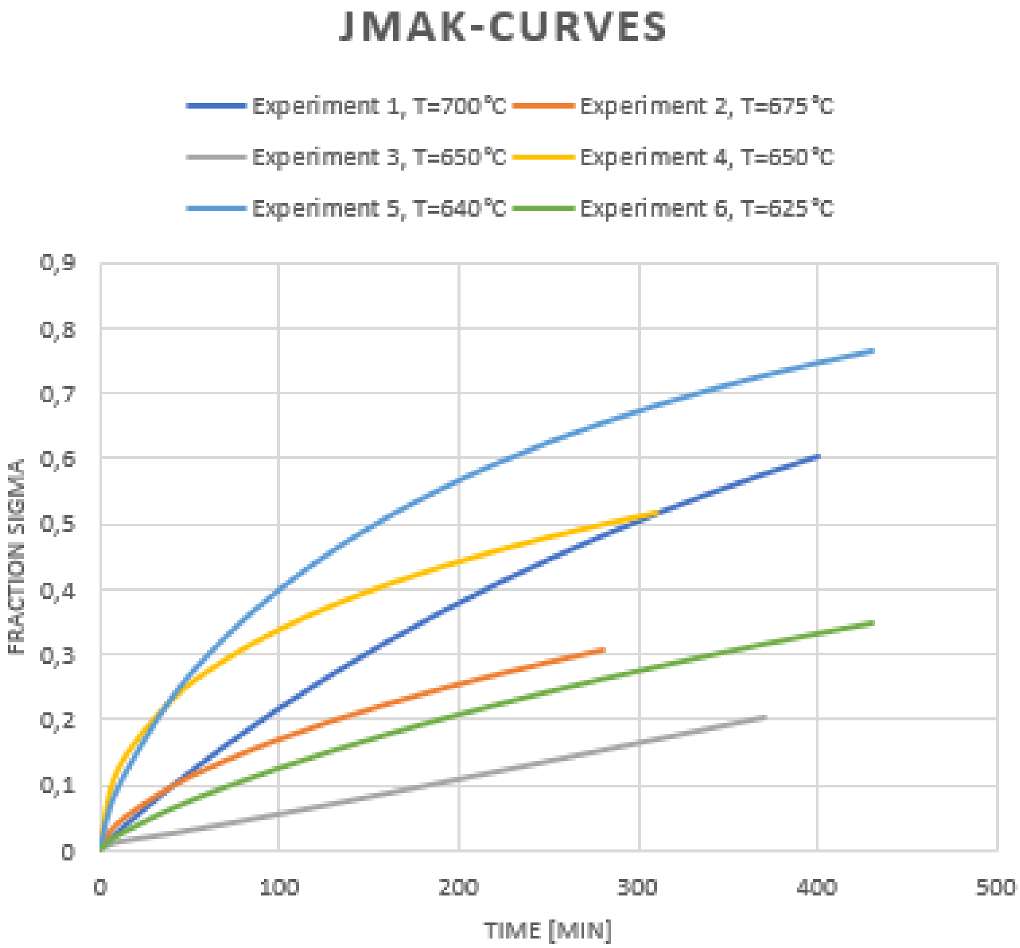

Figure 4.19: The JMAK curves for the six first experiments

Table 21: The parameters used for the curves in Figure 4.19

Experiment	**n**	**k***10^3 **[min**$^{-n}$**]**
1	1.07	1.47
2	0.79	4.11
3	1.14	0.23
4	0.61	21.98
5	0.80	10.68
6	0.89	1.88

5 Discussion

5.1 Effect of Long-Term Heat Treatment

Tensile testing were done on the material alloy UNS S32760 with varying amounts of the intermetallic phases σ and χ before and after a heat treatment at 300°C for four weeks.

For two of the curves for the material with no σ-phase, Figure 4.1, one with and one without long term heat treatment at 300°C, the fracture went outside the extensometer, and therefore the strain after necking is wrong in these two, but still it is possible to deduct other factors from these curves. It can be seen from these curves, as well as from Table 11, that the long term heat treatment at 300°C causes a decrease in the yield strength and an increase in the ductility. The ductility increases with a significant value, from 21.2% to 29.9% and the yield strength decreases from 655.4 MPa to 624.5 MPa. The ultimate tensile strength is also increased slightly by the long term heat treatment, from 838.9 MPa to 851.7 MPa. It can be seen from Table 11 that the standard deviation is for some of the properties significantly large. This can be caused by different degree of spinodal decomposition and the distribution of the new ferritic phases. Previous literature have reported to see a decrease in ductility with the spinodal decomposition [52]. Only two parallels for both before and after long term heat treatment were carried out for the samples with no σ. To be able to calculate the mean and standard deviation values for the different parameters properly, more parallels should have been included. It can still be seen that the increasing tensile yield strength leads to a decreasing ductility for these samples.

Tensile testing were also done on the material alloy containing 5% σ before and after long term heat treatment at 300°C. From Figure 4.2 it can be seen that the long term heat treatment leads to an increase in the tensile strength and a decrease in the elongation. However, if the yield tensile strength is investigated in Table 12, it can look like the yield tensile strength decreases with the long term heat treatment. This is effected by the blue curve that fractures after a strain of 0.006 with a yield tensile strength of 622.6 MPa. This sample fractured in the head, which was probably caused by a defect in the specimen. It can be seen from Figure 4.2 that a decrease in the yield tensile strength leads to an increase in strain. The decrease of the ductility with the long term heat treatment corresponds with previous studies [52, 53].

The material containing about 35% intermetallic phases was also investigated before and after long term heat treatment with tensile testing. From Figure 4.3 it can be seen that the samples with higher ductility have a lower yield tensile strength. There is also a quite big difference for the curves tested as parallels both before and after the long term heat treatment. This can be caused by distribution of the intermetallic phases which might depend on the area, as well as the fact that the degree of spinodal decomposition might vary. It can be seen from the phase maps in the experiments done with this work, Figures 4.8 and 4.15 how the σ-phase is distributed in the material. The heat treatments and tensile testing were also done in two batches, which may have affected the results. The author is not aware of anything wrong with the furnace Nabertherm N17/HR used to do the high temperature, short-term heating, but noticed that in the salt furnace used for long-term heating, large amounts of salt was solidified in both of the batches.

If the curves for the different σ-content, Figures 4.1, 4.2 and 4.3 are compared, it can be seen that the material containing no σ-phase has clearly the highest ultimate tensile strength, both before and after the long term heat treatment, as well as the highest ductility for the material long term heat treated. This means that the σ-formation leads to a decrease in tensile strength and ductility. It can also be seen from all the experiments that the ductility decreases with increasing yield strength. It can be seen from Tables 11, 12 and 13 that the ductility decreases with increasing amount of intermetallic phases. This corresponds with theory saying that the σ-phase makes the material more brittle. It can also be noticed from the figures illustrating the stress-strain curves that the deviation from one parallel to the other increases with increasing amounts of intermetallic phases. This may be caused by a bigger effect from statistical distribution of the phases.

5.2 Temperature Uncertainty and Reliability of Data

5.2.1 Temperature Uncertainty

Slightly different temperatures were used in the different experiments. This was done to be able to see the formation of both the χ- and the σ-phase. It can be noticed from Table 7 that the temperature was decreased with the later experiments, with exception of the last one. This was to make the formation of the phases, especially from χ-phase to σ to go slower. According to the TTT-diagram for the intermetallic phases in a UNS S32760, see Figure 2.5, the σ-phase should not be developed before after three hours at a temperature of 700°C. Still a developed σ-phase can already be seen in the first scan from Experiment 3, taken 10 minutes after heating done at T = 650°C. This is an indication that the temperature measured in the oven is wrong. Another indication for this specific experiment is that the temperature measured by the thermocouple in the sample is higher by a significant value than the one in the oven, 685°C measured in sample versus 650°C measured in the oven. This probably means poor thermal contact for the thermocouple in the oven, and good thermal contact for the one in the sample, and definitely means that the oven has a higher temperature than 685°C.

The oven is most likely not in full contact with the sample in all of the experiments, and this will also affect the amount of heat transfer between these two elements. The oven is most likely warmer than the sample in all the experiments, due to inadequate contact area. This is also shown in most of the experiments, where the temperature measured in the sample is lower than the temperature measured in the oven. It can be seen from all the other experiments in Table 7 that the temperature difference measured in the two thermocouples for sample and oven differs slightly in every experiment. This is caused by a difference in contact area between thermocouple and sample, and thermocouple and oven and low heat transfer in vacuum.

All of this causes a difficulty in concluding at exactly which temperatures these experiments were carried out, and how to reproduce them. The uncertainty is related to thermal contact area between the thermocouples and the sample and oven, as well as the contact area between the oven and the sample, but there is also uncertainties related to the indexing and analyses of patterns.

5.2.2 Reliability of Data

The CI values for the intermetallic phases σ and χ is usually not especially high because of the difficulty of indexing these phases [27]. As can be seen from Figures 4.10 and 4.17 for a ferritic grain, and Figures 4.11 and 4.18 for austenitic grain boundaries it can be seen that these phases were also difficult to index in this study. In these phase maps, a lot of the points indexed as intermetallic phases disappear with the removing of the patterns with a CI less than 0.1. At the same time there are some patterns indexed as intermetallic phases that has a CI value above 0.1, which is very good, especially good amounts of decent patterns from Experiment 3, see Figure 4.10 and Figure 4.11, where clusters of both intermetallic phases, χ in Figure 4.10 and σ in Figure 4.11 both originating from a ferritic grain, have good CI values. Seen together with theory saying that both the intermetallic phases will start to nucleate on ferrite-ferrite and ferrite-austenite grain boundaries, makes this data more reliable. If the sigma evolution is also studied more in detail over time, see Figures 4.8 and 4.15 it is also easier to rely on the data and indexing because it shows the same as earlier studies of these phases [11, 28].

5.3 Phase Transformation

The χ-phase is said by literature[4, 31] to nucleate before the σ-phase. The χ-phase was mainly observed on the γ-γ grain boundaries as well as single patterns inside the σ-phase in most of the experiments done in this work including Experiment 6, see Figure 4.15. As discussed in a previous paragraph, it is difficult to know the validity of these single patterns because of their low CI-values and it may be caused by the difficulty of indexing grain boundaries [54]. It can also be seen that the χ-phase on the γ-γ grain boundaries does not disappear nor grow during the heat treatment. According to theory the χ-phase should transform to σ after prolonged aging [4, 31]. This has not happened on these grain boundaries, which may be an indication that these patterns have been wrongly indexed. Previous studies has also shown that the χ usually nucleates at α-α grain boundaries, but may also nucleate at α-γ grain boundaries [37]. This is also not corresponding to the discoveries from this experiment. This seen together with Figures 4.11 and 4.18 may lead to the conclusion that the points indexed as χ on the γ-γ grain boundaries might be wrongly indexed. It is more difficult to index the patterns on the grain boundaries due to interfering patterns from the two different grains.

Studies have shown that both χ and σ nucleates at both α-α grain boundaries as well as α-γ grain boundaries [55]. This can also be seen in both the experiments described in this thesis. σ and χ are firstly found on the grain boundaries, and after a while the ferritic grains are totally consumed by these phases, mostly the σ-phase. This can especially be seen in Figure 4.15 from Experiment 6. This figure also shows a clear nucleation on especially the α-α grain boundaries as well as some nucleations inside of the ferritic grains. It has previously be seen that the intermetallic phases can also be nucleated on dislocations [27], and this may be an explaination on why the sigma appears in the middle of some grains. It can be seen from Figure 4.15, especially from Figures 4.15b and 4.15d that the σ-phase grows from all of the grain boundaries in some grains, and only some in others. It can also clearly be seen from all the experiments that there is no phase transformation of the austenitic phase. Theory says that sigma may nucleate from the austenitic phase after the ferritic phase is consumed [31, 32]. Clearly the material has not been heated long enough for this to happen.

If Figure 4.15 is compared to Figure 4.8, the morphology of the σ-phase developed is clearly different in the two experiments. According to Pohl et. al [34] the morphology of the σ-phase is dependent on temperature. At lower temperatures the σ-phase will have a coral-like structure due to lower diffusion velocity which will lead to more single sigma nuclei. This corresponds quite well with Experiment 6. At higher temperatures the σ-phase will become more compact and bigger, which can be seen as happening in Experiment 3. This can therefore lead to the assumption that the sample in Experiment 3 has reached higher temperatures than the sample in Experiment 6. This also corresponds with the temperatures measured in the thermocouples for both the oven and the sample. However, the evolution of the σ-phase seems to be faster in Experiment 6, Figure 4.15. This can also be seen from the JMAK-curves given in Figure 4.19 where Experiment 3 given as the grey curve is clearly below the green curve representing Experiment 6. Here it can be seen that the rate of the sigma evolution is higher for Experiment 6. In this figure it is also not possible to see an increase in sigma fraction at a specific time with temperature. This may be caused by the temperature uncertainty related to the experiments, but can also be caused by the small ROI, usually 85μmx85μm, which is not a representative area. Therefore, in some of the experiments the area chosen might contain more ferritic grains, or grains where σ-phase is more easily formed. Therefore the fraction of sigma formed in some will be higher purely because of this.

The parameters used to calculate the JMAK-curves is given in Table 21. k is dependent on temperature, and as can be seen, it varies quite a lot. The value of n also varies quite a lot, from 0.61 to 1.14. Magnabosco et. al [56] found n=0.92 for a SDSS sample aged at 800°C, which is close to the values from some of the experiments. Again, the area chosen is not big enoguh to be able to properly construct these curves, and naturally this will also affect the parameters used to construct the curves.

The χ-phase can also be found in clusters, see grain 1 and 6 from Figure 4.9 in Figure 4.8. The χ-clusters have been developed in these two grains after 160 minutes, Figure 4.8b. As can be seen from this figure, the χ-phase is developed partly together with the σ-phase in grain 1, but in grain 6 the χ-phase has nucleated almost without any σ. In the last phase map from this Experiment, Figure 4.8d it can be seen that some of the χ-phase is removed in favour of σ-phase which also previous studies show [4, 31], but most of the phase remains in the same clusters after they have been formed. This might be due to not long enough aging time due to still remaining ferritic phase that can transform to σ in favour of χ, but might also be an indicator that some of the χ-phase will remain among the σ-phase.

In Experiment 6, like most of the experiments, the χ-phase is only observed as single patterns in the σ-phase. This might be noise and wrong indexing, but can also be that the χ is formed in smaller nuclei, similar to the σ-phase, at the temperatures used in this experiment. If the indexing of χ in the experiment is assumed to be true, this means that some χ will remain in the alloy after the consumption of ferrite, and will therefore not transform into σ.

Theory expresses that the χ-phase is removed in preference for the σ-phase after prolonged aging. This can partly be seen in some of the grains in Figure 4.8. Here some of the clusters of χ is slowly being removed for σ. At the same time, the fraction χ-phase can be observed increasing in both the experiments, see Tables 14 and 18. Still there is not so many new clusters developing in Experiment 3, which means that most of the existing χ-phase is not removed, but rather grows in this experiment.

When σ is formed, the remaining ferrite is depleted from Cr and Mo which is caught by the σ-phase. This remaining ferrite is therefore rich in elements like Ni and it can transform to secondary austenite [31, 32]. This can be seen happening in Experiment 3, Figure 4.8 where austenite is formed together with the σ-phase in the ferritic grains. This has also previously been seen [34, 57], having three different mechanisms where σ can be formed. Fraction γ is in some grains almost equal to fraction σ formed. This has also been observed in previous studies [58]. The austenitic phase formed also has quite high CI-values, see Figure 4.10, where all the data in Figure 4.10b has CI-values above 0.1. According to Ramirez et al. [33] the austenite formed can either be intergranular or intragranular secondary austenite. The secondary austenite formed in Experiment 3, Figure 4.8, can be observed to be intergranular, meaning that it nucleates at the α/γ grain boundaries.

The formation of secondary austenite can not be seen in Experiment 6, Figure 4.15. In these phase maps, no austenite can be seen inside the ferritic grains. This may be because of temperature. One of the other three mechanisms where σ is formed[31, 32], is nucleation and growth from the original ferrite. Earlier studies have found secondary γ for almost the entire temperature interval [59]. Some literature have also reported a difference for different temperatures, where σ-phase formed at 900°C has an isolated particles morphology, while between 700°C and 800°C an eutectoid decomposition of ferrite was observed, resulting in a lamellar morphology of σ and secondary γ [56]. The results from Experiment 3 can look very much like an eutectoid decomposition, and this also corresponds with the temperatures measured in this experiment, that the temperature has been between 700°C and 800°C.

In Figure 4.8, there can be observed some γ on the grain boundaries between grain 2 and 5. This γ-phase is apparently formed almost alone without any nucleation of σ close to the grain boundary, see Figure 4.8a. This observation is very special, and have not been reported much before, and therefore it might be wrong indexing. At the same time, the CI values for these patterns mostly have values around 0.4-0.5, and therefore the confidence in these patterns being austenite is relatively high. If this region from the phase map is compared to the same in the IQ-map, see Figure

4.6a, this grain boundary in the IQ-map looks different, thicker, compared to the other grain boundaries in this IQ-map.

The IQ maps, Figures 4.6 and 4.13, show the areas where σ and χ are dark. This means that the patterns that come from these areas are poor. In Experiment 6, see Figure 4.13, it seems like some of the grains get a black diffuse layer over it. This layer is very dark, darker than any of the areas in the later scans. Later what looks like dark needles consisting of bad patterns appear in the IQ maps. This is clearly the intermetallic phases which nucleates if compared to the phase maps in Figure 4.15. The areas which was covered early on, becomes lighter during the heat treatment. This also corresponds with the CI-values. In Experiment 3 the CI value increases from 0.03 to 0.07 for the sigma phase shown in Table 15 and for Experiment 6 it is constant 0.02 shown in Table 19, and for the chi phase from 0.03 to 0.04 for Experiment 3 and constant 0.02 in Experiment 6. This corresponds with all of the experiments in that the CI value never gets worse with the heating. A reason for better patterns during the heating can be that contamination on the surface is removed with the heating.

5.4 Orientation of Grains and Misorientation between Grains

The orientation of the ferritic grains were investigated in both of the experiments. This was done because the σ-phase seemed to develop in some ferritic grains before others, see Figures 4.8 and 4.15. From the phase map it may seem like the σ-phase grows from all the grain boundaries inside the specific grains as well as in the middle of the grain. The grain boundaries where the sigma phase appeared first was investigated, see Tables 17 and 20, but there were not found any relationship between the different boundaries, other that they are all high angle grain boundaries (above 15°). Having said that, almost all of the grain boundaries in this material are high angle grain boundaries. A reason for the σ-phase appearing in the middle of the grains might be the location of a grain boundary underneath the surface, since the analysis is only done two-dimensionally. It is also a possibility, that is mentioned earlier, that σ might start nucleation in the middle of the grain on a dislocation.

If Grain 4 marked in Figure 4.9 is investigated more in detail, it can be seen that the phase grows in a distinctive direction in this grain, see Figure 4.8c compared to Figure 4.8b. From this it can look like the σ-phase is developed in a special plane and continues to grow in this plane before it consumes more of the grain. The orientation of the σ-phase relative to their parent grain was investigated for this experiment, see Table 16. This table shows that the σ does not have a distinctive misorientation to its parent ferritic grain, but it is typically around a value of 40°. Warren et al. [36] concluded that there were no specific σ nucleation orientation relationship relative to the parent δ grain. Hosseini et al. [60] also found that the σ-phase showed no trend of specific texturing at different aging temperatures.

The misorientation of the parent ferritic grain in relation to the χ-phase was also investigated, see Table 16. In contrast to the σ-phase showing no specific misorientation, large amounts of the χ-phase was found to have a misorientation angle at 60° around the (1 1 1) axis, as well as some found having similar orientation as the parent grain.

The secondary austenite formed also seems to have a specific misorientation to the parent grain, see Table 16. All of the measured points, chosen randomly shows a misorientation angle of 40° around a (1 1 6) axis.

The IPF-maps from most of the experiments, with exception of Experiment 3, does not show a specific orientation for the new developed phases. The new phase that is developed can appear to have nucleated in small precipitates, corresponding to the studies done by Pohl et. al [34] saying that at lower temperatures the diffusion velocity will be lower, which causes more single sigma nuclei to form, while at higher temperatures the diffusion velocity is higher and this causes the σ-phase to be bigger and more compact. This can also be a indicator that the σ-phase does not have a preferred orientation relative to their parent grain because all the single σ-nuclei grows in different orientations.

5.5 Contrasting

It can be seen from Figures 4.5 and 4.12 that the contrast between the phases increases with the heating. This can be due to the heating or it can be due to the change of phases. There has not been many studies discussing this topic. If the last electron images, Figures 4.5b and 4.12b are compared to the ones showing the phase maps, Figures 4.8d and 4.15d, it can be seen that the phases indexed as σ are brighter in the electron images than ferrite. The secondary electron yields for electron bombardment increases with atomic number for metals [40]. This may mean that the σ-phase has a higher mean atomic number than the ferritic phase. If the last phase map is compared to the first phase map from Experiment 3, it can be seen that some of the ferritic phase in grain 5 remains during the entire heating experiment. Still the contrasting does change. It can therefore be concluded that the contrast difference is not dependent on the phases. However, the contrasting might be affected by the diffusion of elements from the ferritic phase with higher atomic weights.

6 Conclusion

The objective of this work was to investigate the nucleation and growth of the intermetallic phases σ and χ in the SDSS-alloy UNS S32760 to find the mechanisms behind the nucleation with the help of an in situ heating stage and EBSD (Electron Backscatter Diffraction) characterization. In addition the effect of long term heat treatment on the tensile properties for the same alloy with varying grade of sigma fraction was investigated. With basis on the experimental work and analyses these conclusions can be drawn:

- The spinodal decomposition will happen with varying degree after a heat treatment at 300°C for four weeks, and the heat treatment will therefore have varying effect on the tensile properties. The σ-phase leads to a less ductile material, and the deviation from one sample to another of the same material with the same heat treatment will vary more with increasing amounts of intermetallic phases.
- The temperature uncertainty is large because of varying degree of thermal contact area for the thermocouples used in the experiments.
- The σ-phase is formed at the α-α grain boundaries as well as the α-γ grain boundaries. Sometimes the σ was observed starting to nucleate in the middle of the grain. This can either be caused by precipitation on dislocations or that it is nucleated from a grain boundary underneath (since the measurements is done two-dimensionally). There were also found no relationship between the orientation of the σ-phase related to the parent grain.
- The χ-phase was observed mainly in clusters inside the σ-grains. Some disappear after a while, and is replaced by σ, but most remains during the entire heat treatment, and the χ-fraction increases during the heat treatment in both the experiments.

- There seems to be a specific misorientation relationship between the formed χ-phase and the parent grain. The misorientation is either 60°around [1 1 1] or close to the same orientation as the parent grain.
- During the nucleation of σ-phase, a big fraction of secondary γ is also formed at one of the temperatures. This secondary austenite has a specific misorientation relative to their ferritic parent grain, 45°around [1 1 6]. At the other temperatures, no nucleation of secondary austenite can be seen.
- The secondary electron image contrast increases with the heat treatment.
- There were found no relationship for the grain boundaries where the sigma-phase nucleated first, other than these were high-angle grain boundaries.

7 Further Work

To better understand the microstructure evolution in super duplex stainless steels the following points for further work is suggested:

- Investigate the effect of spinodal decomposition alone as well as the combined effect with intermetallic phases to the properties of a super duplex stainless steel
- Develop a heating stage which can obtain higher certainties around the temperatures measured.
- Investigate the microstructure evolution of the intermetallic phases with lower temperatures.
- Investigate the difference in morphology for the sigma-phase developed at different temperatures.
- Investigate the orientation of the intermetallic phases formed relative to the parent grain.

8 References

References

[1] Y. Kim. Phase transformations in cast duplex stainless steels. *Retrospective Theses and Dissertations*, 1175, 2004.

[2] H. G. Ong and A Yeap. Challenges in avoiding sigma phase embrittlement of duplex stainless steel in assets. 01 2018.

[3] M. V. Biezma, C. Berlanga, and G. Argandona. Relationship between microstructure and fracture types in a UNS S32205 duplex stainless steel. *Materials Research*, 16:965 – 969, 10 2013.

[4] K. W. Chan and S. C. Tjong. Effect of secondary phase precipitation on the corrosion behavior of duplex stainless steels. *Materials*, 7:5268–5304, 07 2014.

[5] NS-EN 10020:2000:Definition and classification of grades of steel. Standard, 9 2000.

[6] L. Pezzato, M. Lago, K. Brunelli, M. Breda, and I. Calliari. Effect of the heat treatment on the corrosion resistance of duplex stainless steels. *Journal of Materials Engineering and Performance*, Volume 27 (8), August 2018.

[7] K. Migiakis and G. D. Papadimitriou. Effect of nitrogen and nickel on the microstructure and mechanical properties of plasma welded uns s32760 super-duplex stainless steels. *Journal of Materials Science*, 44(23):6372–6383, Dec 2009.

[8] R. W. Revie. Uhlig's corrosion handbook (3rd edition), 2011.

[9] N. Llorca-Isern and et. al. Identification of sigma and chi phases in duplex stainless steels. *Materials Characterization*, Volume 112:20–29, February 2016.

[10] J. R. Davis. *Stainless Steels*, volume 3rd Edition. Materials Park, Ohio: ASM International, 1994.

[11] T. A. DeBold. Duplex stainless steel—microstructure and properties. *JOM*, 41(3):12–15, Mar 1989.

[12] P. Cunat. Alloying elements in stainless steel and other chromium-containing alloys. 01 2004.

[13] Total Materia. Austenitic steels, 2003.

[14] CALPHAD. Computational thermodynamics calculation of phase diagrams using the calphad method, 2011.

[15] S Sharafi. Microstructure of super-duplex stainless steels, 1993.

[16] A. Padilha, R. Lesley, and P. Rios. Stainless steels heat treatment (chapter 12). *Steel Heat Treatment Handbook. Second Edition*, pages 695–739, 01 2007.

[17] T. Sourmail and H. K. D. H. Bhadeshia. Stainless steels.

[18] H.K.D.H. Bhadeshia and et. al. *Steels - Microstructure and Properties*, volume 3rd Edition. Butterworth-Heinemann, 2006.

[19] C. A.and et. al. Fortulan. Microstructure by thermal attack under vacuum of a superduplex stainless steels and electrochemical behavior in h2s/co2-saturated synthetic seawater. *Journal of the Brazilian Chemical Society*, Vol.29(9):p.1803–1810, 2018.

[20] Oxford Instruments Analytical. Electron backscattered diffraction, 2004.

[21] V. Randle. Grain boundary geometry: Measurement.

[22] V. A. Hosseini, M. Thuvander, S. Wessman, and L. Karlsson. "spinodal decomposition in functionally graded super duplex stainless steel and weld metal". *"Metallurgical and Materials Transactions A"*, "49"("7"):"2803–2816", "Jul" "2018".

[23] F. M. Elsabbagh, A El-Sabbagh, R. M. Hamouda, and M. Taha. Analysis of super duplex stainless steel properties as an austenite-ferrite composite. *Materials Sciences and Applications*, 06:1121–1136, 01 2015.

[24] V. H. C. de Albuquerque, E. M. Silva, J. P. Leite, E. P. de Moura, V. L. A. Freitas, and J. M. R.S. Tavares. Spinodal decomposition mechanism study on the duplex stainless steel uns s31803 using ultrasonic speed measurements. *Materials Design*, 31(4):2147 – 2150, 2010. Design of Nanomaterials and Nanostructures.

[25] J.O. Nilsson and A. Wilson. Influence of isothermal phase transformations on toughness and pitting corrosion of super duplex stainless steel saf 2507. *Materials Science and Technology*, 9(7):545–554, 1993.

[26] J. Michalska and M. Sozańska. Qualitative and quantitative analysis of σ and χ phases in 2205 duplex stainless steel. *Materials Characterization*, 56(4):355 – 362, 2006. 9th ECSIA and 7th STERMAT: Stereology and Image Analysis in Materials Science.

[27] J. Michalska and B. Chmiela. Phase analysis in duplex stainless steel: Comparison of ebsd and quantitative metallography methods. *IOP Conference Series: Materials Science and Engineering*, 55:012010, 03 2014.

[28] K. W. Chan and S. C. Tjong. Effect of secondary phase precipitation on the corrosion behavior of duplex stainless steels. *Materials*, 7:p 5268–5304, July 2014.

[29] L. JooSuk and et. al. Application of small punch test to evaluate sigma-phase embrittlement of pressure vessel cladding material. *Journal of Nuclear Science and Technology*, 40(9):664–671, 2003.

[30] S. Atamert and J.E. King. Sigma-phase formation and its prevention in duplex stainless steels. *Journal of Materials Science letters*, 12(14):1144–1147, 7 1993.

[31] D.M. Escriba, E. Materna-Morris, R.L Plaut, and A.F. Padilha. Chi-phase precipitation in a duplex stainless steel. *Materials Characterization*, 60(11):1214 – 1219, 2009.

[32] A. Rocha, A. Santos, and G. R. Pereira. *Phase Transformations in Duplex Stainless Steel: An Assessment by In Situ X-Ray Diffraction*. 11 2018.

[33] A. J. Ramirez, J. C. Lippold, and S. D. Brandi. The relationship between chromium nitride and secondary austenite precipitation in duplex stainless steels. *Metallurgical and Materials Transactions A*, 34(8):1575–1597, Aug 2003.

[34] M. Pohl, O. Storz, and T Glogowski. Effect of intermetallic precipitations on the properties of duplex stainless steel. *Materials Characterization*, 58(1):65 – 71, 2007.

[35] L. Duprez, B. De Cooman, and N. Akdut. Redistribution of the substitutional elements during sigma and chi phase formation in a duplex stainless steel. *Steel Research*, 72, 08 2001.

[36] A. D. Warren, R. L. Harniman, Z. Guo, C. M. Younes, P. E. J. Flewitt, and T. B. Scott. Quantification of sigma-phase evolution in thermally aged 2205 duplex stainless steel. *Journal of Materials Science*, 51(2):694–707, Jan 2016.

[37] Y.H. Lee, K. T. Kim, Y. D. Lee, and K. Y. Kim. Effects of w substitution on ς and χ phase precipitation and toughness in duplex stainless steels. *Materials Science and Technology*, 14(8):757–764, 1998.

[38] J.S. Kasper. The ordering of atoms in the chi-phase of the iron-chromium-molybdenum system. *Acta Metallurgica*, 2(3):456 – 461, 1954.

[39] P. W. Hawkes and J. C.H. Spence. *Science of Microscopy*, volume 1. Springer, 2007.

[40] Y. Sakai, T. Yamada, T. Suzuki, and T. Ichinokawa. Contrast mechanisms of secondary electron images in scanning electron and ion microscopy. *Applied Surface Science*, 144-145:96 – 100, 1999.

[41] J. Hjelen. *Scanning elektron-mikroskopi*. SINTEF, Avdeling for metallurgi AND Metallugisk institutt, NTH, 1986.

[42] A. J. Schwartz and et. al. *Electron Backscatter Diffraction in Materials Science*, volume 2nd Edition. Springer, 2009.

[43] A. J. Wilkinson and T. B Britton. Strains, planes, and ebsd in materials science. *Materials Today*, 15(9):366 – 376, 2012.

[44] F. Brisset. Electron backscattered diffraction basics and applications, 2010.

[45] R. O. Duda and P. E. Hart. Use of the hough transformation to detect lines and curves in pictures. *Commun. ACM*, 15(1):11–15, January 1972.

[46] TSL. Oim analysis 5.3, 1997.

[47] H. Chien, B. El-Dasher, A. Rollett, and G. Rohrer. Understanding the tsl ebsd data collection system, 2011.

[48] Total Materia. Engineering stress-strain curve: Part one, 2001.

[49] Chapter 1: Introduction to Tensile Testing. Standard, ASM International, Ohio, USA, 2004.

[50] K.R. Elstad and et. al. In situ tensile testing during continuous ebsd mapping of super duplex stainless steel containing sigma phase. 2016.

[51] A. Enstad and et. al. Ebsd-karakterisering av et hsla-stål under in situ varmebehandling, 2011.

[52] M. K. Miller, J. M. Hyde, M. G. Hetherington, A. Cerezo, G.D.W. Smith, and C. M. Elliott. Spinodal decomposition in fe-cr alloys: Experimental study at

the atomic level and comparison with computer models—i. introduction and methodology. *Acta Metallurgica et Materialia*, 43(9):3385 – 3401, 1995.

[53] E. Herny, P. Lours, E. Andrieu, J. Cloué, and P. Lagain. Evolution of microstructure and impact-strength energy in thermally and thermomechanically aged 15-5 ph. *Proceedings of the Institution of Mechanical Engineers, Part L: Journal of Materials: Design and Applications*, 222:299–304, 2008.

[54] S. I. Wright, M. M. Nowell, S. P. Lindeman, P. P. Camus, M. de Graef, and M. A. Jackson. Introduction and comparison of new ebsd post-processing methodologies. *Ultramicroscopy*, 159:81 – 94, 2015.

[55] S. Byun, N. Kang, T. Lee, S. Ahn, H. W. Lee, W. Chang, and K. Cho. Kinetics of cr/mo-rich precipitates formation for 25cr-6.9ni-3.8mo-0.3n super duplex stainless steel. *Metals and Materials International*, 18, 04 2012.

[56] R. Magnabosco. Kinetics of sigma phase formation in a Duplex Stainless Steel. *Materials Research*, 12:321 – 327, 09 2009.

[57] J. Kleppen and et. al. Mikrostrukturutvikling i superdupleks rustfritt stål og effekten av prøvepreparering på identifisering og kvantifisering av sigmafase gjennom ebsd-karakterisering, 2018.

[58] J Elmer, T. Palmer, and E. Specht. Direct observations of sigma phase formation in duplex stainless steels using in-situ synchrotron x-ray diffraction. *Metallurgical and Materials Transactions A*, 38:464–475, 01 2007.

[59] S. K. Ghosh and S. Mondal. High temperature ageing behaviour of a duplex stainless steel. *Materials Characterization*, 59(12):1776 – 1783, 2008.

[60] V. A. Hosseini, L. Karlsson, S. Wessman, and N. Fuertes. Effect of sigma phase morphology on the degradation of properties in a super duplex stainless steel. *Materials*, 11:933, 06 2018.

A OIM Analysis Manual

In this project both the IQ-, IPF- and the phase map function in OIM Analysis has been used. This and further settings that can be used is going to be shown in this section.

A.1 Upload File

- Press File and then Open
- Find the file that you want to open (”Pattern.osc”). The file .dat needs to be processed in TSL Data Collection before it can be opened in TSL OIM Analysis.

A.2 Creating Maps

One of the main function of OIM Analysis is to create different IQ- IPF- and phase maps. The shortcuts to make these maps and some others are shown in Figure A.1, where the shortcuts are following:

- 1: IPF (Inverse Pole Figure) map
- 2: IQ (Image Quality) map
- 3: Unique Grain Colour Map
- 4: Grain boundary map
- 5: Phase map

(a) Tool line

(b) Map symbols in tool line

Figure A.1: Tool line to make quick maps

A.3 Saving Images and Information

To save images or information in a word document, the cursor need to be on the map that should be saved. Then you right click and click "Image..." and "Save Image...". The image will be saved as a bmp file if not other is chosen. To save it as a jpg file, choose this in the scrolldown menu in the lower part of the saving window. To save information in a text document the cursor also needs to be marked over the information wanted to be saved. Thereafter, you right click and choose "Export..." and save the txt document with a chosen name.

A.4 Pole Figure

To get a pole figure of your sample, it is possible to use the shortcut "Quick Pole Figure". How to navigate to this is shown in Figure A.2 with a red circle. Then the pole figure with direction [001] will appear. If the material analyzed is a multiphased material, only the pole figure for one of the phases will appear. To get other directions and other phases right click on the generated pole figure and click ”Properties”. Then the menu in Figure A.3a will appear. Here more pole figures can be added by clicking ”Add” and choose the phase that you want in the scroll down menu, shown in Figure A.3b. Then choose the plane and the plane normal direction.

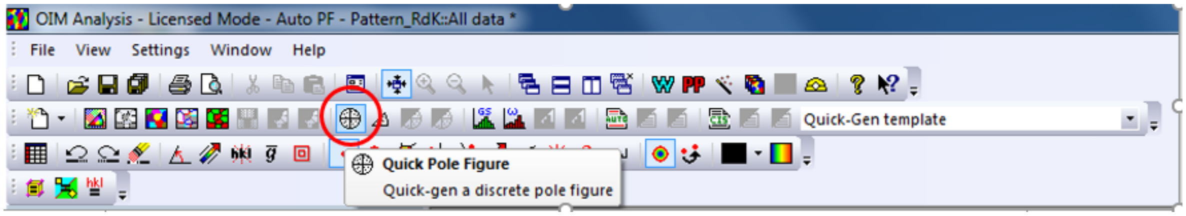
OIM Analysis - Licensed Mode - Auto PF - Pattern_RdK::All data *

Figure A.2: Choosing pole figure

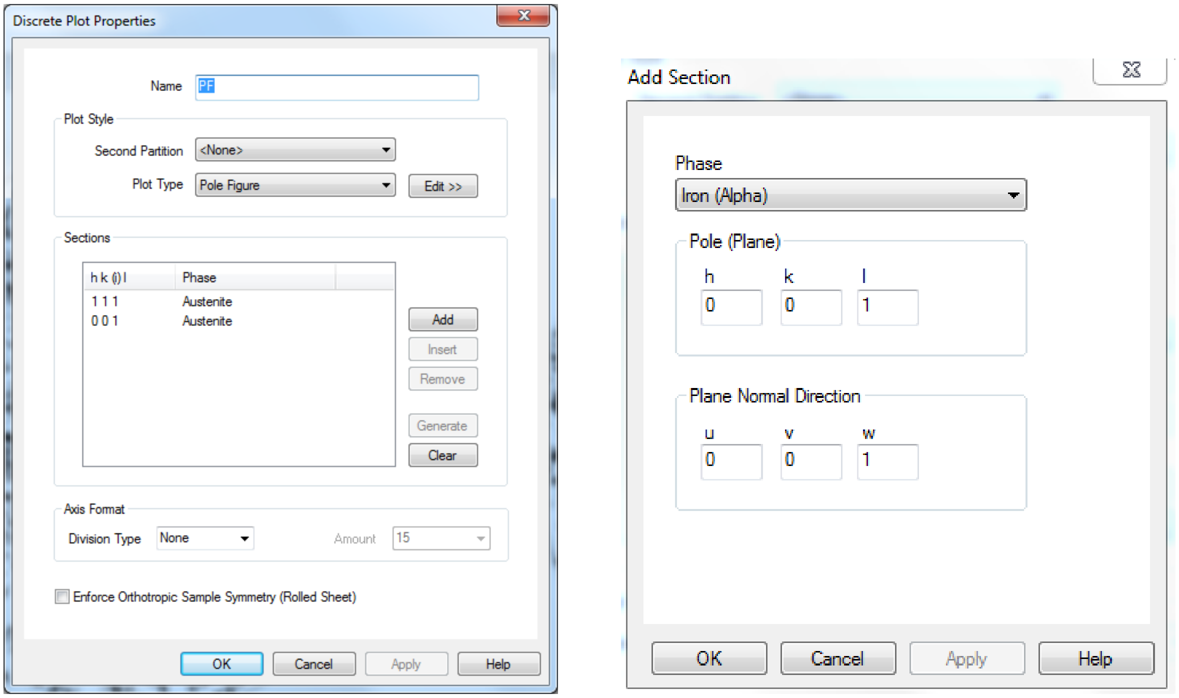
Discrete Plot Properties

Name: PF

Plot Style

Second Partition: <None>

Plot Type: Pole Figure

Sections

h k (i) l	Phase
1 1 1	Austenite
0 0 1	Austenite

Axis Format

Division Type: None

Amount: 15

☐ Enforce Orthotropic Sample Symmetry (Rolled Sheet)

Add Section

Phase: Iron (Alpha)

Pole (Plane): h 0, k 0, l 1

Plane Normal Direction: u 0, v 0, w 1

(a) Menu for discrete plot properties (b) Menu after choosing "Add"

Figure A.3: Menus when making pole figures

A.5 Finding Orientation

It is possible to see the orientation of a grain by simply moving the cursor over the grain. But there are several ways to show orientations. If a special method to write orientation is wanted, it is possible to change it by following steps:

- Choosing ”Settings” on the upper menu in the tool line.
- Choosing ”Preferences...”
- Choosing ”Maps and GBs”.

If these steps were done correctly the menu shown in Figure A.4 will appear. Here the status bar text can be chosen as Point Data (hkl)[uvw] (integers) to get it in this format.

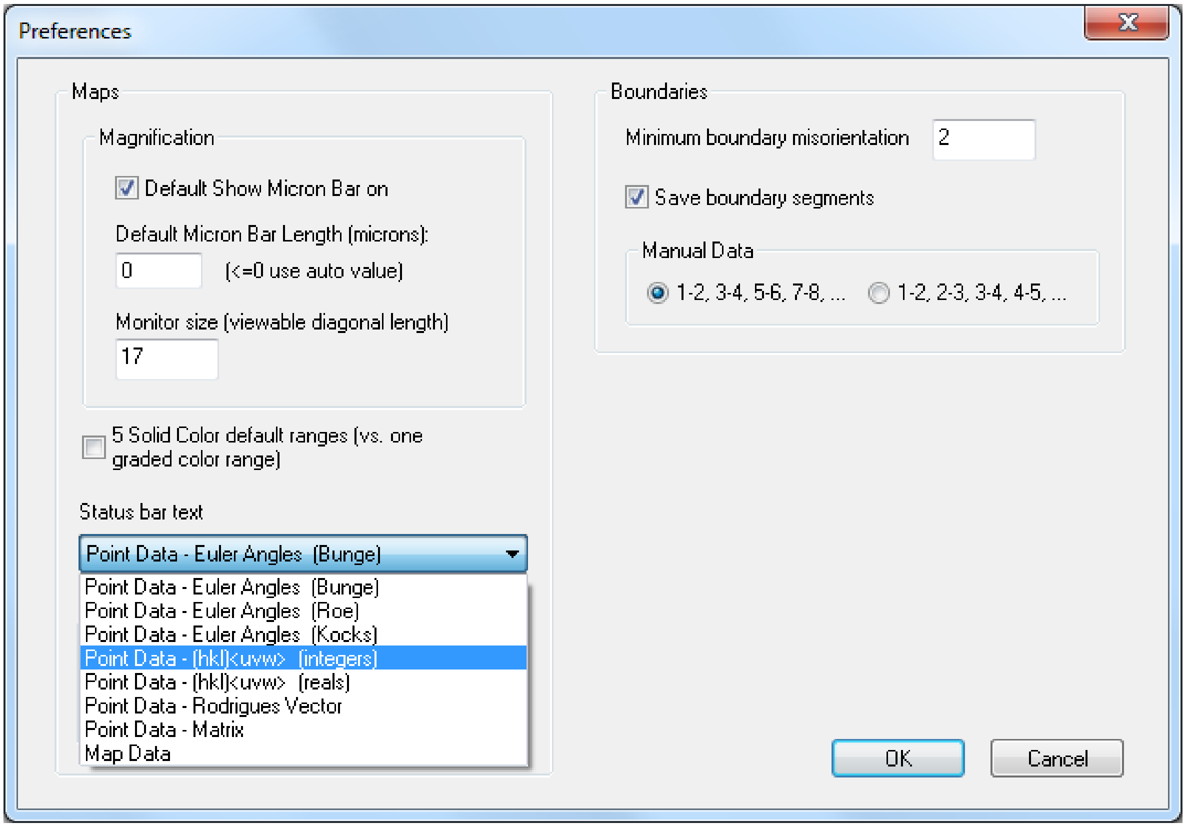

Preferences

Maps

Magnification

☑ Default Show Micron Bar on

Default Micron Bar Length (microns): 0 (<=0 use auto value)

Monitor size (viewable diagonal length) 17

☐ 5 Solid Color default ranges (vs. one graded color range)

Status bar text: Point Data - Euler Angles (Bunge)

Boundaries

Minimum boundary misorientation 2

☑ Save boundary segments

Manual Data

● 1-2, 3-4, 5-6, 7-8, ... ○ 1-2, 2-3, 3-4, 4-5, ...

Figure A.4: Menu when choosing Settings–> Preferences –> Maps and GBs

If its wanted to record the orientation data, its possible with choosing the ”Record data” symbol on the upper left corner, choosing the ”Interactive” folder shown with a red arrow in Figure ... and clicking the grain you want to identify. It is also possible to record other data this way, like CI- and fit value.

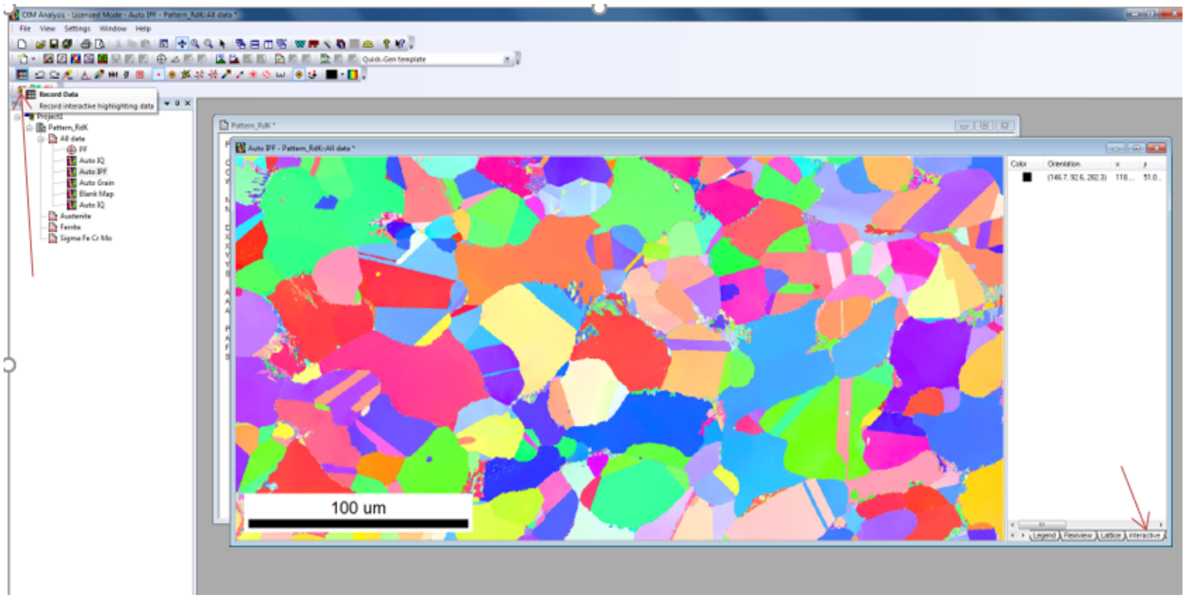

Figure A.5: Arrows showing how to record data and where the data end up

A.6 Misorientation Profile

Misorientation profile can be used to show the difference between the orientation of neighbouring grains over a line. By choosing both the ”Record data” and the ”Maps: Profile Vector”, both shown in Figure A.6 with a red square and drawing a line in the map, you will get the menu shown in Figure A.7a. Here the user can choose to show point to point misorientations or point to origin misorientations. If you choose point to origin, a possible solution is shown in Figure A.7b.

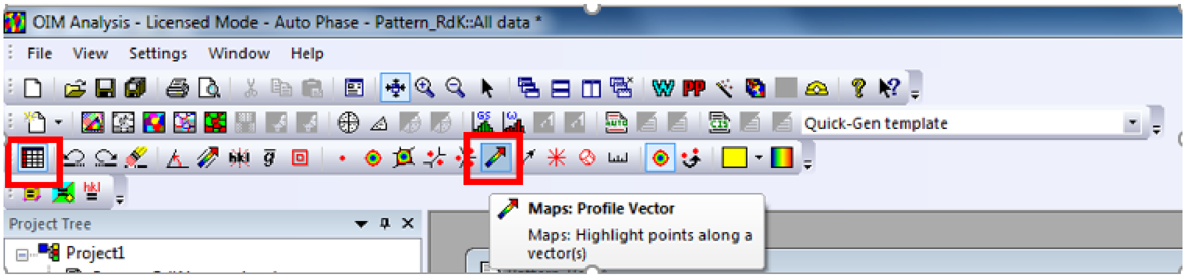

Figure A.6: How to get misorientation profile

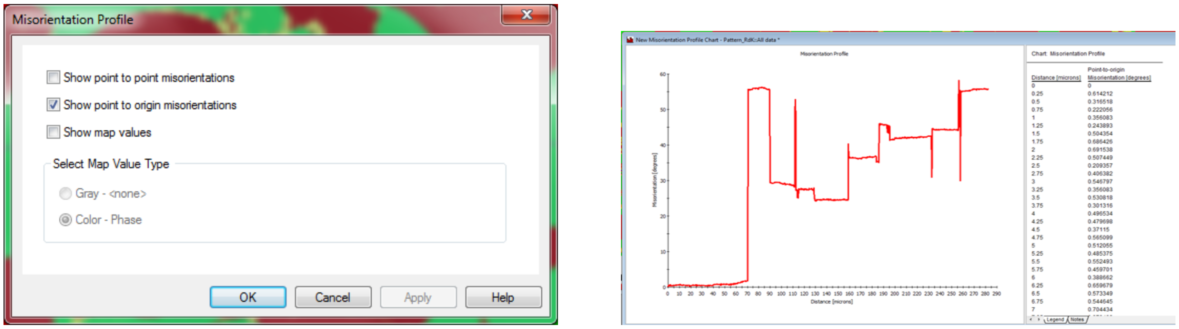

☐ Show point to point misorientations
☑ Show point to origin misorientations
☐ Show map values

Select Map Value Type
○ Gray - <none>
● Color - Phase

Chart: Misorientation Profile

Distance [microns]	Point-to-origin Misorientation [degrees]
0	0
0.25	0.614212
0.5	0.316518
0.75	0.222056
1	0.356083
1.25	0.243893
1.5	0.504354
1.75	0.686426
2	0.691538
2.25	0.507449
2.5	0.209357
2.75	0.406382
3	0.546797
3.25	0.356083
3.5	0.530818
3.75	0.301316
4	0.496534
4.25	0.479698
4.5	0.37115
4.75	0.565099
5	0.512055
5.25	0.485375
5.5	0.552493
5.75	0.459701
6	0.388662
6.25	0.659679
6.5	0.573349
6.75	0.544645
7	0.704434

(a) Misorientation menu (b) Misorientation figure

Figure A.7: Misorientation figures

A.7 Clean up

One setting that can be used to remove single points/pixels that does not fit with the surroundings is clean up, which is found with right clicking ”Pattern” or ”All data” in the left menu, shown in Figure A.8a, and then choosing ”Cleanup”. Then the menu shown in Figure A.8b pops up. One option is to use the ”Neighbor CI Correlation”, which is also chosen in Figure A.8b. In this method a CI value is chosen and the clean up is only performed on data below this CI value. If a data point has a CI less than the value chosen, the point is compared to the neighbors to check which neighbor has the highest CI. Then the CI and orientation of the point is reassigned to match the orientation and CI of the neighbor with the maximum CI [47].

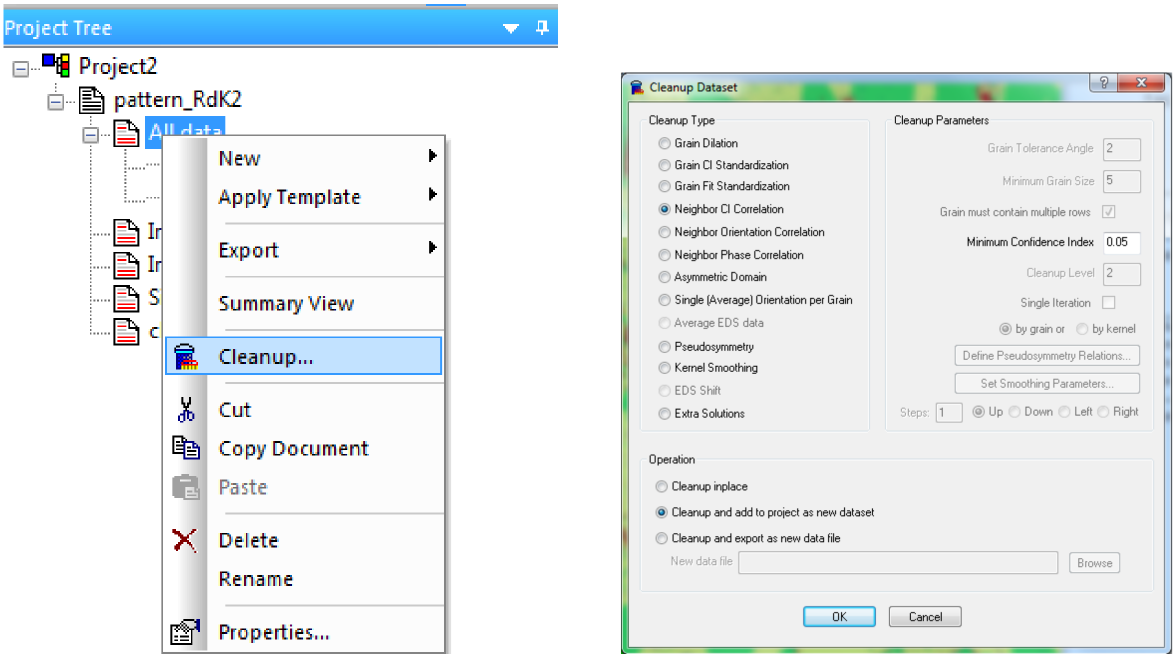

Cleanup Type
○ Grain Dilation
○ Grain CI Standardization
○ Grain Fit Standardization
● Neighbor CI Correlation
○ Neighbor Orientation Correlation
○ Neighbor Phase Correlation
○ Asymmetric Domain
○ Single (Average) Orientation per Grain
○ Average EDS data
○ Pseudosymmetry
○ Kernel Smoothing
○ EDS Shift
○ Extra Solutions

Cleanup Parameters
Grain Tolerance Angle 2
Minimum Grain Size 5
Grain must contain multiple rows ☑
Minimum Confidence Index 0.05
Cleanup Level 2
Single Iteration ☐
● by grain or ○ by kernel
Steps: 1 ● Up ○ Down ○ Left ○ Right

Operation
○ Cleanup inplace
● Cleanup and add to project as new dataset
○ Cleanup and export as new data file
New data file

(a) How to get to the clean up menu (b) Menu for choosing clean up method

Figure A.8: Clean up process

Another option is ”Neighbor Phase Correlation”. This clean up also only performs the clean up on the data points below a chosen CI value. These points are reassigned orientation and phase belonging to the majority of the neighbors. If there is no majority, the point is randomly changed [46].

The changes done for the phase map is shown in Figure A.9. Noticeable are only small changes.

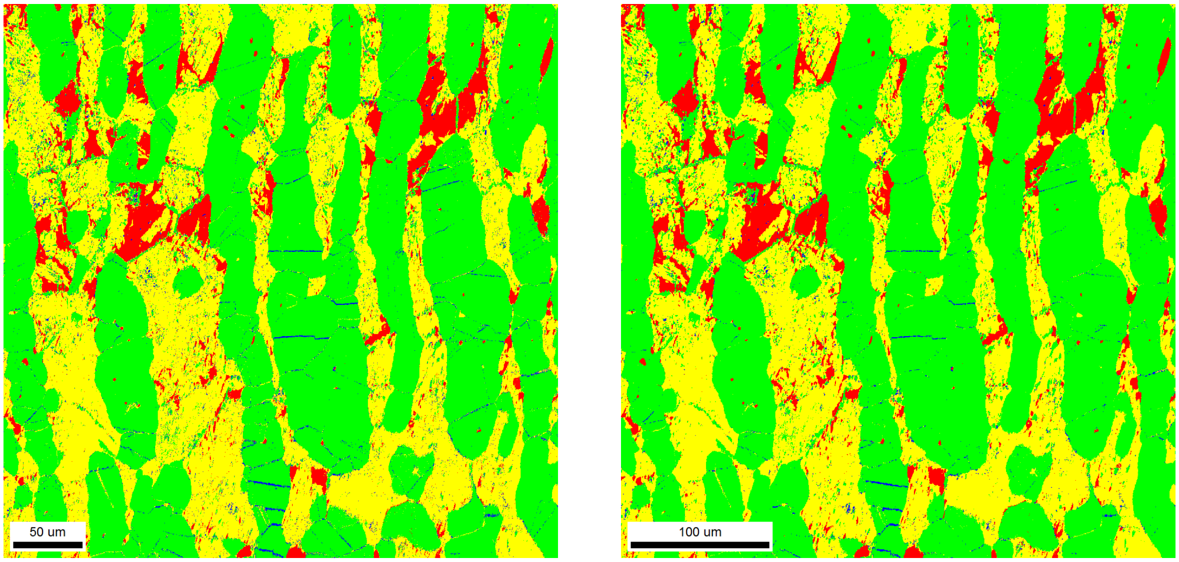

(a) Before cleanup (b) After cleanup

Figure A.9: Phase maps of the material heat treated at 750 °C before and after cleanup with method "Neighbor Phase Correlation" with CI minimum value 0.05

A.8 Removing Points

Clean up is often used to optimize the output from the data, but there are also other options that can be used. One option is to only show one phase. This is done with choosing ”Properties” in the menu shown in Figure A.8a. Then the menu shown in Figure A.10 will pop up. Here there are several choices to choose from, both point properties and grain properties. In this manual the choices ”Confidence Index” and ”Phase” will be shown. If ”Confidence Index” is chosen, the menu shown in Figure A.11a will pop up. In this figure the minimum CI = 0.05 is chosen. Then the phase map will look like Figure A.12a. Then it becomes very obvious that many of the points indexed as sigma phase have a low CI value. If instead ”Phase” is chosen, the menu shown in Figure A.11b will pop up. Then the choice between choosing every phase except one, or only showing one phase will be given. Shown in Figure A.12b is a phase map where only sigma is shown.

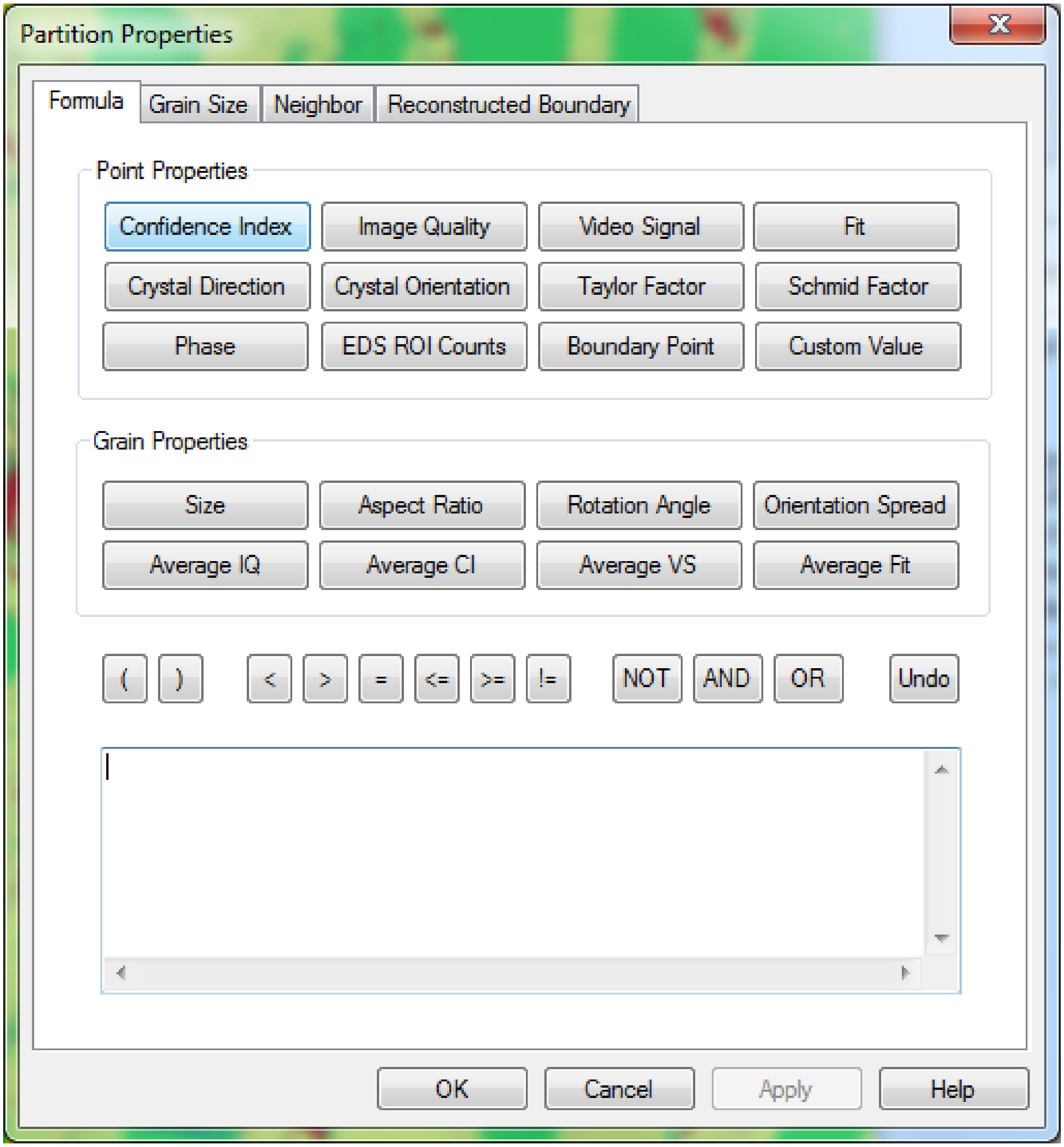

Figure A.10: Menu for partition properties

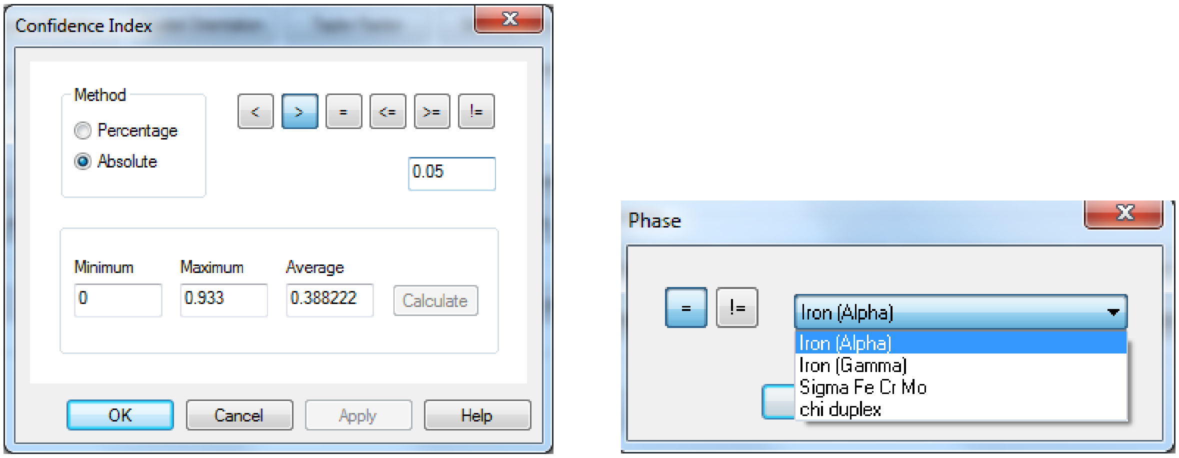
Confidence Index

Method
○ Percentage
● Absolute

Value: 0.05

Minimum: 0
Maximum: 0.933
Average: 0.388222

Phase

Iron (Alpha)

(a) Menu for confidence index

(b) Menu for phase

Figure A.11: Menu after choosing a)confidence index and b)phase from Figure A.10

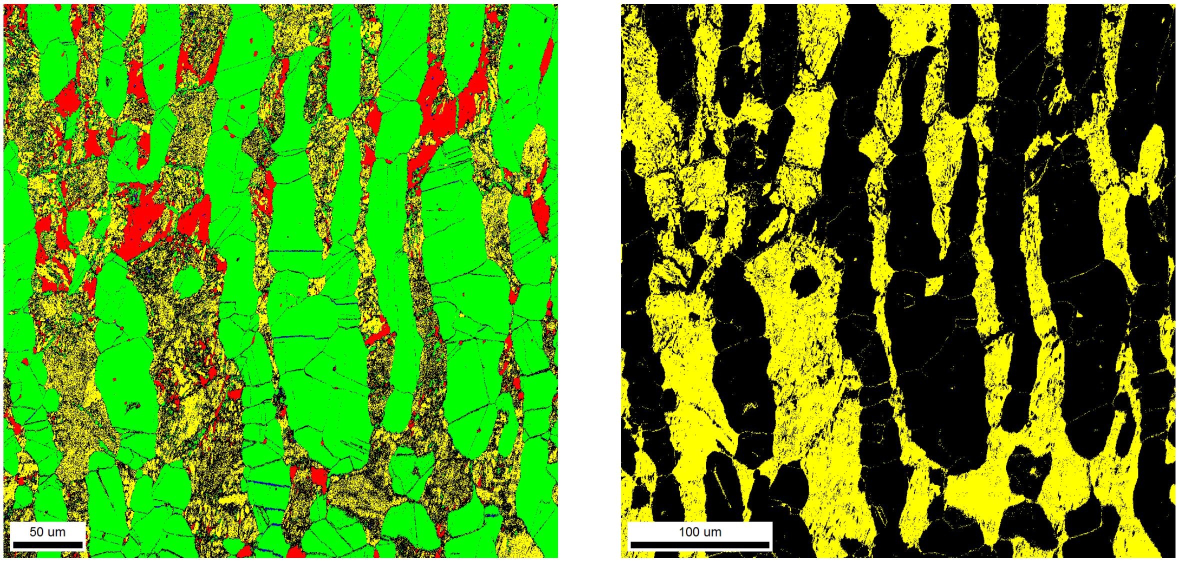

(a) Showing only points with CI values larger than 0.05

(b) Showing only points indexed as sigma phase

Figure A.12: Phase maps of material heat treated at 750 °C for four hours after partition properties treatment

B Scan mode "Timed" in NORDIF 3.1

B.1 Pattern Acquisition

NORDIF 3.1 provides a new function where it is possible to do scans in a given time interval automatically, and how to use this will be presented in this part.

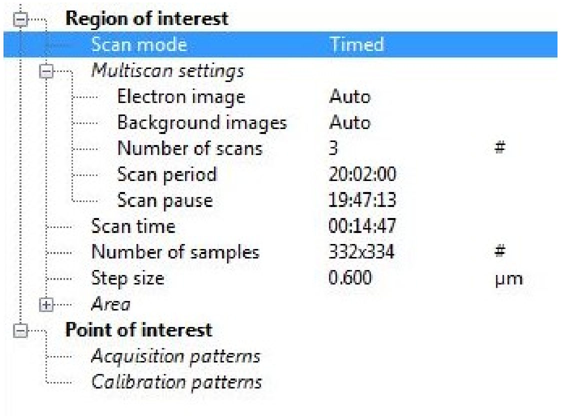

Region of interest		
Scan mode	Timed	
Multiscan settings		
Electron image	Auto	
Background images	Auto	
Number of scans	3	#
Scan period	20:02:00	
Scan pause	19:47:13	
Scan time	00:14:47	
Number of samples	332x334	#
Step size	0.600	µm
Area		
Point of interest		
Acquisition patterns		
Calibration patterns		

Figure B.1: The menu for choosing timed scan

These steps can be used when using the software:

1. Choose step size
2. Choose number of scans
3. Choose region of interest/area and pattern acquisition parameters. From this the scan time will be given.
4. Choose a scan period which is bigger than the scan time. From this you will get a given pause.
5. Choose manual or auto electron images and background images

If manual electron image and background is chosen and it is not taken, previous electron image and background image will be used for the scan. Remember that once you have chosen a number of scans, you can not change any of the parameters during these scans except what you can control with the SEM (contrast, brightness etc.). This means that you cannot choose another area with "drawing" a square, but you have to do it with moving the sample in the microscope. The scan will also begin automatically after the pause and the given pause is therefore the only time you have to refocus and choose the same area, therefore you should adjust the scan period, and scan pause, from this.

B.2 Changing Scan Order

To be able to index the scan in a batch which will be shown in the next subsection, the scans need to in order. To do this you have to open the folder that you want to change. Then, when you are in this folder, you choose "File", "Multiple project" and then "Scan order", shown in Figure B.2a. When this is clicked, a new window will pop up, shown in Figure B.2b. In this window, choose a scan order from the "Size" scroll down menu, then click "Update project". By doing this, it is possible to choose from the "Pattern location" scroll down menu "Pattern folder" shown in Figure B.2c. Then all of the pattern.dat files will be placed in the parent folder named pattern_r1c1.dat, pattern_r1c2.dat etc.

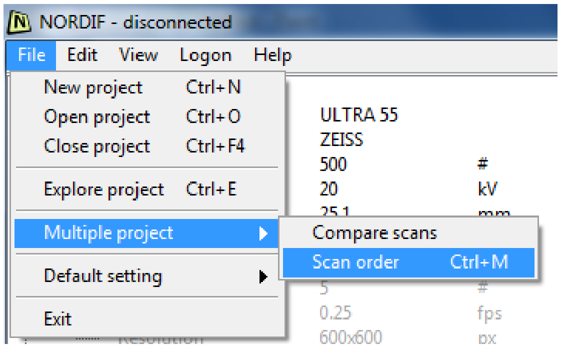

(a) First step to change the scan order

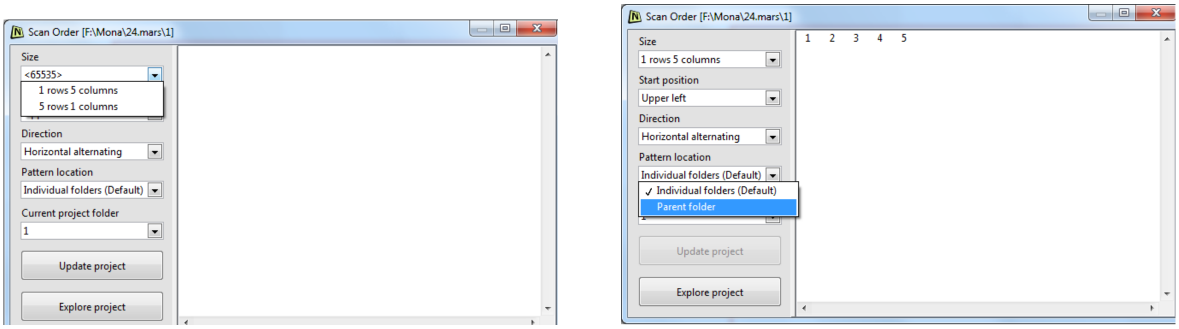

Size
<65535>
1 rows 5 columns
5 rows 1 columns
Direction
Horizontal alternating
Pattern location
Individual folders (Default)
Current project folder
1

Size
1 rows 5 columns
Start position
Upper left
Direction
Horizontal alternating
Pattern location
Individual folders (Default)
✓ Individual folders (Default)
Parent folder

(b) Second step to change scan order (c) Third step to change scan order

Figure B.2: How to define the scan order

B.3 Data Processing

To be able to process data in batches, you should define the scan order, see last subsection. After this, TSL/OIM Analysis is used as usual, choosing phases and Hough parameters. To index all the patterns inside one batch, choose the first file called "Pattern_r1c1.dat". Index the calibration patterns, and thereafter click "Yes" in the pop-up window shown in Figure B.3, and thereafter choose "Start Batch".

B.4 How to Scan Individual Scans

It might be wanted to process only one of the scans. Since there is only calibration patterns for the first scan, the calibration pattern information is only contained in the first setting-file, and not in the later ones. This is possible to do yourself if you only

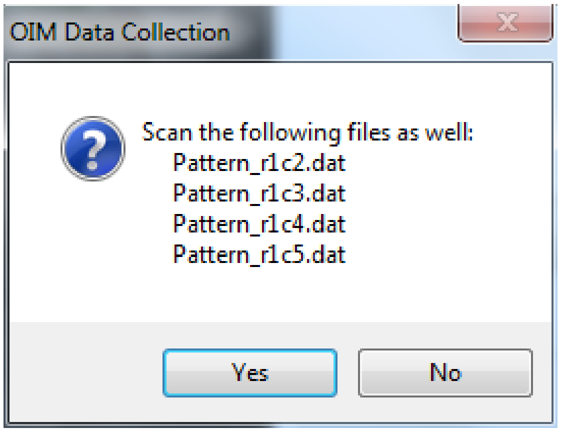

Scan the following files as well:
Pattern_r1c2.dat
Pattern_r1c3.dat
Pattern_r1c4.dat
Pattern_r1c5.dat

Figure B.3: How to copying calibration data from one setting file to another

want to process one of the scans. Then you need to do the following steps:

1. Make a copy of the Setting.txt file that you want to change (The one for the patterns you want to process)
2. Open the Setting.txt file from the first scan and copy the calibration pattern coordinates which is located at the bottom of the file, shown in Figure B.4, to the original Setting.txt file that you wanted to change and paste them at the same location under "[Calibration patterns]".
3. Copy the calibration patterns (.bmp file), and background and electron image if this is not taken for the scan, from the first scan folder to the scan folder you want to process
4. Process the scan

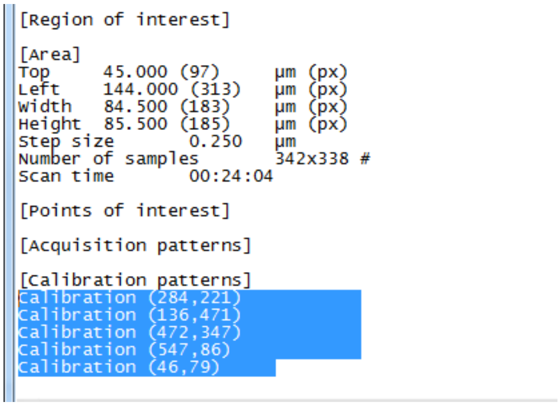

```
[Region of interest]

[Area]
Top     45.000 (97)      µm (px)
Left    144.000 (313)    µm (px)
Width   84.500 (183)     µm (px)
Height  85.500 (185)     µm (px)
Step size        0.250   µm
Number of samples        342x338 #
Scan time        00:24:04

[Points of interest]

[Acquisition patterns]

[Calibration patterns]
Calibration (284,221)
Calibration (136,471)
Calibration (472,347)
Calibration (547,86)
Calibration (46,79)
```

Figure B.4: How to copying calibration data from one setting file to another

C EMAS paper

CHARACTERISATION OF SUPER DUPLEX STAINLESS STEEL BY OPTIMISATION OF EBSD PARAMETERS

M Haukali[1], I Westermann[1], M Karlsen[2], Y Yu[1], R de Kloe[3] and J Hjelen[1]

[1] Norwegian University of Science and Technology, Department of Material Science and Engineering, Alfred Getz vei 2, 7491 Trondheim, Norway

[2] Equinor ASA, Stavanger, Norway

[3] Ametek B.V., EDAX Business Division, Ringbaan Noord 103, P.O. Box 4144, 5004 JC Tilburg, the Netherlands

* e-mail: monahauk@stud.ntnu.no

ABSTRACT

Electron backscatter diffraction (EBSD) [1] was used to characterise the microstructure of a super duplex stainless steel (SDSS) alloy Zeron 100 and the intermetallic phases sigma and chi in this material. The material was analysed in three conditions; as-received, heat treated at 900 °C for eight minutes, and heat treated at 750 °C for four hours. The heat treatments were done to introduce the intermetallic phases in the steel. It is difficult to get reliable indexing of the sigma- and chi-phase due to noisy and overlapping patterns. To get the best results, the Hough transformation parameters were optimised, and an averaging technique [2] was used. The optimisation was done by removing some of the reflectors in the sigma- and chi-phase in the original TSL material files used to index the patterns. By changing the Hough parameters, considerable improvements in the indexing of the patterns were observed, which was amongst other factors observed in an increase in average confidence index (CI) value for both the intermetallic phases. The applied SEM, Zeiss Ultra 55 FESEM was equipped with a NORDIF UF-1100 EBSD detector to acquire and stream patterns to HD. Indexing and data processing were performed by TSL/OIM 7.3. In the present study, four different phases are present in the SDSS at the most.

INTRODUCTION

Super duplex stainless steels are used in petrochemical industry because of their high corrosion resistance and good mechanical properties. These properties come from high content of alloying elements, especially high chromium content which provides high corrosion resistance. However, the wrong heat treatment for these steel grades can lead to embrittlement of the materials through intermetallic phases like sigma- and chi-phase. This can happen during fabrication, welding processes and prolonged exposure to high temperatures during their service lives. The embrittlement can lead to catastrophic service failure of components.

A way to investigate the intermetallic phases is with EBSD (Electron Backscatter Diffraction) in the SEM(Scanning Electron Microscope). But the intermetallic phases, sigma and chi, can be challenging to index. The aim of this study is to investigate a super duplex stainless steel alloy, UNS S37260 or Zeron 100, with focus on the intermetallic phases with EBSD for phase analyses. The project is done together with Equinor ASA.

MATERIALS AND METHODS

The material used in this study was the alloy Zeron 100, a super duplex stainless steel in annealed condition. The material was provided by Equinor ASA with composition shown in Table 1.

Table 1: Chemical composition of alloy UNS S32760 (wt%)

Alloy Element	Cr	Ni	Mo	Cu	Mn	W	Si	N	C	P	S
Wt%	25.55	8.28	3.46	0.72	0.52	0.52	0.42	0.2-0.3	0.018	0.017	0.001

The three samples investigated was one as received as reference, one heat treated at 900°C for eight minutes (~5% sigma) and one heat treated at 750°C for four hours (~30% sigma). The samples were firstly indexed with default Hough transform parameters and default material files for all the phases. Thereafter, both the Hough parameters and the material file for sigma and chi in TSL OIM was changed.

Heat Treatments

The heat treatments were done to introduce different amounts of the intermetallic phases sigma and chi. The heat treatments were done with Nabertherm P300 muffle furnace and afterwards the samples were quenched in room tempered water. One of the samples was heat treated at 900°C for eight minutes, which introduces about 5% sigma, and the other at 750°C for four hours, which introduced about 35% intermetallic phases.

Sample Preparation

The samples were grinded with ATM Saphir 330 with 150 rpm, and SiC paper up to grit 4000 with water as lubricant. Thereafter the samples were polished with Struers DP-U3 with 150 rpm with belonging polishing disks, diamond suspension with particle size 3.0 µm and 1.0 µm and with ethanol based lubricant for 15 minutes. After that vibration polishing with amplitude 70% and a weight of 200 grams was done with Buehler Vibromet 2. After every grinding and polishing step, the samples were cleaned with water and ethanol. Lastly the samples were plasma cleaned with Fischione Model 1020 for five minutes.

Scanning Electron Microscope (SEM)

The SEM used to study and to acquire Kikuchi patterns from the material was Zeiss Ultra 55 FESEM. The parameters used in the SEM is shown in Table 2.

Table 2: Parameters used in Zeiss Ultra 55 FESEM

Parameter	Value
Accelerating voltage	20kV
Working distance	25 mm
Magnification	200x
Aperture size	300 µm
Angle	70°
High current mode	ON
Dynamical focus	10-15%

Electron Backscatter Diffraction (EBSD)

EBSD was done on the three investigated samples. The software used was NORDIF 3.0.43 and the parameters used are shown in Table 3. Step size used was 0.25 µm and the region of interest varied, with the biggest area being 400x400 µm. Thereafter, the area was cropped to get a more detailed look at specific phases. For every measurement five calibration patterns were collected, one in each corner and one in the middle of the area. A background image was acquired before the start of acquiring the patterns. This was done to get better signal and avoid background noise.

Table 3: Parameters used in NORDIF 3.0.43.

Parameter	Acquisition	Calibration
Averaging	2	5
Speed	400 fps	500 fps
Resolution	120x120 px	160x160 px
Exposion time	2450 µs	7092 µs
Gain	4	1

TSL OIM Analysis

The data from the EBSD was characterized with TSL OIM Analysis. The data was first analyzed with default bmt-files for the phases ferrite, austenite, sigma and chi. Thereafter the same acquired patterns were characterized with new bmt-files for sigma and chi provided by Rene de Kloe, Ametek. The difference in the chi bmt-material file was that some of the reflectors was removed, the reflectors [4 2 2] and [6 6 0] were removed in the new, optimized file. The only change in the sigma bmt-file was the symmetry group of sigma, changing it from Tetragonal C4h/[4/m] to Tetragonal D4h[4/mmm].

Table 4: OIM Data Analysis Hough Parameters

Parameter	Before Optimization	After Optimization
Binned Pattern Size	96	96
Theta Step Size	1°	0.5°
Rho Fraction	85	88
Max Peak Count	3	3
Hough Type	Classic	Classic
Hough Resolution	Low	Low
Convolution Mask	9x9	7x7
Min Peak Magnitude	5	1
Max Peak Magnitude	15	10
Peak Symmetry	0.70	0.70
Vertical Bias	0%	0%

RESULTS

Optimization of Hough Parameters

Optimization of Hough parameters was done to characterize the sigma- and chi-phase in the best possible manner. The optimization was used on the sample treated at 900°C for eight minutes and the sample treated at 750°C for four hours. The results are presented in this part. Cleanup below CI = 0.05 has been used. The colors of the phases are indicated in Figure 1.

Figure 1: Colors for the different phases

Material treated at 900°C for Eight Minutes

In Figure 2 the IQ map for this sample is shown. The area of the measurement is 37.75μmx 32.50μm. This is obviously a small area, and the phase composition is not representable for the entire sample, but it is used to show the difference in the use of the parameters. The step size used to acquire the signals is 0.25 μm. As can be seen, there are some dark areas on the IQ maps. It can also be observed that the maps are not of optimal quality. The grain boundaries appear dark but relatively clear.

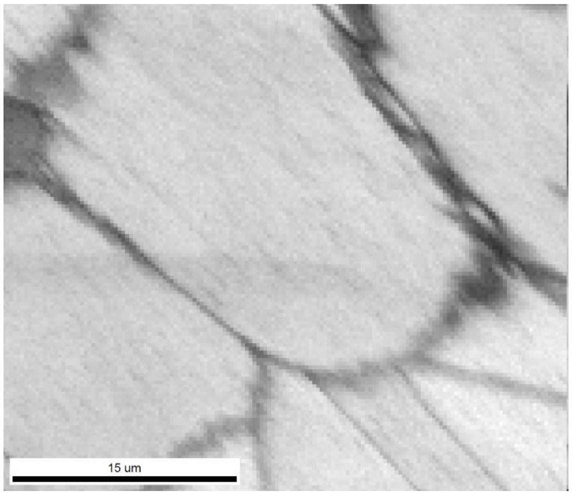

Figure 2: IQ map of sample heat treated at 900°C for eight minutes

Figure 3 shows the phase maps of the material heat treated at 900°C for eight minutes before and after the Hough parameter optimization. The austenite is the green phase, ferrite is red, and sigma is yellow. From the figure it can be observed that the optimization leads to less noise in the map and less points are characterized as sigma-phase. This can also be seen in Table 5 which shows a higher fraction of austenite after the optimization.

Table 5: Phase fraction of the material heat treated at 900°C for eight minutes before and after Hough parameter optimization

Phase	α	γ	σ
Before Optimization	45.4%	45.4%	7.4%
After Optimization	44.2%	50.7%	5.1%

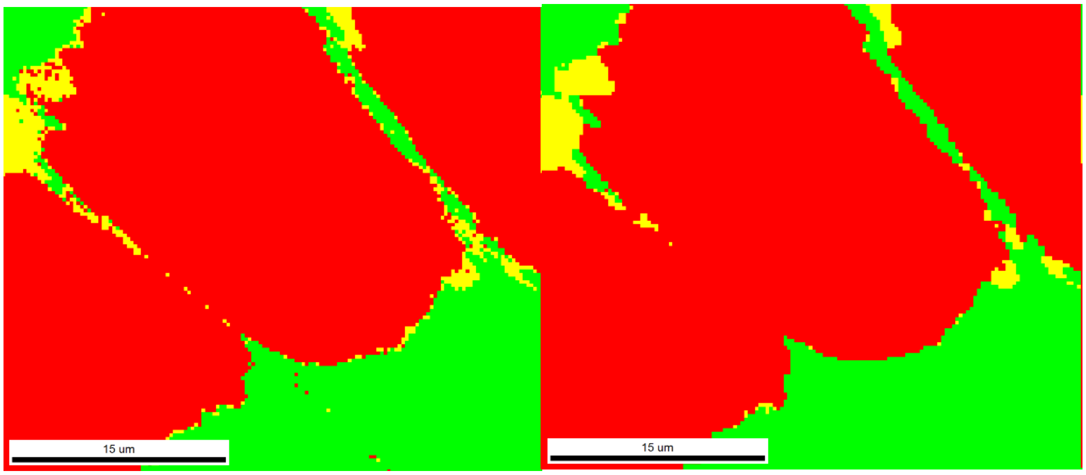

Figure 3: Phase map for material heat treated at 900°C for eight minutes. Left:Before Optimization. Right: After Optimization

Table 6 shows that the CI value for the sigma-phase increases, from 0.08 to 0.14. The CI value for ferrite (alpha) also increases with the optimization, while the value for austenite (gamma) decreases slightly. The IQ values for all the phases increase after the optimization. The fit for all the parameters decreases and gets closer to zero.

Table 6:Average IQ, CI and fit values for the material heat treated at 900°C for eight minutes before and after optimization

Parameter	γ+α+σ	α	γ	σ
CI, Before	0.64	0.66	0.7	0.08
CI, After	0.73	0.79	0.67	0.14
Fit, Before	0.90	0.85	0.93	1.53
Fit, After	0.71	0.66	0.72	1.46

Material treated at 750°C for Four Hours

In Figure 4 the IQ maps for this sample is shown. The area of the measurement is 39.40µm x 33.60µm. Again, the area is not representative for the phase composition of the entire sample. As can be seen, a lot of the IQ map is covered by dark areas. It can also be observed that the picture is not of optimal quality. It can be seen some lighter areas in the upper left corner and on the right side of the map, as well as some smaller points in between the darker areas. The grain boundaries appear darker.

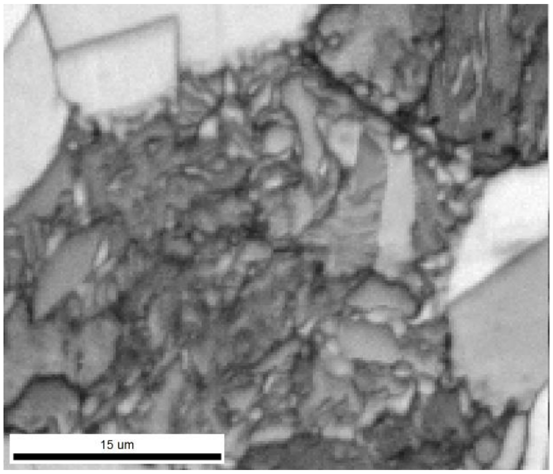

Figure 4: IQ map of sample heat treated at 750°C for four hours

Figure 5 shows the phase maps of the material heat treated at 750°C for four hours before and after the Hough parameter optimization. The austenite is illustrated as the green phase, ferrite as red, sigma is yellow and the chi-phase is blue. From the figure it can be seen that the optimization leads to a considerable amount less noise in the map. It can also be observed that most of the noise comes from the chi-phase. After the optimization less phase is indexed as chi and more as ferrite (alpha) on the optimized phase map. This is also shown in Table 7. More of the points are also indexed as sigma-phase after the optimization.

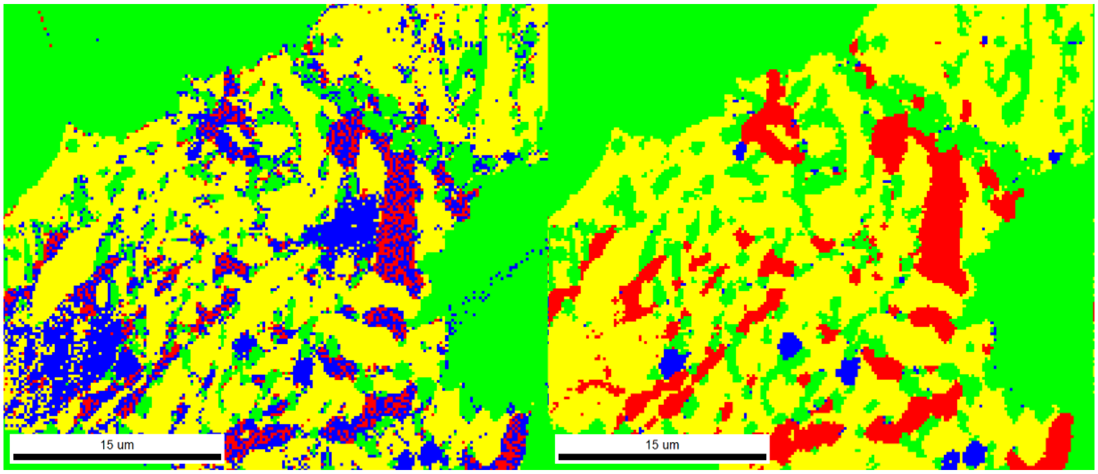

Figure 5: Phase map for material heat treated at 750°C for four hours. Left: Before Optimization. Right: After Optimization

Table 7: Phase fraction of the material heat treated at 750°C for four hours before and after Hough parameter optimization

Phase	α	γ	σ	χ
Before Optimization	5.6%	36.5%	41.4%	16.5%
After Optimization	10.9%	38.0%	49.1%	2.0%

Table 8 shows that the CI value for the sigma-phase increases, from 0.08 to 0.14. The same does the CI value for chi, from 0.12 to 0.17. Especially worthy of mentioning is the rise in CI value for alpha from 0.01 before the optimization to 0.45 after the optimization. It can be seen that the fit increase for all the phases except the sigma phase, with the optimization, with the average increasing from 1.04 to 1.09.

Table 8: Average IQ, CI and fit values for the material heat treated at 750°C for four hours before and after optimization

Parameter	α+γ+σ+χ	α	γ	σ	χ
CI, Before	0.22	0.01	0.47	0.08	0.12
CI, After	0.30	0.45	0.48	0.14	0.17
Fit, Before	1.04	0.97	0.73	1.28	1.16
Fit, After	1.09	1.07	0.92	1.21	1.5

DISCUSSION

Hough Parameter Optimization

The Hough parameter optimization leads to clear changes in the indexing of the different phases, especially the sigma- and chi-phase. The IQ-, CI- and fit values will be discussed as well as the IQ- and phase maps for the two relevant samples. The changes done with the optimization will be discussed.

Effect on Characterization of Phases

The optimization of the parameters leads to a clear improvement of the characterization of the sigma- and chi-phase. Figure 3 for the material treated at 900°C and Figure 5 for the material heat treated at 750°C show that the amount of noise is much bigger before the optimization. This is especially shown in Figure 5. Most of the pixels that are wrongly indexed in Figure 3 are sigma-phase that is converted to either ferrite or austenite, but also some ferrite that are converted to austenite. The ferrite that has been converted to austenite are from the cleanup process.

Figure 3 describes the difficulties of characterizing the chi-phase. Presumably there is added difficulties when there are two phases that are difficult to characterize. This is also illustrated by the optimization, because a lot of the previously indexed chi is after the optimization indexed as sigma, shown in Figure 5, and is also observable in Table 7. The chi phase is reported to both have a BCC-structure [6], while sigma has a tetragonal structure which is similar. Some of the previously indexed chi-phase is converted to ferrite after the optimization. This is because the unit cells have a lot of the same reflectors and the unit cells are similar [9]. The optimization contains a disabling of a reflector in the chi-phase that is also used in the ferritic phase.

The optimization leads to a smaller amount of sigma-phase in the material treated at 900°C, see Table 5, and a significant smaller fraction of chi-phase and a higher amount of sigma-phase in the material treated at 750°C, see Table 7. This clearly shows the results of processing of data. Some of the points indexed as chi in Figure 5 can be imagined to be ruled out as noise, but some of the points look like clear clusters of chi. In Figure 3 the difficulty of indexing probably mostly comes from the difficulties of indexing grain boundaries and the mixing signals from the different grains. Grain boundaries are indexed with the help of misorientation angle, so all boundary segments with an angle higher than the defined critical angle are considered grain boundaries [3].

The fraction of austenitic phase increases with the optimization in both the samples, see Tables 5 and 7. It is to be expected that the fraction of austenite stays the same, or even increases, compared to the as-received material, and alpha decreases after the short term heat treatments. This is because sigma (and chi) is formed where the elements molybdenum and chromium are saturated, which is in the ferritic phase. This reaction also causes new austenite to be formed.

The symmetry group of sigma is changed with the optimization, from tetragonal C4h/[4/m] to Tetragonal D_{4h}[4/mmm]. In other literature the space group for sigma has been identified as $P4_2$/[mnm] which is the same space group as D_{4h} [5, 6]. This corresponds to the optimzed case.

Effect on CI, IQ and Fit Values

The optimization of the parameters leads to a clear improvement in the CI, IQ and fit values for the sigma- and chi-phase, but also for the ferritic and austenitic phase. The overall CI value increases after the optimization both for the material heat treated at 900°C, see Table 6 and for the material heat treated at 750°C, see Table 8. For the material treated at 900°C the average CI value for all the phases goes from 0.64 before the optimization to 0.73 after the optimization. The reason for an increase in this value is mostly caused by the increase in the CI value for the ferrite (alpha) from 0.66 to 0.79. Sigma also contribute positively with an increase from 0.08 to 0.14. For the material heat treated at 750°C that contains a significantly larger amount of sigma and chi, the average CI value for all the phases increases from 0.22 to 0.30 after the optimization, see Table 8. The value for sigma increases from 0.08 to 0.14, and from 0.12 to 0.17 for the chi-phase. Another value to notice is the increase from 0.01 to 0.45 for ferrite. A reason for this might be the difficulty with extinguishing between ferrite and chi. After removing the strong reflector from the chi-phase, the number of votes on the chi-phase decrease, and the CI of ferrite rises. The increase in CI value means that the second solution for phase identification is less likely in the optimized case.

The IQ (Image Quality) indicate something about the sharpness of the peaks measured [1]. It can be taken from Tables 6 and 8 that the IQ value after the optimization is higher than before the optimization. The higher IQ value means that the bands collected are sharper and easier to identify. In addition it can be seen that the ferrite grains are darker than the austenite grains in the IQ map, Figures 2 and 4, which can also be deducted from Tables 6 and 8 where the IQ value for the austenite phase is bigger than the same for the ferrite phase, both before and after the optimization.

Observed from Figure 4 compared to Figure 2 there is much more dark areas in this sample, therefore it is expected to be more of the intermetallic phases. The darkest areas in Figure 4 can be identified as sigma-phase if compared to Figure 5. Dark areas in the picture is due to low IQ value, which happens when the band edges are diffuse.

The perfect value for the fit is zero. This means that the angular deviation between recalculated and detected bands is zero [7]. The average fit decreases from 0.90 to 0.71 for the material heat treated at 900°C after the optimization and increases from 1.04 to 1.09 for the material treated at 750°C. One possible reason for this can be the change of convolution mask, from 9x9 to 7x7, see Table 4. The default value is 9x9, but for narrower bands it better to use 7x7 [8]. For the investigated phases sigma and chi, the fit value for sigma is decreases in both samples, and the fit value for chi increases in the sample treated at 750°C for four hours.

The aim of the stud is to characterize the sigma- and chi-phase better. From the analyses of the values, it seems like the characterization of the sigma-phase is better after the optimization.

CONCLUSION

Changing the Hough parameters as well as the bmt material files in TSL/OIM 7.3 for sigma and chi lead to a better indexation of these intermetallic phases in a SDSS UNS S32760. This was proved with an increase in the average CI values in both the samples, from 0.6 4 to 0.73 in the material containing around 5% sigma and from 0.22 to 0.30 in the material containing about 30% sigma. The average for the one containing 5% sigma, from 0.90 to 0.71.

ACKNOWLEDGEMENTS

The authors would like to thank Rene de Kloe from Ametek B.V., the Netherlands for providing bmt-files for TSL OIM Analysis Software.

REFERENCES

[1] Schwartz A J et. al. *Electron Backscatter Diffraction in Materials Science*, volume 2nd Edition. Springer, 2009.

[2] Kleppen J 2018 *Quantification of the sigma phase in super duplex stainless steel by scanning electron microscopy* SCANDEM 2018, Copenhagen, Denmark

[3] Chan K W and Tjong S C. Effect of secondary phase precipitation on the corrosion behavior of duplex stainless steels. *Materials*, **7**:p 5268–5304, July 2014.

[4] Warren A D, Harniman R L, Guo Z, Younes C M, Flewitt P E J, and Scott T B. Quantification of sigma-phase evolution in thermally aged 2205 duplex stainless steel. *Journal of Materials Science*, **51**(2):694–707, Jan 2016.

[5] Grain size and grain boundary characterisation in sem. http://www.ebsd.com/solvingproblems-with-ebsd/grain-size-and-grain-boundary-characterisation-in-sem. Accessed:2018-11-30.

[6] Chail G and Kangas P. Super and hyper duplex stainless steels: structures, properties and applications. Procedia Structural Integrity, 2:1755 – 1762, 2016. 21st European Conference on Fracture, ECF21, 20-24 June 2016, Catania, Italy.

[7] Oxford Instruments Analytical. Electron backscattered diffraction, 2004.

[8] TSL. OIM Analysis 7.2 Manual, 1997

D ISOPE paper

EBSD Characterization of the Microstructure Evolution in (σ, χ)-containing SDSS Subjected to Long Term Heating

Mona Haukali [1], *Ida Westermann* [1], *Morten Karlsen* [1,2], *Jarle Hjelen* [1]
[1] Norwegian University of Science and Technology, Trondheim, Norway
[2] Equinor ASA, Stavanger, Norway

ABSTRACT

Super duplex stainless steels (SDSS) are used in oil wells with high temperature and high pressure in the oil and gas industry due to the good combination of high corrosion resistance and excellent mechanical properties. But SDSS are susceptible to formation of brittle intermetallic phases like sigma- and chi-phase at high temperature which gives a significant decrease in the mechanical properties of the steel. The SDSS material heat treated at 900°C for eight minutes and another treated at 750°C for four hours were examined by use of electron backscatter diffraction (EBSD) in SEM. The SDSS samples containing secondary phases were heat treated at 300°C over a period of four weeks. The use of SDSS is limited to temperatures below 250°C, mainly due to spinodal decomposition of alloying elements in the austenite and ferrite. The main objective in this work is to investigate whether the presence of the unwanted alloying element rich chi- and sigma-phase influence the microstructure during long term heating or not.

KEY WORDS: SDSS, sigma, chi, heat treatment, EBSD, SEM, spinodal decomposition

INTRODUCTION

Super duplex stainless steels are widely used in the petrochemical industry because of its good properties. Their high corrosion resistance and good mechanical properties are due to a high content of alloying elements and the high chromium content is especially important for the corrosion resistance. However, the wrong heat treatment to these metals can lead to embrittlement of the materials through intermetallic phases like sigma and chi phase. This can happen during fabrication, welding processes and prolonged exposure to high temperatures during their service lives. Even small amounts of these phases can be responsible for catastrophic service failure of components (Ong et.al (2018)).

A way to investigate the intermetallic phases is using EBSD (Electron Backscatter Diffraction) in the SEM (Scanning Electron Microscope). EBSD is well suited for crystallographic analysis like determination of orientation of individual crystallites, phase identification and characterization of grain boundaries. The aim of this project is to investigate a super duplex stainless steel alloy, UNS 32760 exposed to different heat treatments with EBSD for phase analyses, and EDX (Energy Dispersive X-ray Spectroscopy) for elemental analyses. The project is done in collaboration with Equinor ASA.

MATERIALS AND METHODS

Heat Treatments and Tensile Testing

The material used in the experiments was an UNS 32760 (Zeron 100), which is an SDSS, in annealed condition. The material was provided by Equinor ASA, and the chemical content of the steel is provided in Table 1.

Table 1: Chemical composition of UNS 32760 (wt%)

Alloy Element	Cr	Ni	Mo	Cu	Mn	W
wt%	25.55	8.28	3.46	0.72	0.52	0.52
Alloy Element	Si	N	C	P	S	
wt%	0.42	0.2-0.3	0.018	0.017	0.001	

Three samples were mainly investigated in this paper, one as-received as reference, one heat treated at 900°C for eight minutes (~5% sigma) and one heat treated at 750°C for four hours (~30% sigma). The samples were then investigated before and after a heat treatment at 300°C for three weeks for the as-received material, and four weeks for the sigma containing samples with SEM. Tensile testing were also done to samples with the same heat treatments.

Sample Preparation

Before the long term heat treatment, the samples were prepared using standard metallographic preparation with the following final preparation steps, grit 4000 with the machine ATM Saphir 330 with 150 rpm and water as a lubricant for five minutes. Thereafter the samples were polished with 3.0 µm and 1.0 µm for 20 minutes with Struers Tegramin-30. A force of 20 N was used on the sample in the machine. The last polishing step was vibration polishing with Buehler Vibromet 2 with an amplitude of 70% and a weight of 200 grams for 24 hours. The final step was plasma polishing for five minutes in Fischione Model 1020. After the long term heat treatment the final preparation steps were repeated.

Scanning Electron Microscope (SEM)

The SEM used to study the material was Zeiss Ultra 55 FESEM. This microscope was used both to acquire the EBSD data and for the EDX analyses. The SEM was equipped with a NORDIF UF-1100 EBSD detector. The parameters used for EBSD and EDX in the SEM are listed in Table 2. The parameters used for acquiring the pictures with backscatter electrons was the same as the parameters with EDX.

Table 2: Parameters used in SEM for the characterization with EBSD and EDX

Parameter	EBSD	EDX
Accelerating voltage	20kV	15kV
Working distance	25 mm	10 mm
Magnification	200x 300x	1000x 2000x
Aperture	300µm	60µm
Angle	70°	0°
High current mode	ON	ON
Dynamical focus	10-15%	No

The accelerating voltage used for EDX was 15 kV, see Table 2. The EDX requires a lower accelerating voltage compared to EBSD in addition to lower aperture size. A high magnification was used to find the chi precipitates. The value for accelerating voltage implies that only the Lα-signal for Mo is registered, since Kα for Mo is higher energy than 15 kV (actual value 17.48 kV).

Energy Dispersive X-ray Spectroscopy (EDX)

The EDX was used to differentiate the phases σ and χ from each other. The two different phases can be differentiated because of the different content of molybdenum. This was done through mapping of the structure. In addition BSE pictures were taken to compare with the EDX analyses.

Electron Backscatter Diffraction (EBSD)

EBSD analyses were done on all the samples. The settings for the acquisitions are presented in Table 3. For optimization the solid angle was increased compared to standard setup and was between 72-75°.

Table 3: Parameters used in NORDIF 3.0.43 Software

Parameter	Acquisition
Averaging	2/4
Speed	400 fps
Resolution	120x120 px
Exposion time	2450 µs
Gain	4

Step sizes used were from 0.25 to 1.0 µm on the reference material, and 0.20 to 0.25 µm on the sigma containing samples. The areas measured differed a little, but the largest areas measured were 400x400µm. For every measurement five calibration patterns were collected, one in each corner and one in the middle of the area. A background picture was acquired before the start of acquiring the patterns. This was done to get better signal and avoid background noise during acquisition.

TSL OIM Analysis

The stored patterns, acquired by the NORDIF EBSD acquisition software 3.0.34, were indexed by TSL OIM DC version 7.3 Analysis. The data was first analyzed using the standard Hough transform parameter settings in the software data base ahead of the start of the indexing. Thereafter, the same data was indexed with optimized Hough parameter settings. The difference in parameters used for the analyses before and after the optimization is seen from Table 4. The main change was done with modifying the reflector list in the EBSD structure files. The Hough transform for the ferritic and austenitic phase were the same, but for the sigma- and the chi-phase some corrections were done. For the sigma phase, all the hkl directions used in the old file was also used in the new file. The only change was the symmetry group. The old file characterized the sigma phase as a Tetragonal C4h/[4/m]. The new file characterized the phase as Tetragonal D4h[4/mmm]. The chi phase had some changes in the hkl directions used. In the old the directions [4 2 2] and [6 6 0] were used, and these were not used in the optimized file.

Table 4: OIM Data Analysis Hough Parameters

Parameter	Before optimization	After optimization
Binned Pattern Size	96	96
Theta Step Size	1°	0.5°
Rho Fraction	85	88
Max Peak Count	7	10
Min Peak Count	3	3
Hough Type	Classic	Classic
Hough Resolution	Low	Low
Convolution Mask	9x9	7x7
Min Peak Magnitude	5	1
Max Peak Magnitude	15	10
Peak Symmetry	0.70	0.70
Vertical Bias	0%	0%

RESULTS

Reference Material

The IQ maps of the as-received reference material before and after long term heat treatment are shown in Figures 2 and 3, respectively. The acquisition was done on an area of 250 µm x 250 µm. The measurement before the heat treatment was done with step size 1µm and averaging 2. The acquisition after the heat treatment was done with step size 0.25 µm and averaging 2. As can be seen there are no dark areas in either of the pictures, and the IQ maps look quite similar. The grain boundaries are clear and no topography can be observed on the sample surface. Some polishing marks can be observed from both IQ maps. The grain size is in average around 30 µm for the austenite and around 50 µm for the ferrite. Twin formation is observed in several grains. When comparing with the phase maps in Figure 4 and 5, it is seen that the twin formation only occurs in the austenite.

In Figures 4 and 5 the phase maps of the as-received material before and after the long term heat treatment is presented. The colors used are illustrated in Figure 3. The distribution of phases is about 50/50 for austenite (γ) and ferrite (α) in both cases. Austenite is represented as the green phase and ferrite as the red. This can also be seen from Table 6.

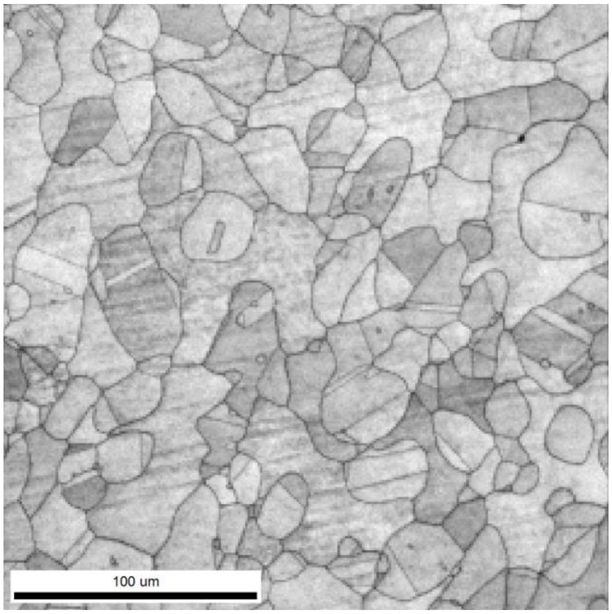

Figure 1: IQ map of the as-received material before heat treatment at 300°C for three weeks

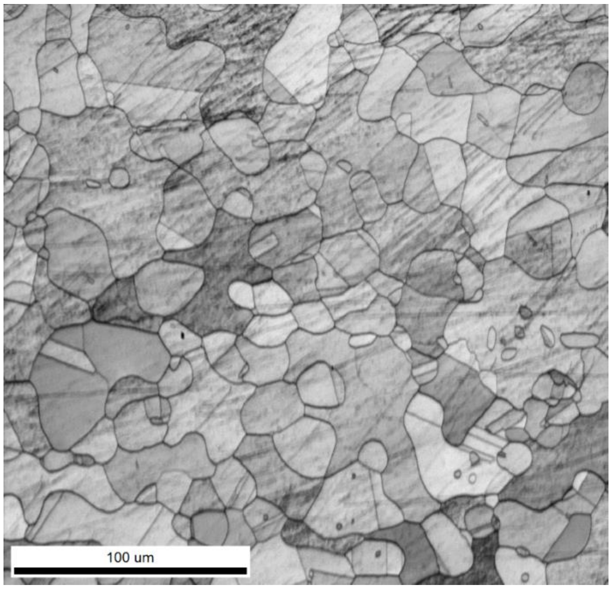

Figure 2: IQ map of the as-received material after heat treatment at 300°C for three weeks.

The fraction might differ slightly based on chosen area of interest. The ferrite phase is more or less a continuous matrix with islands of austenite in the size range of 100 µm maximum distributed within the matrix.

	Phase
🟨	Sigma
🟦	chi
🟥	Ferrite
🟩	Austenite

Figure 3: Color codes for the different phase

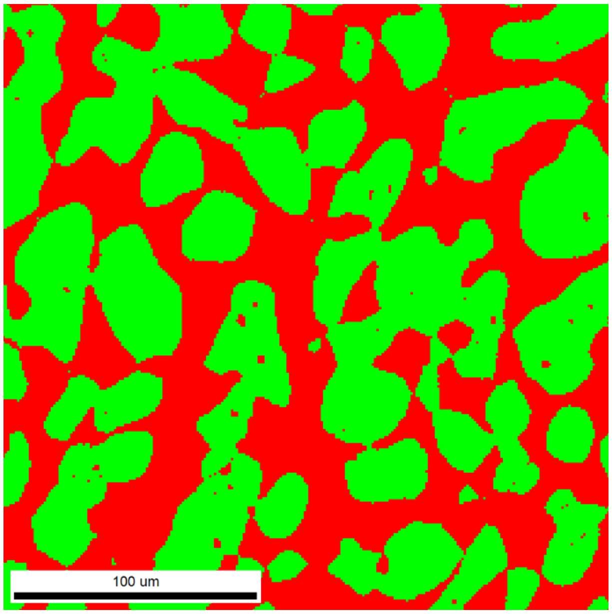

Figure 4: Phase map of the as-received material before heat treatment at 300°C for three weeks

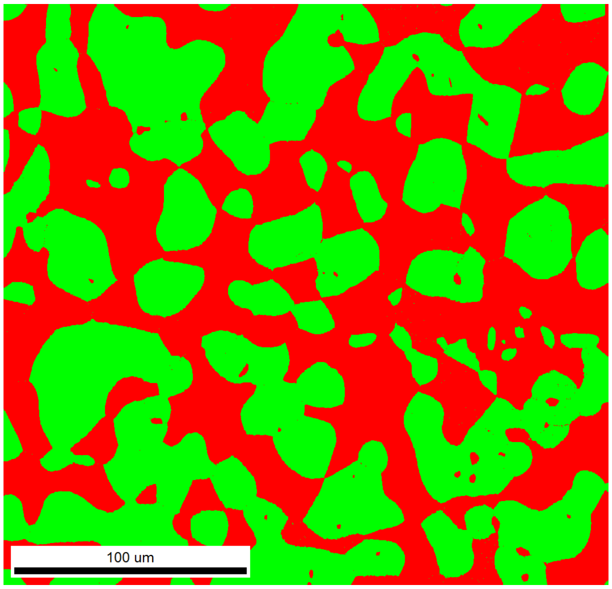

Figure 5: Phase map of the as-received material after heat treatment at 300°C for three weeks

Table 5: Fraction of phases in the as-received in the area before and after long term heat treatment

Phase	α	γ
Before heat treatment	51.0%	49.0%
After heat treatment	50.5%	49.5%

Material containing ~ 5% Sigma

The IQ maps of the material treated at 900°C for eight minutes is shown in Figure 6 and 7 before and after long term heat treatment. The area of the measurement is 250µm x 250µm. In the measurement before the heat treatment, the parameters used was step size 0.25µm and averaging 2. The same parameters were used after the heat treatment. As can be seen there are small fractions of dark areas in both maps.

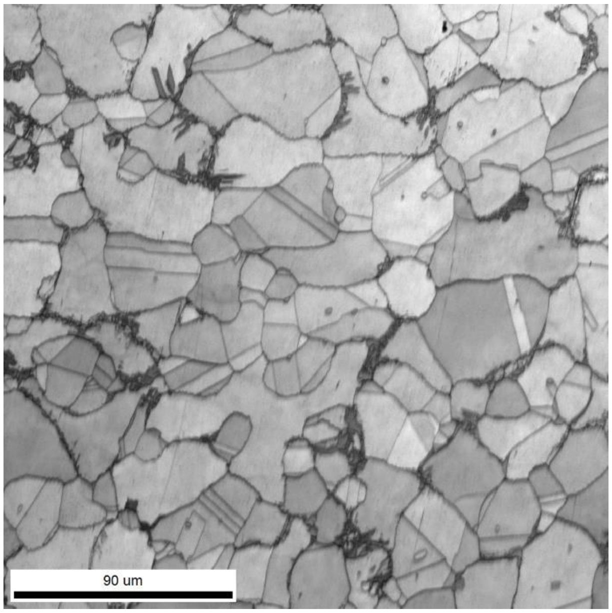

Figure 6: IQ map of the material treated at 900°C for eight minutes before heat treatment at 300°C for four weeks

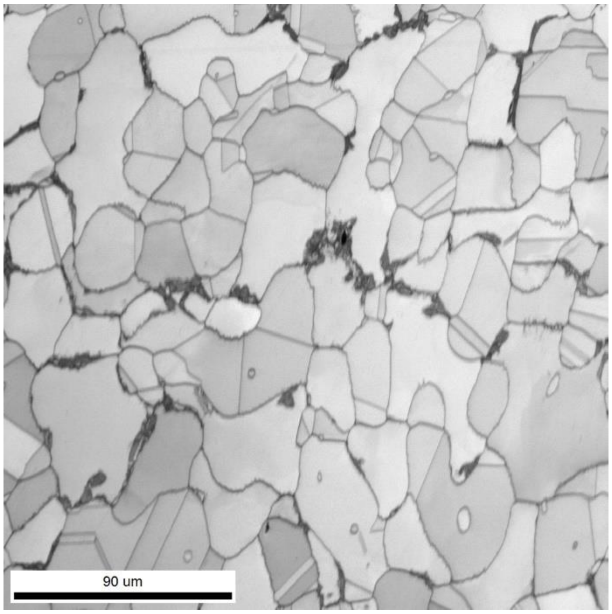

Figure 7: IQ map of the material heat treated at 900°C for eight minutes after heat treatment at 300°C for four weeks

There is a variation of darker and lighter grains in both the pictures, and the grain size seems unchanged compared to the reference material. The dark areas are regions with sigma phase, where the pattern quality is poor. The grain boundaries are clear, and no topography can be observed on the sample surface. In Figures 8 and 9 the phase maps of the material treated at 900°C for eight minutes before and after the long term heat treatment are presented. Small fractions of sigma-phase (~5%) are observed on both maps. Sigma-phase is represented as the yellow phase. The fractions of the different phases are listed in table Table 6. The composition might vary slightly based on chosen area. The sigma-phase is observed mainly on the austenite-ferrite grain boundaries and seems to grow into the ferrite phase. From Figure 8 and 9 the ferrite phase is no longer continuous as sigma and thin regions of austenite form along some of the ferrite-ferrite grain boundaries.

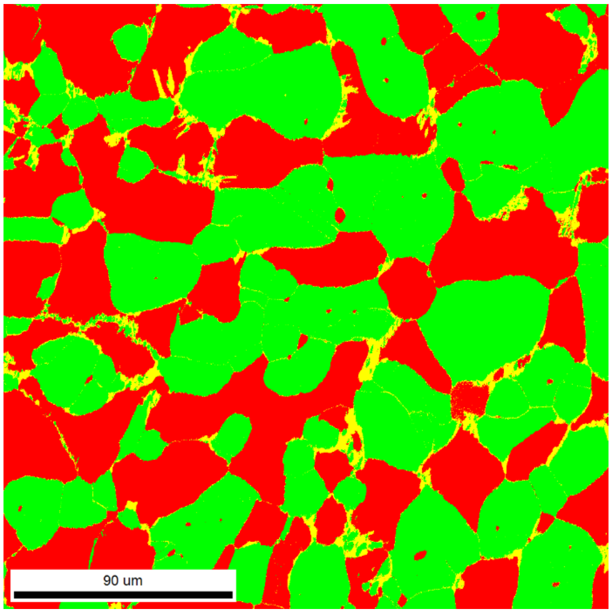

Figure 8: Phase map of the material heat treated at 900°C for eight minutes before heat treatment at 300°C for four weeks

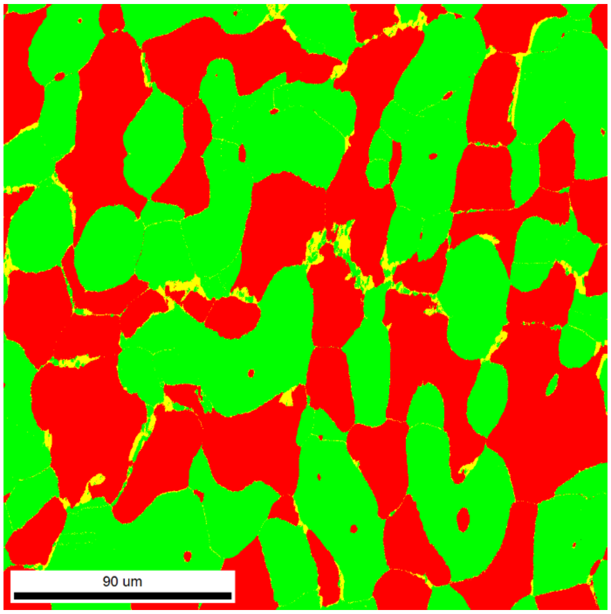

Figure 9: Phase map of the material heat treated at 900°C for eight minutes after heat treatment at 300°C for four weeks.

Table 6: Fraction of phases in the material heat treated at 900°C for eight minutes in the area before and after long-term heat treatment

Phase	α	γ	σ
Before heat treatment	47.4%	48.4%	4.2%
After heat treatment	46.5%	48.6%	4.9%

Material containing ~30% Sigma

The IQ maps of the material treated at 750° C for four hours are shown in Figures 10 and 11 before and after long-term heat treatment at 300°C for four weeks, respectively. The area measured was 250 µm x 250 µm in both the cases. The parameters used to acquire the data both before and after the heat treatment were step size 0.25 µm and averaging 2.

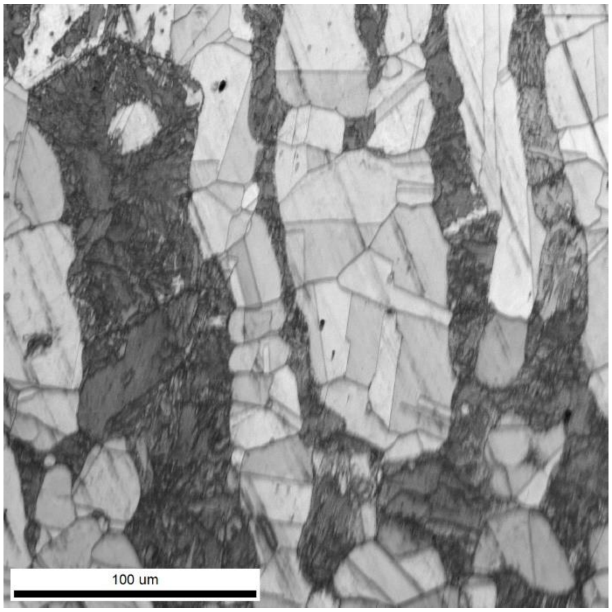

Figure 10: IQ map of the material heat treated at 750°C for four hours before heat treatment at 300°C for four weeks

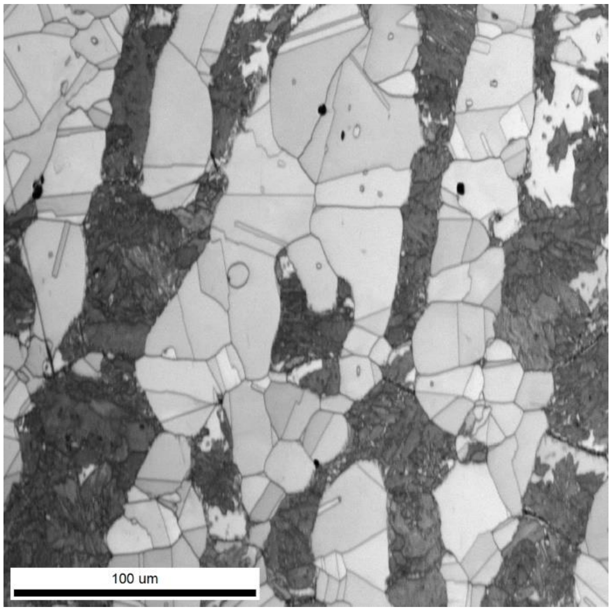

Figure 11: IQ map of the material heat treated at 750°C for four hours after heat treatment at 300°C for four weeks

There are relatively much dark areas in both maps. Here, an extreme amount of ~30% sigma phase has been obtained, as seen from Table 7. There is also a gradient in the lighter parts of both the maps. The grain boundaries are clear, and no topography can be observed on the sample surface. In Figures 12 and 13 the phase maps before and after the long-term heat treatment are presented. Here, a small amount of chi phase is present in blue. The fraction of ferrite has decreased to only 6-7% and there is an increase in austenite compared to the reference material. The microstructure is now a mixture of large bands of continuous austenite and sigma-phase, several hundred µm in length. The ferrite is mainly situated in the vicinity of the sigma-phase. The chi phase is either observed on austenite-austenite grain boundaries in the short direction of the austenite phase bands or inside the sigma clusters. The fraction of the different phases might defer slightly based on chosen area of interest.

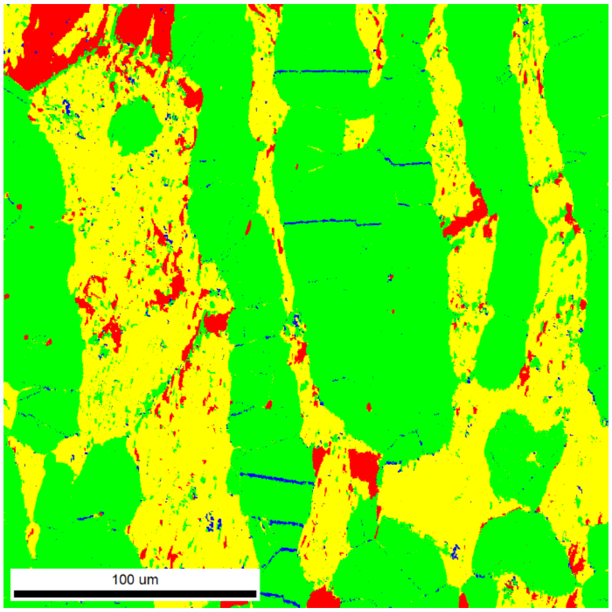

Figure 12: Phase map of the material heat treated at 750°C for four hours before heat treatment at 300°C for four weeks

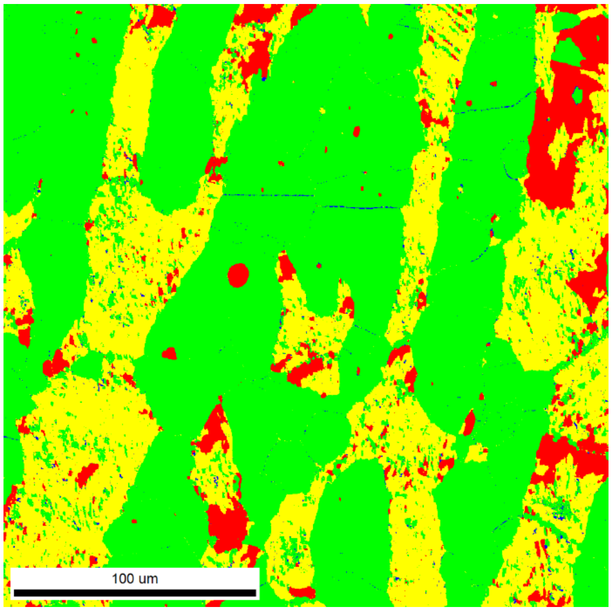

Figure 13: Phase map of the material heat treated at 750°C for four hours after heat treatment at 300°C for four weeks

Table 7: Fraction of phases in the material heat treated at 750°C for four hours in the area before and after long-term heat treatment

Phase	α	γ	σ	χ
Before heat treatment	6.7%	57.1%	34.7%	1.5%
After heat treatment	6.4%	61.5%	31.1%	1.1%

Energy Dispersive X-ray Spectroscopy (EDX)

Mapping was done on the sample containing ~30% sigma phase where the chi phase was also present. The parameters used in the SEM were a magnification of 1000x, an accelerating voltage of 15 kV and a working distance of around 10.0 mm. The results of the mapping can be seen in Figure 14. It is clearly seen from Figure 14 that chromium, shown in green, has a higher content in some of the grains, while nickel, shown in dark blue, is mostly in the other grains. Molybdenum, shown in light blue, has a significantly higher content in some points (~2-5 µm in diameter) as well as at the grain boundaries. It is also seen that molybdenum has a higher content in the same grains as the higher chromium concentration.

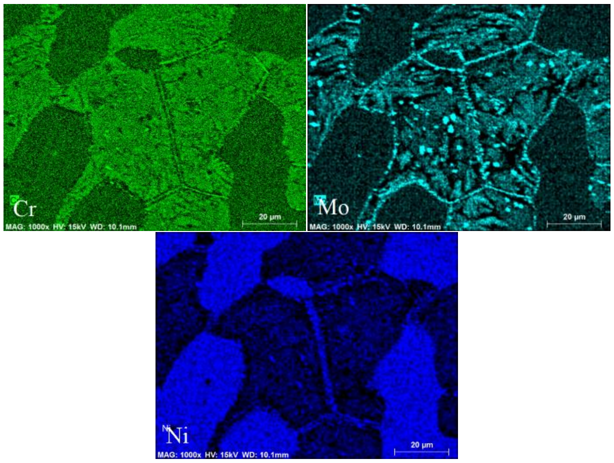

Figure 14: Mapping analysis of chromium, molybdenum and nickel in the sample containing ~30% sigma

Tensile Testing

Table 8 shows the yield strength and elongation of the materials with various sigma content before and after long term heat treatment. It can be seen that the elongation decreases drastically by the long term heat treatment. The elongation is also decreased with heat treatment at 750°C. The yield and ultimate strength of the as-received material is higher than after the heat treatments. The yield strength after the heat treatments are similar.

Table 8: Mechanical properties to the material after different heat treatments

Material treated at	Yield Strength [MPa]	Ultimate Tensile Strength [MPa]	Elongation [%]
900°C/8min	535	782	32.7
900°C/8min + 300°C/4w	536	786	20.0
750°C/4h	536	783	17.6
750°C/4h + 300°C/4w	568	743	2.6
As-received	654	841	26.9

Discussion

Figures 2-5 show the IQ- and phase maps of the reference material. The base material contains no intermetallic phases. This material has not gone through any critical heat treatments to induce such phases. This can also be observed from Table 6, where the content of ferrite versus austenite is almost 50% of each.

After the heat treatment at 900°C, see Figures 6-9 some sigma phase has started to nucleate. This is because sigma is formed in the temperature range 700-900°C, even after a few minutes (Pohl et al. (2007)). It can be seen from Figure 8 and 9 that the sigma phase nucleates at the grain boundaries, especially between austenite and ferrite. There is also a small increase in the size of the austenite grains.

The heat treatment at 750°C for four hours have led to an extreme fraction of sigma phase, see Figures 12 and 13, compared to the other two samples. The heat treatment at 750°C for four hours is not likely to happen industrial, but is here used to create a material with a large fraction of sigma. Even small amounts of sigma can lead to catastrophic failures (Børvik et al. (2010)) and (Paulsen et al. (2018)). Figures 12 and 13 compared to Figures 8 and 9 also show an increase in the austenite fraction in the material containing ~30% sigma. The ferrite content has decreased considerably with the heat treatment at 750°C, from almost 50% in the base material, see Table 6, to around 6% in the material heat treated at 750°C, see Table 8. It can be observed from Figures 12 and 13 that sigma phase is formed mostly in the ferritic phase, which is in agreement with previous literature e.g. (Escriba et al. (2009)). The previous ferritic phase has been transformed into austenite and sigma: $\delta \rightarrow \sigma + \gamma_{new}$. Even though the austenite form large bands, cf. the phase maps in Figures 12 and 13, the austenite grains are still relatively small as seen in Figures 10 and 11.

Chi phase is observed in the material heat treated to form intermetallic phases at 750°C. Chi phase is usually formed between 600 and 900°C (Nilsson et al. (1993)) and according to the findings by Pohl et al. (2007) this phase forms prior to the sigma phase and is then consumed by the sigma phase. Previous literature shows that the chi phase should have a higher content of molybdenum (Escriba et al. (2009)). Fluctuations in molybdenum content are also observed in this project as seen in Figure 14. It is clearly seen that there is a higher content of molybdenum in some special points in the grains with higher chromium content.

From Figure 12 and 13 it seems that the blue chi phase nucleates on specific austenite/austenite grain boundaries. Padilha and Rios (2002) have in their review article reported that the chi phase is well known in austenitic stainless steels, and that there is a orientation relationship between the austenite and the chi phase in case of intragranular precipitation. This may explain that only a few austenite/austenite grain boundaries show formation of chi. From the element mapping in Figure 14 it is seen that the chi phase both nucleates on grain boundaries and in clusters inside the previous ferritic grains. Since the chromium containing phase observed in Figure 14 most likely is shown as sigma phase in Figure 12, we may conclude that the EBSD technique in this study does not have high enough resolution to show the grain boundary chi phase that is seen in the molybdenum map in Figure 14.

The EDX analyses were done to distinguish between the phases sigma and chi. From Figure 14 it can clearly be seen that there is a higher content of nickel in some of the grains. Nickel is a known austenite stabilizer, and consequently, these grains are assumed to be austenite. From Figure 14 it can clearly be seen that there is a higher content of chromium in the opposite grains from nickel. Chromium is a known ferrite stabilizer, but also goes in the sigma phase, and therefore these grains can be both, but is most likely sigma phase because of the high amount of this phase in the metal. To distinguish sigma and ferrite, literature says that the chromium content in sigma should be higher than the ferrite, and that iron content is higher than in the ferritic phase (Villalobos et. al (2009)). The iron content was not analyzed in this project.

From Figures 4 and 5 and Table 6 there are close to no changes in the phase composition of the base material after the heat treatment. The same holds for the sample heat treated at 900°C, Figure 6 and 7 and Table 7, and the sample heat treated at 750°C, Figures 12 and 13 and Table 8. Sigma is reported to be stable, but the chi phase is known to be thermodynamically unstable (Pohl et al. (2007)). There are, however, not observed any significant changes in the amount of intermetallic phases after the long-term heat treatment at 300°C. Villalobos et al. (2009) reported that there were no microstructural changes before 700°C. This corresponds to the analyses done in this project.

The small differences in composition, like 4.2% to 4.9% sigma in the material treated at 900°C, see Table 7 and 1.5% to 1.2% χ for the material treated at 750°C, see Table 8 may be caused by the chosen area of interest. However, the measurements are run on a relatively large area and should be representative. The chi phase is typically formed in clusters, and therefore it is very dependent on the area measured how much phase that is indexed as chi.

The tensile testing shows a distinctive decrease in ductility after the long term heat treatment at 300°C for both the material containing ~5% sigma and the one containing ~30%.. This is probably caused by spinodal decomposition in the material, which a known mechanism that can lead to embrittlement (Hosseini et. al. (2018)).

As already mentioned, further formation of the sigma phase is not possible below a temperature of 700°C. But at a temperature of 300°C, spinodal decomposition can happen, where Fe-rich (α) and Cr-rich (α') ferrite are developed (Pettersson et al. (2015)) This can lead to further embrittlement of the material (Calliari et al. (2010)). Hosseini et al. (2018) discovered that the fractions of α and α' increase with decreasing temperature below 480°C for the alloy 2507 SDSS (UNS S32750). The spinodal decomposed Cr-enriched and Cr-depleted domains have the same crystal structure with very similar lattice constants and therefore it is very difficult to distinguish the two phases from each other with EBSD. The way to detect the spinodal decomposition is with characteristic analysis, for example with EDX, done in several studies (Calliari et al. (2010)). Another important technique is atom probe tomography (APT) which can quantify nanoscale fluctuations (Hosseini et al. (2018)) and (Pettersson et al. (2015)).

CONCLUSION

In this project the intermetallic phases in super duplex stainless steel alloy UNS37260 has been characterized with EBSD. Different short-term and long-term heat treatments has been done on the samples and characterized before and after. There has also been done investigations on the chemical composition of the chi phase with EDX. These conclusions have been drawn by this paper:

- Heat treatments between 750°C and 900°C causes formation of intermetallic phases sigma and chi.
- The heat treatment at 300°C causes no change in the phase composition for the given temperature and time, but may cause possible spinodal decomposition, which is not detectable with EBSD and phase map. This may be investigated with EDX or APT(Atom Probe Tomography).
- The chi phase contains a significantly larger amount of molybdenum than the other phases and is typically formed in clusters and along grain boundaries. The latter is in the size range that has not been resolvable with EBSD in this study. This may cause the fraction of phases found with the different heat treatments to be incorrect.
- Heat treatment at 300°C for four weeks leads to a drastic decrease in ductility in the material.

ACKNOWLEDGEMENTS

The authors would like to thank Rene de Kloe from Ametek B.V., the Netherlands for providing bmt-files for TSL OIM Analysis Software.

REFERENCES

Børvik, T., Lange, H., Marken, L.A., Langseth, M., Hopperstad, O.S., Aursand, M. Rørvik, G. (2010), "Pipe fittings in duplex stainless steel with deviation in quality caused by sigma phase precipitation", *Materials Science and Engineering A, 527(26),* 6945-6955.

Calliari, I., Ramous, E., Bassani, P. (2010), "Phase Transformation in Duplex Stainless Steels after Isothermal Treatments, Continuous Cooling and Cold Working", *Materials Science Forum, Vols. 638-642,* 2986-2991.

Escriba, D.M., Materna-Morris, E, Plaut, R.L., Padilha, A.F. (2009), "Chi-phase precipitation in a duplex stainless steel", *Materials Characterization, 60(11),*1214-1219

Hosseini, V.A., Thuvander, M., Wessmann, S. et al (2018), "Spinodal Decomposition in Functionally Graded Super Duplex Stainless Steel and Weld Metal". *Metallurgical and Materials Transactions A, 49(7),*2803-2816

Nilsson, J. O., & Wilson, A. (1993) "Influence of isothermal phase transformations on toughness and pitting corrosion of super duplex stainless steel SAF 2507", *Materials Science and Technology, 9 (7),* 545-554.

Ong, H. G., & Yeap, A. (2018). "Challenges in Avoiding Sigma Phase Embrittlement of Duplex Stainless Steel in Assets". *Offshore Technology Conference*. doi:10.4043/28393-MSPadilha, A.F., Rios, P.R. (2002) "Decomposition of Austenite in Austenitic Stainless Steels", *ISIJ International, 42(4),* 325-337

Paulsen, C., Broks, R.L., Karlsen, M., Hjelen, J., Westermann, I. (2018), "Microstructure evolution in super duplex stainless steels containing σ-phase investigates a low-temperature using in situ SEM/EBSD tensile testing". *Metals, 8(7),* 478.

Pettersson, N., Wessman, S., Thuvander, M., Hedström, P., Odqvist, J., Pettersson, R.F.A., Hertzmann, S. (2015), "Nanostructure evolution and mechanical property changes during aging of a super duplex stainless steel at 300*℃". Materials Science and Engineering A, 647,* 241-248.

Pohl, M., Storz, O., Glogowski, T. (2007) "Effect of intermetallic precipitations on the properties of duplex stainless steel". *Materials Charaterization, 58 (1),* 65-71.

Villalobos, D., Albiter, A., & Maldonado, C.. (2009). "Microstructural changes in SAF 2507 superduplex stainless steel produced by thermal cycle". *Matéria (Rio de Janeiro), 14(3),* 1061-1069.

E Experiments

E.1 Region of Interest (ROI)

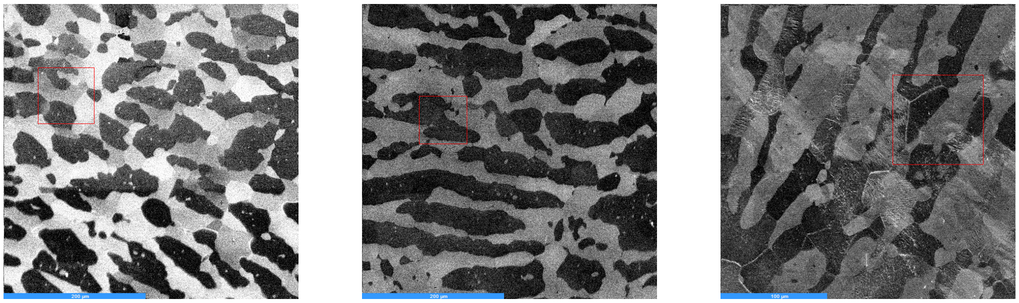

(a) ROI map from Experiment 1

(b) ROI map from Experiment 2

(c) ROI map from Experiment 3

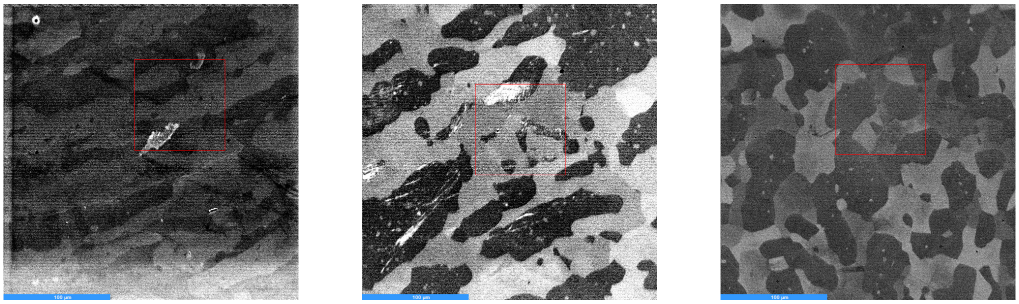

(d) ROI map from Experiment 4

(e) ROI map from Experiment 5

(f) ROI map from Experiment 6

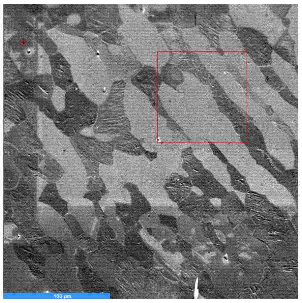

(g) ROI map from Experiment 7

Figure E.1: Regions of interest in the different experiments

E.2 Experiment 1, T=700 °C

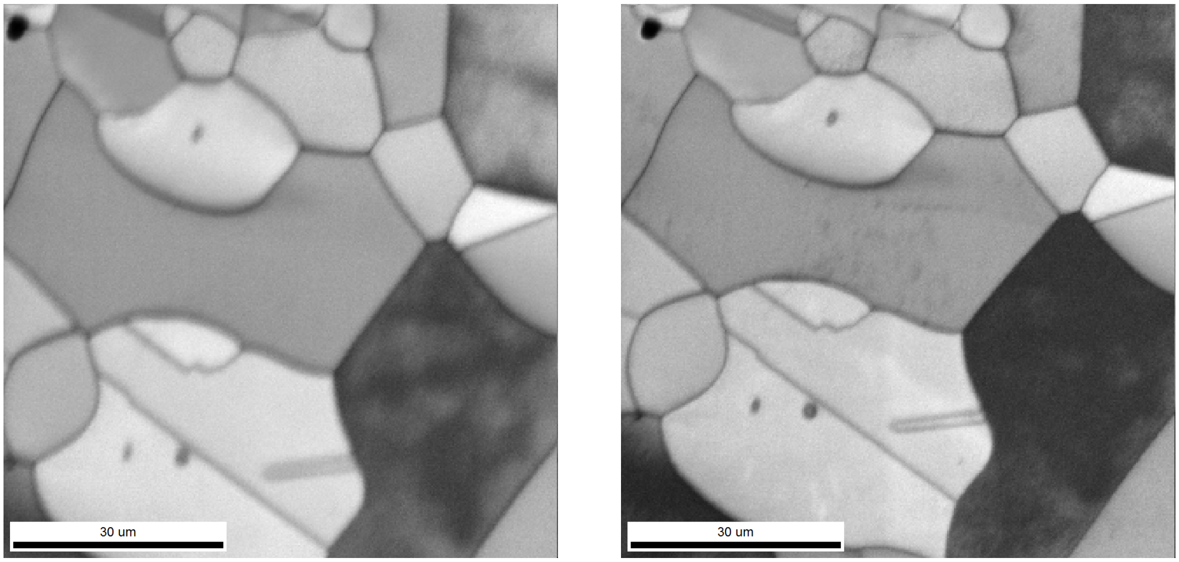

(a) IQ map acquired 10 min after heating

(b) IQ map acquired 40 min after heating

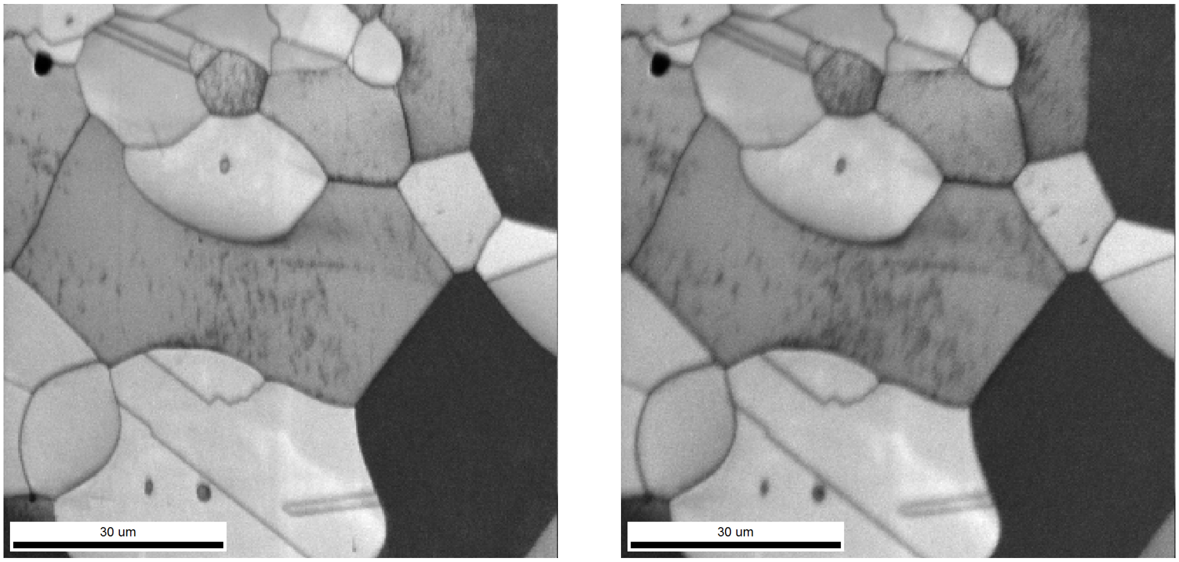

(c) IQ map acquired 70 min after heating

(d) IQ map acquired 100 min after heating

Figure E.2: IQ maps from Experiment 1: Temperature set at 700 °C in oven

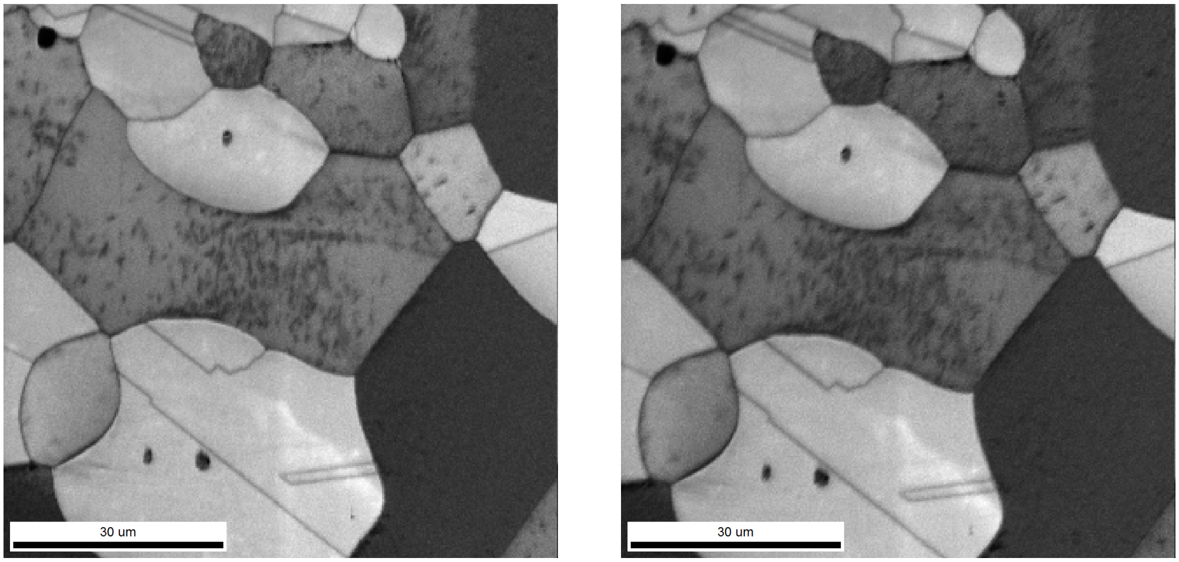

(e) IQ map acquired 130 min after heating

(f) IQ map acquired 160 min after heating

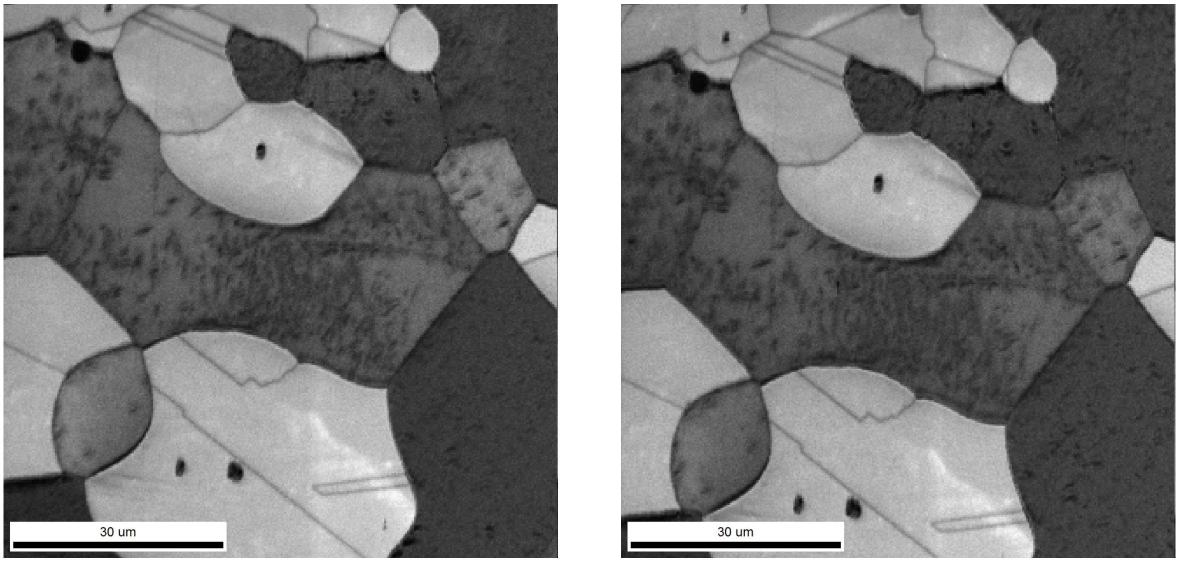

(g) IQ map acquired 190 min after heating

(h) IQ map acquired 220 min after heating

Figure E.2: IQ maps from Experiment 1: Temperature set at 700 °C in oven

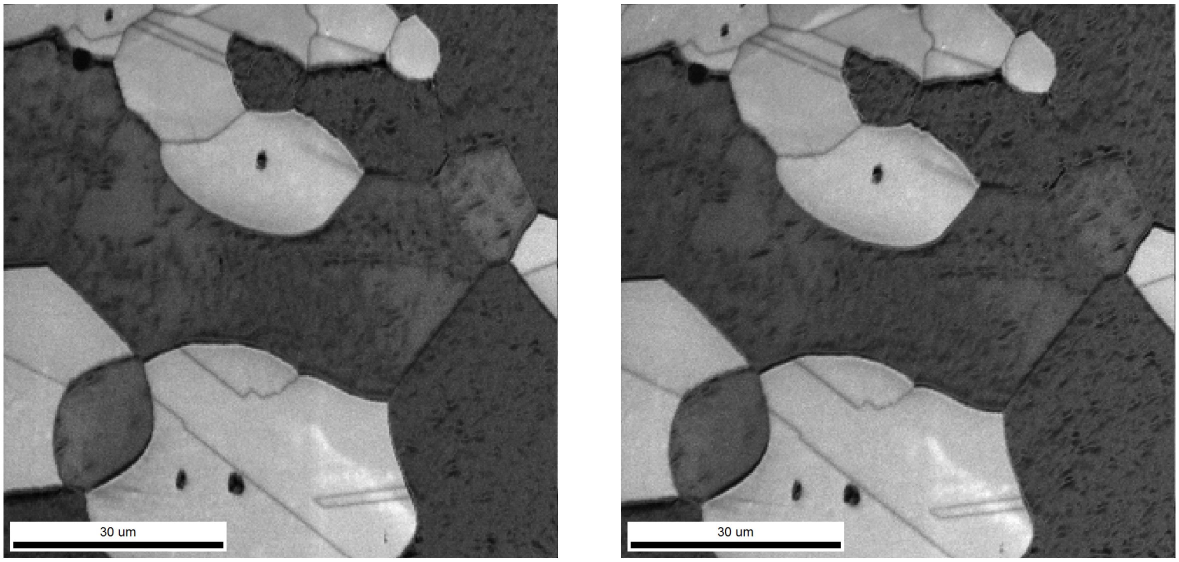

(i) IQ map acquired 250 min after heating (j) IQ map acquired 280 min after heating

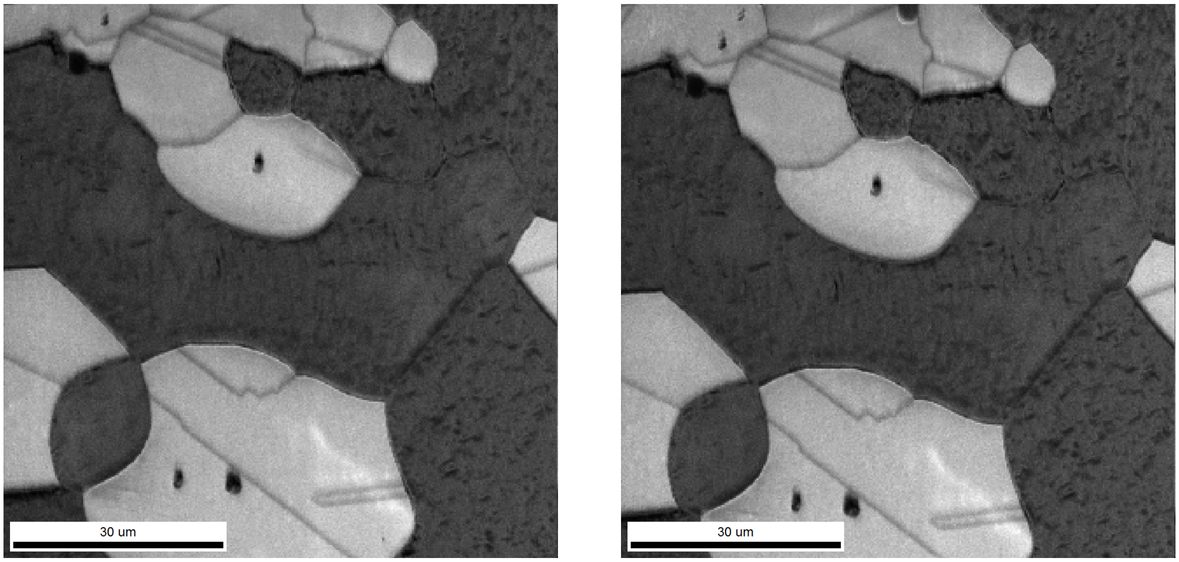

(k) IQ map acquired 310 min after heating (l) IQ map acquired 340 min after heating

Figure E.2: IQ maps from Experiment 1: Temperature set at 700 °C in oven

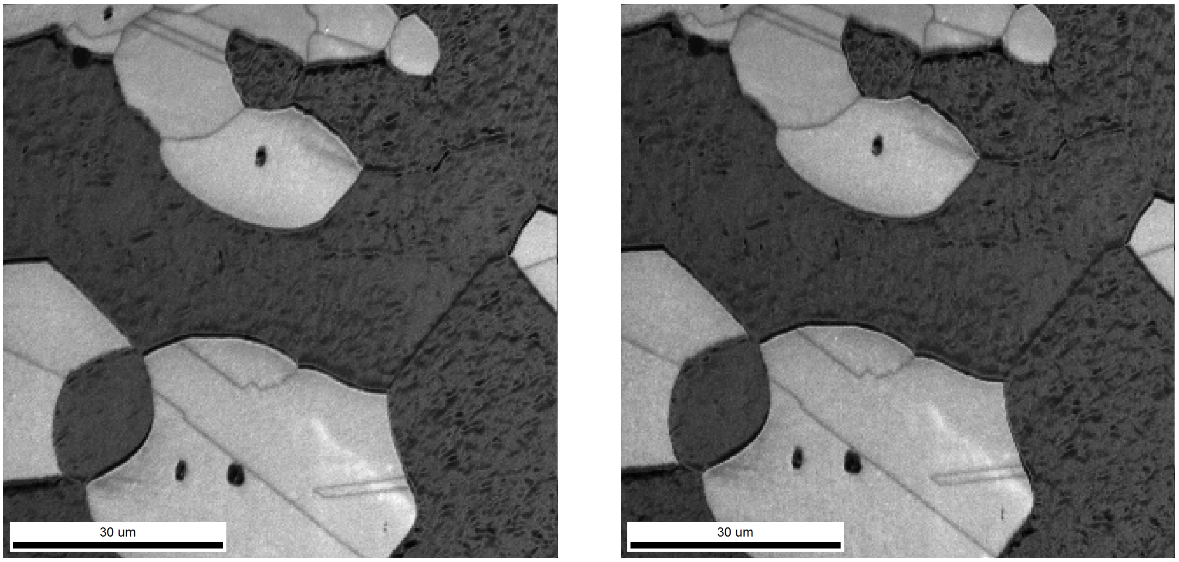

(m) IQ map acquired 370 min after heating

(n) IQ map acquired 400 min after heating

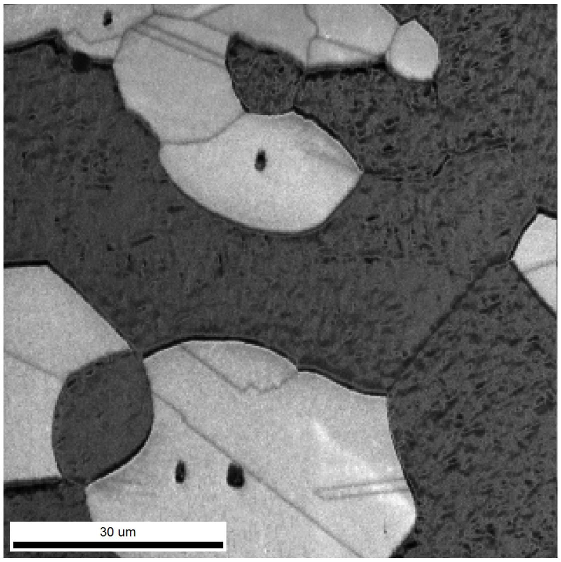

(o) IQ map acquired 430 min after heating

Figure E.2: IQ maps from Experiment 1: Temperature set at 700 °C in oven

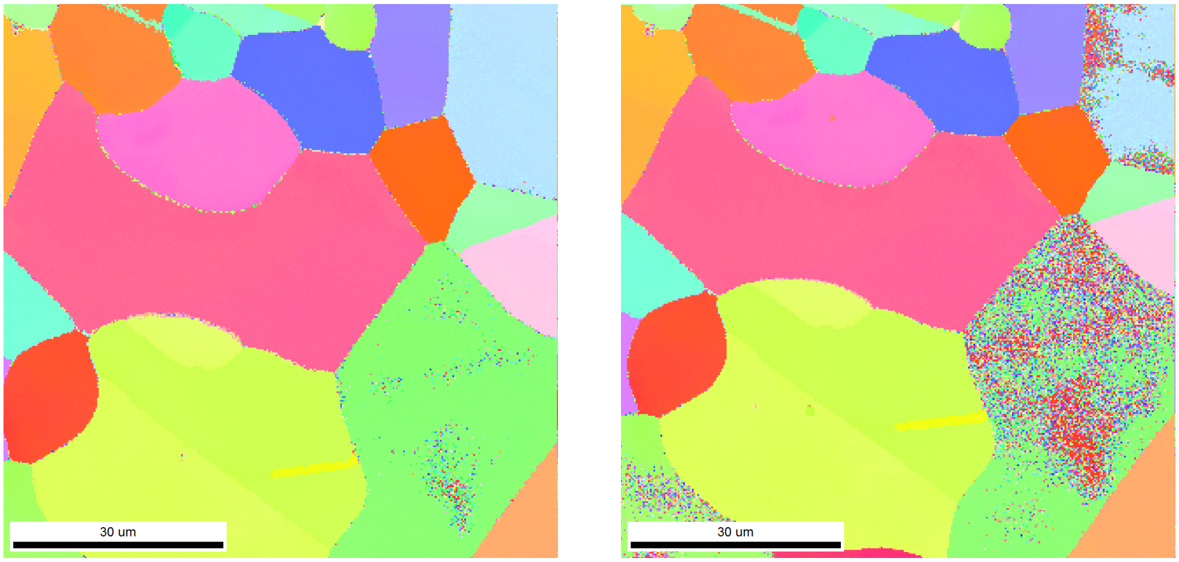

(a) IPF map acquired 10 min after heating (b) IPF map acquired 40 min after heating

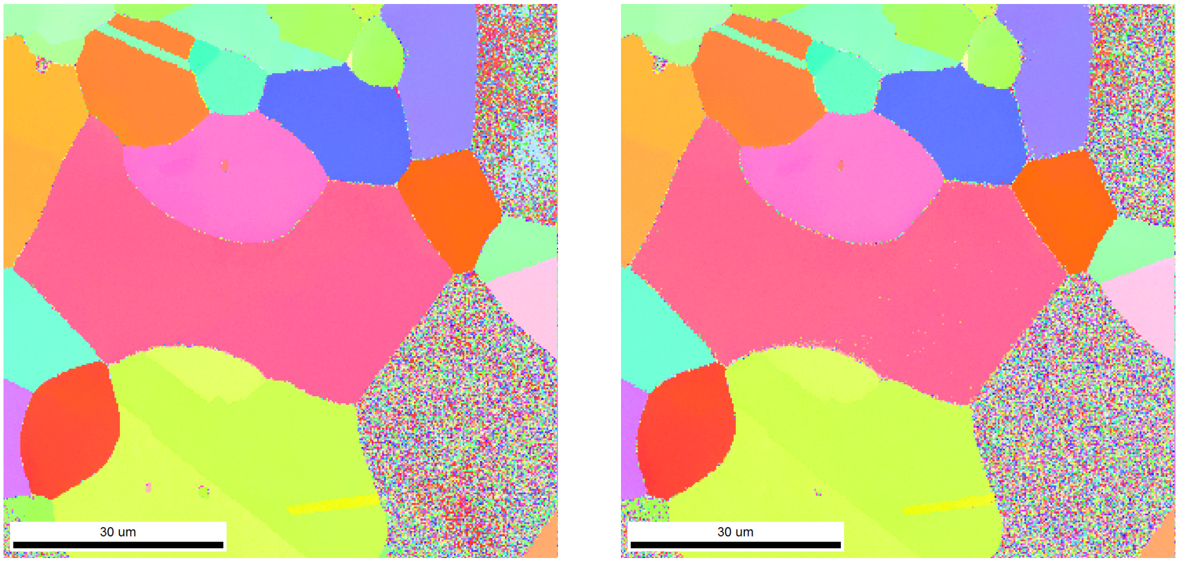

(c) IPF map acquired 70 min after heating (d) IPF map acquired 100 min after heating

Figure E.3: IPF maps from Experiment 1: Temperature set at 700 °C in oven

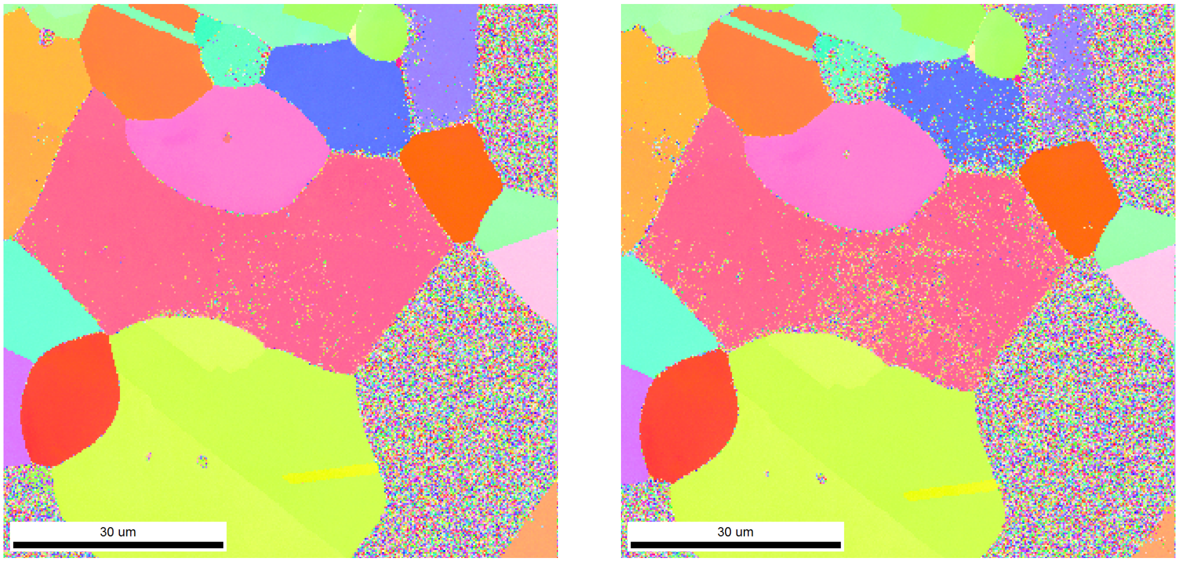

(e) IPF map acquired 130 min after heating (f) IPF map acquired 160 min after heating

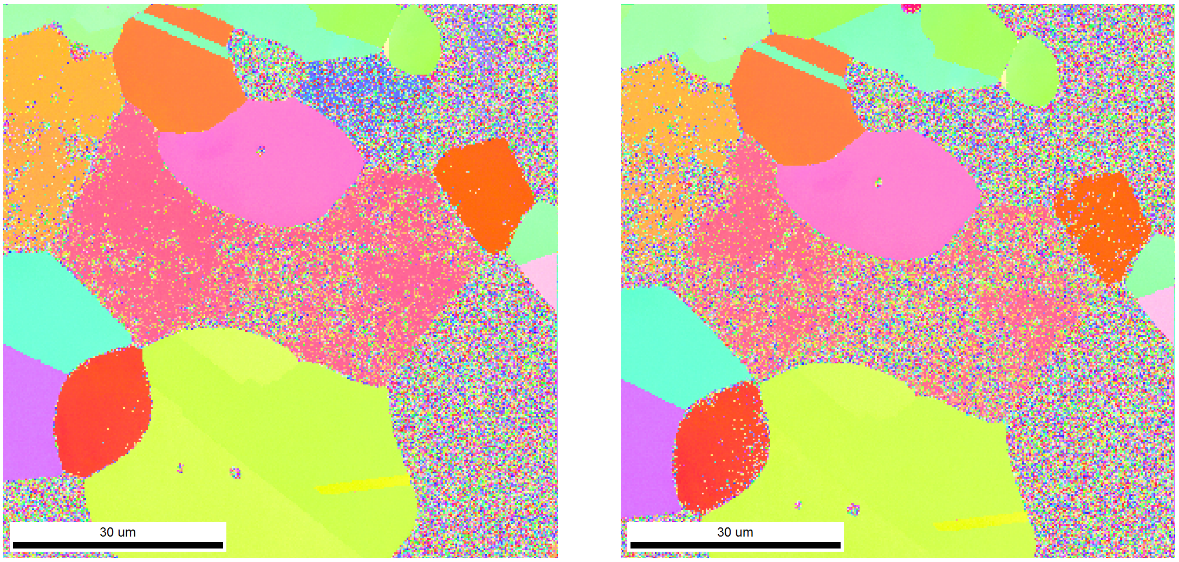

(g) IPF map acquired 190 min after heating (h) IPF map acquired 220 min after heating

Figure E.3: IPF maps from Experiment 1: Temperature set at 700 °C in oven

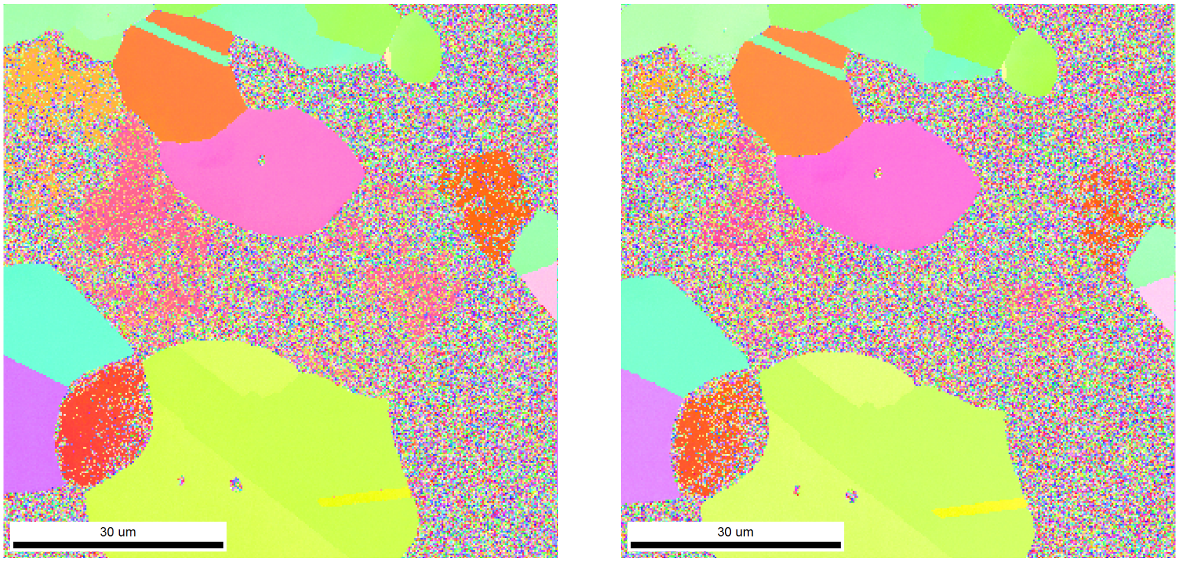

(i) IPF map acquired 250 min after heating (j) IPF map acquired 280 min after heating

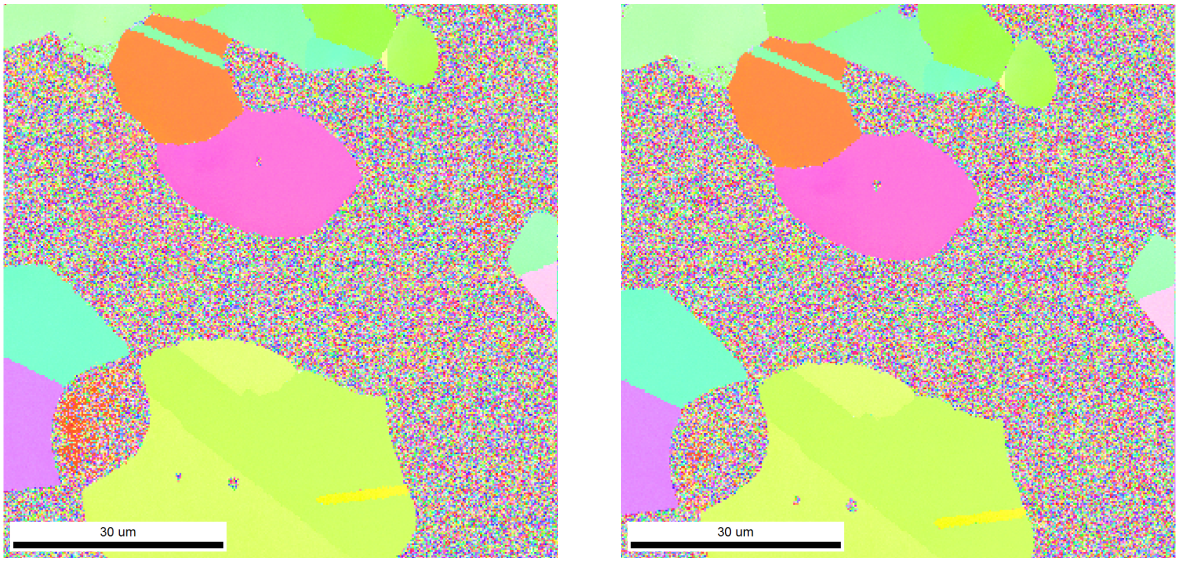

(k) IPF map acquired 310 min after heating (l) IPF map acquired 340 min after heating

Figure E.3: IPF maps from Experiment 1: Temperature set at 700 °C in oven

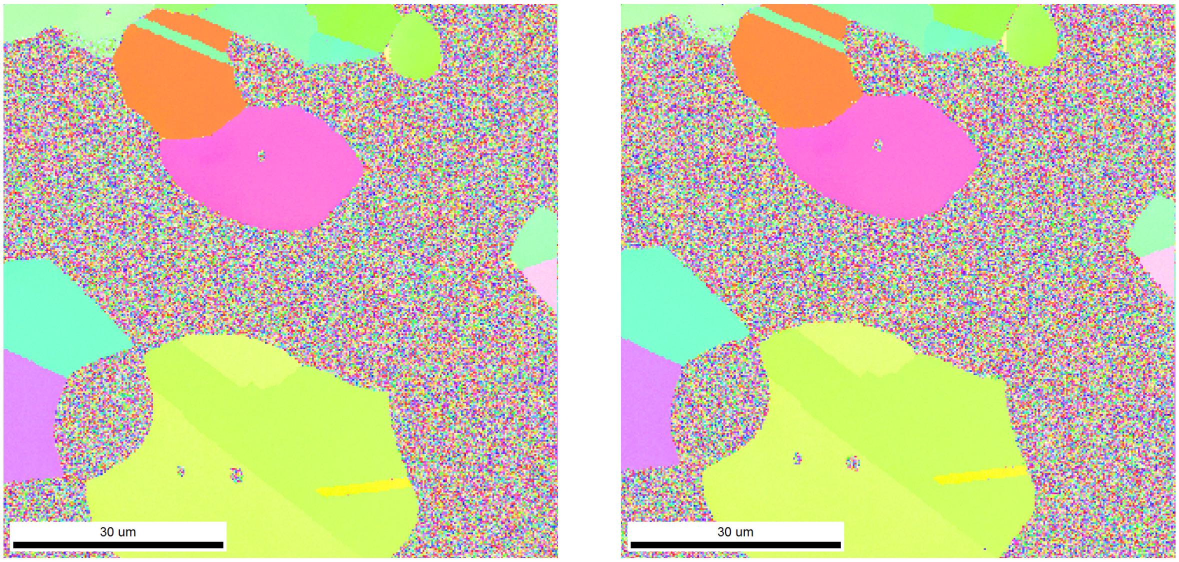

(m) IPF map acquired 370 min after heating

(n) IPF map acquired 400 min after heating

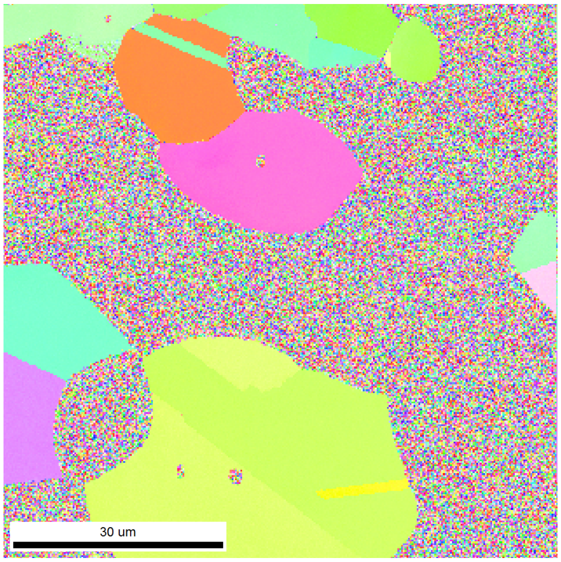

(o) IPF map acquired 430 min after heating

Figure E.3: IPF maps from Experiment 1: Temperature set at 700 °C in oven

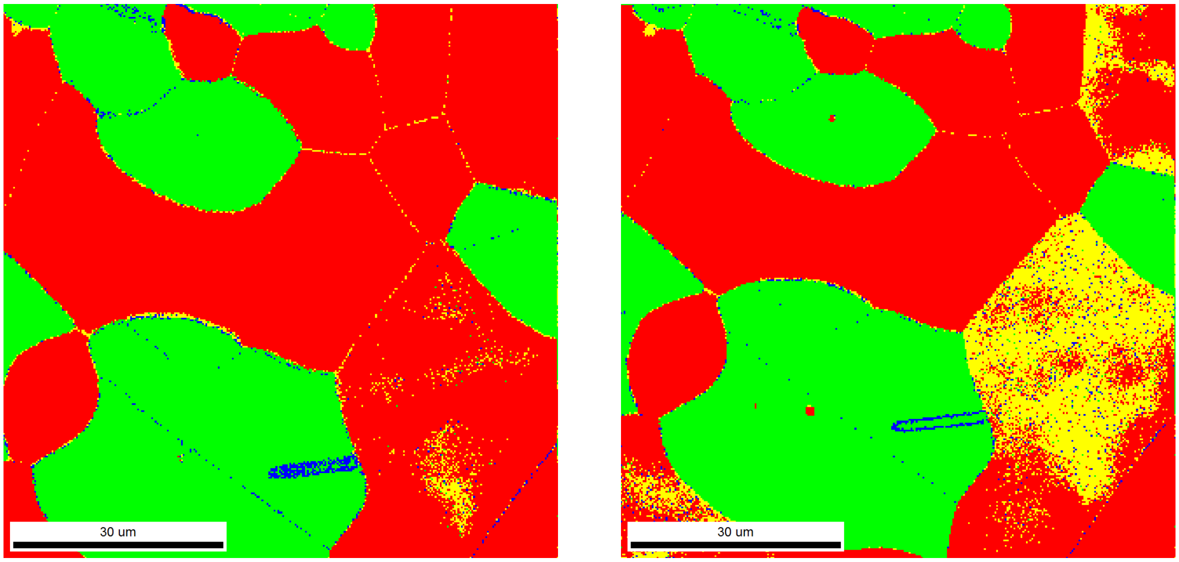

(a) Phase map acquired 10 min after heating (b) Phase map acquired 40 min after heating

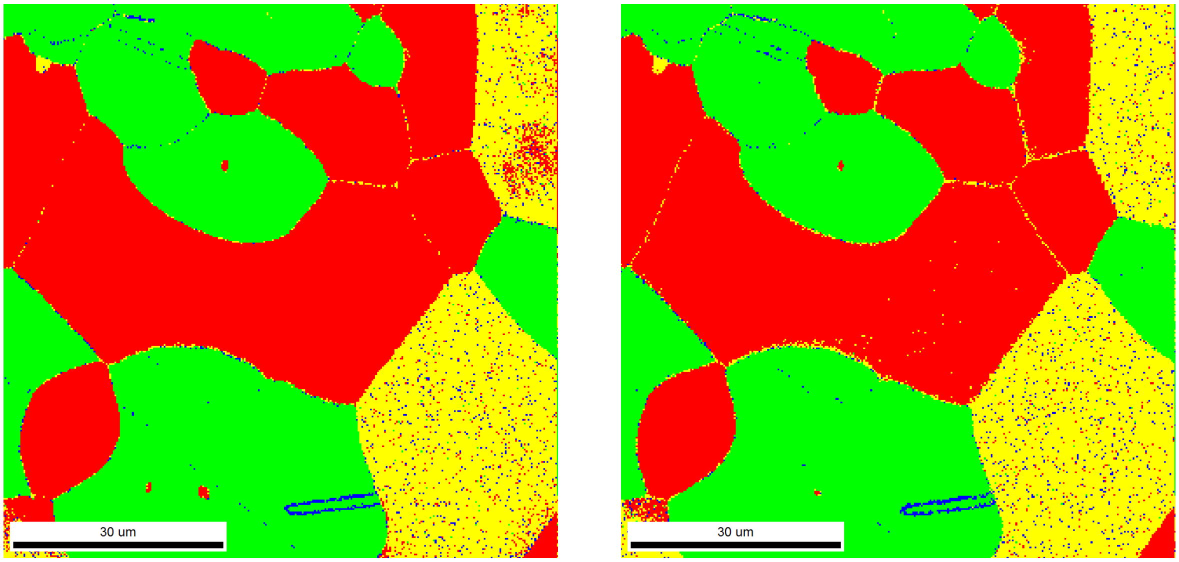

(c) Phase map acquired 70 min after heating (d) Phase map acquired 100 min after heating

Figure E.4: Phase maps from Experiment 1: Temperature set at 700 °C in oven

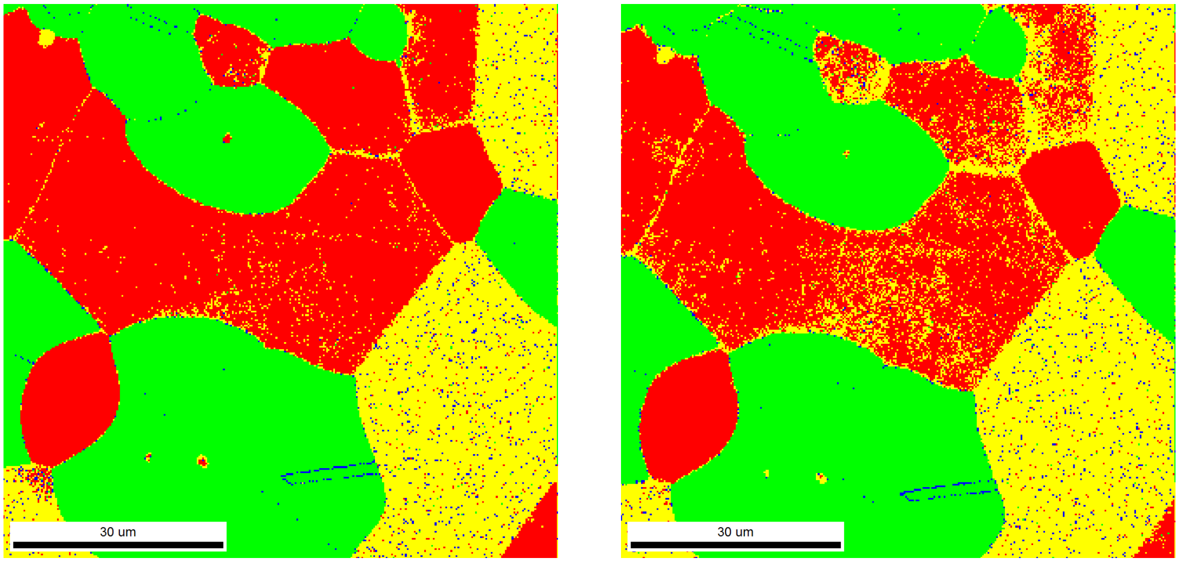

(e) Phase map acquired 130 min after heating (f) Phase map acquired 160 min after heating

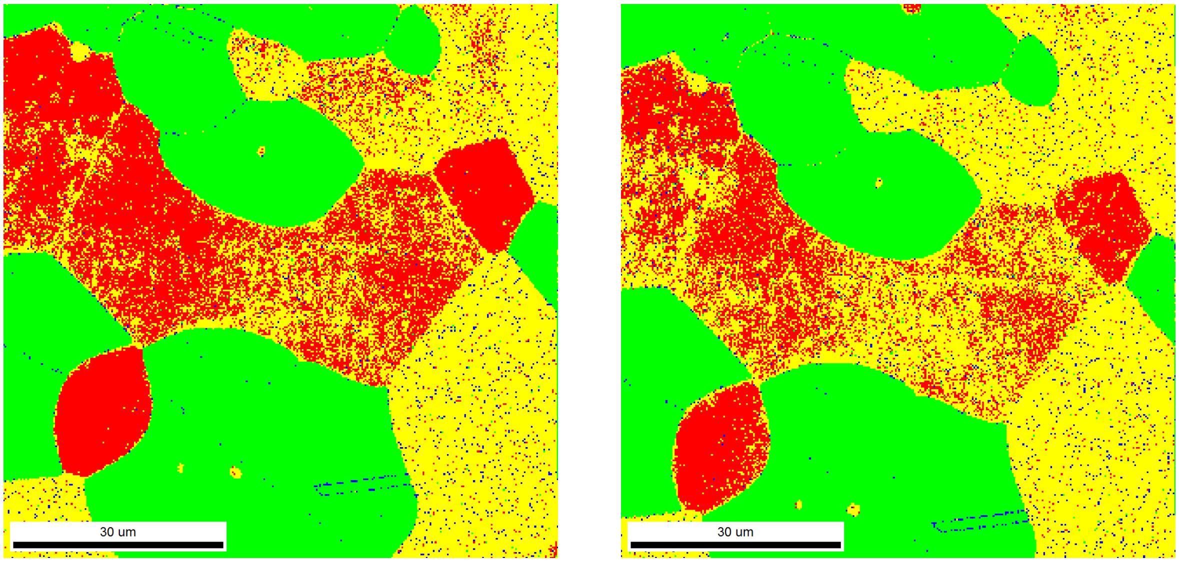

(g) Phase map acquired 190 min after heating (h) Phase map acquired 220 min after heating

Figure E.4: Phase maps from Experiment 1: Temperature set at 700 °C in oven

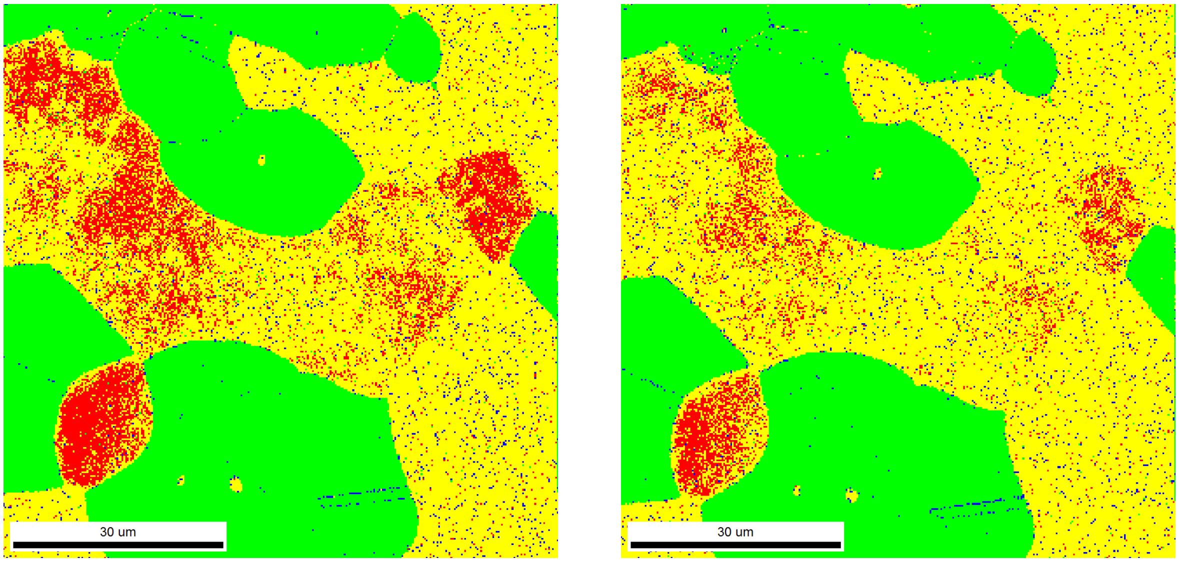

(i) Phase map acquired 250 min after heating

(j) Phase map acquired 280 min after heating

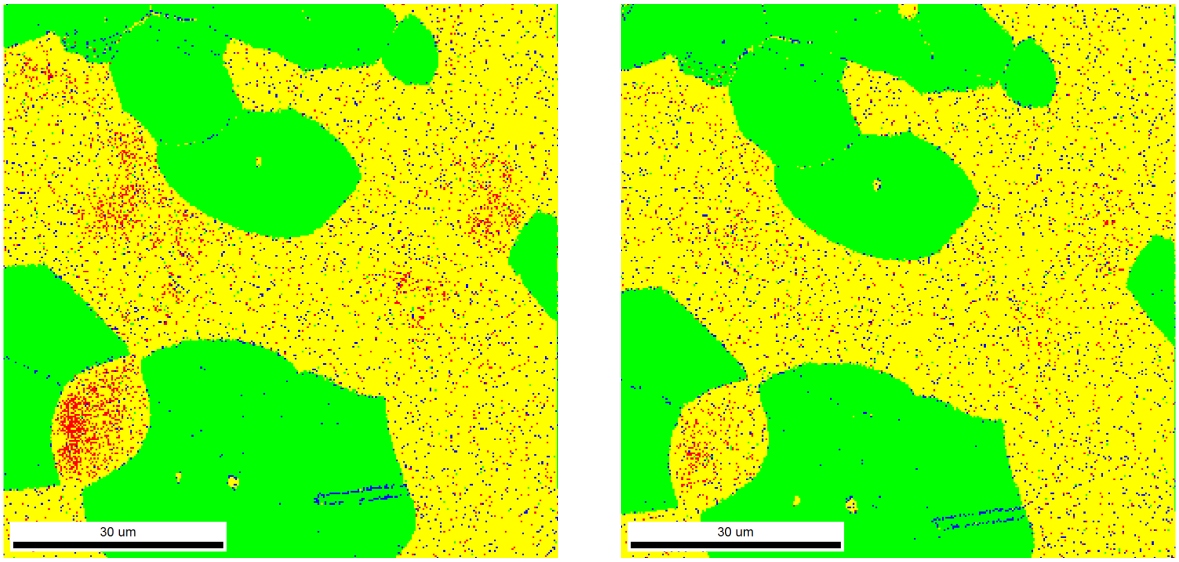

(k) Phase map acquired 310 min after heating

(l) Phase map acquired 340 min after heating

Figure E.4: Phase maps from Experiment 1: Temperature set at 700 °C in oven

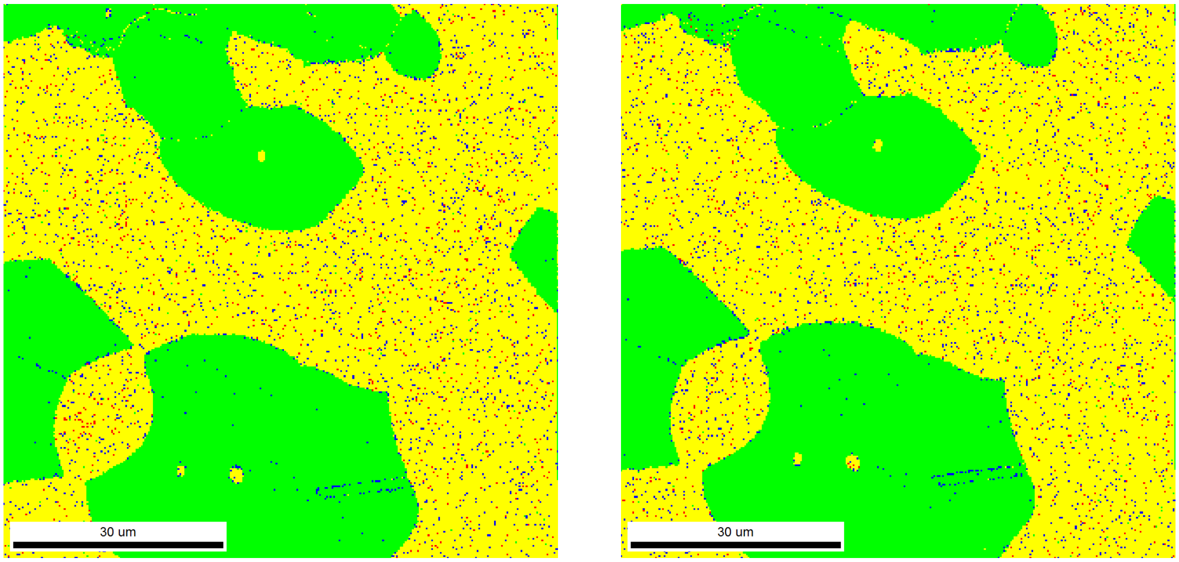

(m) Phase map acquired 370 min after heating (n) Phase map acquired 400 min after heating

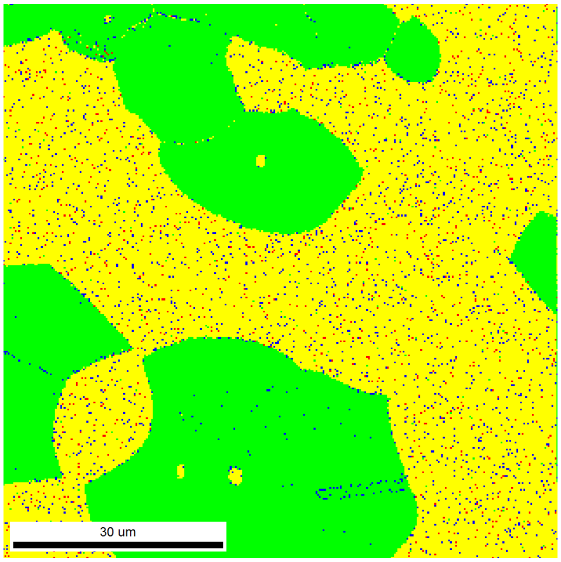

(o) Phase map acquired 430 min after heating

Figure E.4: Phase maps from Experiment 1: Temperature set at 700 °C in oven

E.3 Experiment 2, T=675 °C

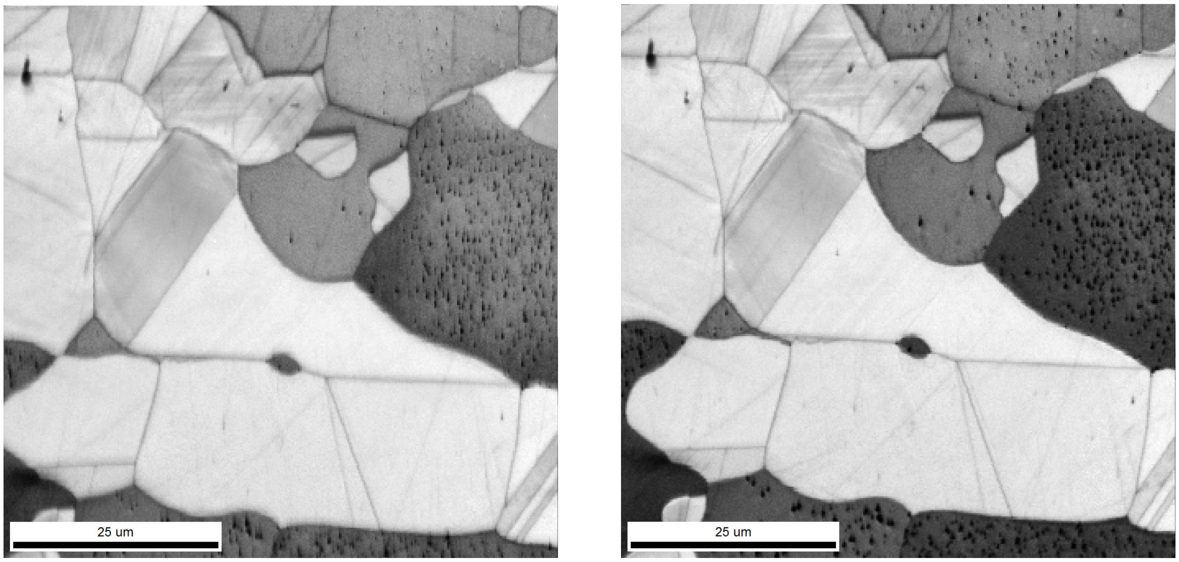

(a) IQ map acquired 10 min after heating

(b) IQ map acquired 40 min after heating

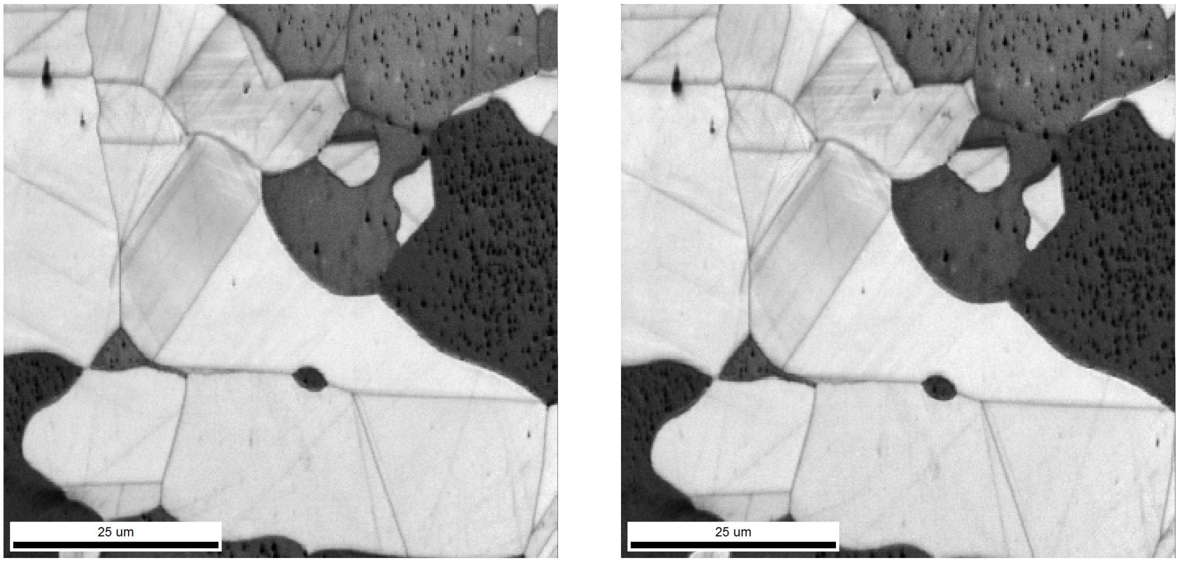

(c) IQ map acquired 70 min after heating

(d) IQ map acquired 100 min after heating

Figure E.5: IQ maps from Experiment 2: Temperature set at 675 °C in oven

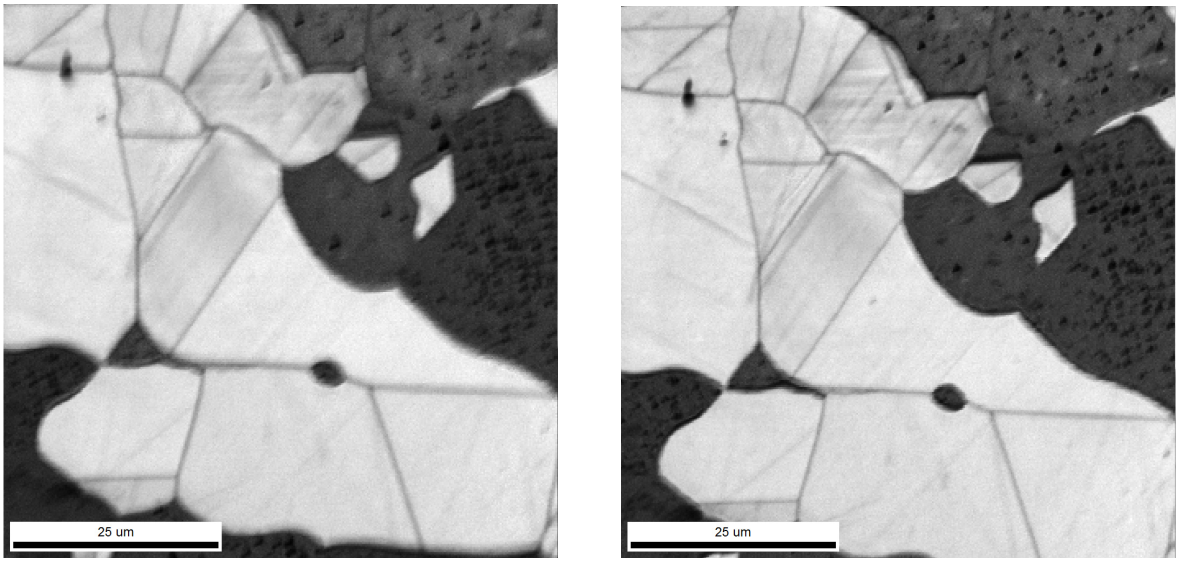

(e) IQ map acquired 130 min after heating

(f) IQ map acquired 160 min after heating

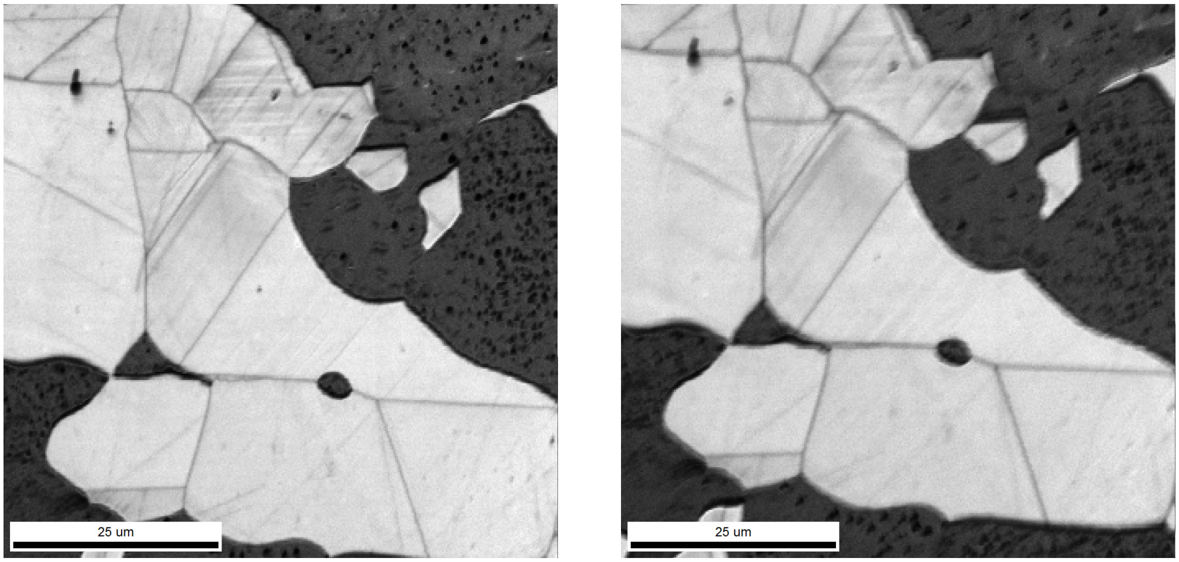

(g) IQ map acquired 190 min after heating

(h) IQ map acquired 220 min after heating

Figure E.5: IQ maps from Experiment 2: Temperature set at 675 °C in oven

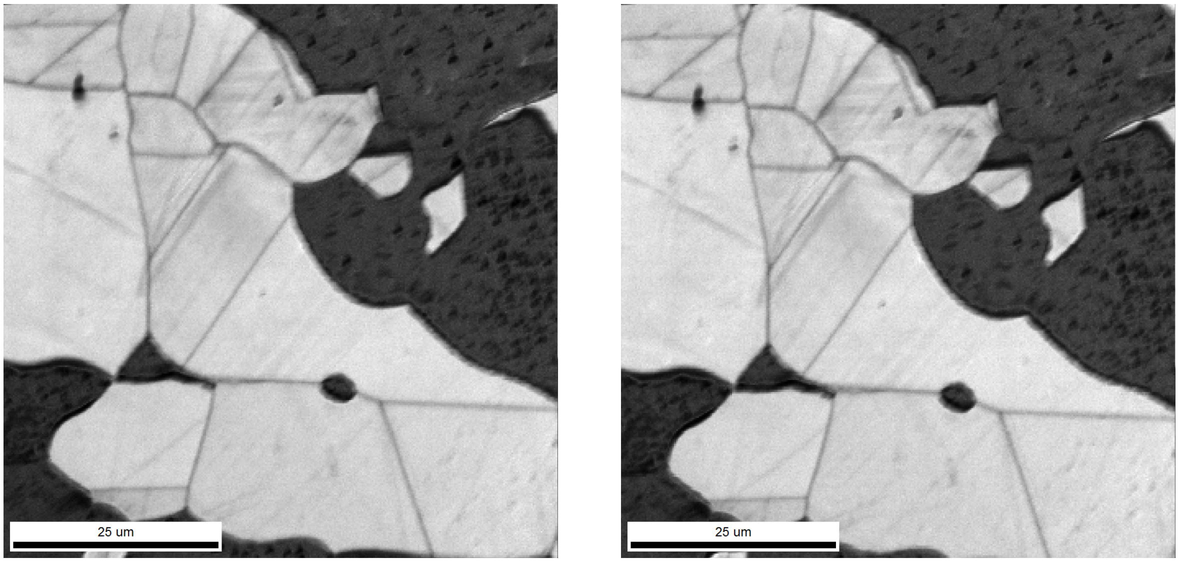

(i) IQ map acquired 250 min after heating (j) IQ map acquired 280 min after heating

Figure E.5: IQ maps from Experiment 2: Temperature set at 675 °C in oven

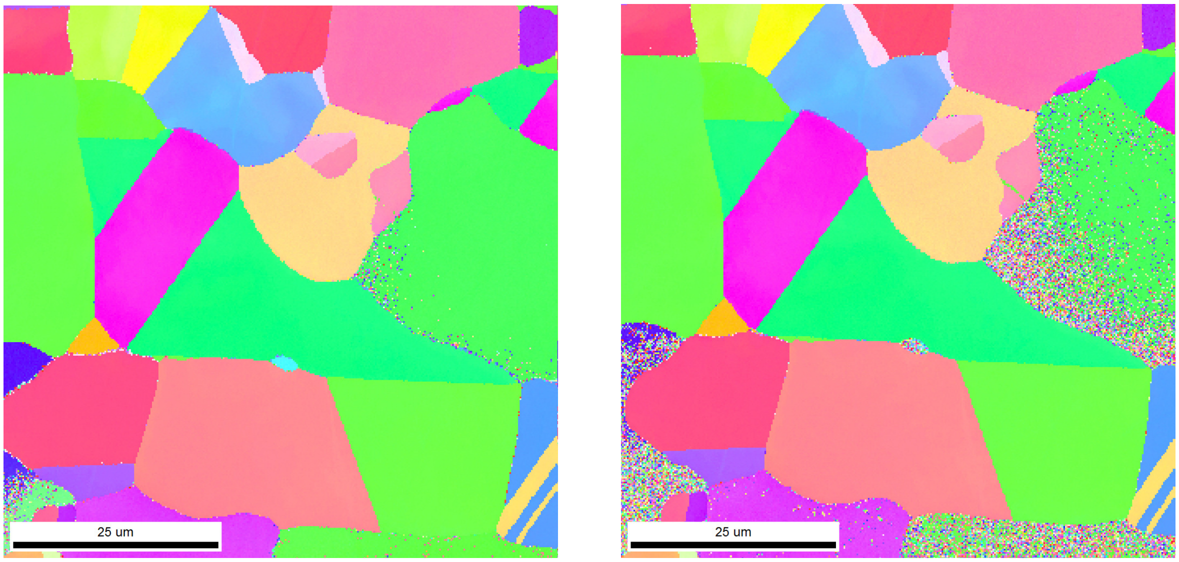

(a) IPF map acquired 10 min after heating (b) IPF map acquired 40 min after heating

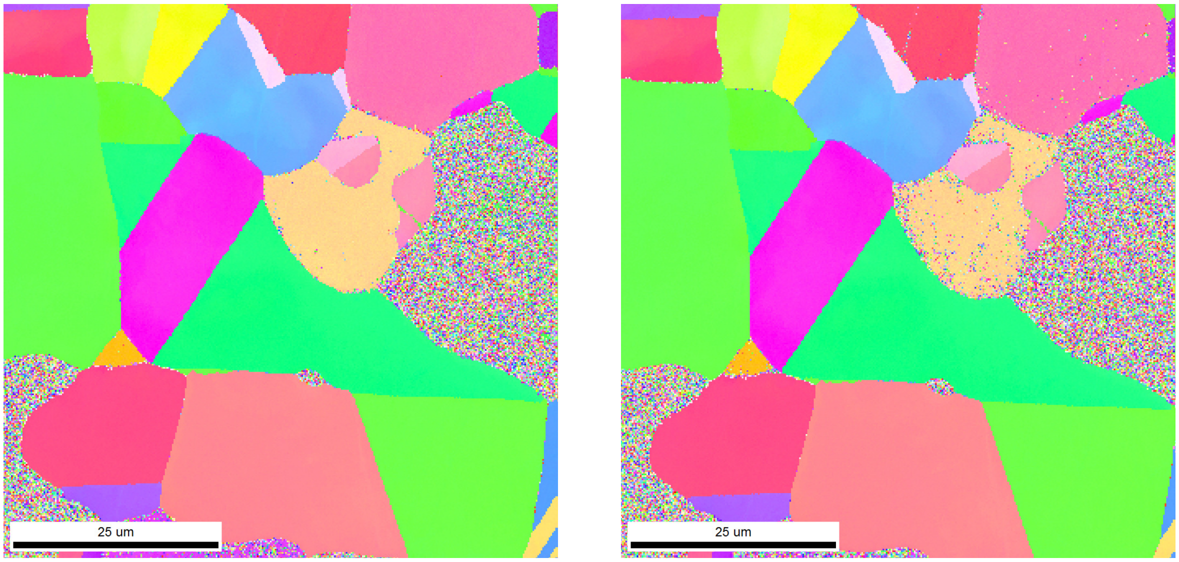

(c) IPF map acquired 70 min after heating (d) IPF map acquired 100 min after heating

Figure E.6: IPF maps from Experiment 2: Temperature set at 675 °C in oven

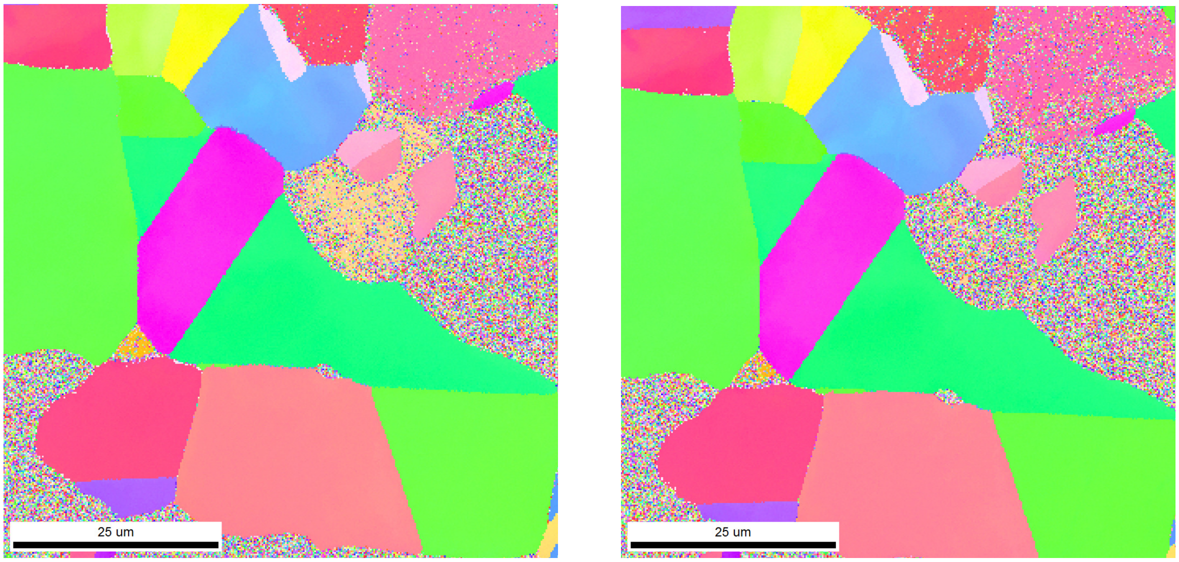

(e) IPF map acquired 130 min after heating (f) IPF map acquired 160 min after heating

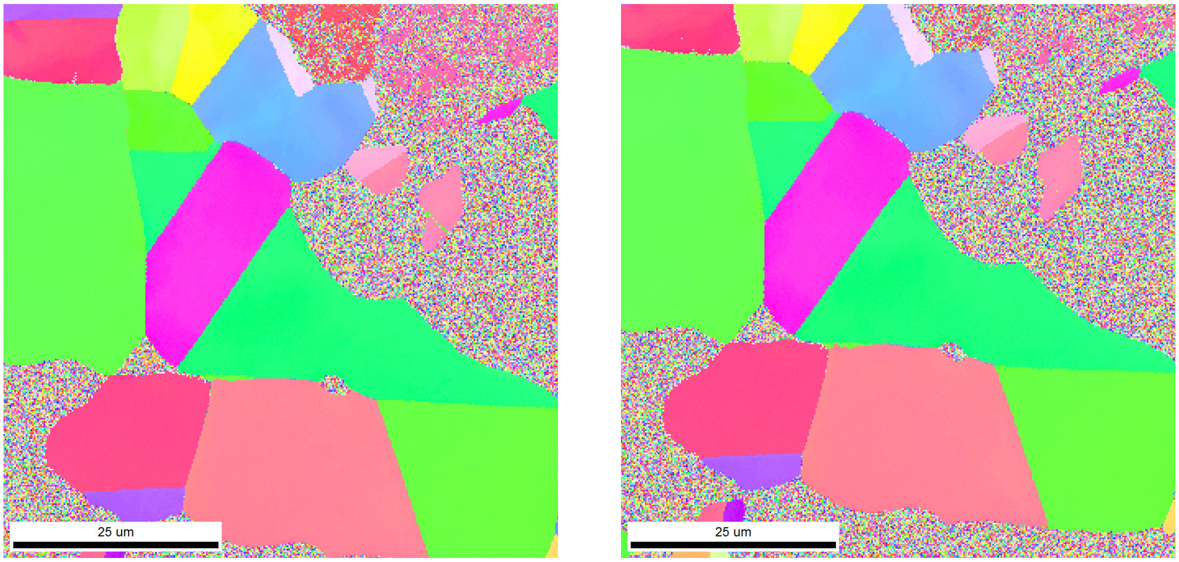

(g) IPF map acquired 190 min after heating (h) IPF map acquired 220 min after heating

Figure E.6: IPF maps from Experiment 2: Temperature set at 675 °C in oven

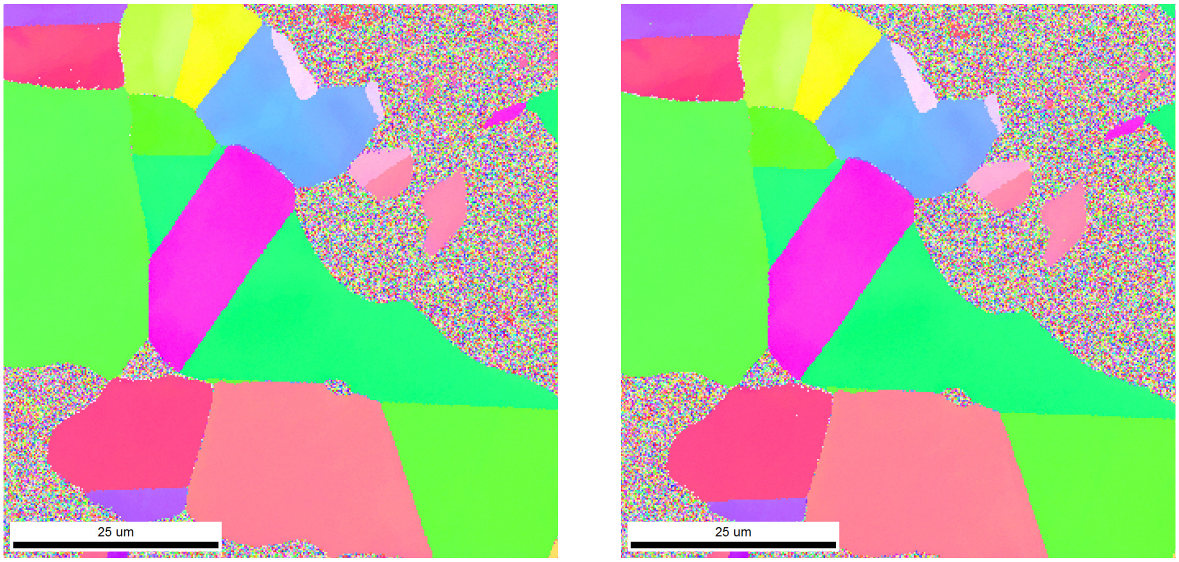

(i) IPF map acquired 250 min after heating

(j) IPF map acquired 280 min after heating

Figure E.6: IPF maps from Experiment 2: Temperature set at 675 °C in oven

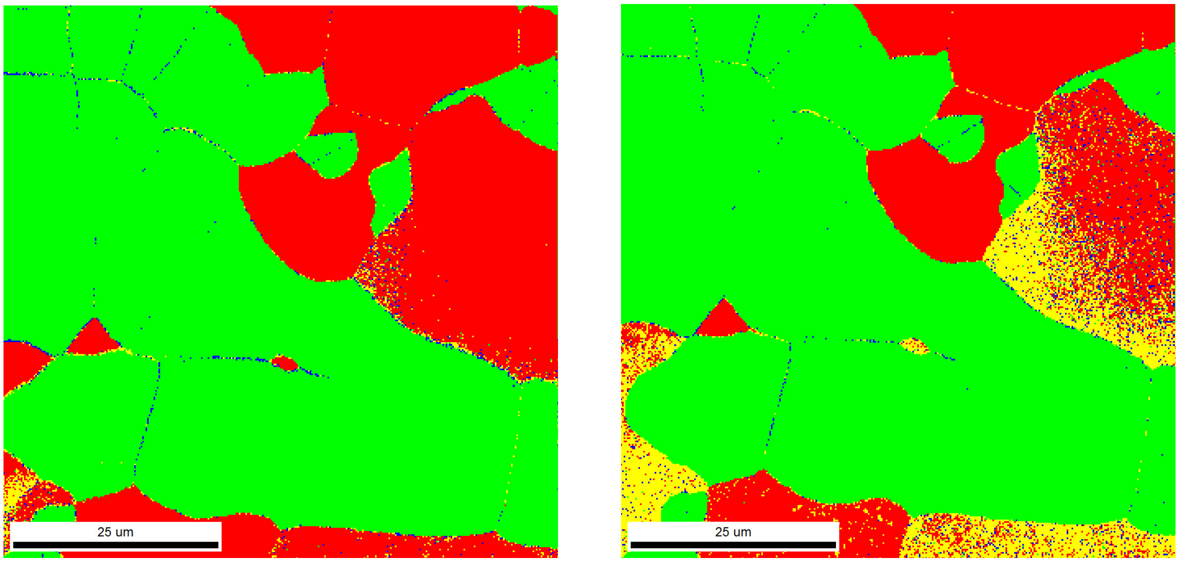

(a) Phase map acquired 10 min after heating (b) Phase map acquired 40 min after heating

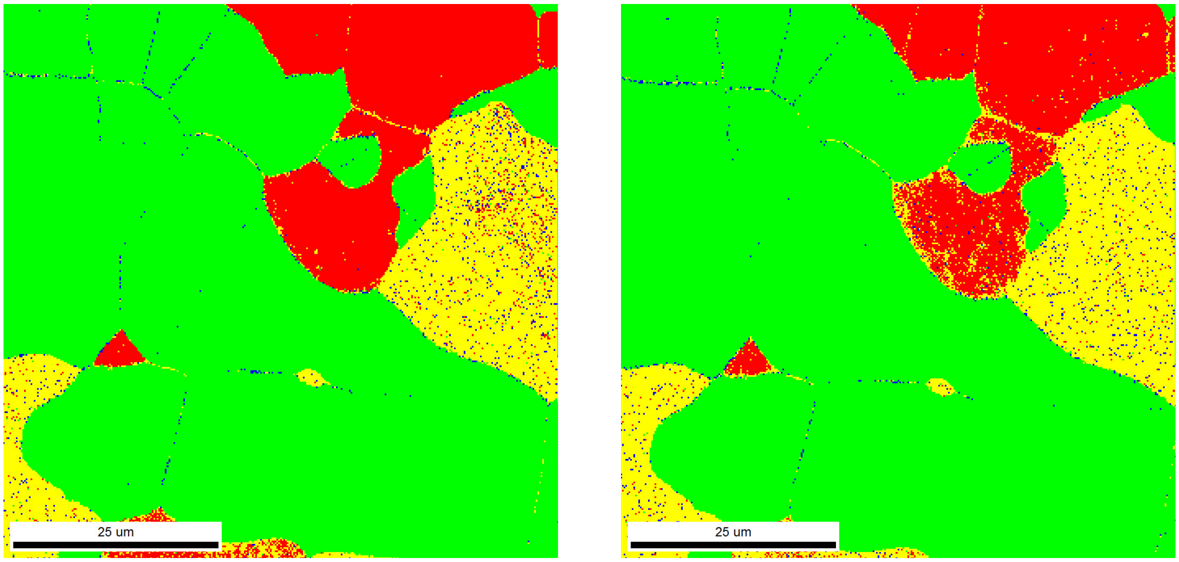

(c) Phase map acquired 70 min after heating (d) Phase map acquired 100 min after heating

Figure E.7: Phase maps from Experiment 2: Temperature set at 675 °C in oven

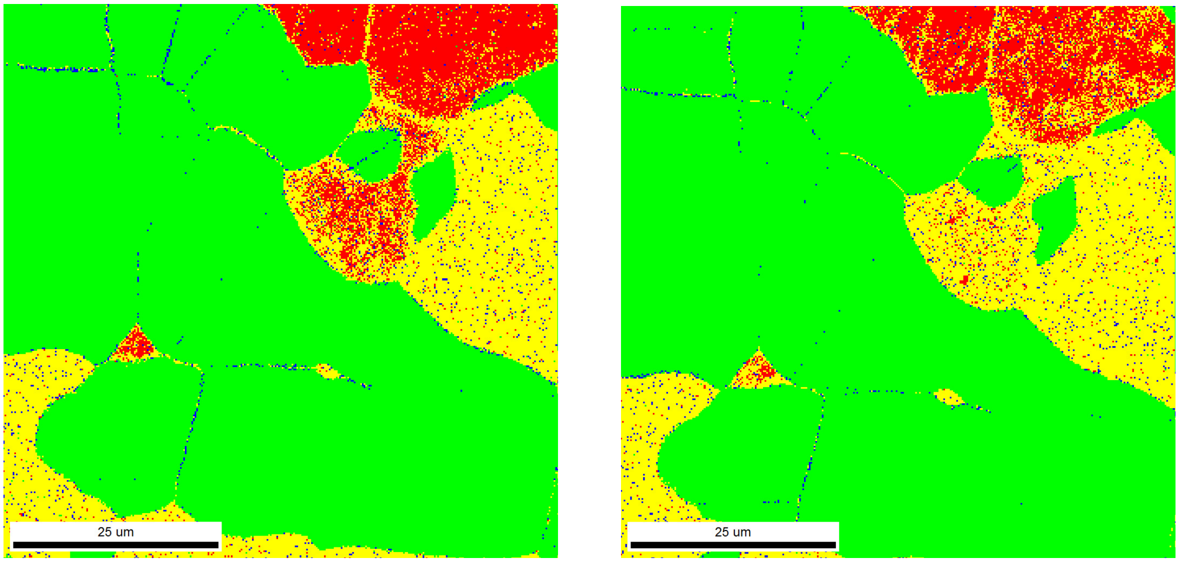

(e) Phase map acquired 130 min after heating (f) Phase map acquired 160 min after heating

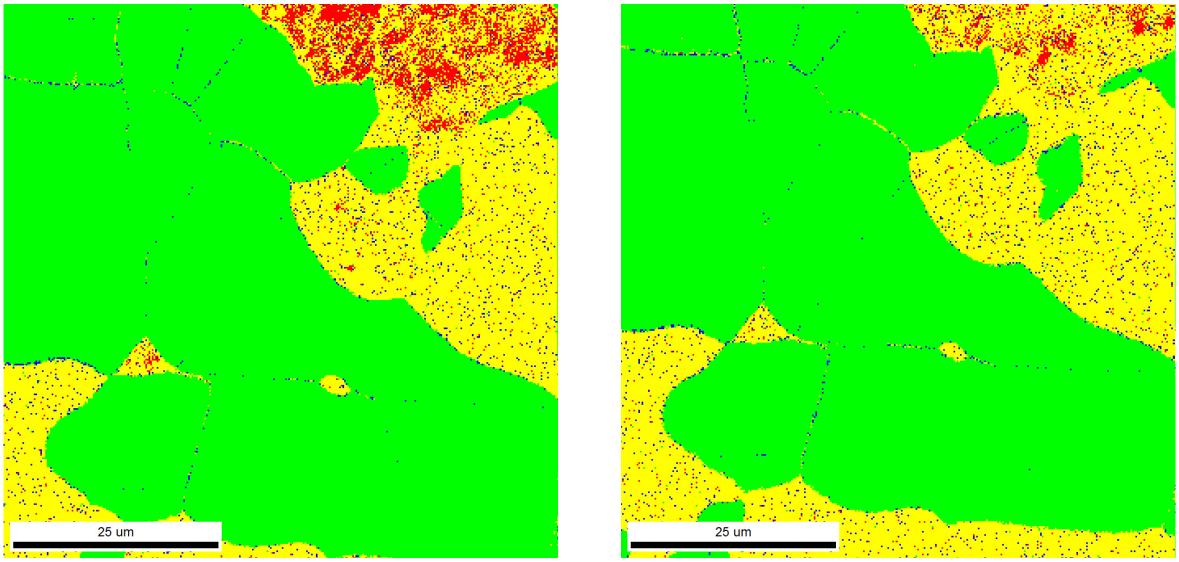

(g) Phase map acquired 190 min after heating (h) Phase map acquired 220 min after heating

Figure E.7: Phase maps from Experiment 2: Temperature set at 675 °C in oven

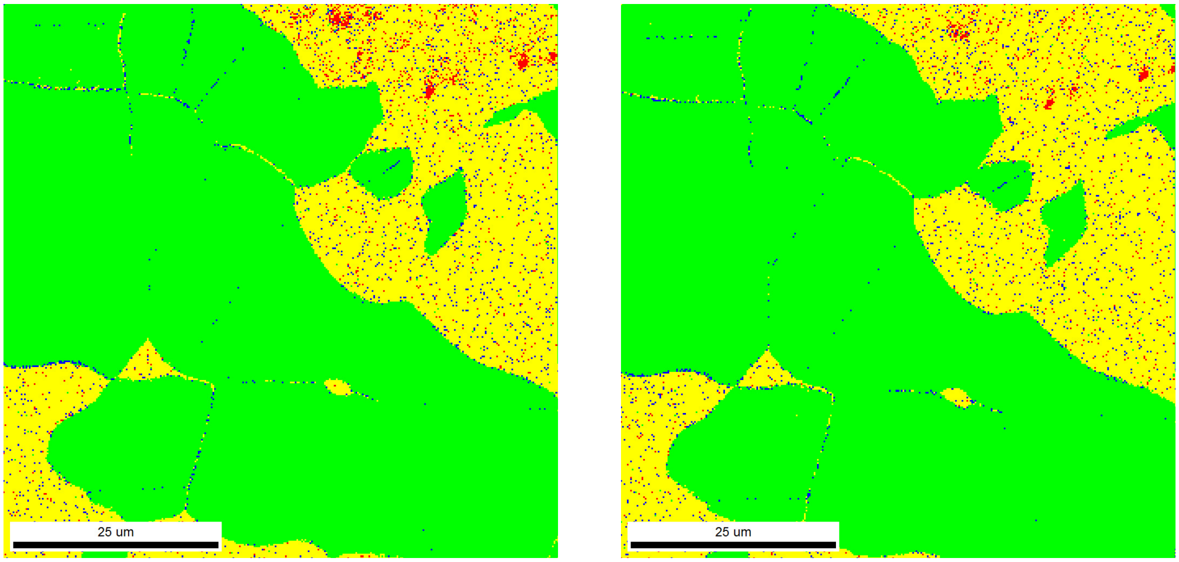

(i) Phase map acquired 250 min after heating

(j) Phase map acquired 280 min after heating

Figure E.7: Phase maps from Experiment 2: Temperature set at 675 °C in oven

E.4 Experiment 3, T = 650°C

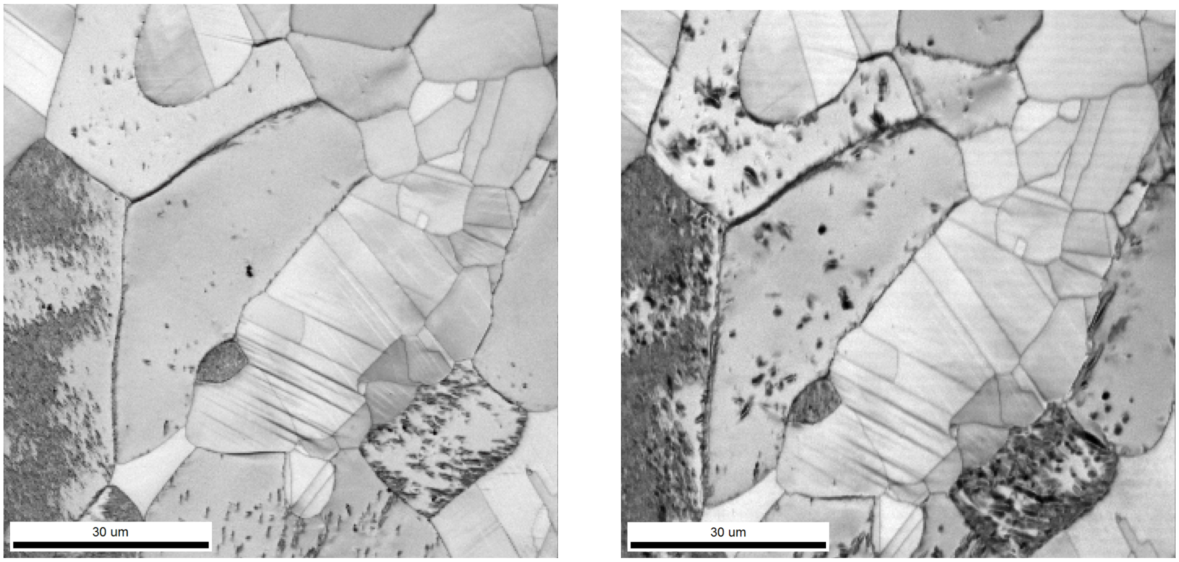

(a) IQ map acquired 10 min after heating

(b) IQ map acquired 40 min after heating

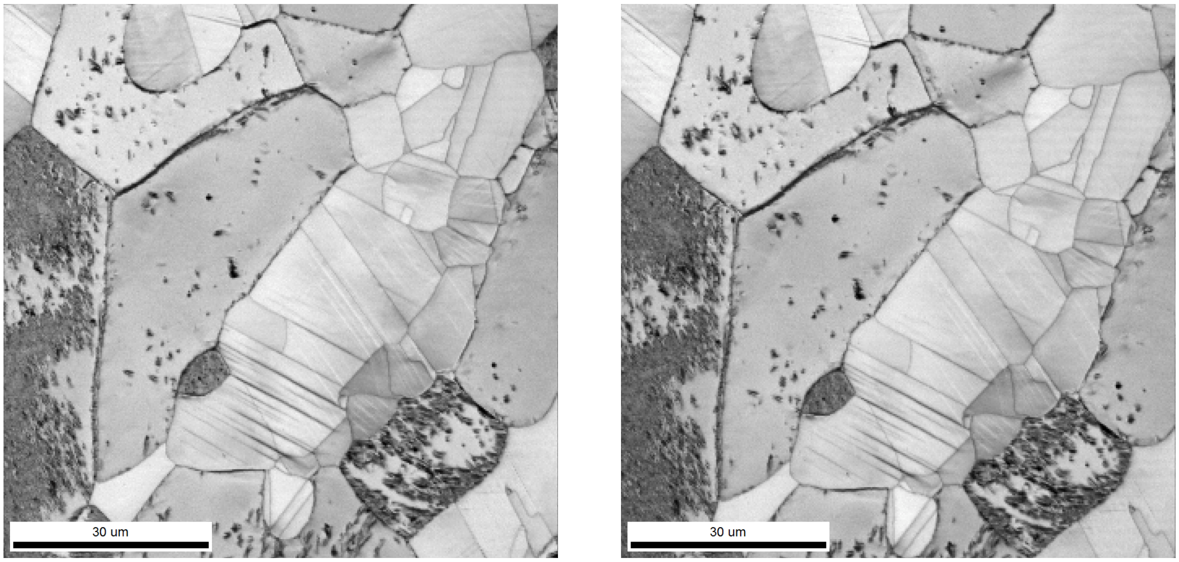

(c) IQ map acquired 70 min after heating

(d) IQ map acquired 100 min after heating

Figure E.8: IQ maps from Experiment 3: Temperature set at 650 °C in oven

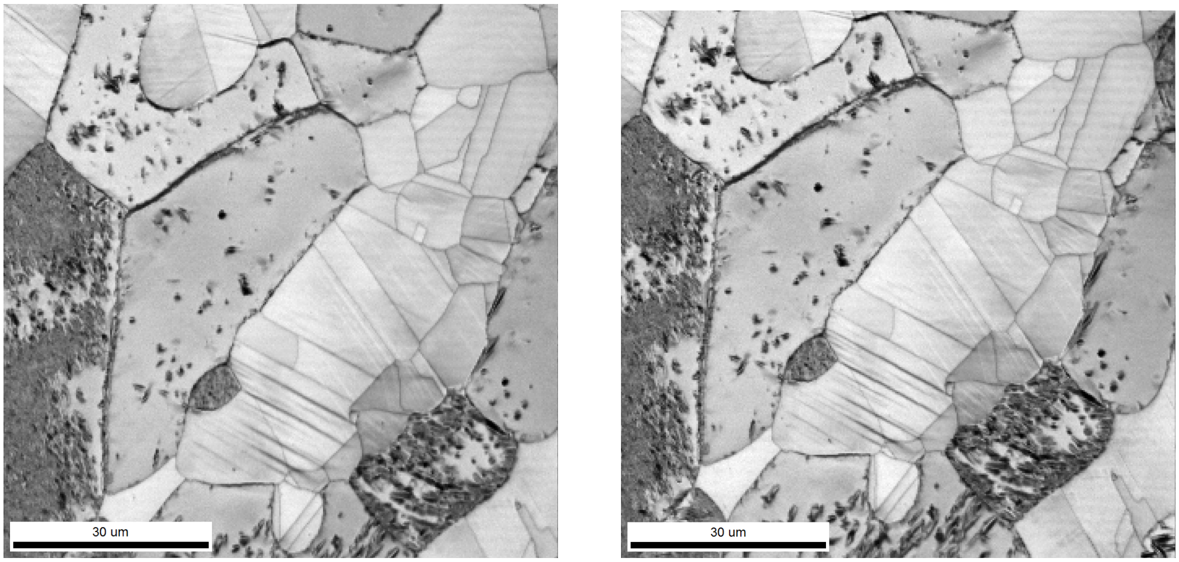

(e) IQ map acquired 130 min after heating

(f) IQ map acquired 160 min after heating

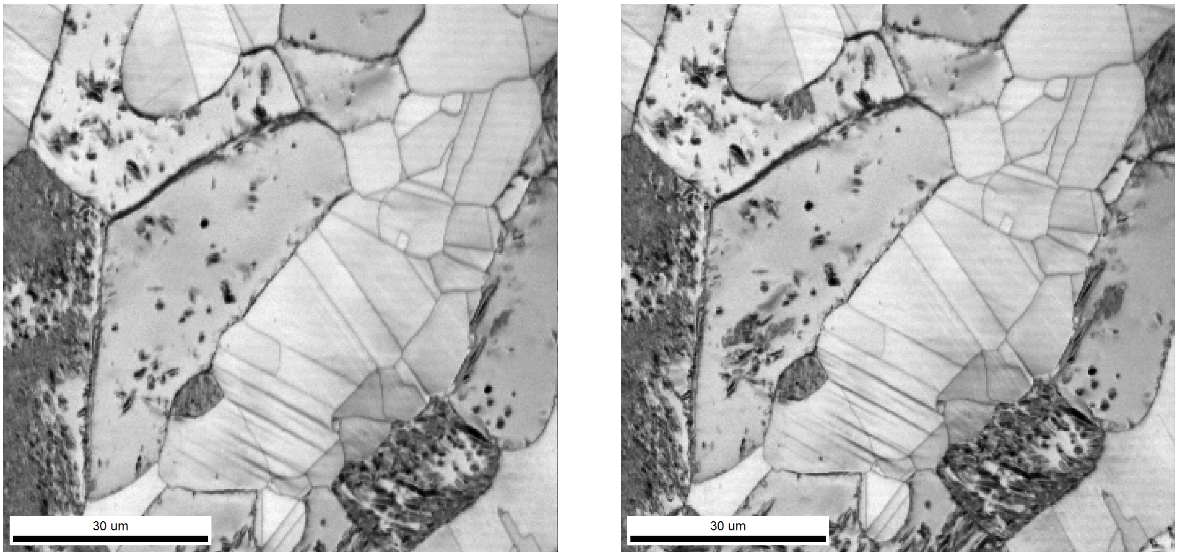

(g) IQ map acquired 190 min after heating

(h) IQ map acquired 220 min after heating

Figure E.8: IQ maps from Experiment 3: Temperature set at 650 °C in oven

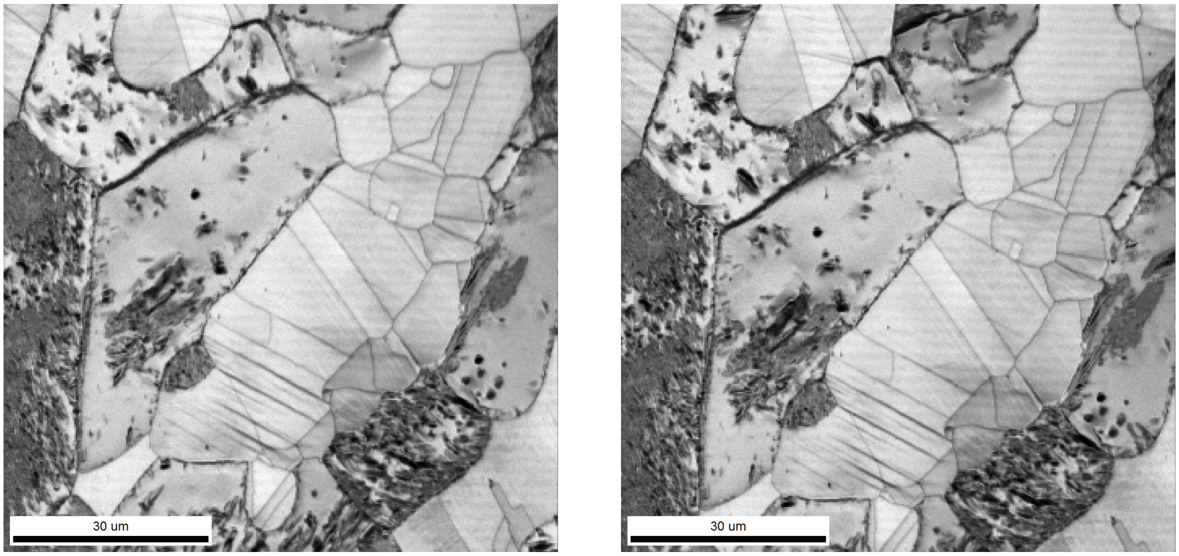

(i) IQ map acquired 250 min after heating

(j) IQ map acquired 280 min after heating

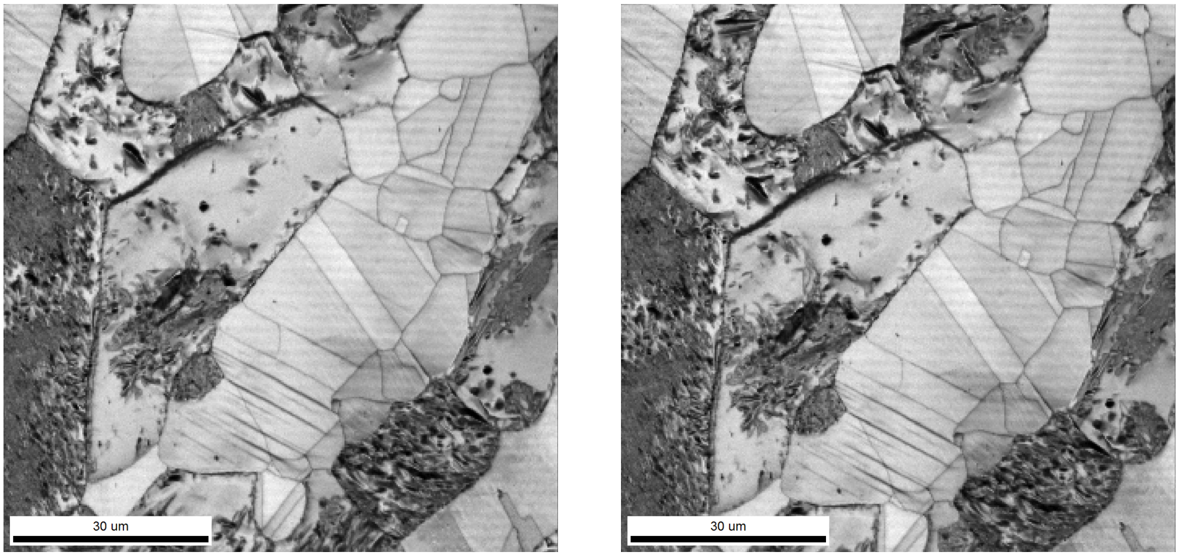

(k) IQ map acquired 310 min after heating

(l) IQ map acquired 340 min after heating

Figure E.8: IQ maps from Experiment 3: Temperature set at 650 °C in oven

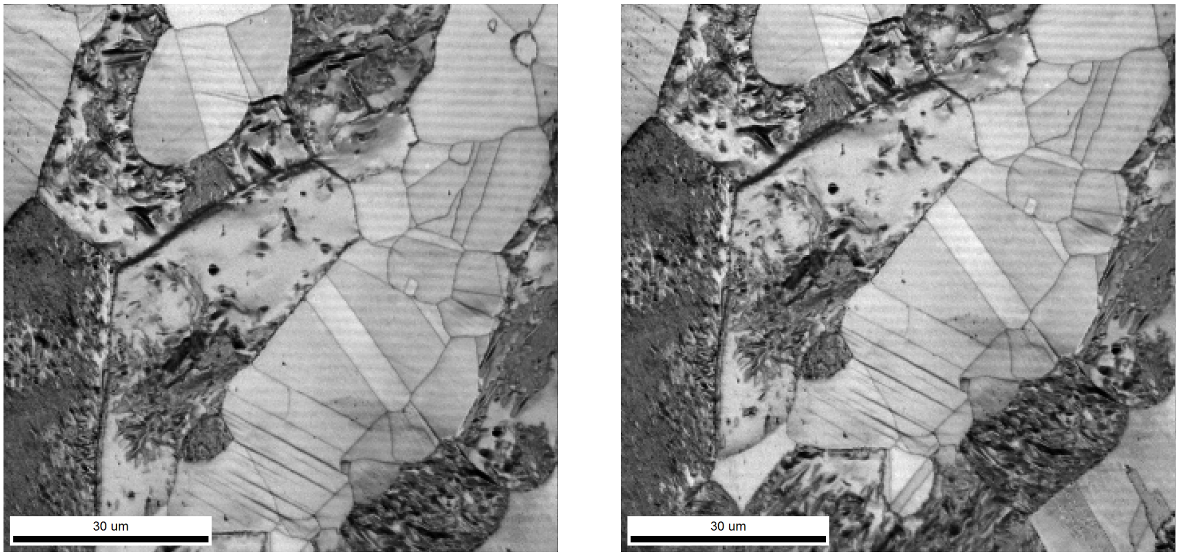

(m) IQ map acquired 370 min after heating

(n) IQ map acquired 400 min after heating

Figure E.8: IQ maps from Experiment 3: Temperature set at 650 °C in oven

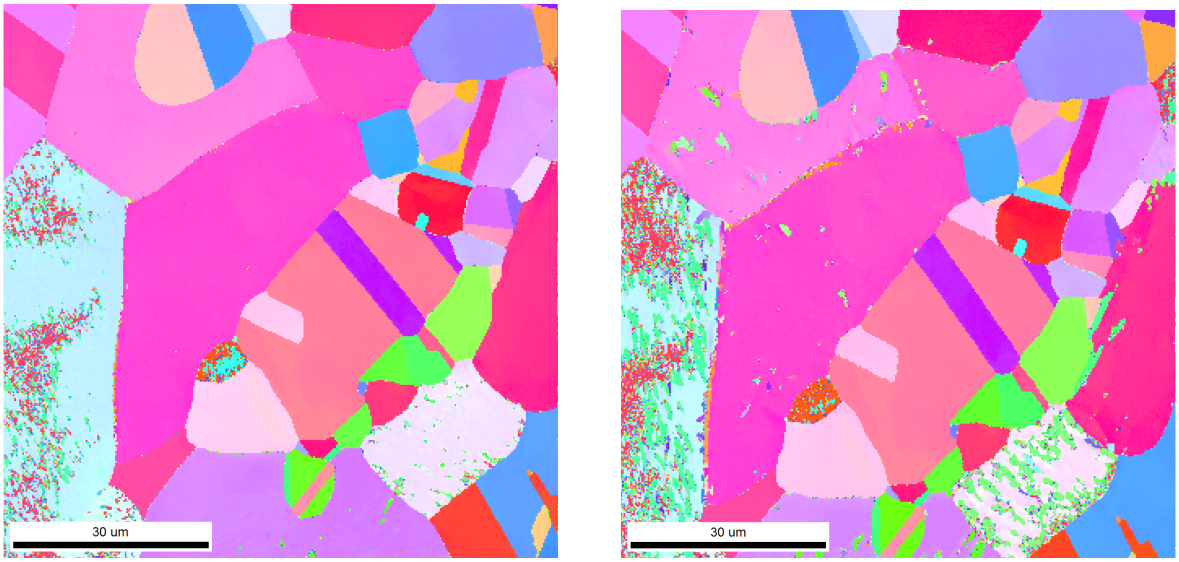

(a) IPF map acquired 10 min after heating (b) IPF map acquired 40 min after heating

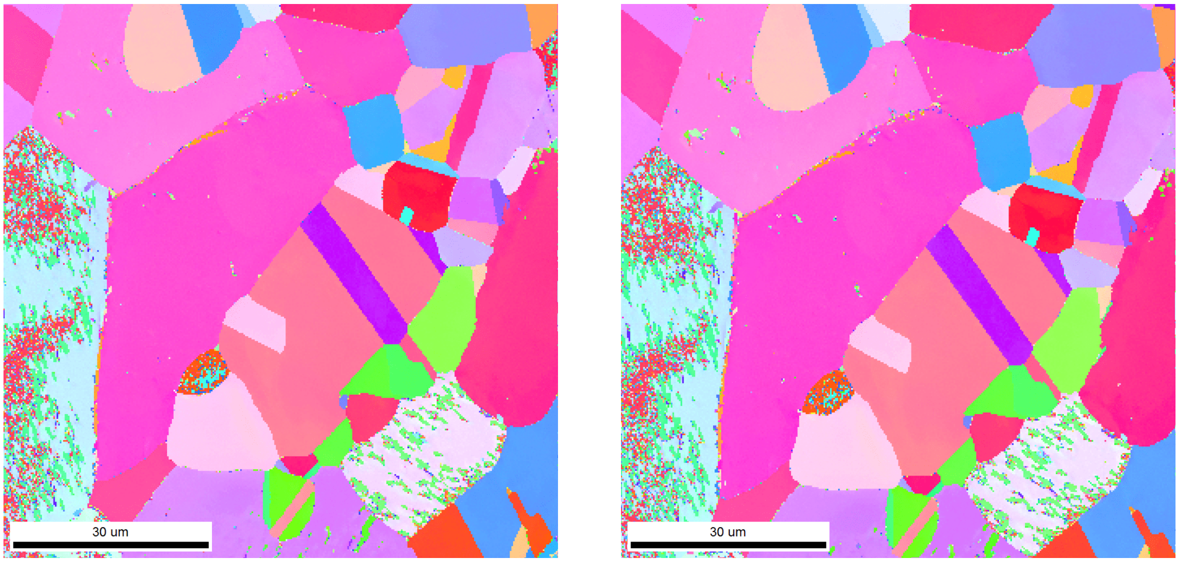

(c) IPF map acquired 70 min after heating (d) IPF map acquired 100 min after heating

Figure E.9: IPF maps from Experiment 3: Temperature set at 650 °C in oven

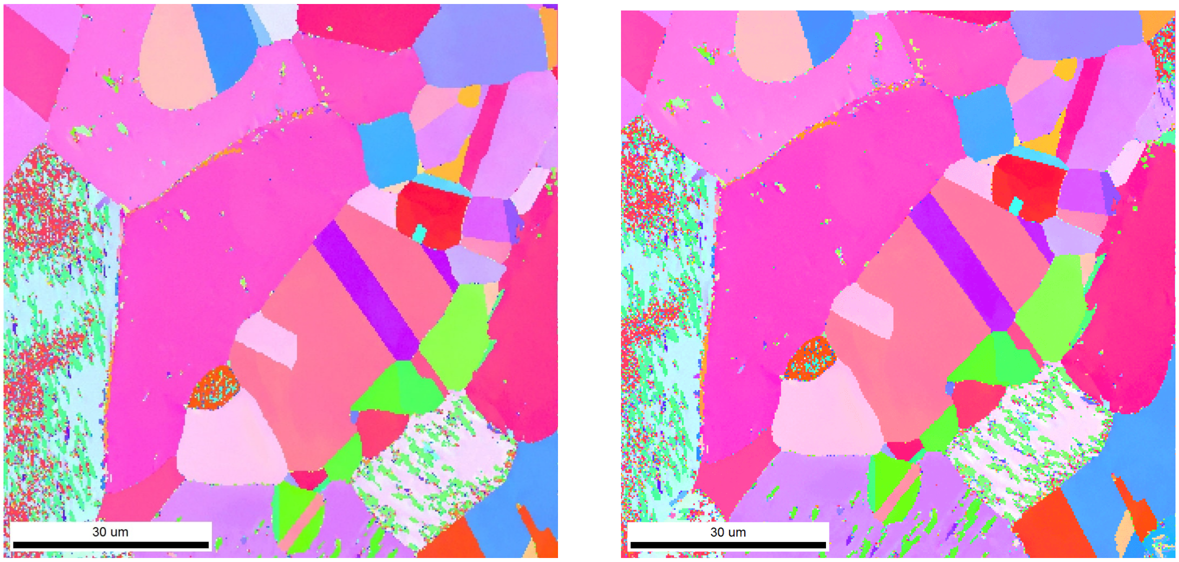

(e) IPF map acquired 130 min after heating

(f) IPF map acquired 160 min after heating

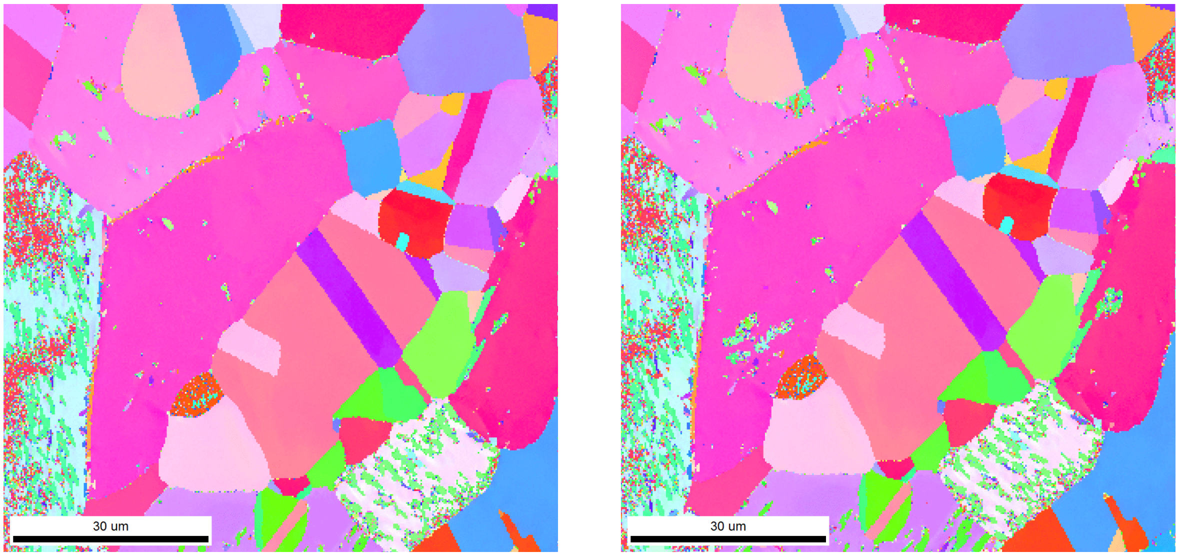

(g) IPF map acquired 190 min after heating

(h) IPF map acquired 220 min after heating

Figure E.9: IPF maps from Experiment 3: Temperature set at 650 °C in oven

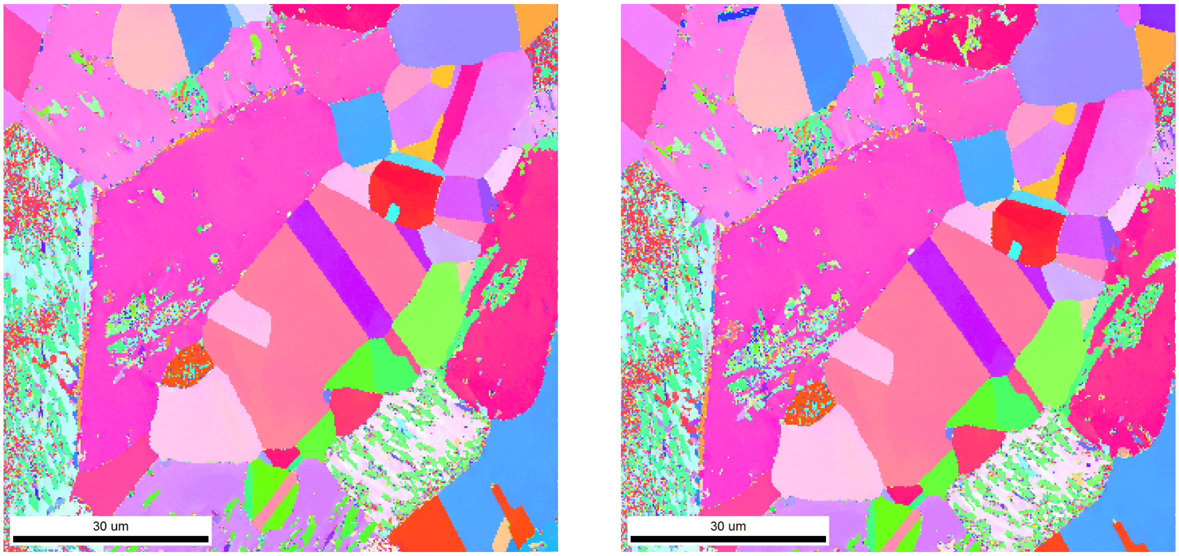

(i) IPF map acquired 250 min after heating (j) IPF map acquired 280 min after heating

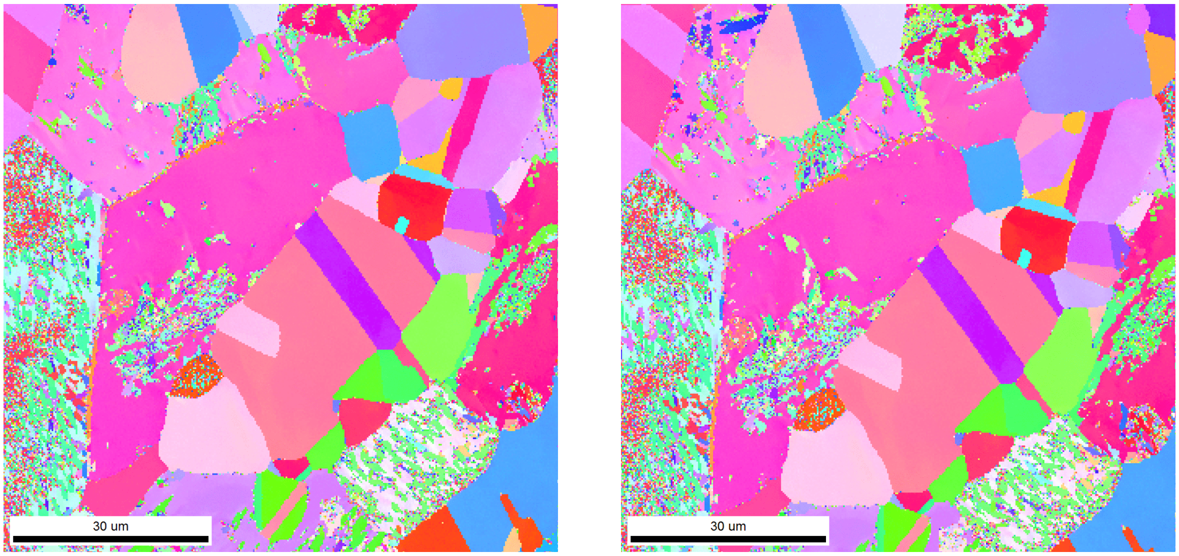

(k) IPF map acquired 310 min after heating (l) IPF map acquired 340 min after heating

Figure E.9: IPF maps from Experiment 3: Temperature set at 650 °C in oven

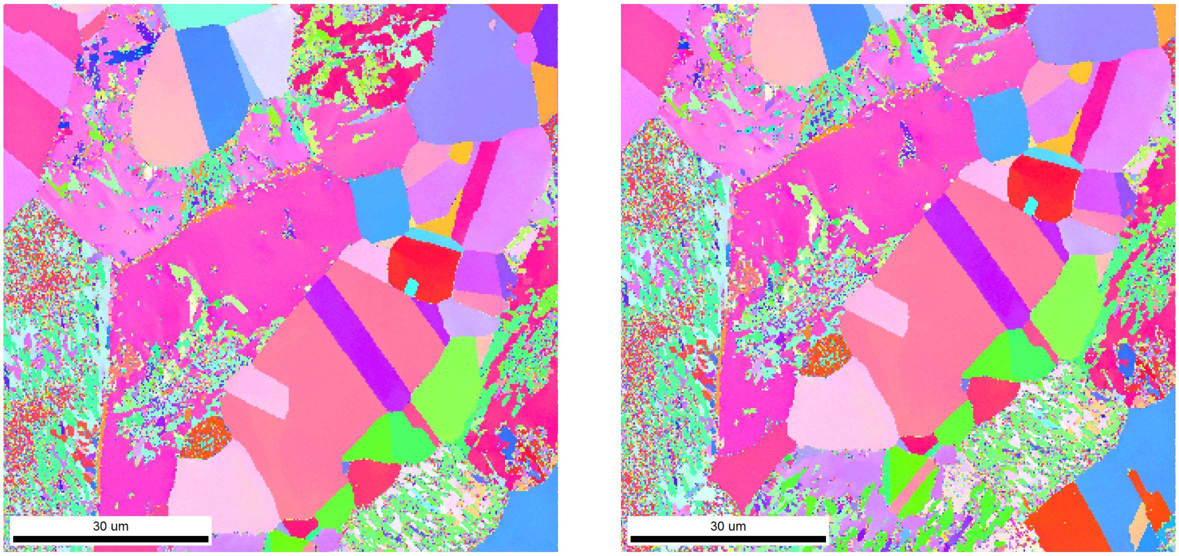

(m) IPF map acquired 370 min after heating

(n) IPF map acquired 400 min after heating

Figure E.9: IPF maps from Experiment 3: Temperature set at 650 °C in oven

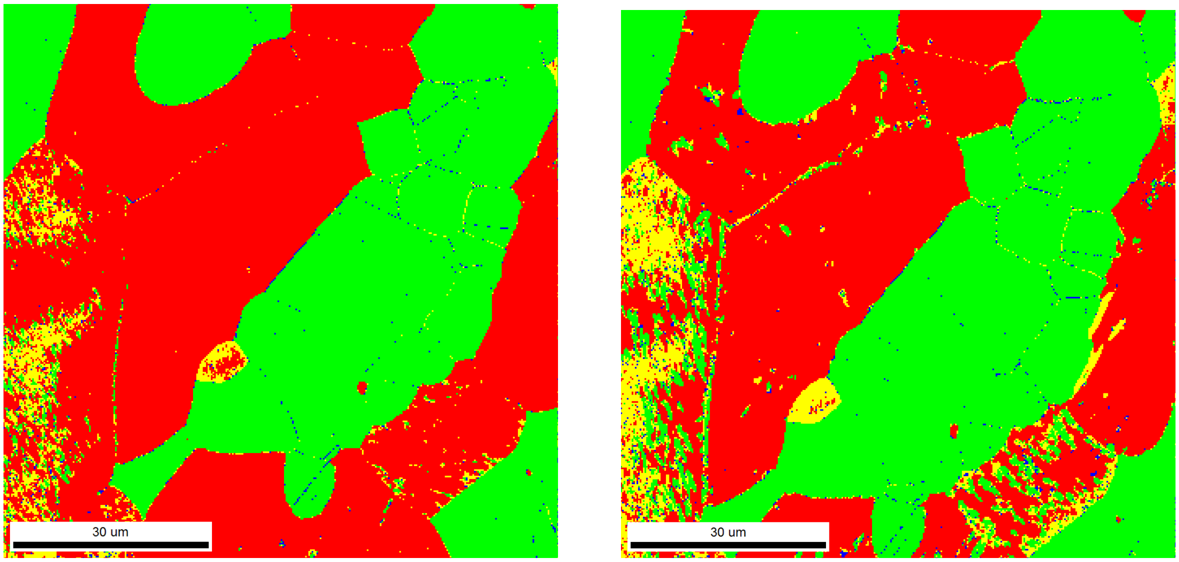

(a) Phase map acquired 10 min after heating (b) Phase map acquired 40 min after heating

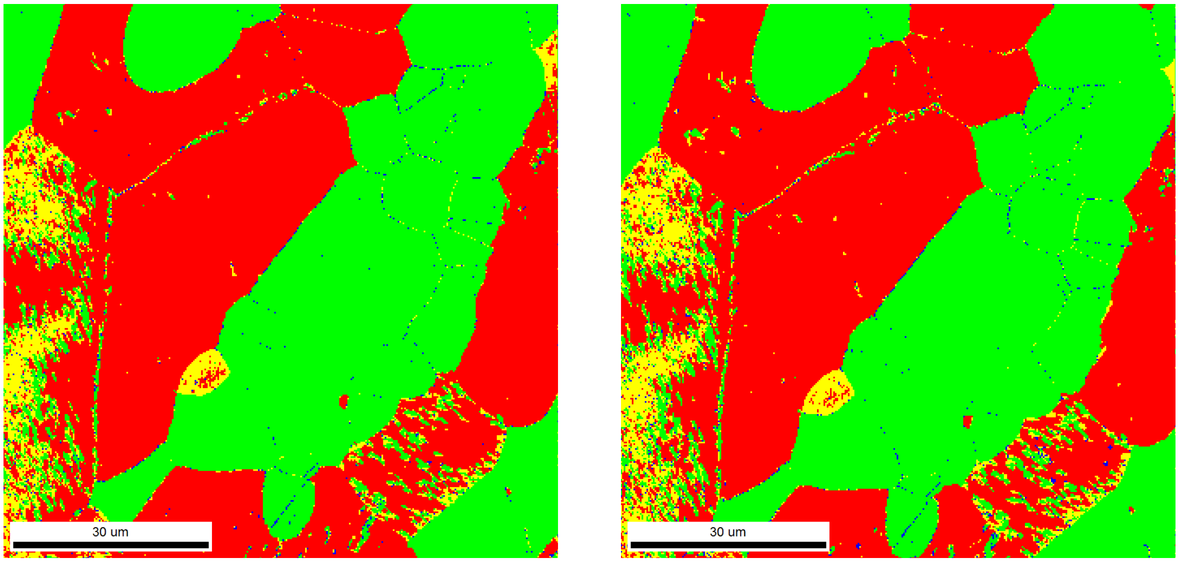

(c) Phase map acquired 70 min after heating (d) Phase map acquired 100 min after heating

Figure E.10: Phase maps from Experiment 3: Temperature set at 650 °C in oven

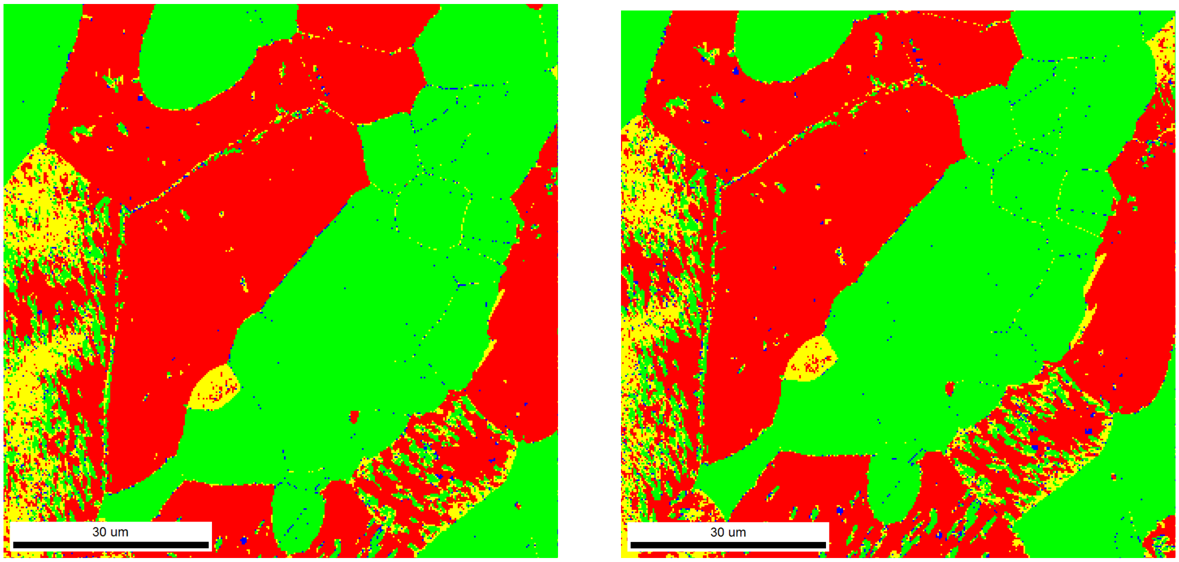

(e) Phase map acquired 130 min after heating

(f) Phase map acquired 160 min after heating

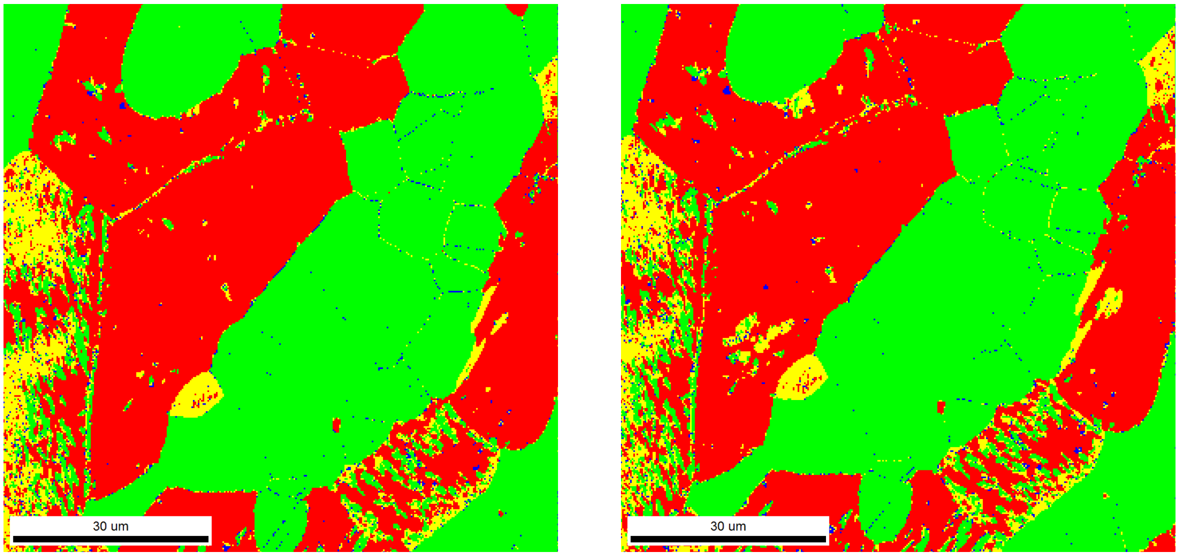

(g) Phase map acquired 190 min after heating

(h) Phase map acquired 220 min after heating

Figure E.10: Phase maps from Experiment 3: Temperature set at 650 °C in oven

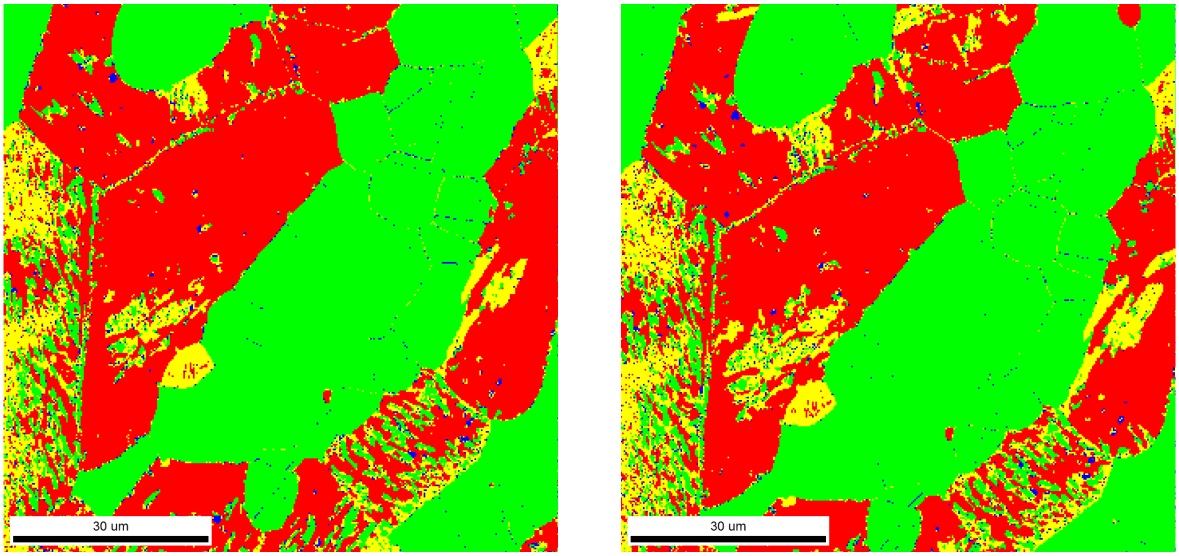

(i) Phase map acquired 250 min after heating (j) Phase map acquired 280 min after heating

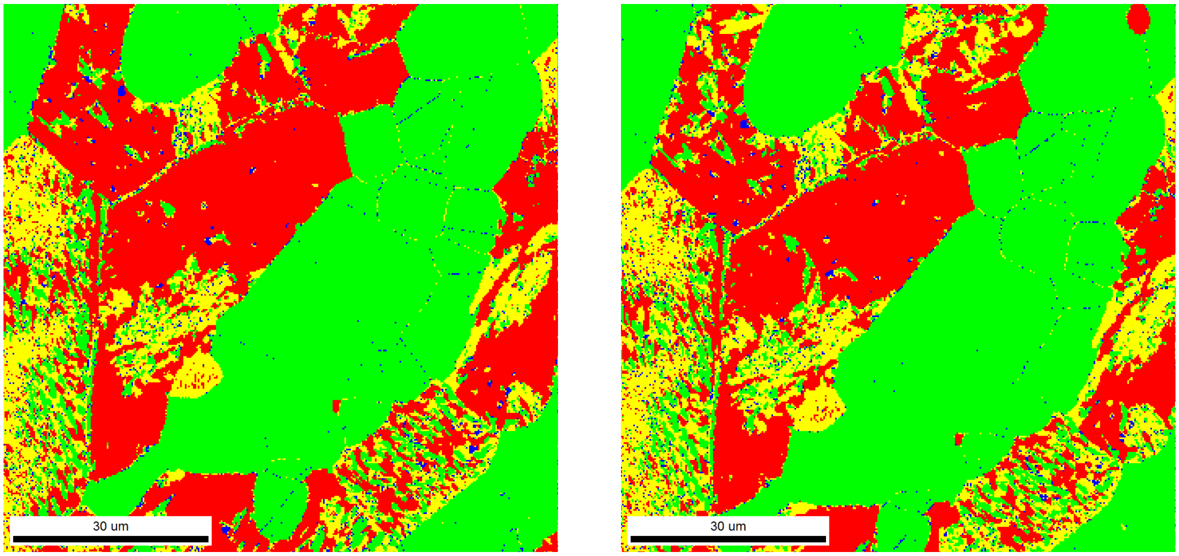

(k) Phase map acquired 310 min after heating (l) Phase map acquired 340 min after heating

Figure E.10: Phase maps from Experiment 3: Temperature set at 650 °C in oven

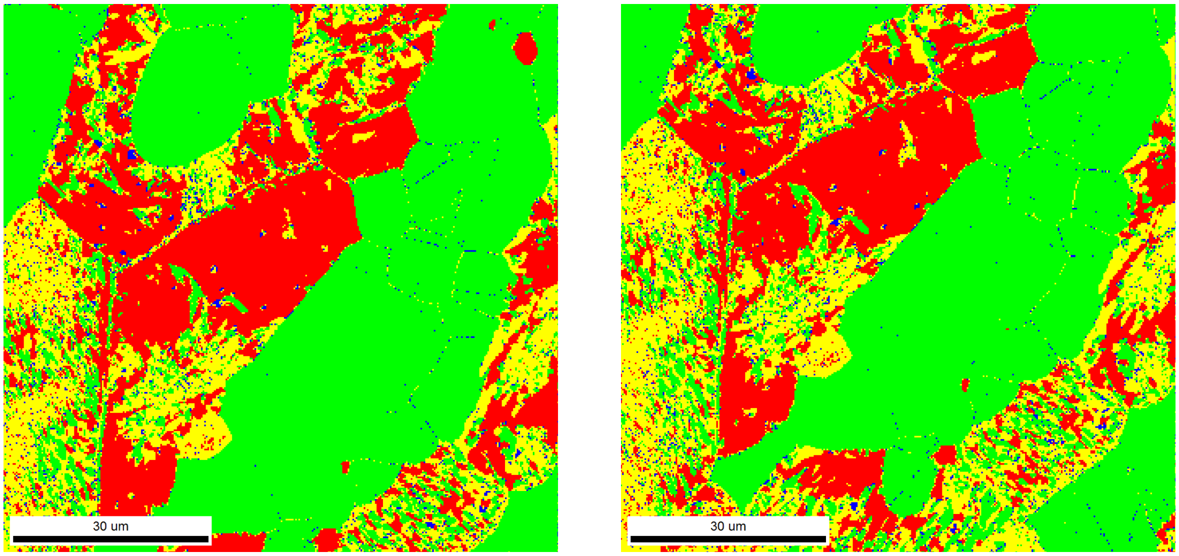

(m) Phase map acquired 370 min after heating

(n) Phase map acquired 400 min after heating

Figure E.10: Phase maps from Experiment 3: Temperature set at 650 °C in oven

E.5 Experiment 4, T = 650°C

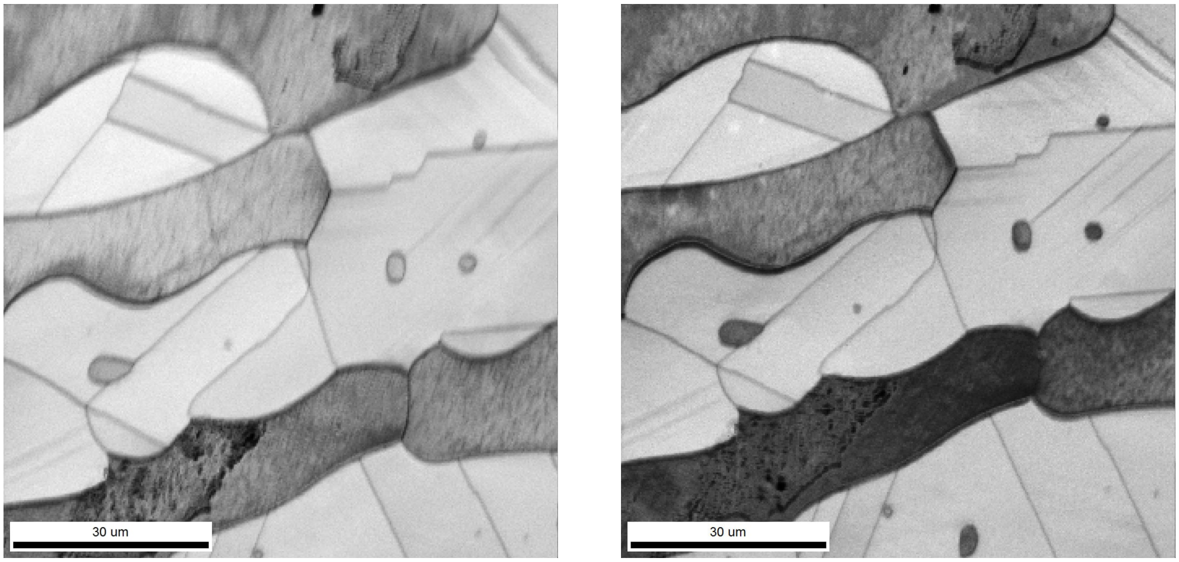

(a) IQ map acquired 10 min after heating

(b) IQ map acquired 40 min after heating

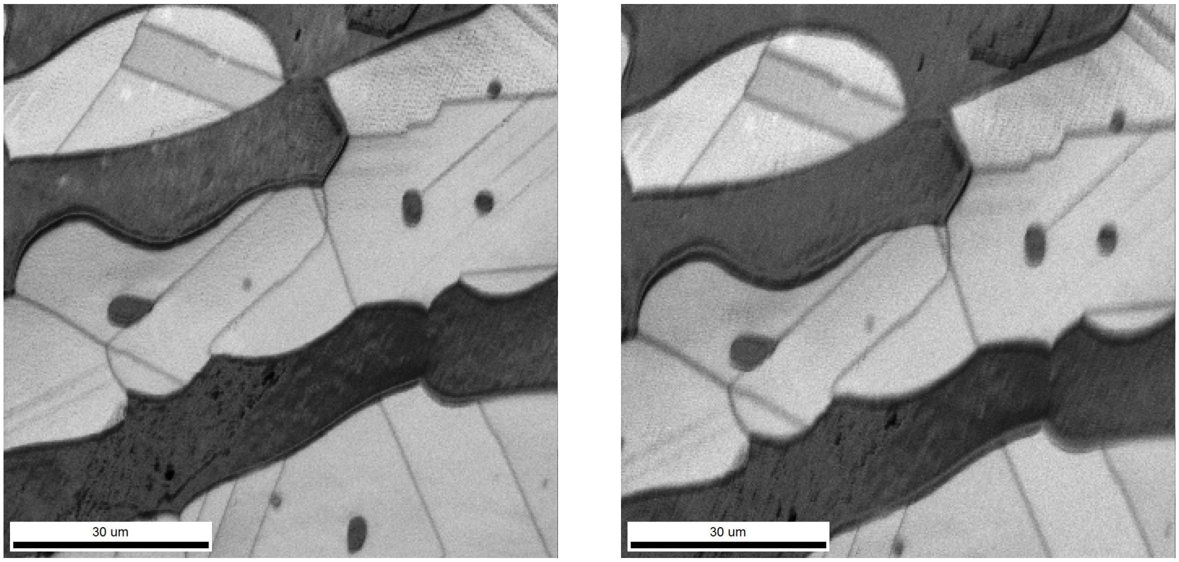

(c) IQ map acquired 70 min after heating

(d) IQ map acquired 100 min after heating

Figure E.11: IQ maps from Experiment 4: Temperature set at 650 °C in oven

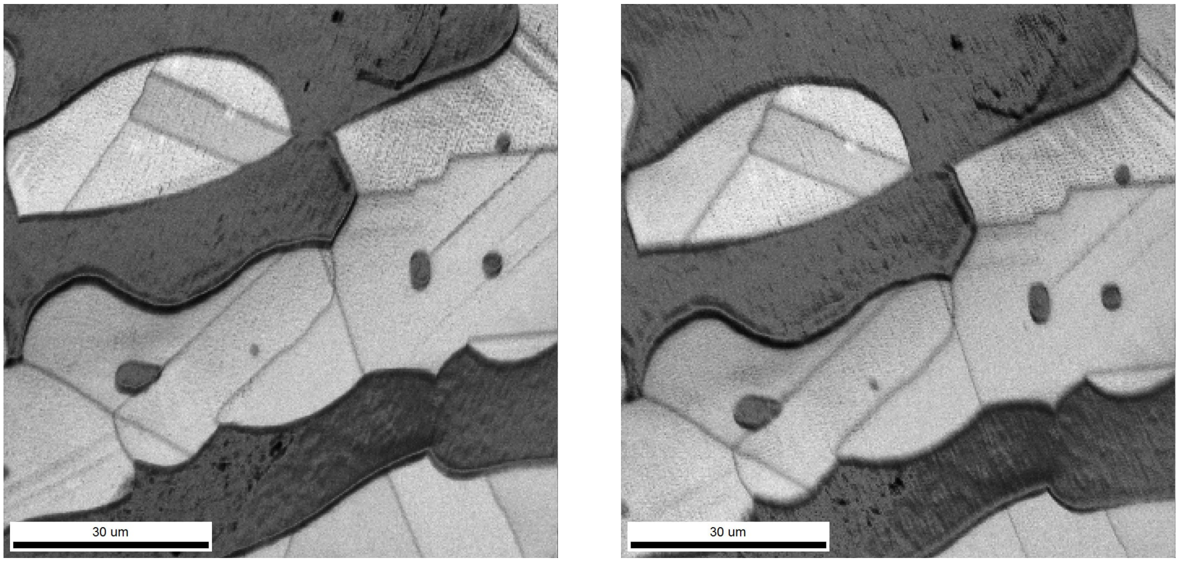

(a) IQ map acquired 130 min after heating

(b) IQ map acquired 160 min after heating

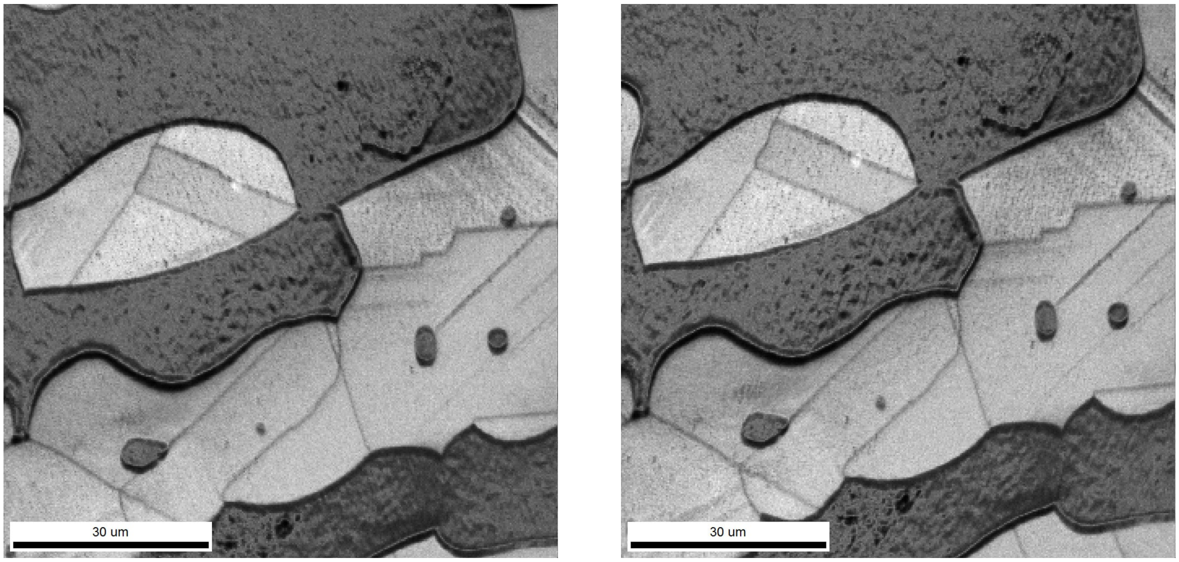

(c) IQ map acquired 190 min after heating

(d) IQ map acquired 220 min after heating

Figure E.12: IQ maps from Experiment 4: Temperature set at 650 °C in oven

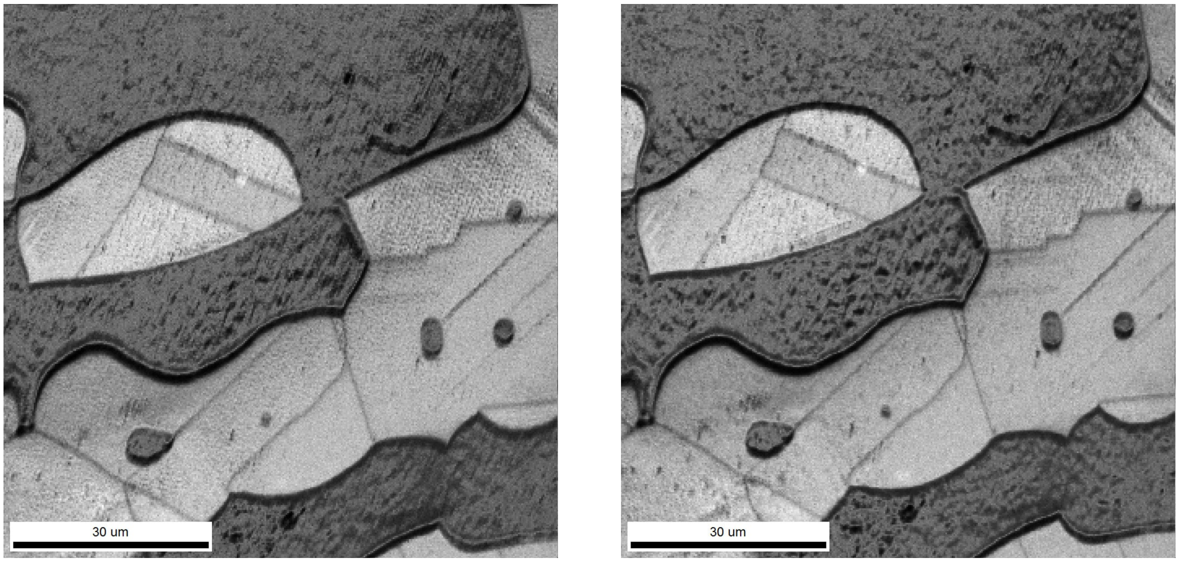

(a) IQ map acquired 250 min after heating (b) IQ map acquired 280 min after heating

Figure E.13: IQ maps from Experiment 4: Temperature set at 650 °C in oven

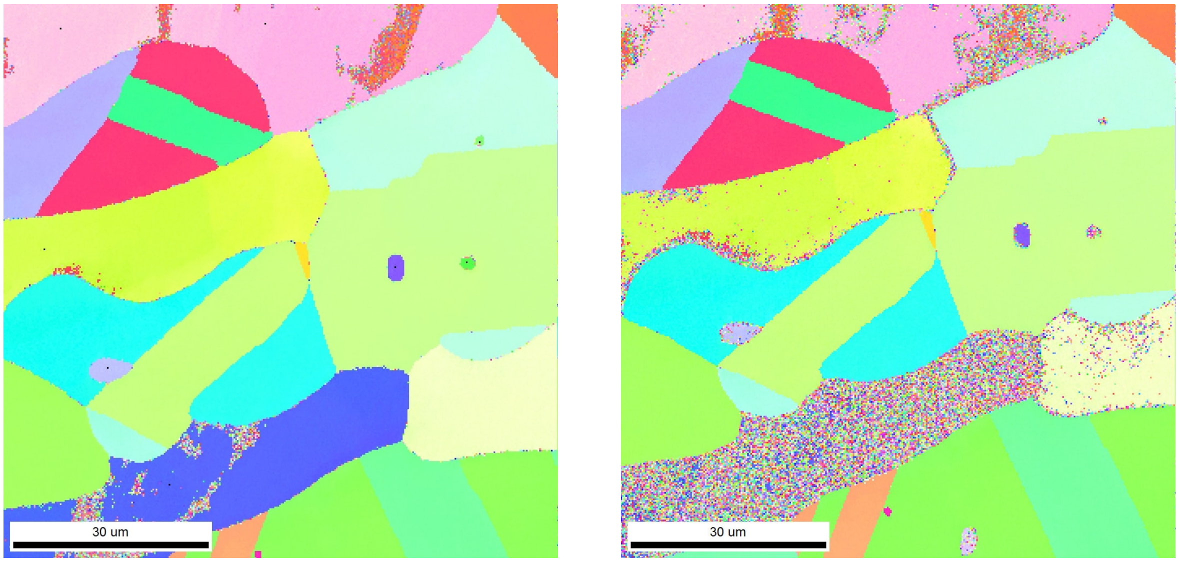

(a) IPF map acquired 10 min after heating

(b) IPF map acquired 40 min after heating

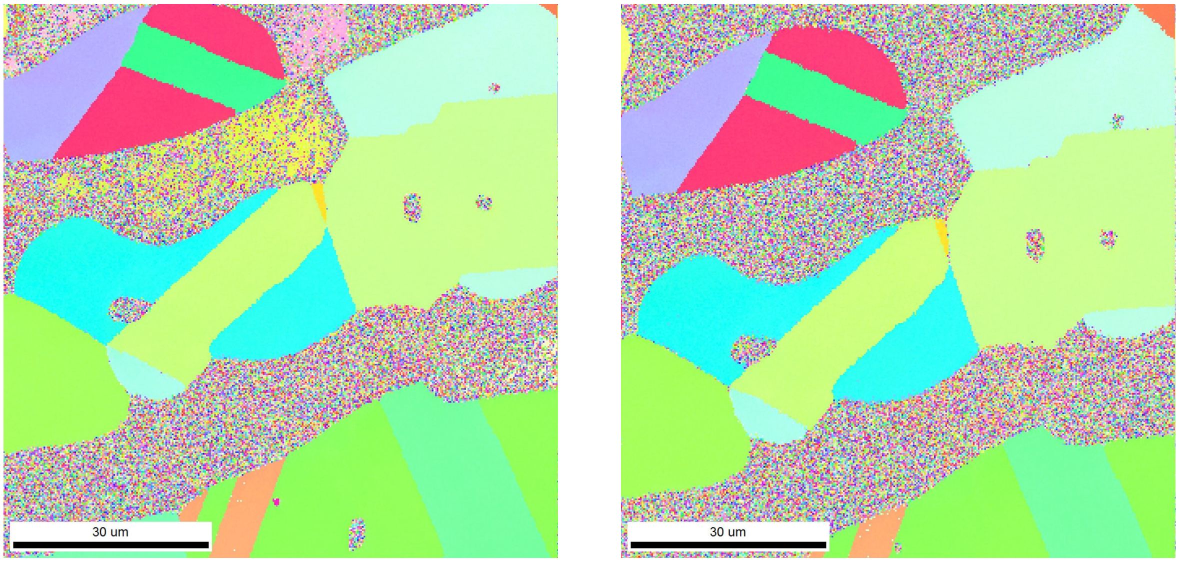

(c) IPF map acquired 70 min after heating

(d) IPF map acquired 100 min after heating

Figure E.14: IPF maps from Experiment 4: Temperature set at 650 °C in oven

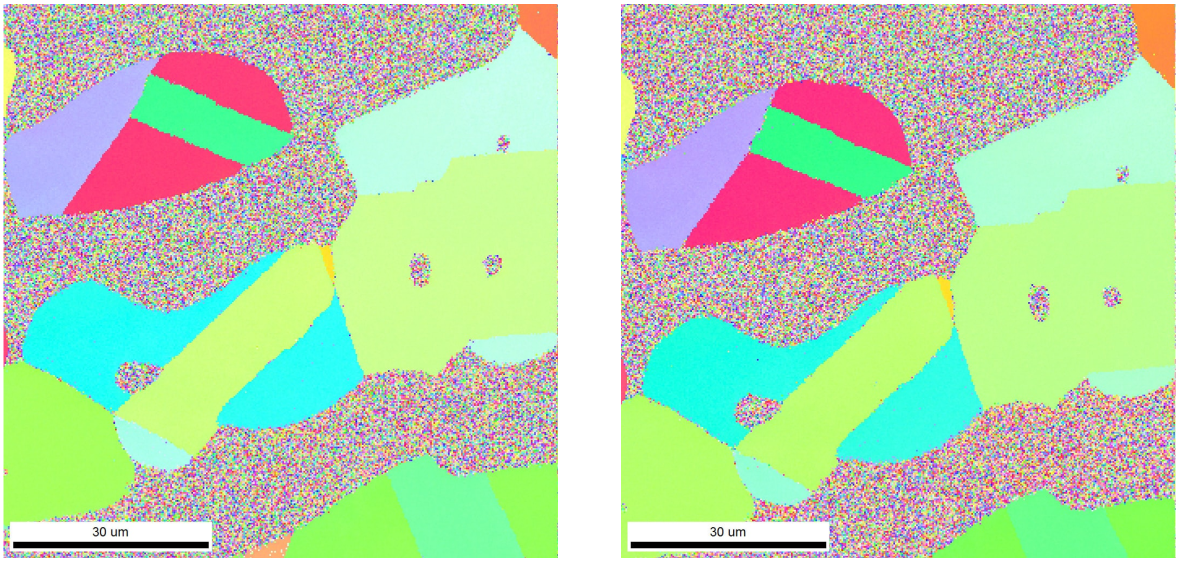

(a) IPF map acquired 130 min after heating (b) IPF map acquired 160 min after heating

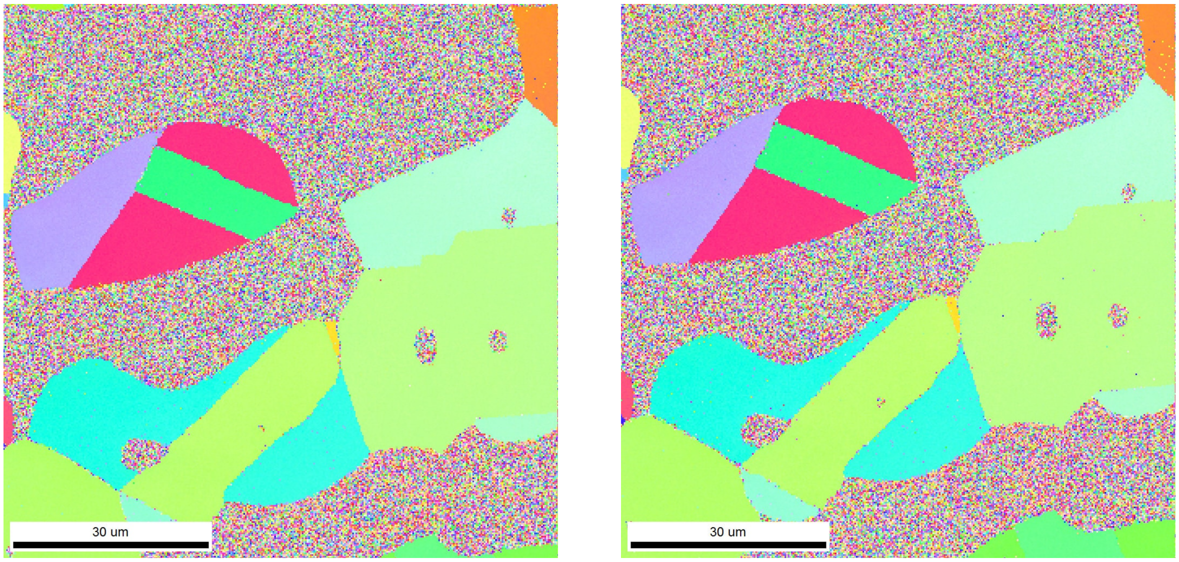

(c) IPF map acquired 190 min after heating (d) IPF map acquired 220 min after heating

Figure E.15: IPF maps from Experiment 4: Temperature set at 650 °C in oven

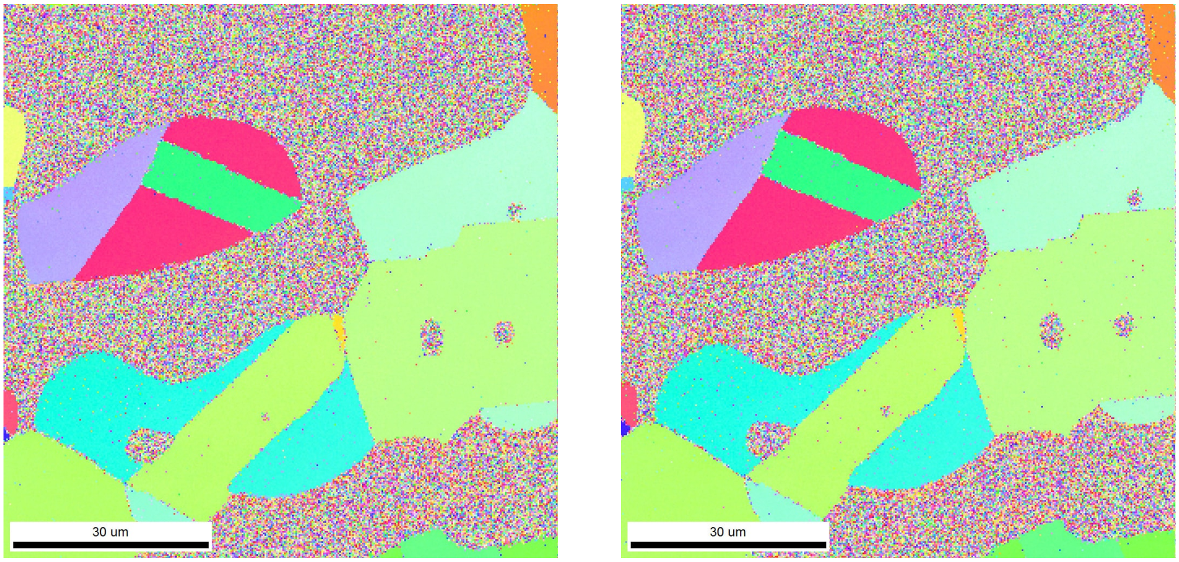

(a) IPF map acquired 250 min after heating (b) IPF map acquired 280 min after heating

Figure E.16: IPF maps from Experiment 4: Temperature set at 650 °C in oven

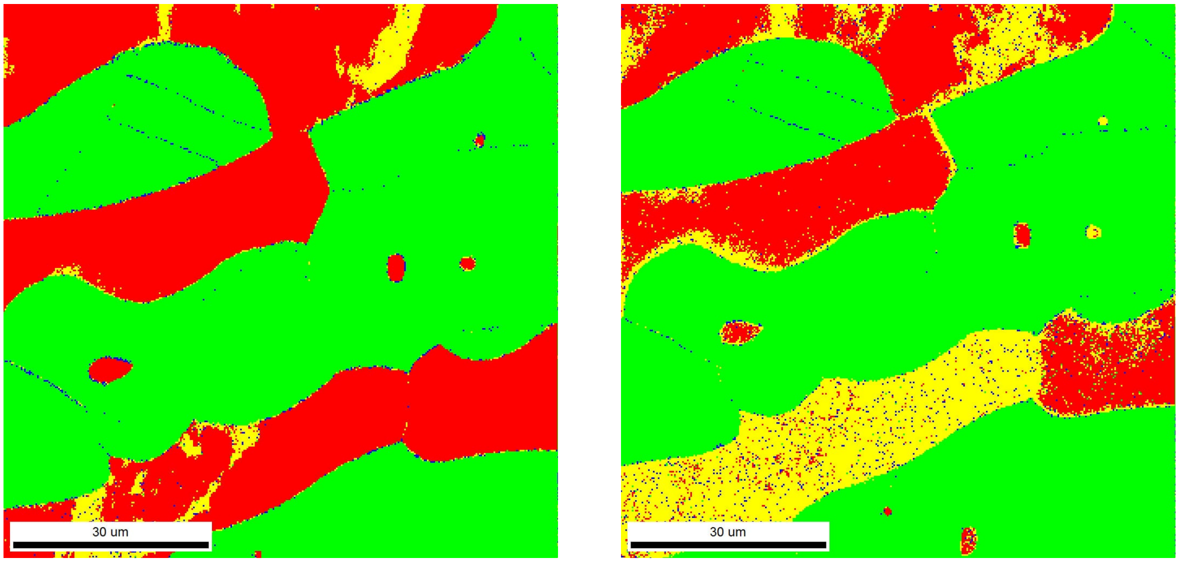

(a) Phase map acquired 10 min after heating (b) Phase map acquired 40 min after heating

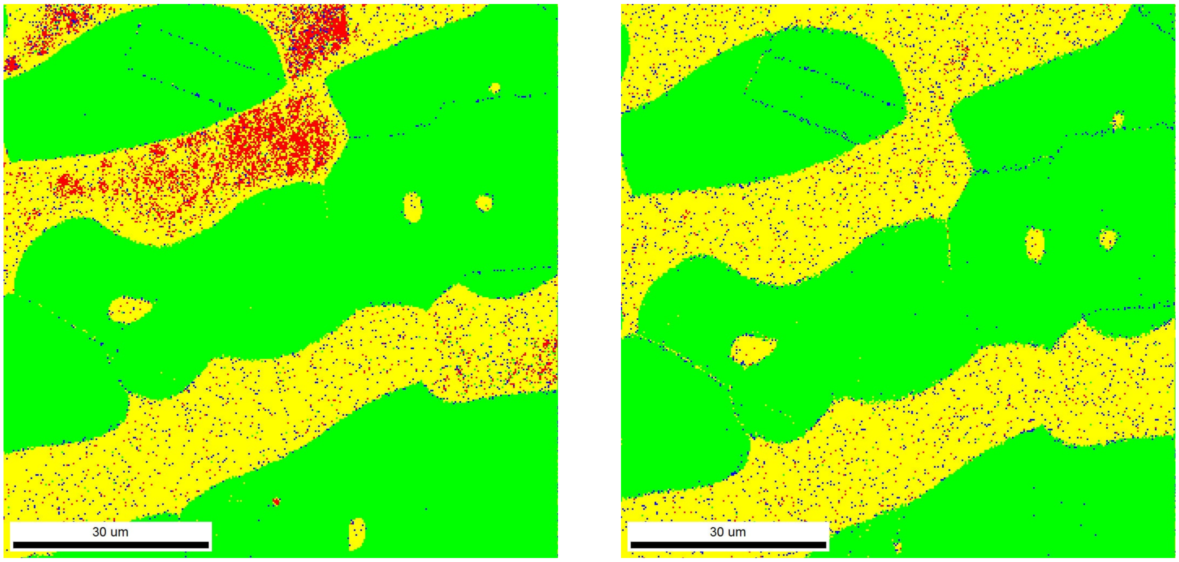

(c) Phase map acquired 70 min after heating (d) Phase map acquired 100 min after heating

Figure E.17: Phase maps from Experiment 4: Temperature set at 650 °C in oven

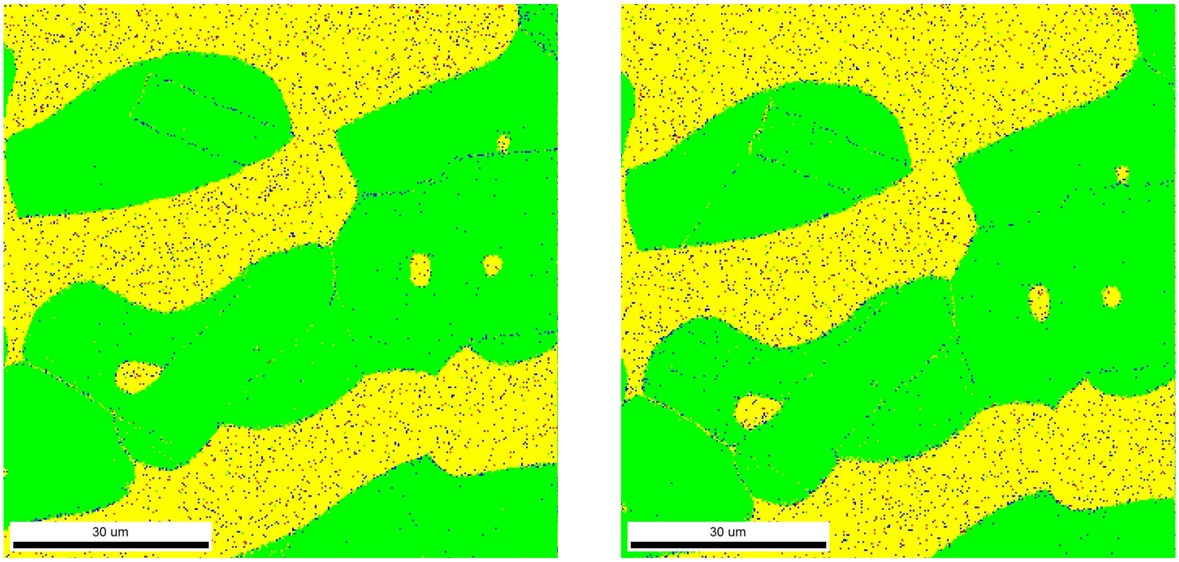

(a) Phase map acquired 130 min after heating (b) Phase map acquired 160 min after heating

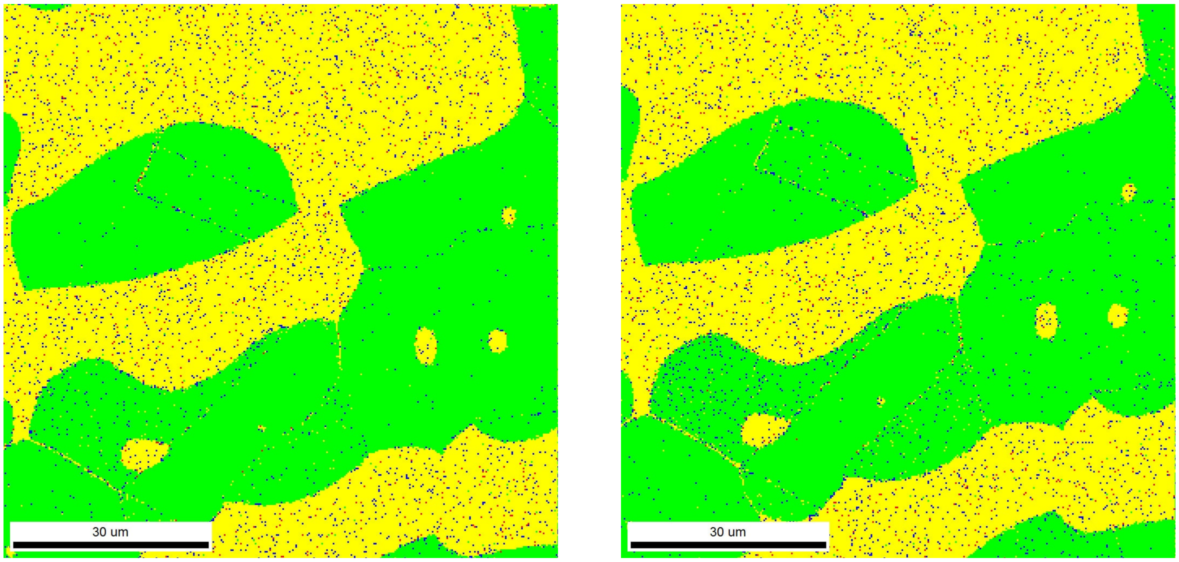

(c) Phase map acquired 190 min after heating (d) Phase map acquired 220 min after heating

Figure E.18: Phase maps from Experiment 4: Temperature set at 650 °C in oven

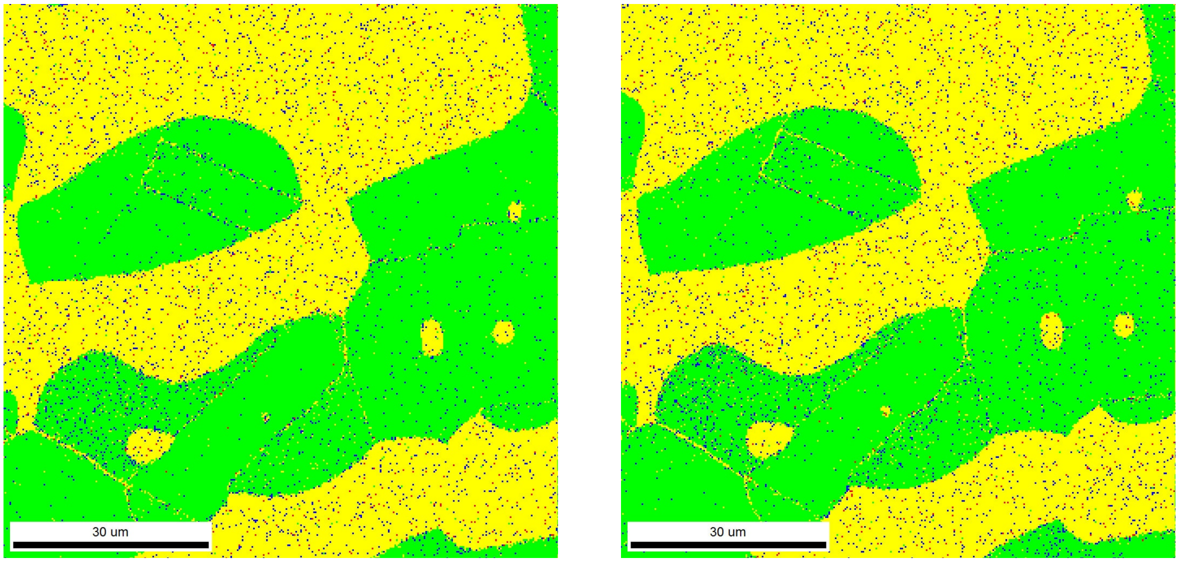

(a) Phase map acquired 250 min after heating (b) Phase map acquired 280 min after heating

Figure E.19: Phase maps from Experiment 4: Temperature set at 650 °C in oven

E.6 Experiment 5, T = 640°C

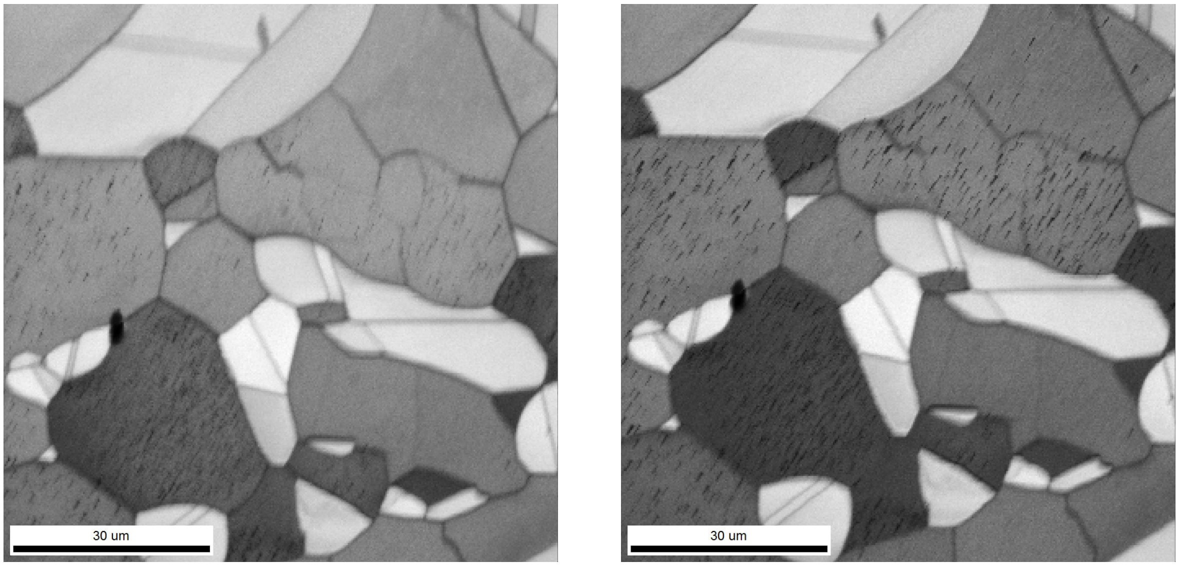

(a) IQ map acquired 10 min after heating

(b) IQ map acquired 40 min after heating

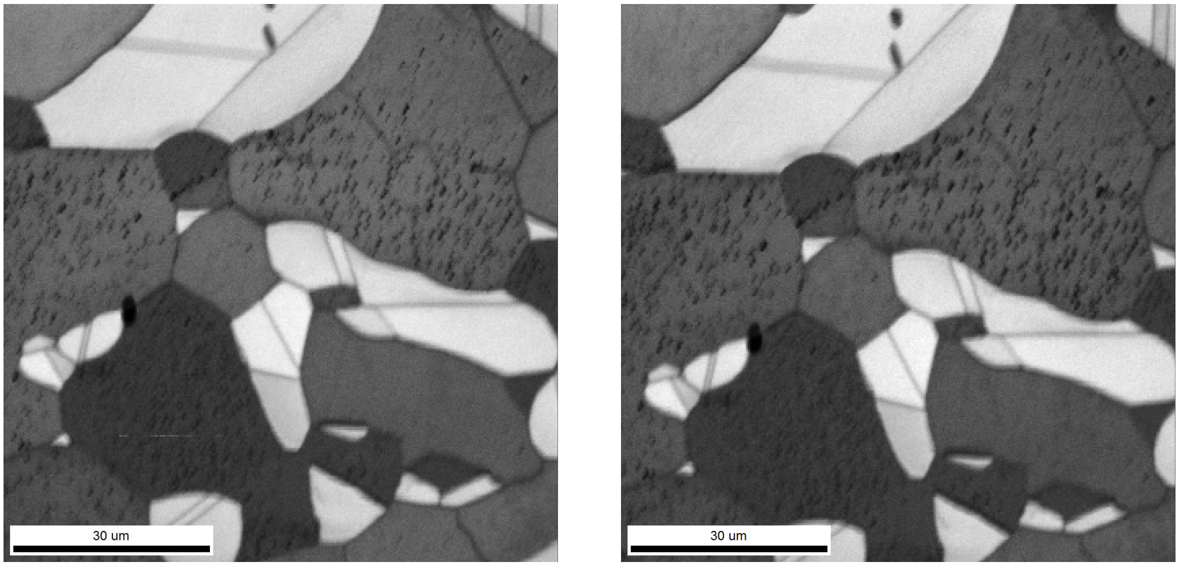

(c) IQ map acquired 70 min after heating

(d) IQ map acquired 100 min after heating

Figure E.20: IQ maps from Experiment 5: Temperature set at 640 °C in oven

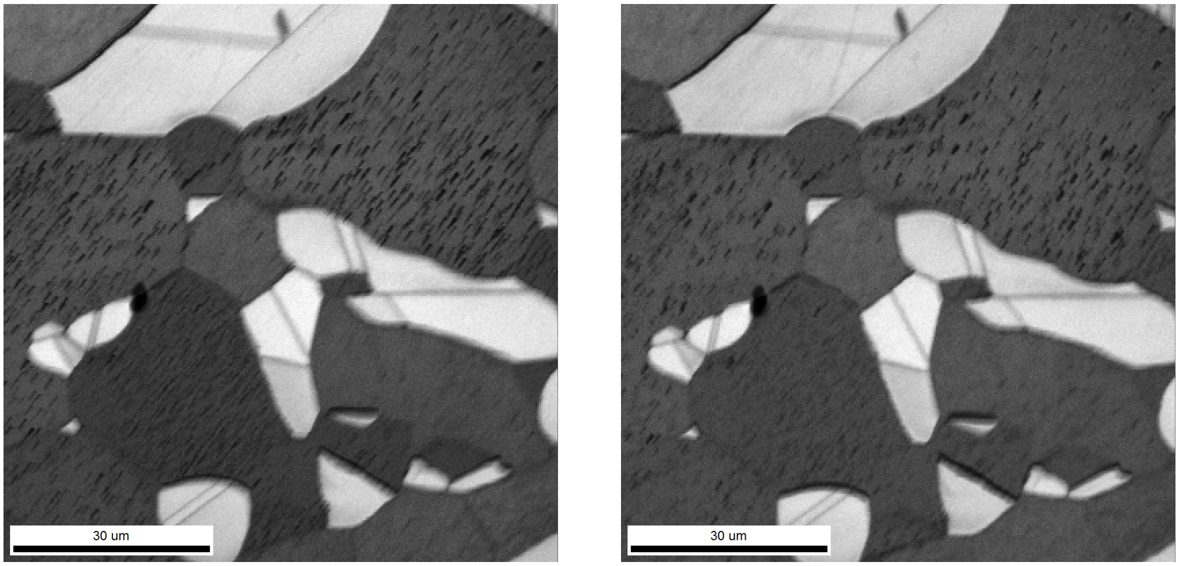

(a) IQ map acquired 130 min after heating

(b) IQ map acquired 160 min after heating

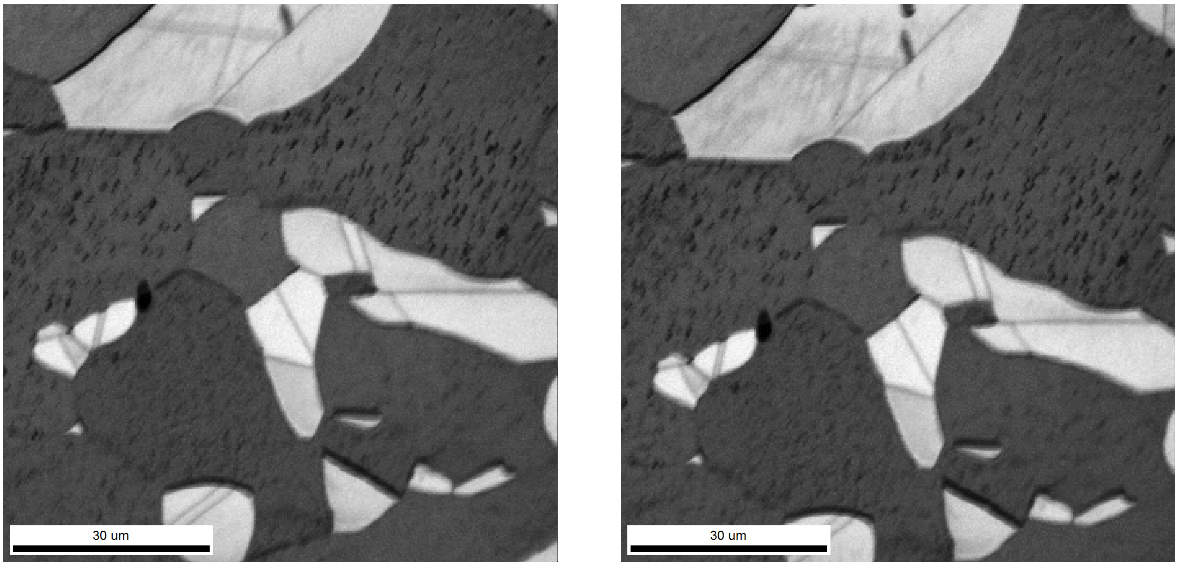

(c) IQ map acquired 190 min after heating

(d) IQ map acquired 220 min after heating

Figure E.21: IQ maps from Experiment 5: Temperature set at 640 °C in oven

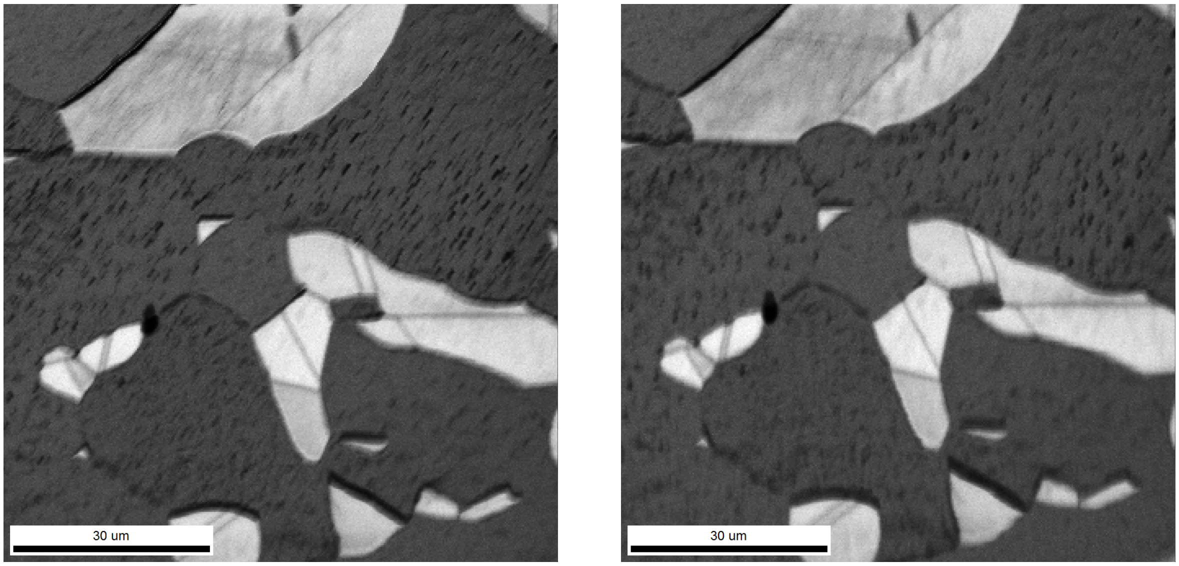

(a) IQ map acquired 250 min after heating (b) IQ map acquired 280 min after heating

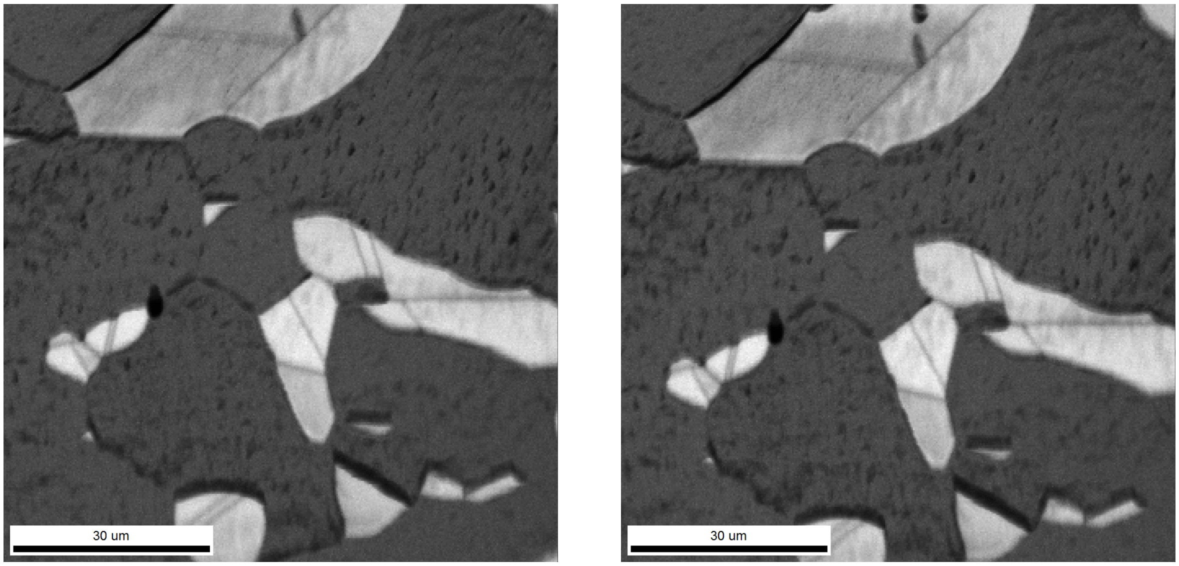

(c) IQ map acquired 310 min after heating (d) IQ map acquired 340 min after heating

Figure E.22: IQ maps from Experiment 5: Temperature set at 640 °C in oven

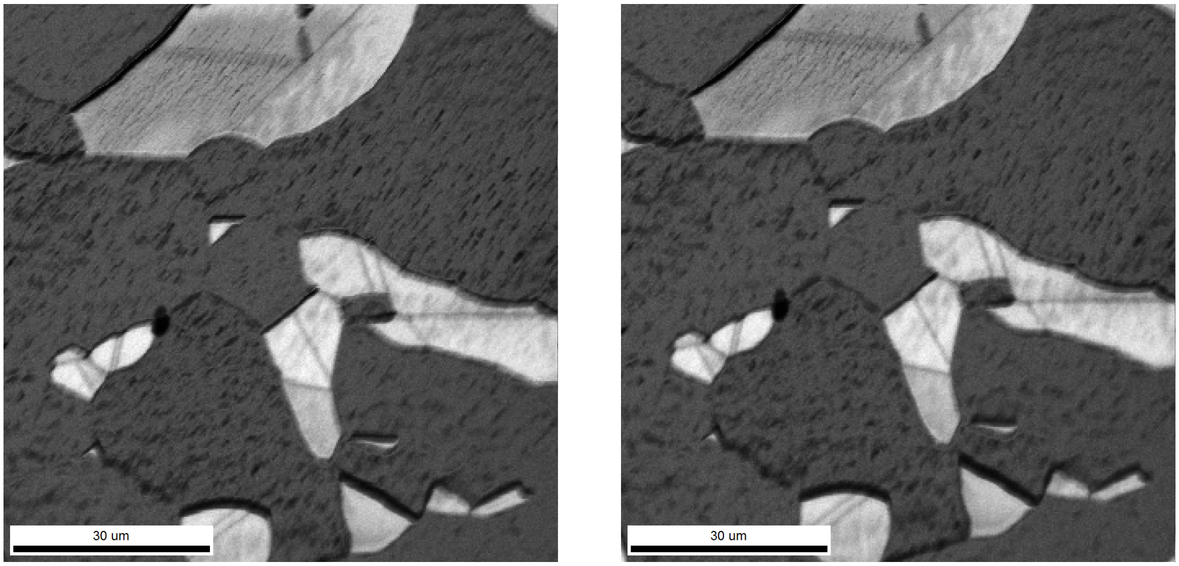

(a) IQ map acquired 370 min after heating (b) IQ map acquired 400 min after heating

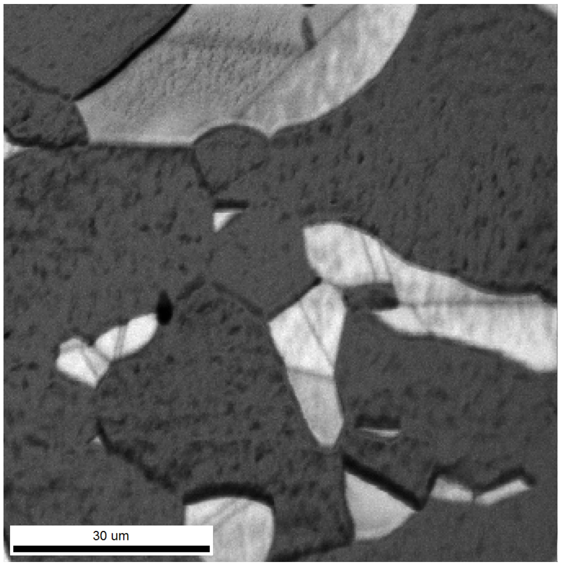

(c) IQ map acquired 430 min after heating

Figure E.23: IQ maps from Experiment 5: Temperature set at 640 °C in oven

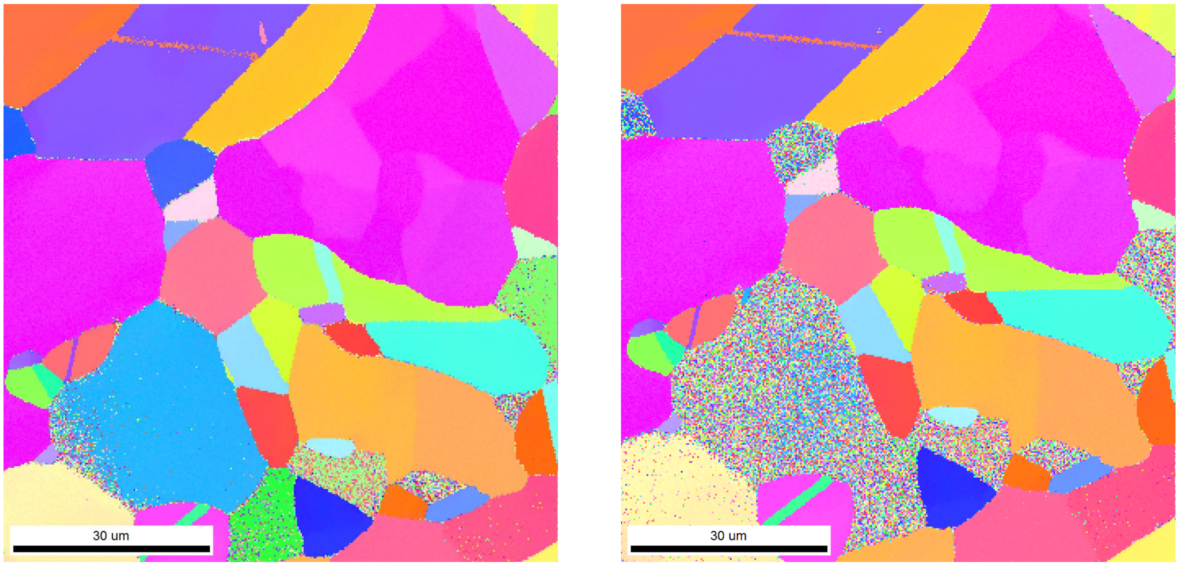

(a) IPF map acquired 10 min after heating

(b) IPF map acquired 40 min after heating

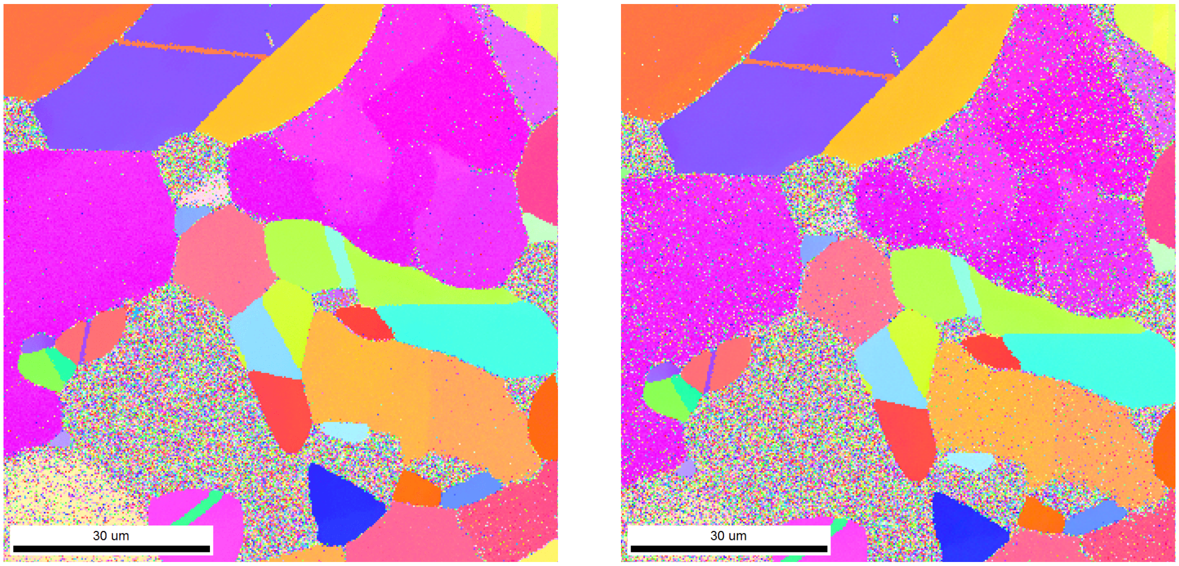

(c) IPF map acquired 70 min after heating

(d) IPF map acquired 100 min after heating

Figure E.24: IPF maps from Experiment 5: Temperature set at 640 °C in oven

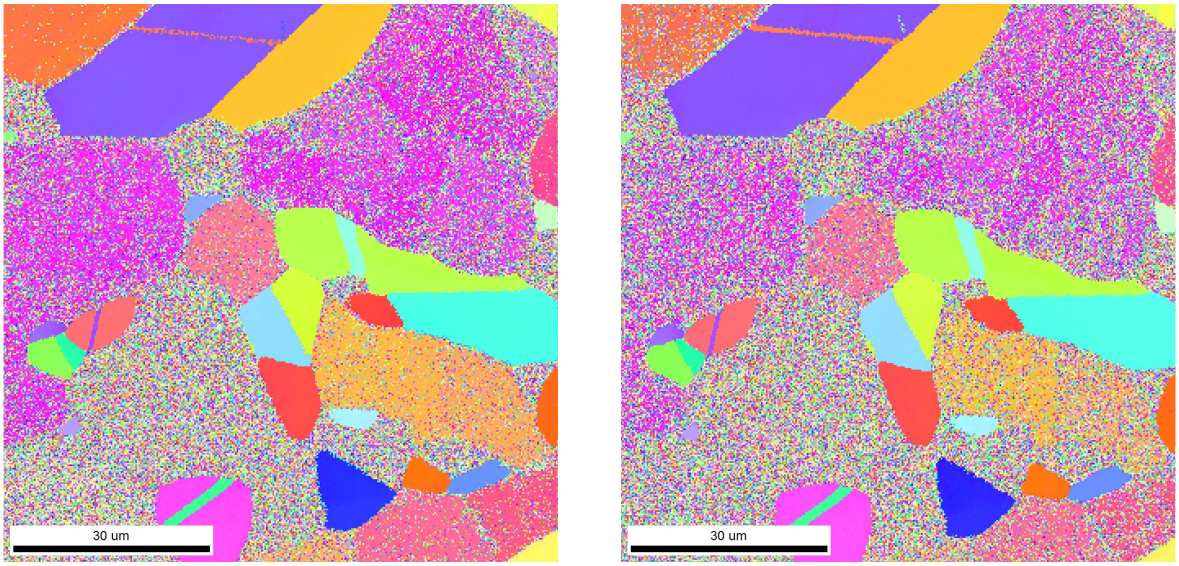

(a) IPF map acquired 130 min after heating (b) IPF map acquired 160 min after heating

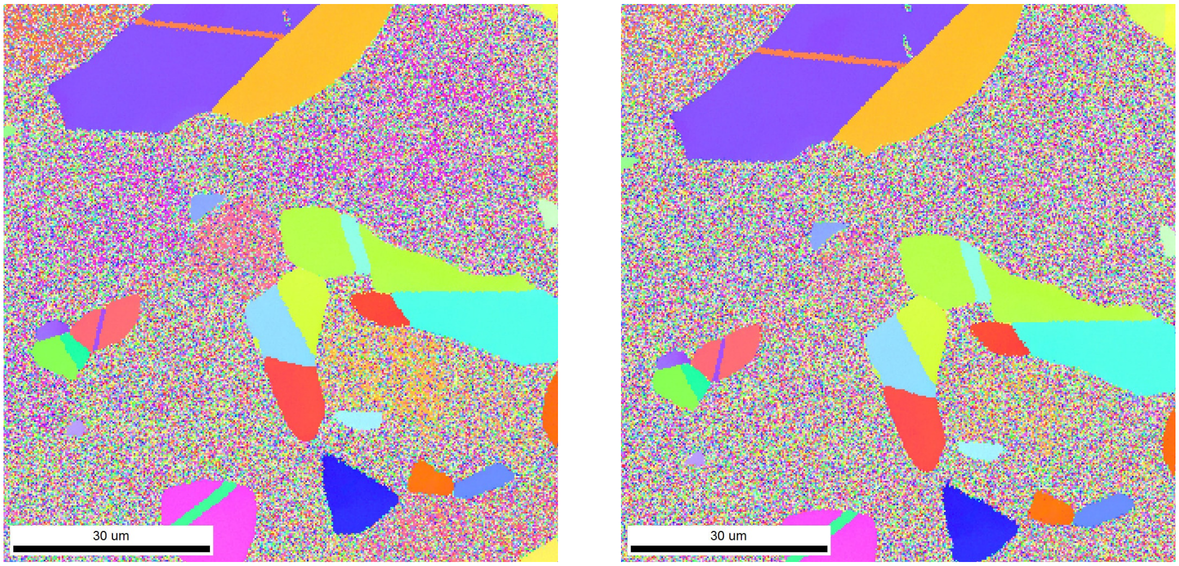

(c) IPF map acquired 190 min after heating (d) IPF map acquired 220 min after heating

Figure E.25: IPF maps from Experiment 5: Temperature set at 640 °C in oven

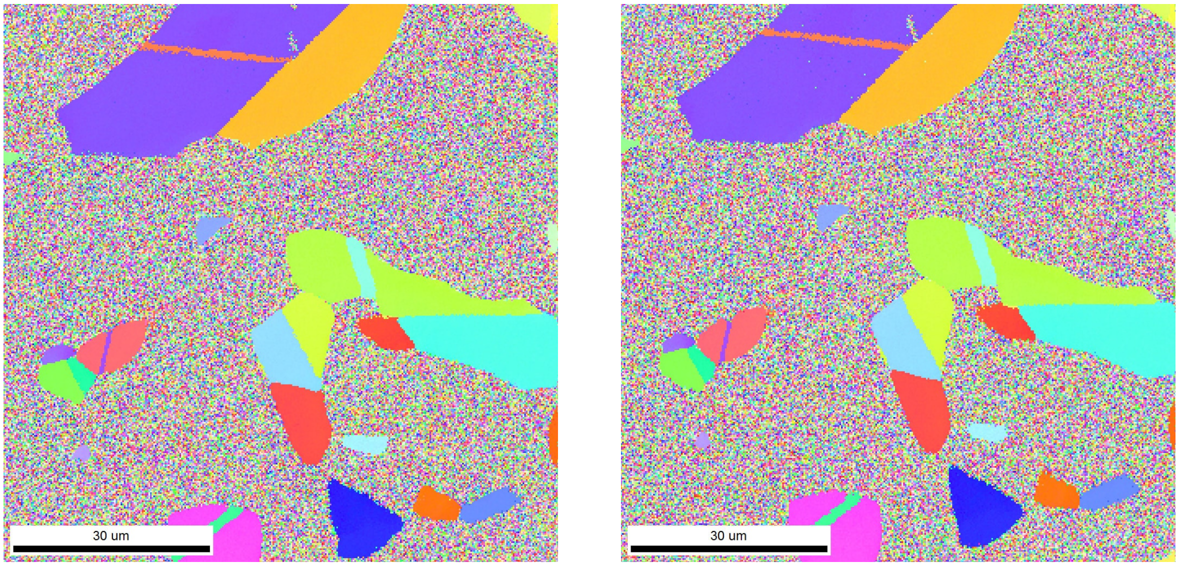

(a) IPF map acquired 250 min after heating (b) IPF map acquired 280 min after heating

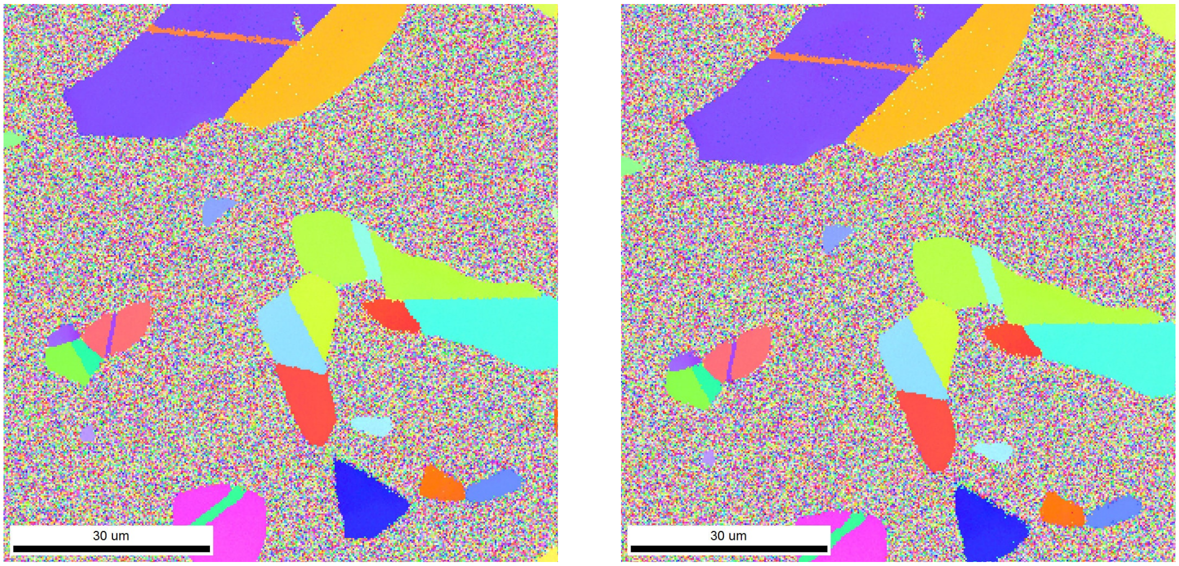

(c) IPF map acquired 310 min after heating (d) IPF map acquired 340 min after heating

Figure E.26: IPF maps from Experiment 5: Temperature set at 640 °C in oven

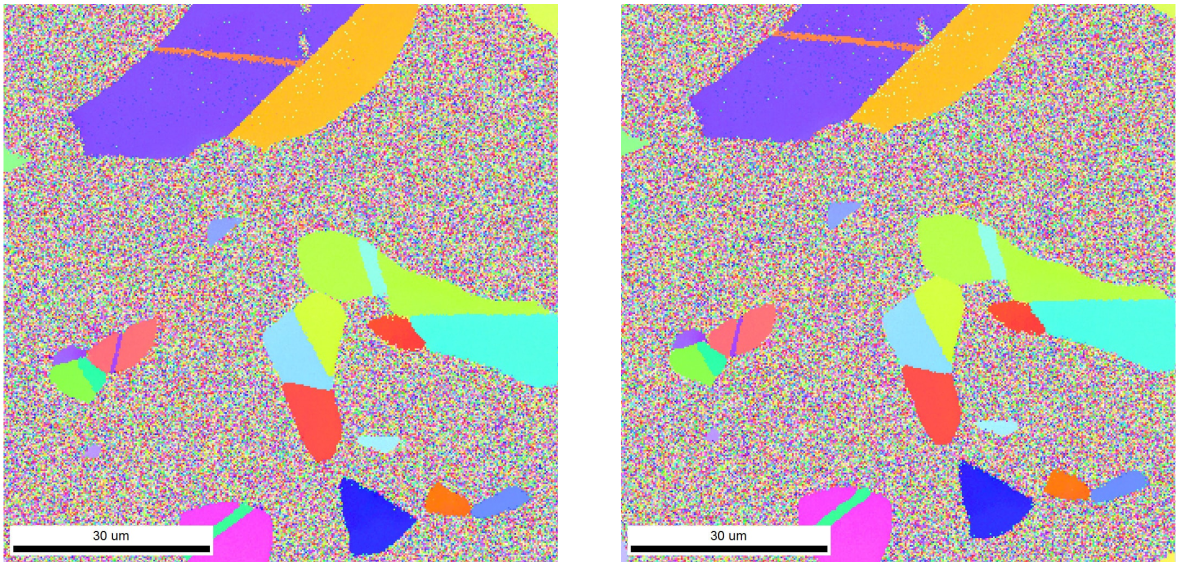

(a) IPF map acquired 370 min after heating

(b) IPF map acquired 400 min after heating

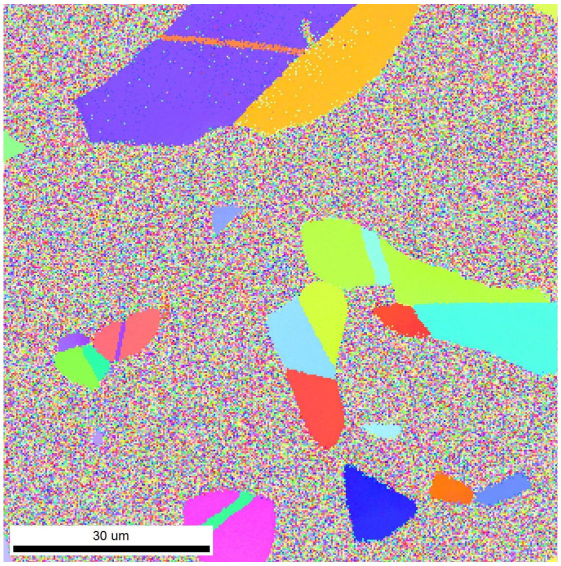

(c) IPF map acquired 430 min after heating

Figure E.27: IPF maps from Experiment 5: Temperature set at 640 °C in oven

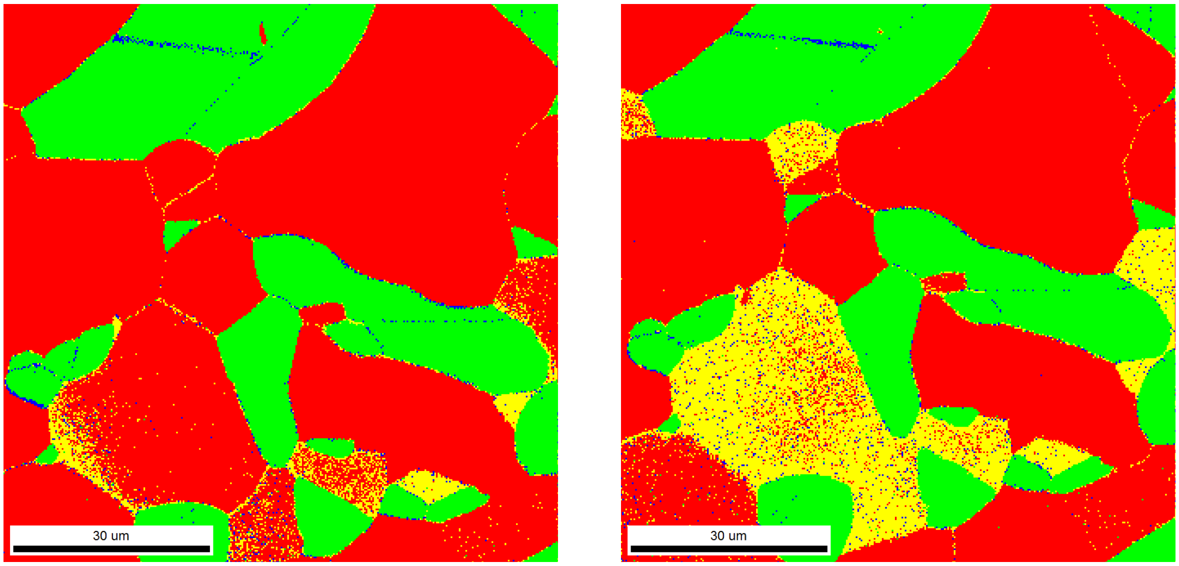

(a) Phase map acquired 10 min after heating (b) Phase map acquired 40 min after heating

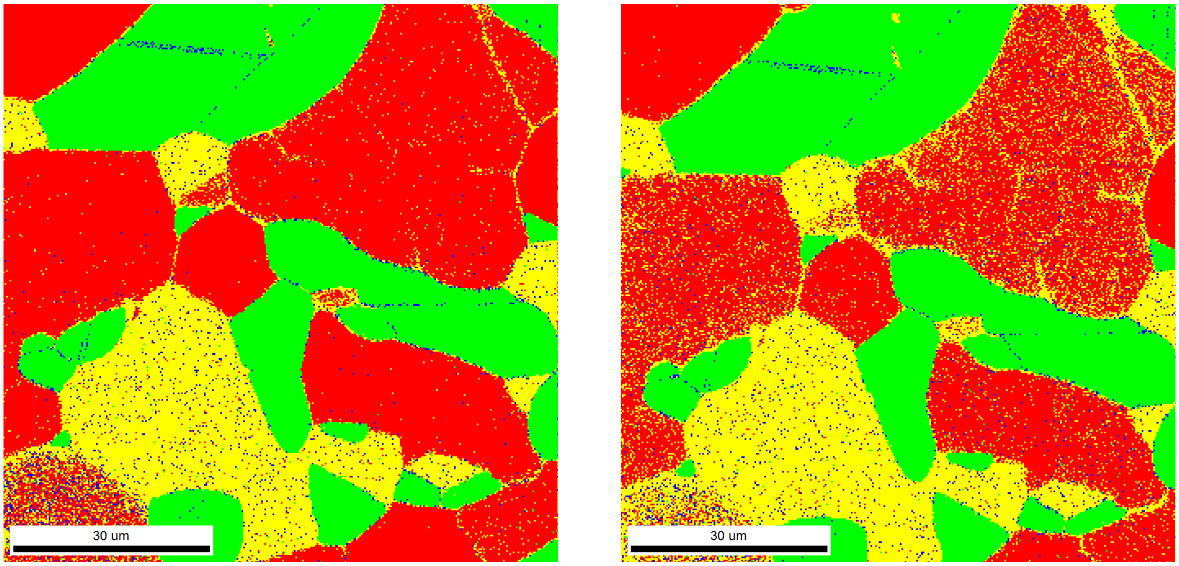

(c) Phase map acquired 70 min after heating (d) Phase map acquired 100 min after heating

Figure E.28: Phase maps from Experiment 5: Temperature set at 640 °C in oven

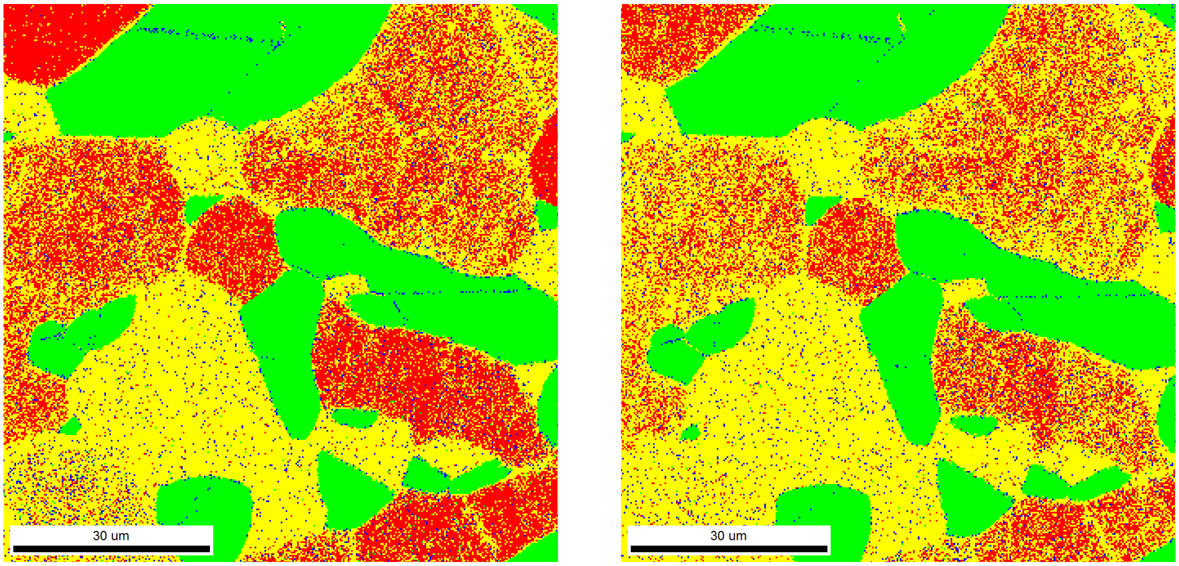

(a) Phase map acquired 130 min after heating

(b) Phase map acquired 160 min after heating

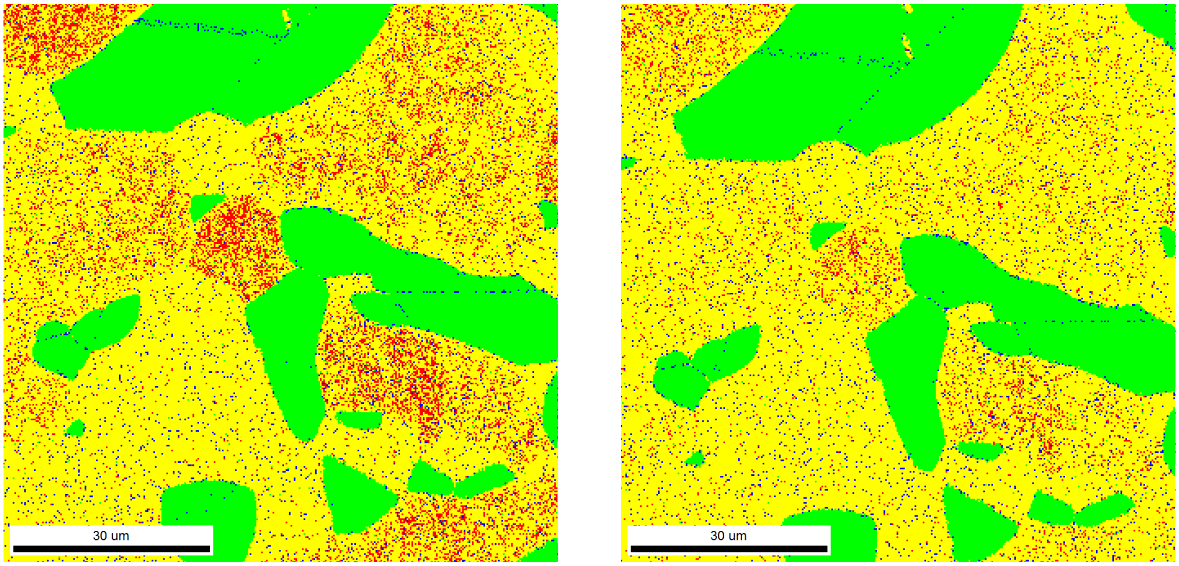

(c) Phase map acquired 190 min after heating

(d) Phase map acquired 220 min after heating

Figure E.29: Phase maps from Experiment 5: Temperature set at 640 °C in oven

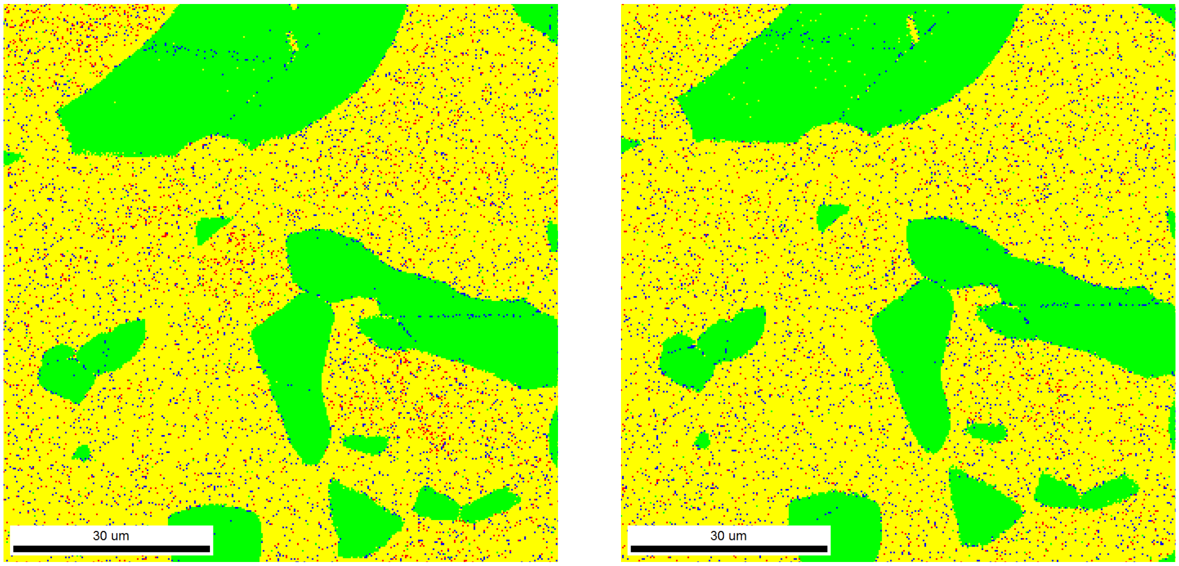

(a) Phase map acquired 250 min after heating

(b) Phase map acquired 280 min after heating

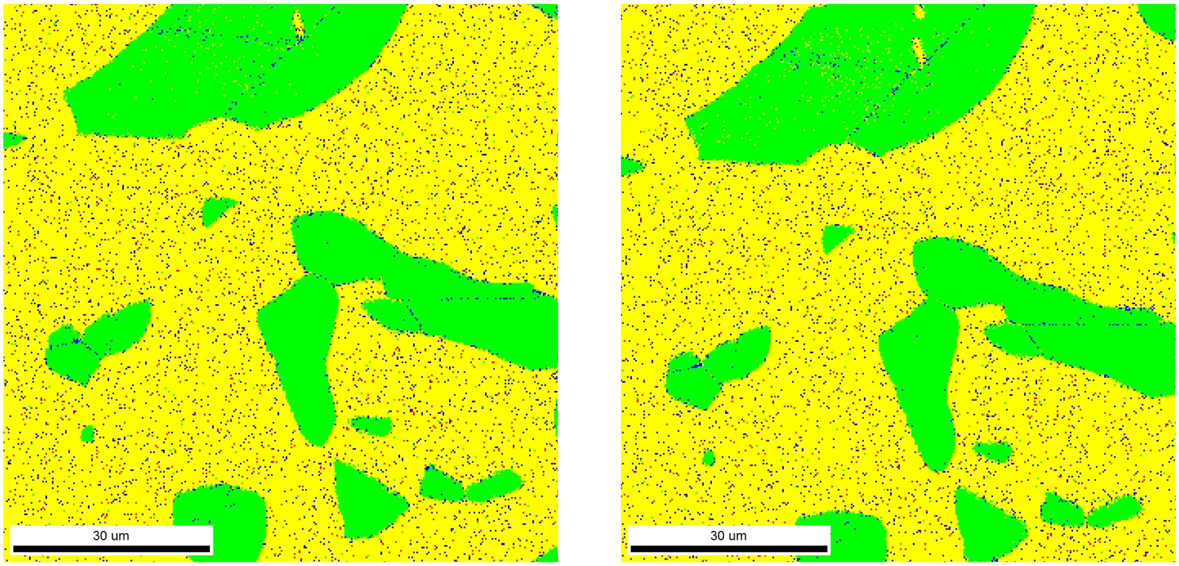

(c) Phase map acquired 310 min after heating

(d) Phase map acquired 340 min after heating

Figure E.30: Phase maps from Experiment 5: Temperature set at 640 °C in oven

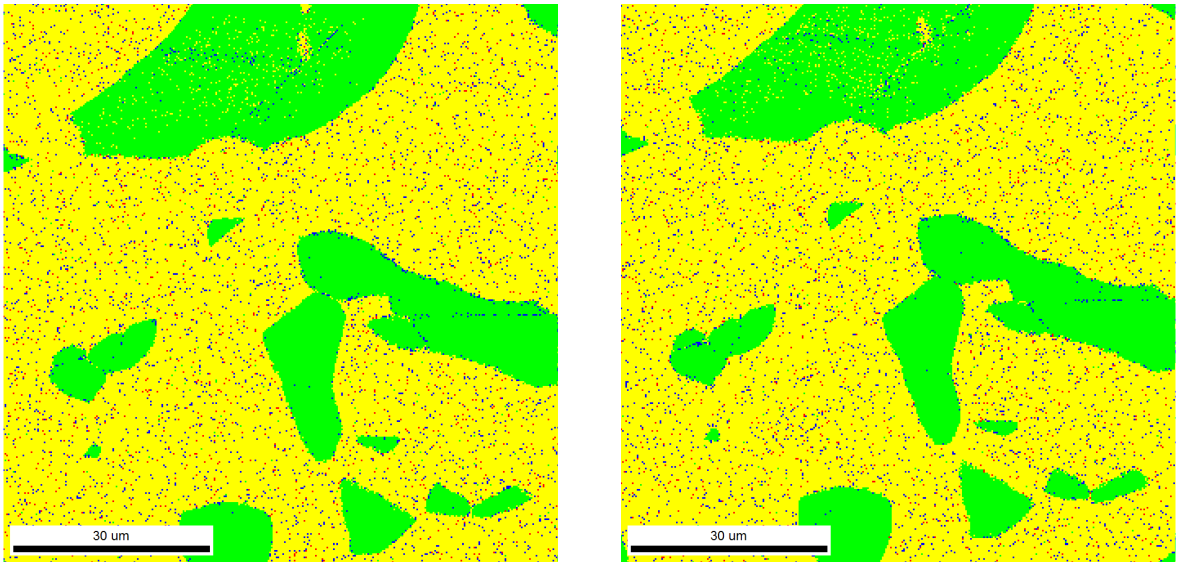

(a) Phase map acquired 370 min after heating (b) Phase map acquired 400 min after heating

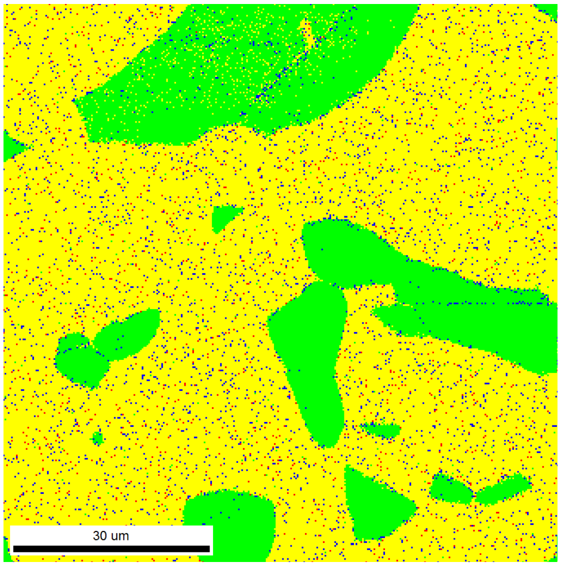

(c) Phase map acquired 430 min after heating

Figure E.31: Phase maps from Experiment 5: Temperature set at 640 °C in oven

E.7 Experiment 6, T = 625°C

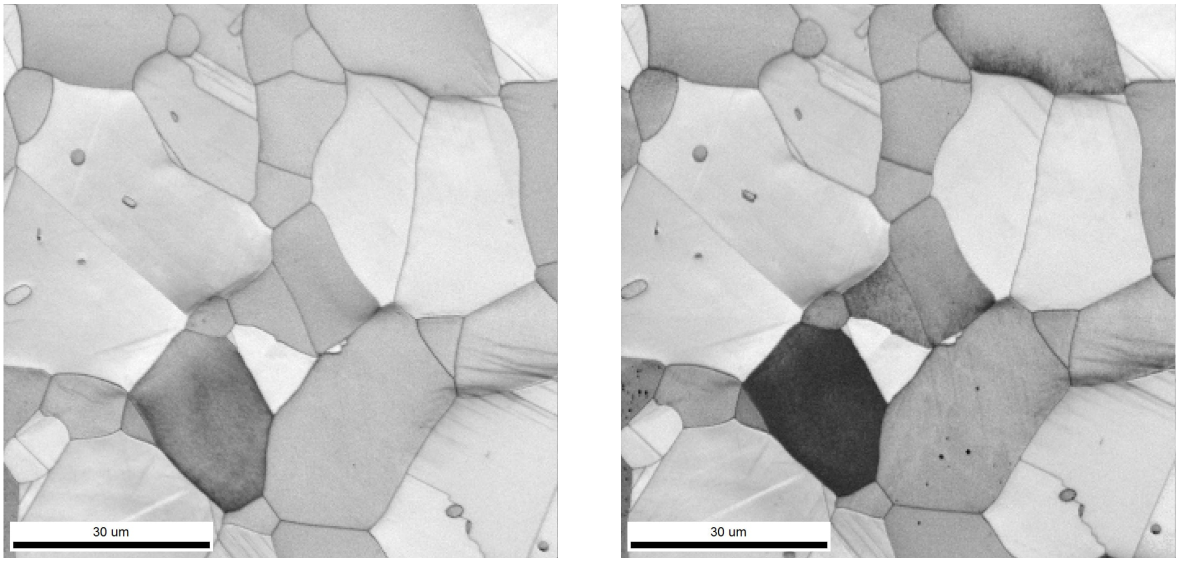

(a) IQ map acquired 10 min after heating (b) IQ map acquired 40 min after heating

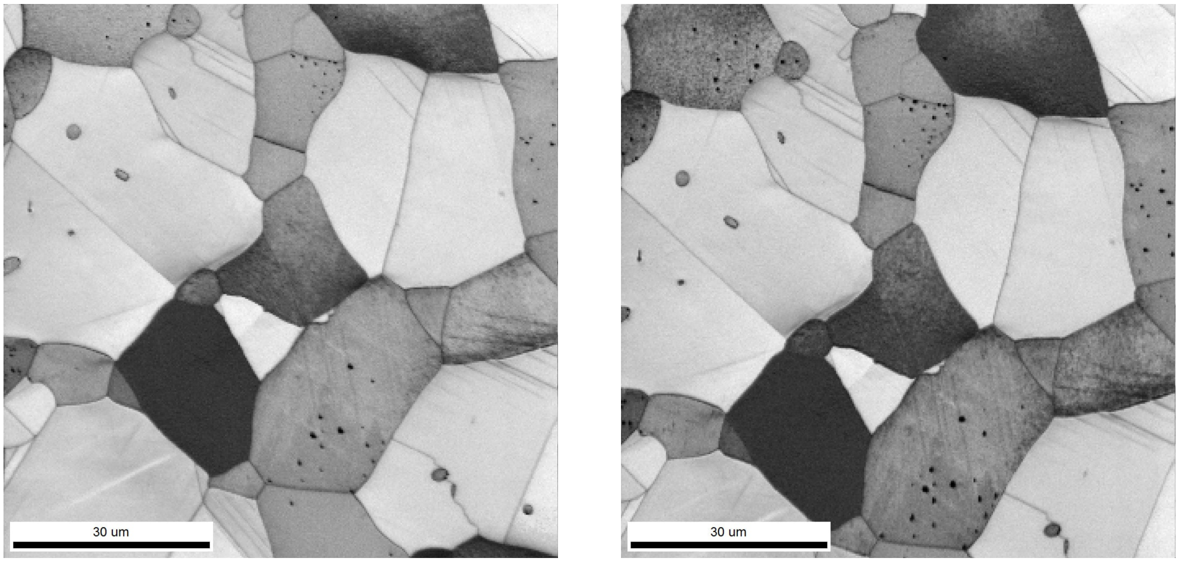

(c) IQ map acquired 70 min after heating (d) IQ map acquired 100 min after heating

Figure E.32: IQ maps from Experiment 6: Temperature set at 625 °C in oven

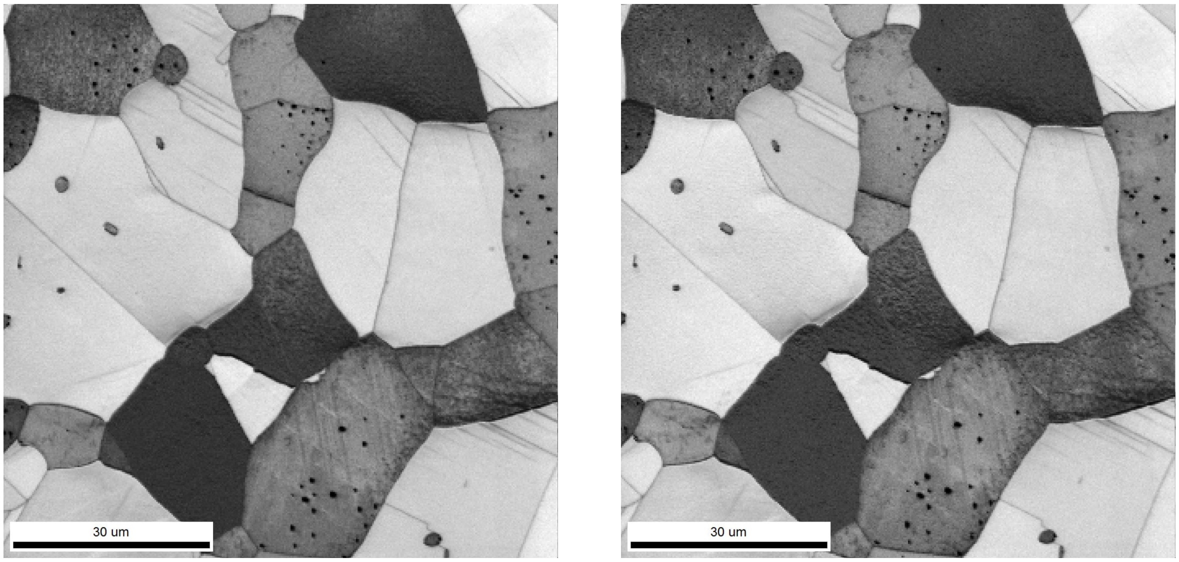

(a) IQ map acquired 130 min after heating (b) IQ map acquired 160 min after heating

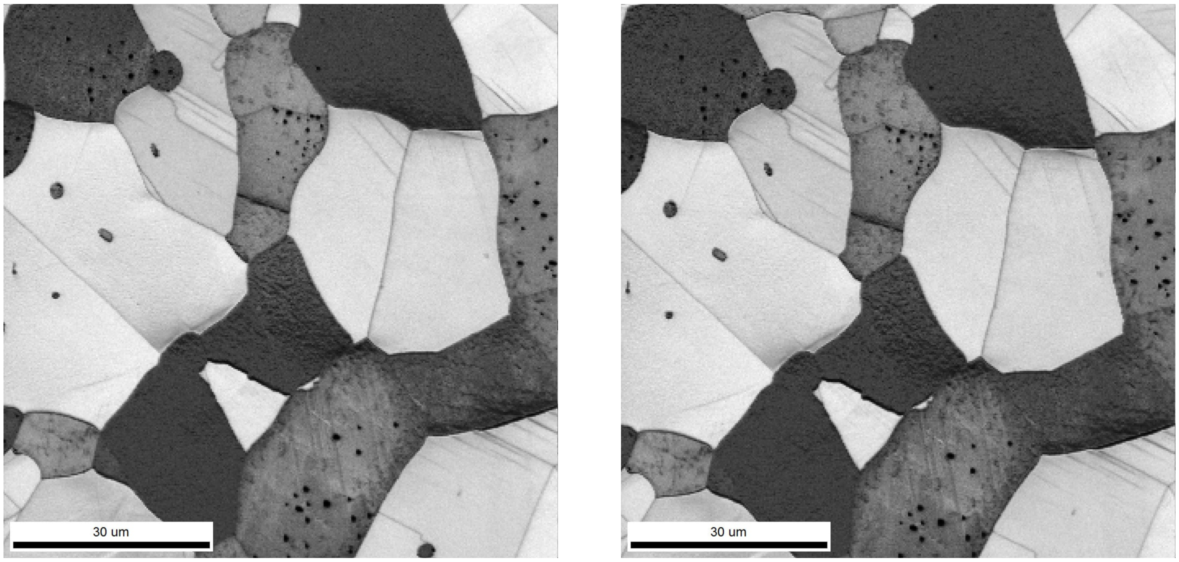

(c) IQ map acquired 190 min after heating (d) IQ map acquired 220 min after heating

Figure E.33: IQ maps from Experiment 6: Temperature set at 625 °C in oven

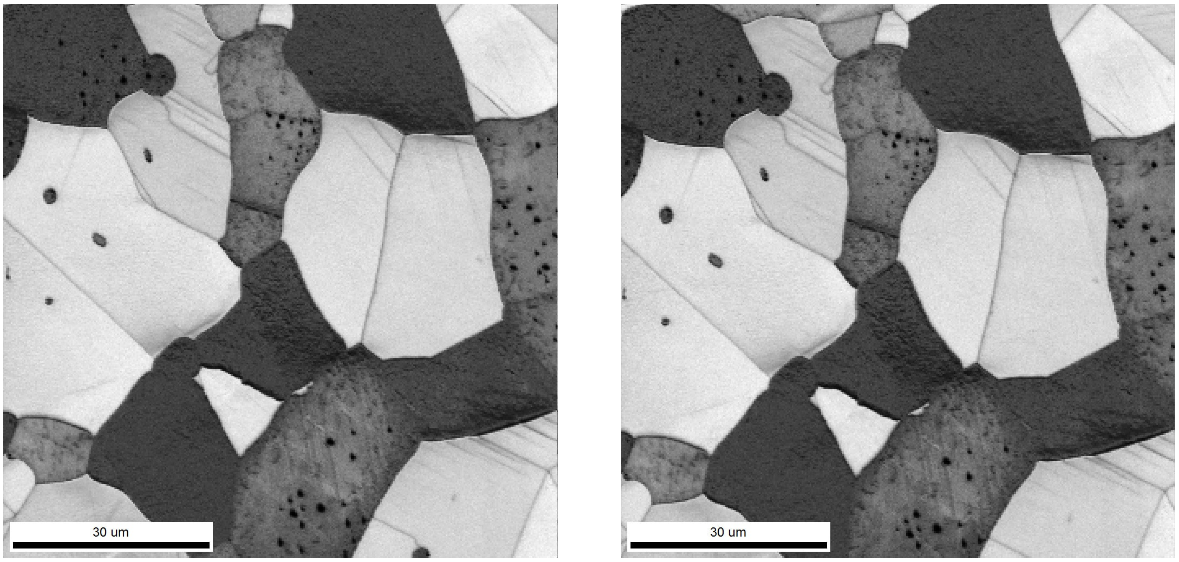

(a) IQ map acquired 250 min after heating

(b) IQ map acquired 280 min after heating

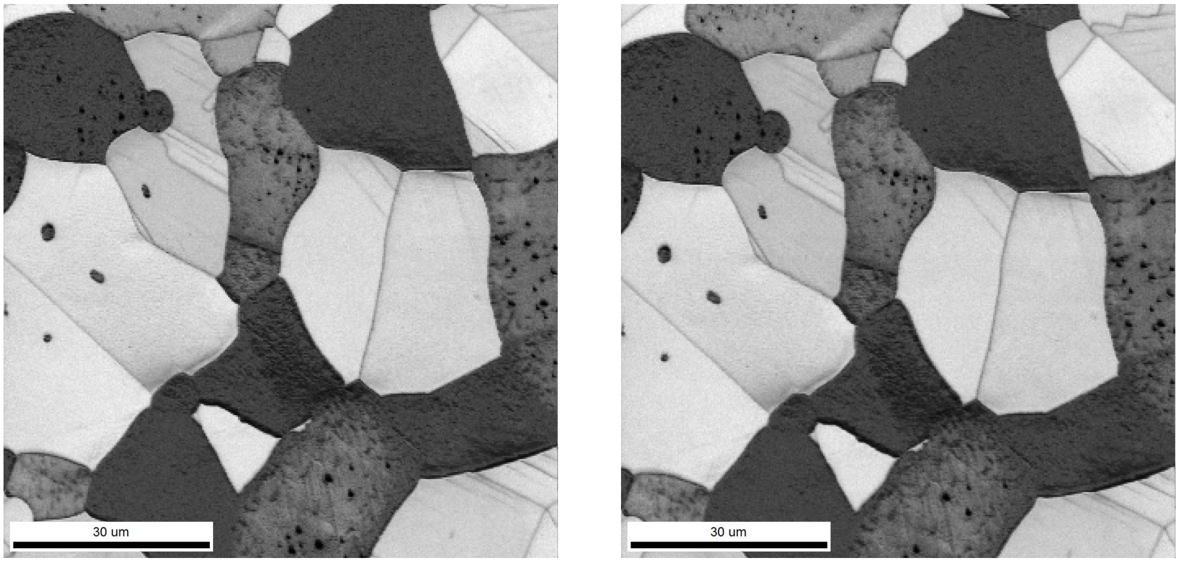

(c) IQ map acquired 310 min after heating

(d) IQ map acquired 340 min after heating

Figure E.34: IQ maps from Experiment 6: Temperature set at 625 °C in oven

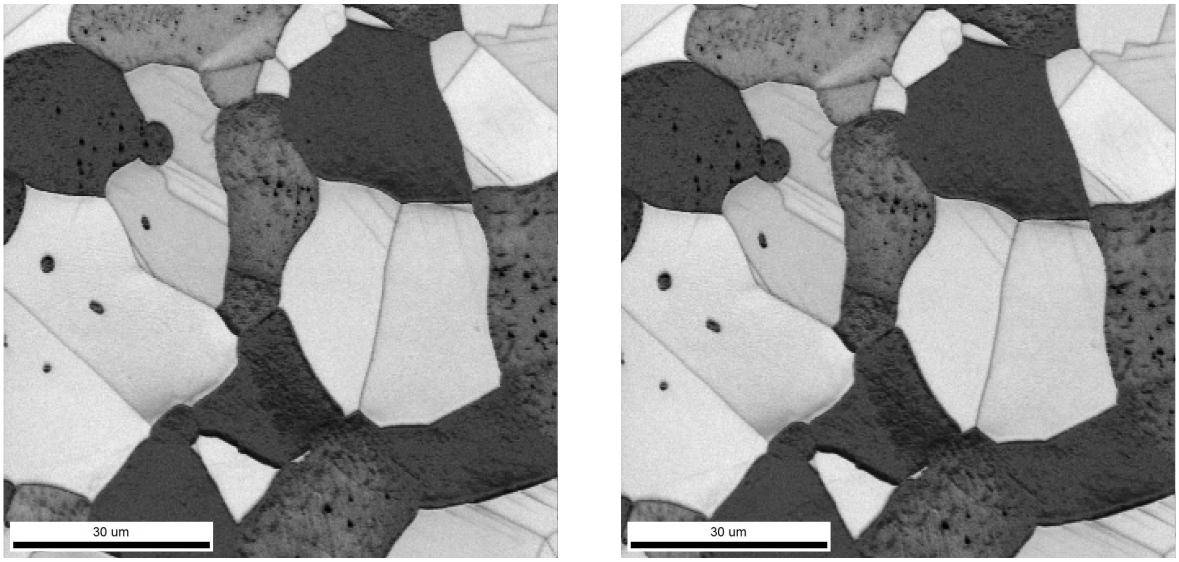

(a) IQ map acquired 370 min after heating (b) IQ map acquired 400 min after heating

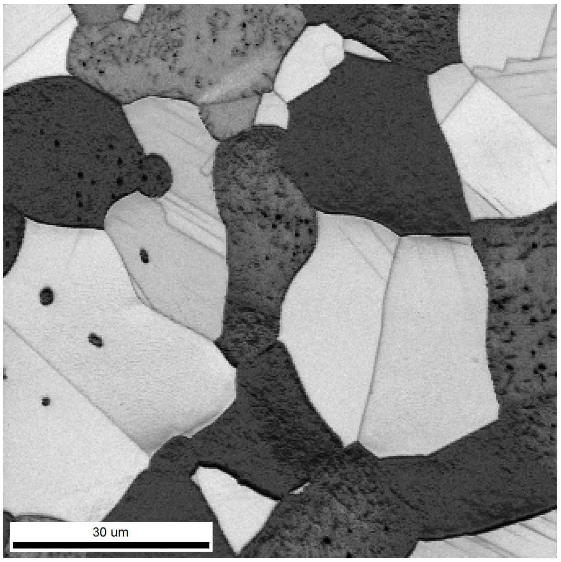

(c) IQ map acquired 430 min after heating

Figure E.35: IQ maps from Experiment 6: Temperature set at 625 °C in oven

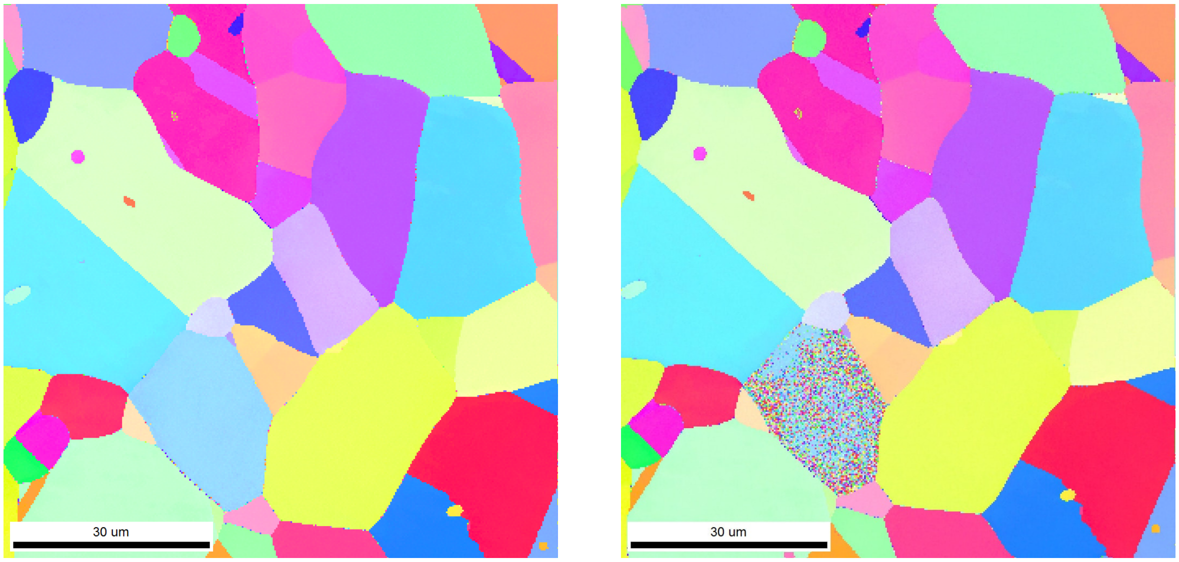

(a) IPF map acquired 10 min after heating (b) IPF map acquired 40 min after heating

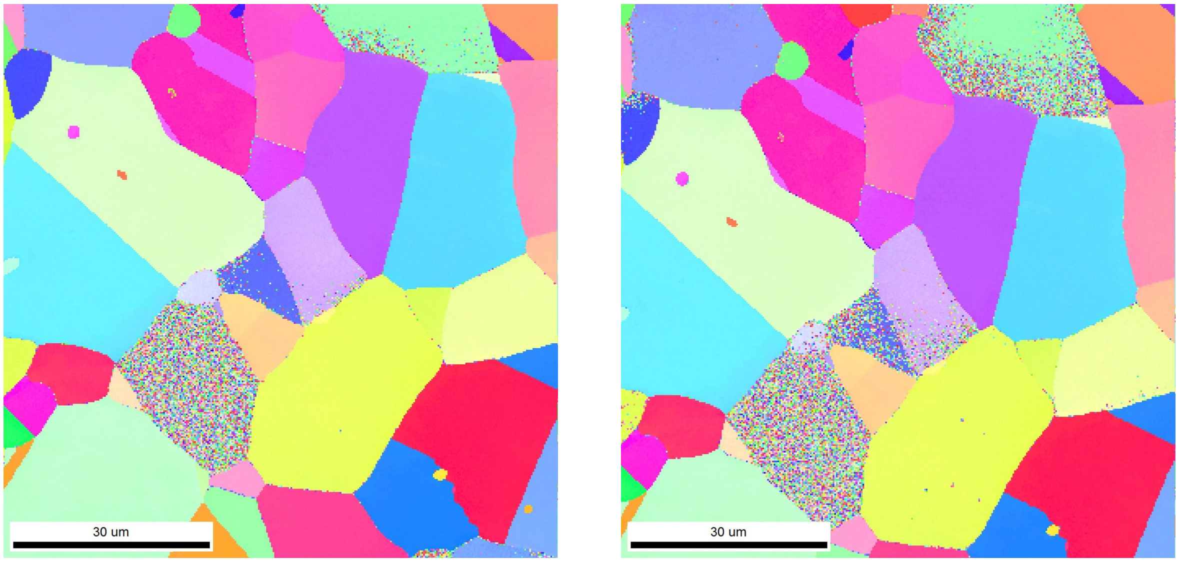

(c) IPF map acquired 70 min after heating (d) IPF map acquired 100 min after heating

Figure E.36: IPF maps from Experiment 6: Temperature set at 625 °C in oven

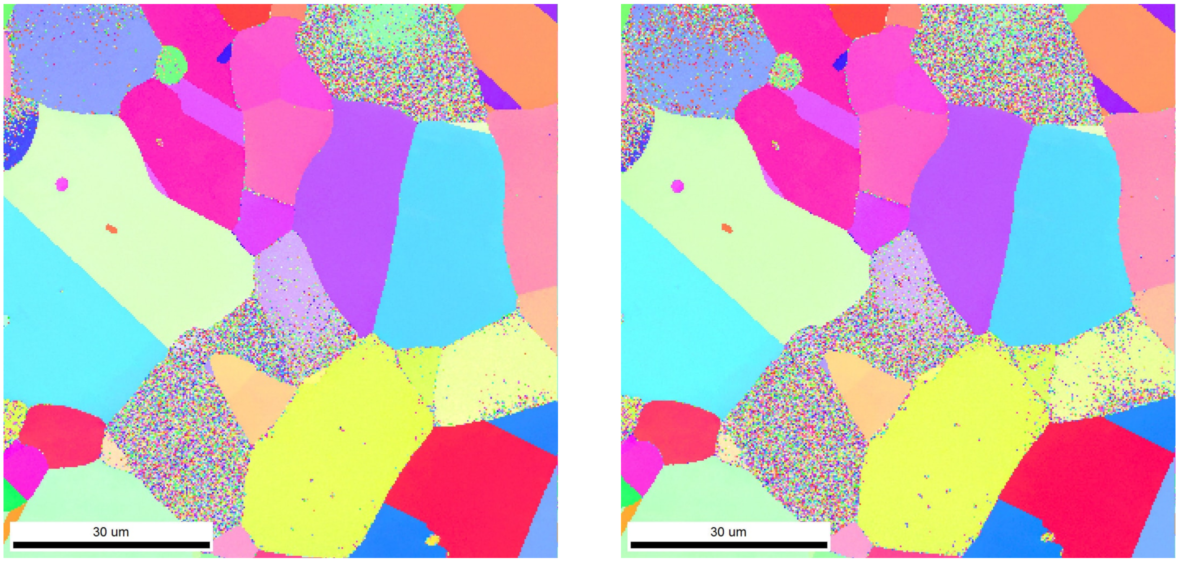

(a) IPF map acquired 130 min after heating (b) IPF map acquired 160 min after heating

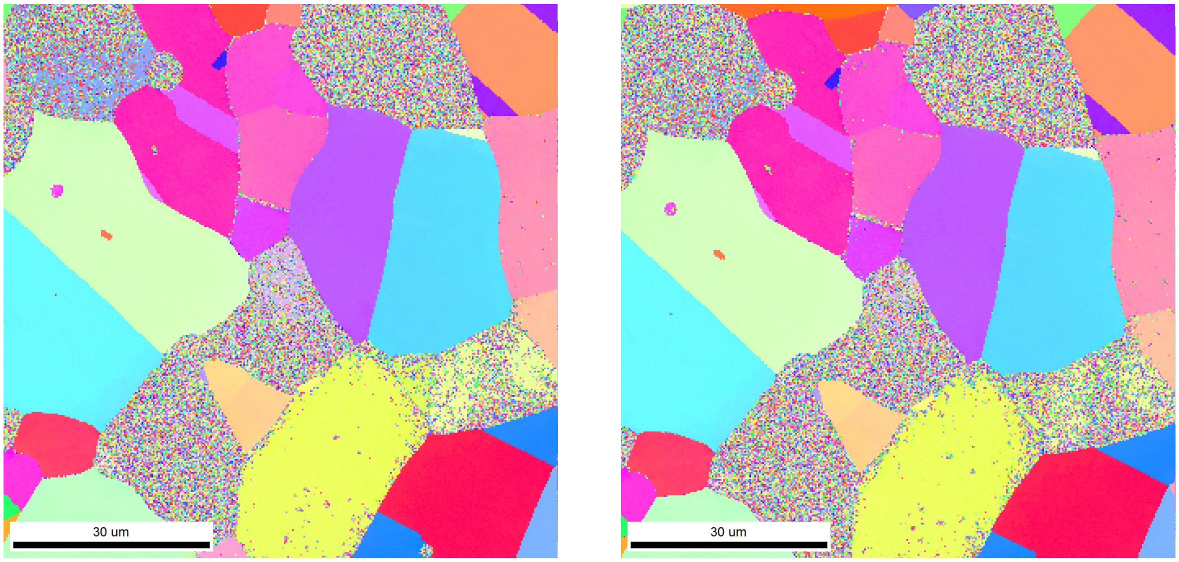

(c) IPF map acquired 190 min after heating (d) IPF map acquired 220 min after heating

Figure E.37: IPF maps from Experiment 6: Temperature set at 625 °C in oven

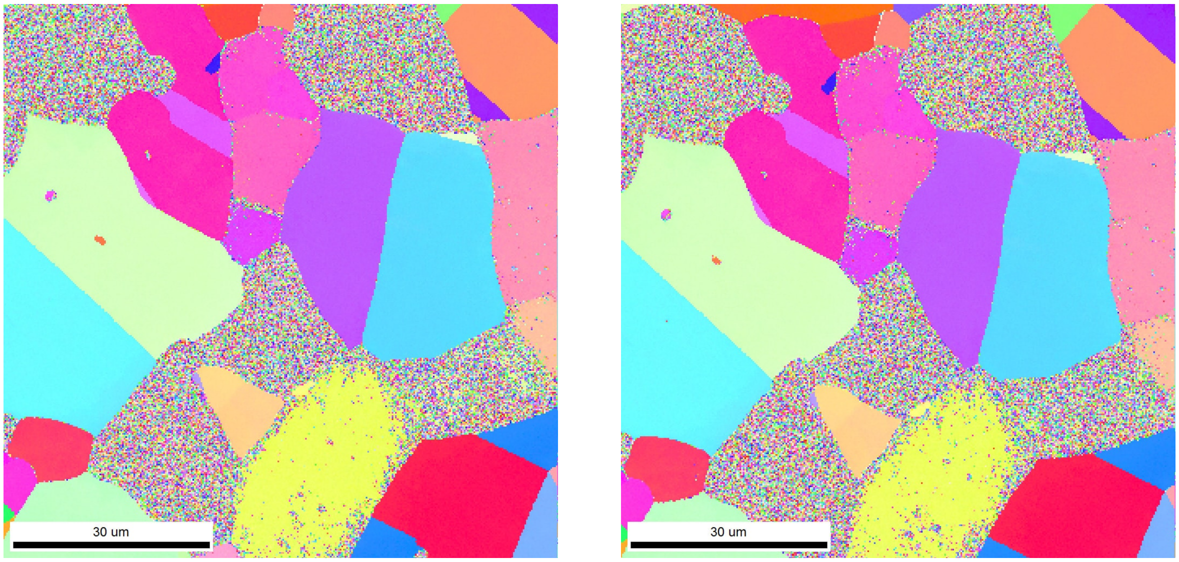

(a) IPF map acquired 250 min after heating (b) IPF map acquired 280 min after heating

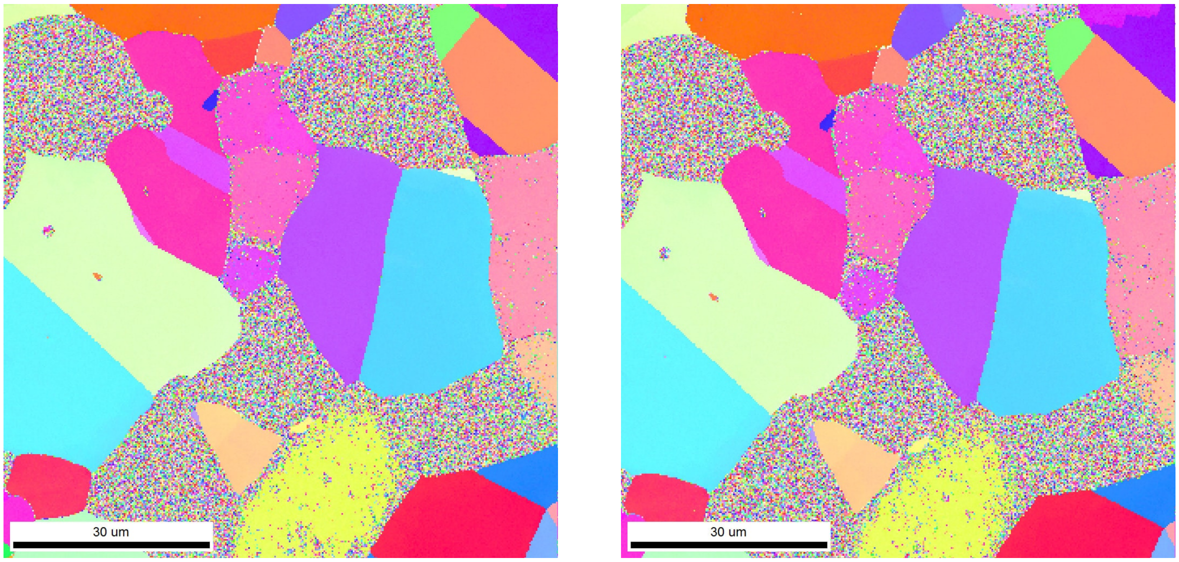

(c) IPF map acquired 310 min after heating (d) IPF map acquired 340 min after heating

Figure E.38: IPF maps from Experiment 6: Temperature set at 625 °C in oven

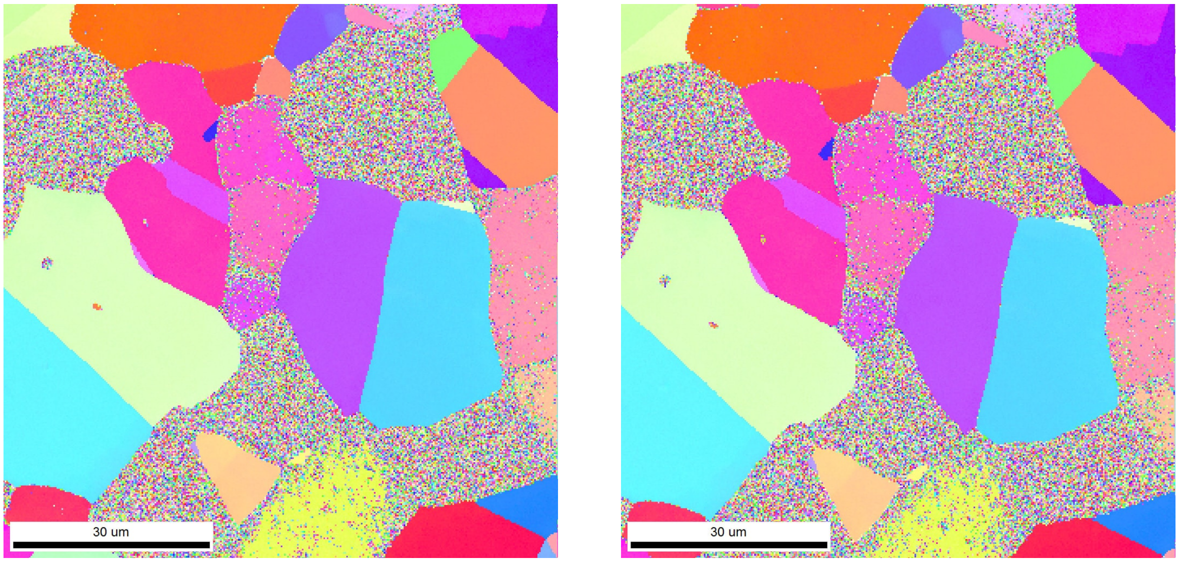

(a) IPF map acquired 370 min after heating

(b) IPF map acquired 400 min after heating

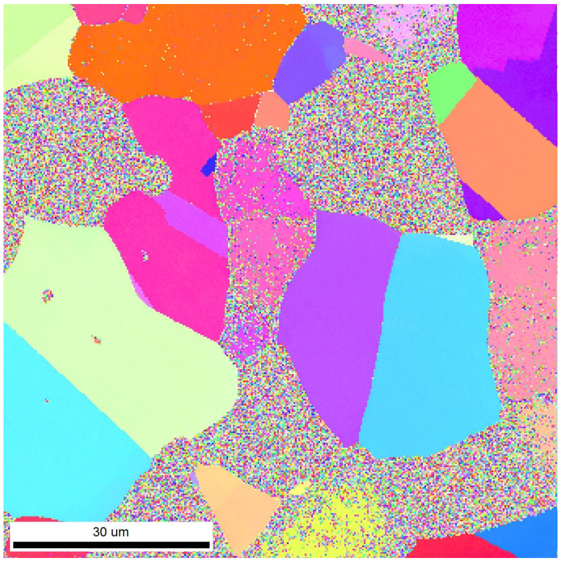

(c) IPF map acquired 430 min after heating

Figure E.39: IPF maps from Experiment 6: Temperature set at 625 °C in oven

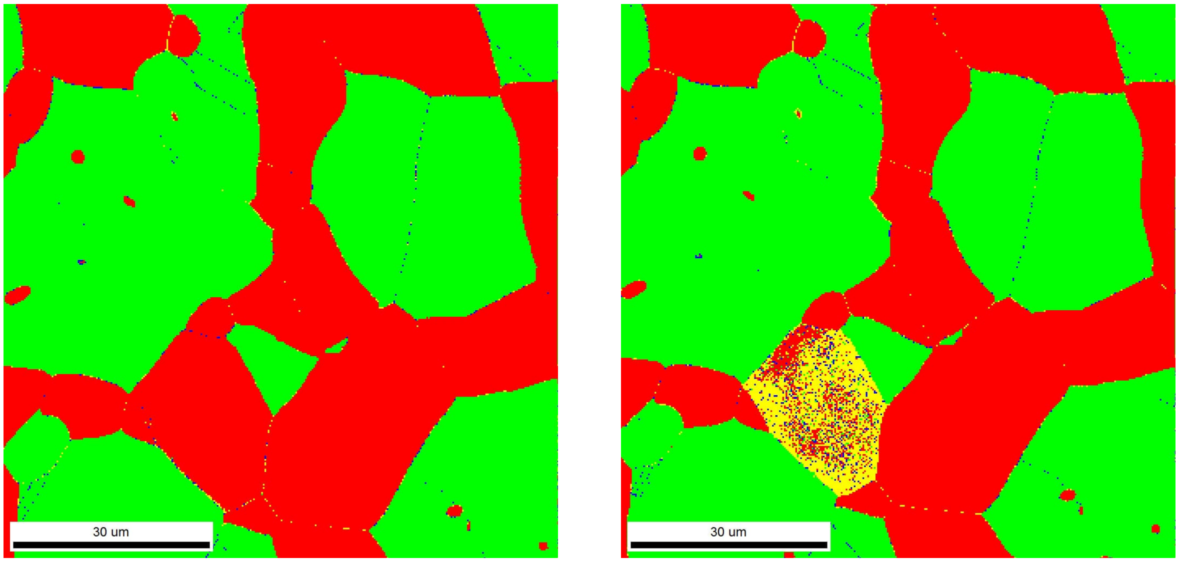

(a) Phase map acquired 10 min after heating (b) Phase map acquired 40 min after heating

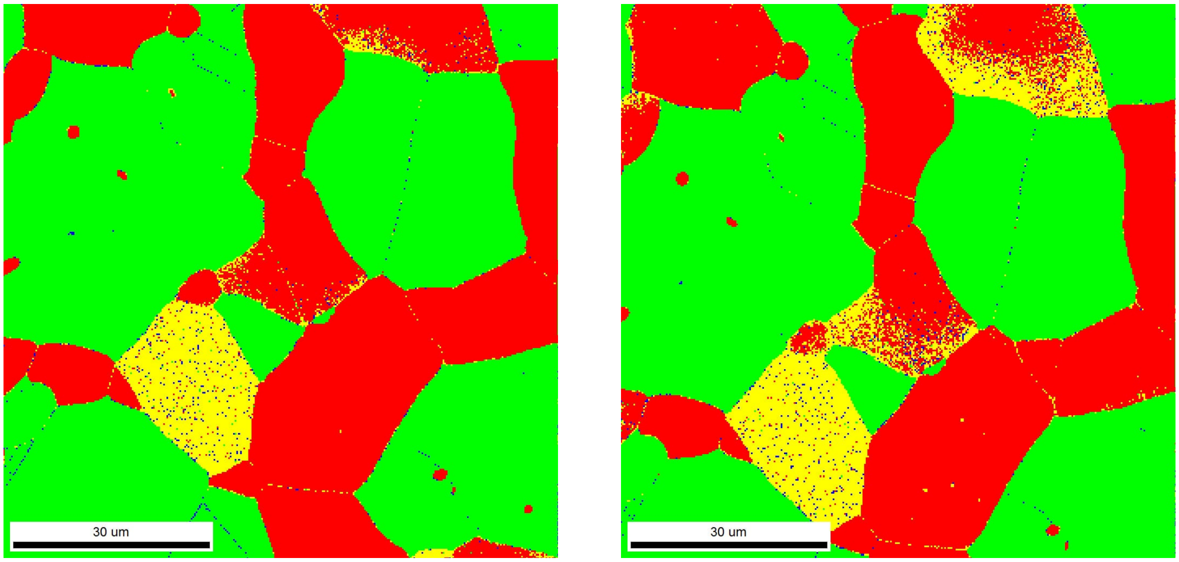

(c) Phase map acquired 70 min after heating (d) Phase map acquired 100 min after heating

Figure E.40: Phase maps from Experiment 6: Temperature set at 625 °C in oven

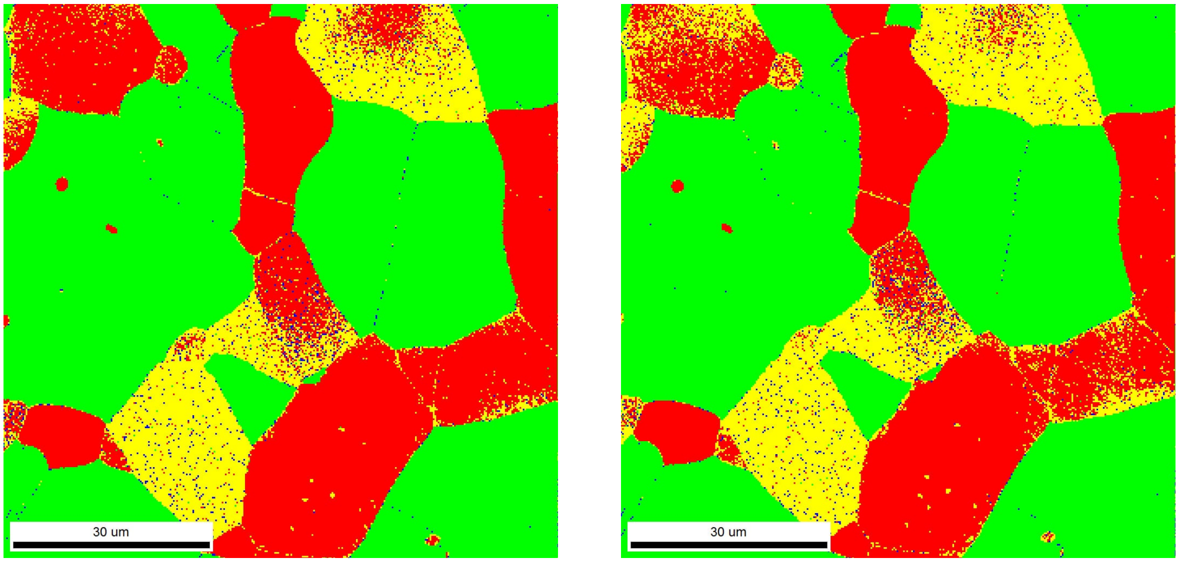

(a) Phase map acquired 130 min after heating (b) Phase map acquired 160 min after heating

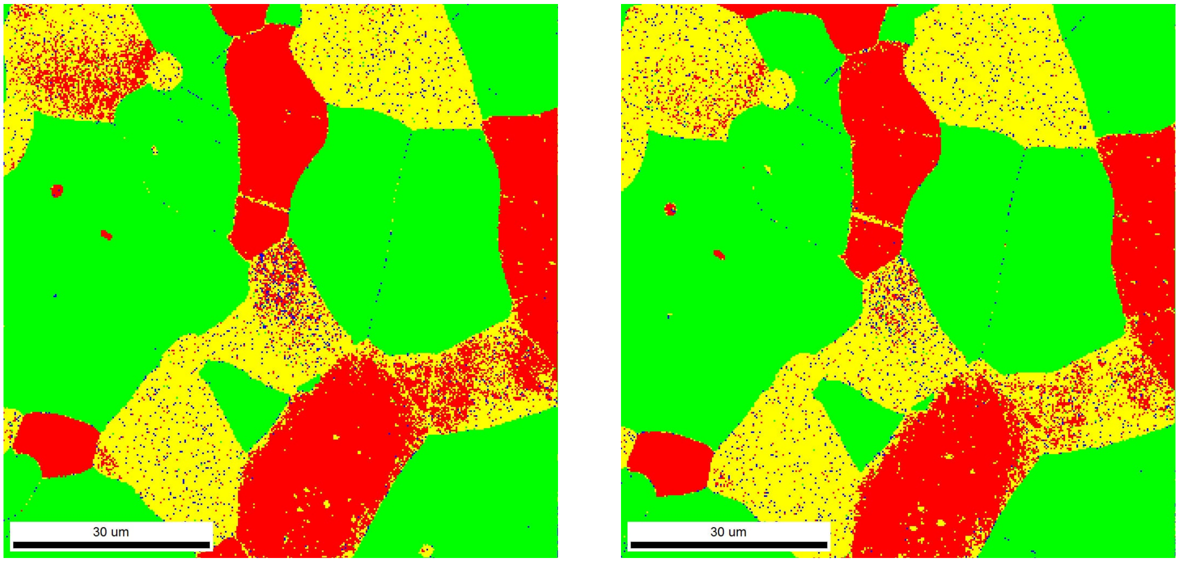

(c) Phase map acquired 190 min after heating (d) Phase map acquired 220 min after heating

Figure E.41: Phase maps from Experiment 6: Temperature set at 625 °C in oven

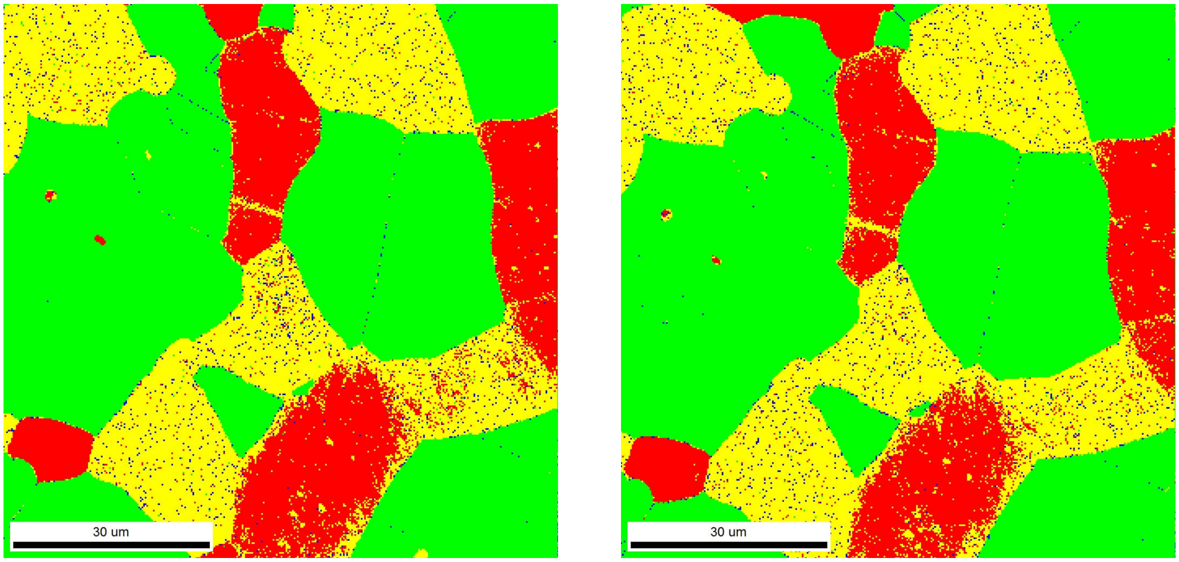

(a) Phase map acquired 250 min after heating (b) Phase map acquired 280 min after heating

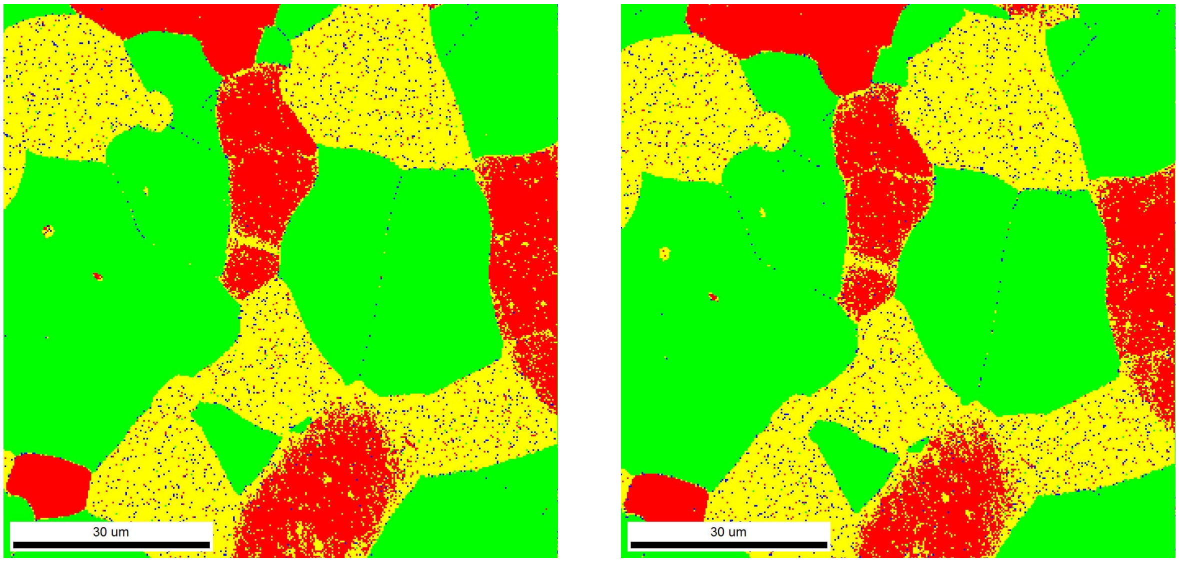

(c) Phase map acquired 310 min after heating (d) Phase map acquired 340 min after heating

Figure E.42: Phase maps from Experiment 6: Temperature set at 625 °C in oven

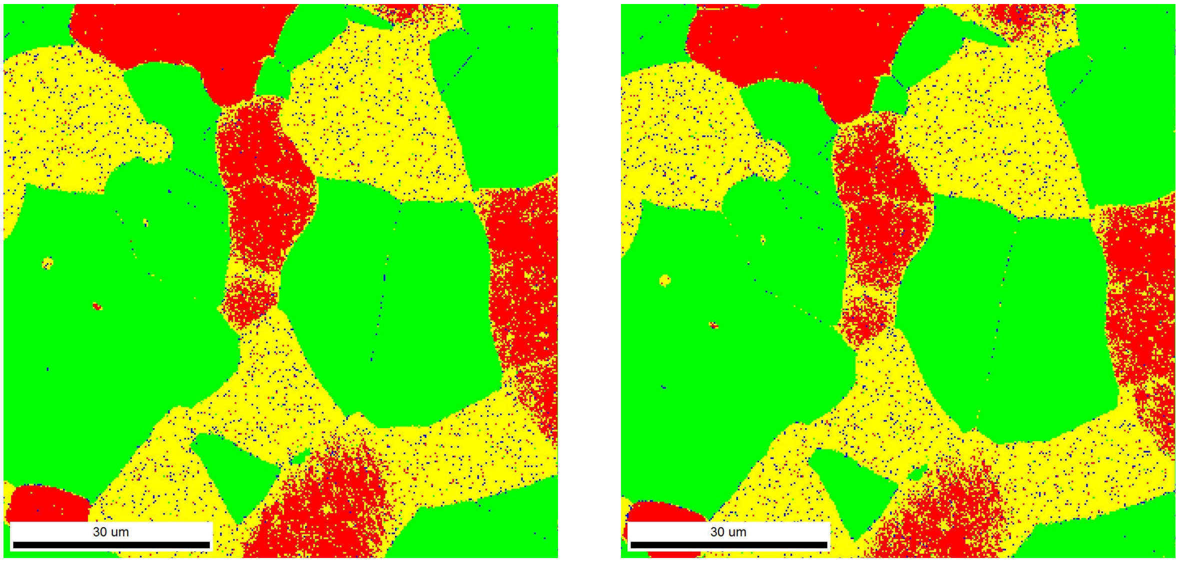

(a) Phase map acquired 370 min after heating

(b) Phase map acquired 400 min after heating

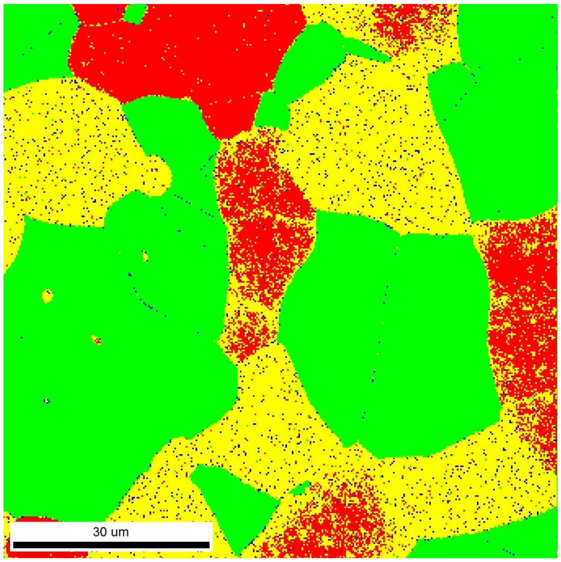

(c) Phase map acquired 430 min after heating

Figure E.43: Phase maps from Experiment 6: Temperature set at 625 °C in oven

E.8 Experiment 7, T = 750°C

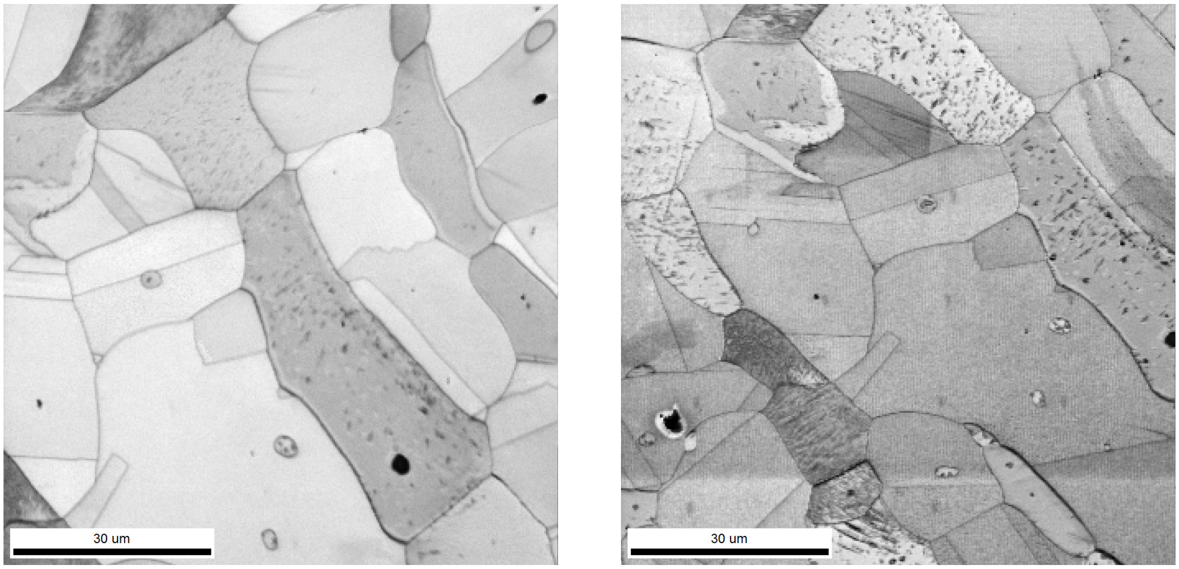

(a) IQ map acquired 10 min after heating

(b) IQ map acquired 40 min after heating

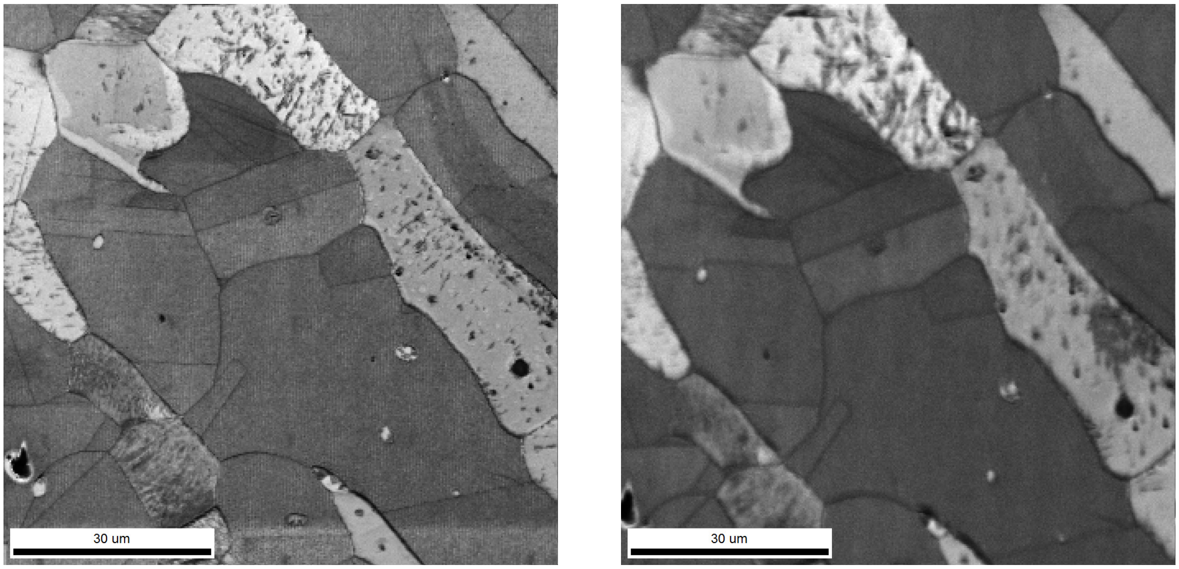

(c) IQ map acquired 70 min after heating

(d) IQ map acquired 100 min after heating

Figure E.44: IQ maps from Experiment 7: Temperature set at 750 °C in oven

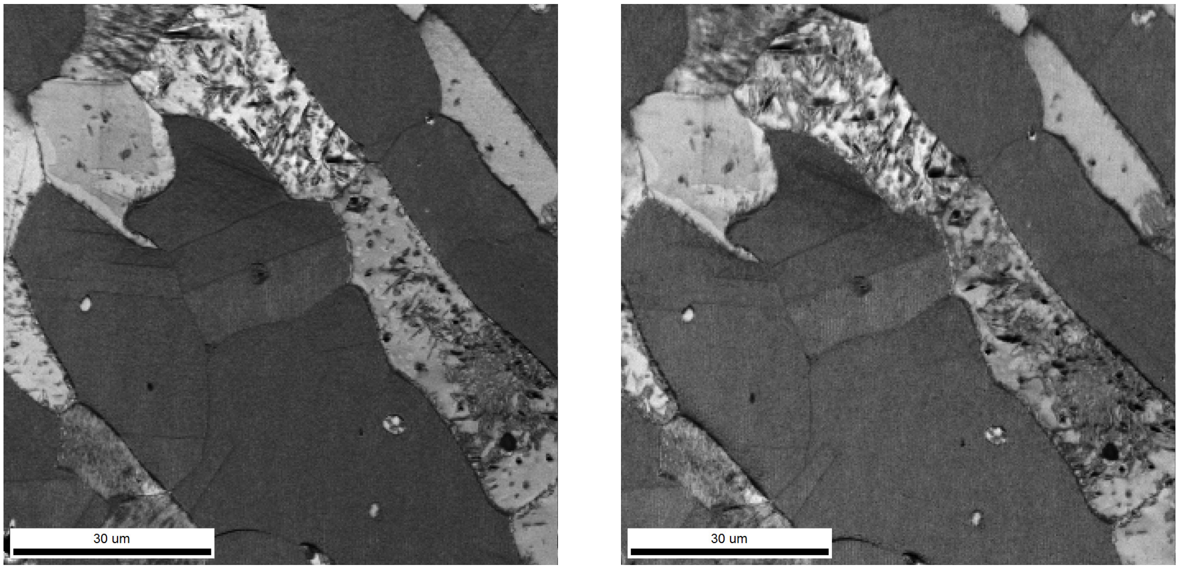

(a) IQ map acquired 130 min after heating

(b) IQ map acquired 160 min after heating

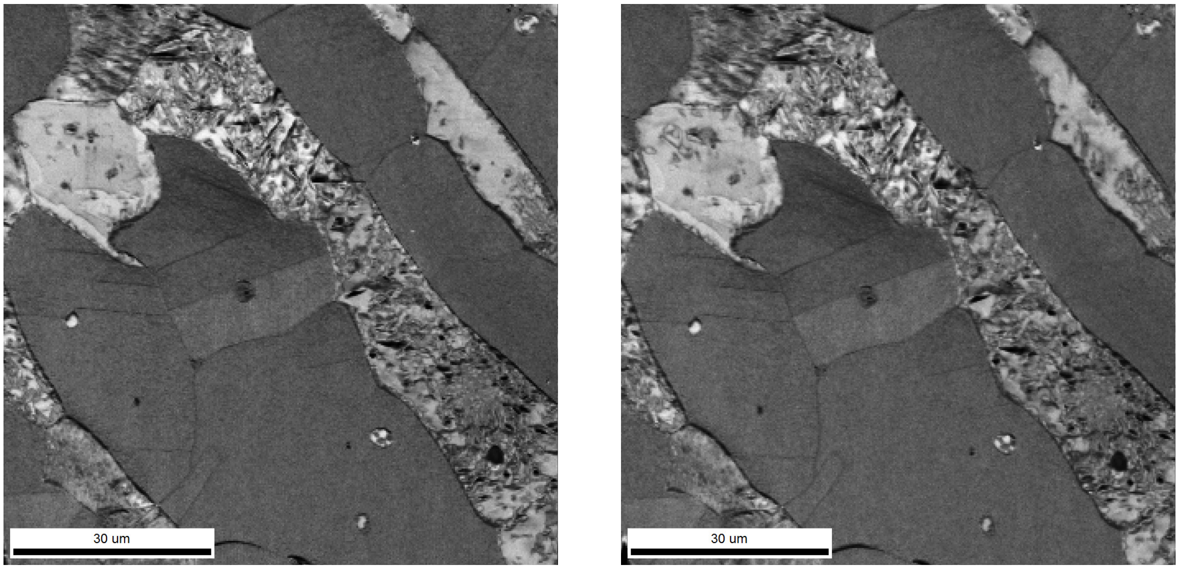

(c) IQ map acquired 190 min after heating

(d) IQ map acquired 220 min after heating

Figure E.45: IQ maps from Experiment 7: Temperature set at 750 °C in oven

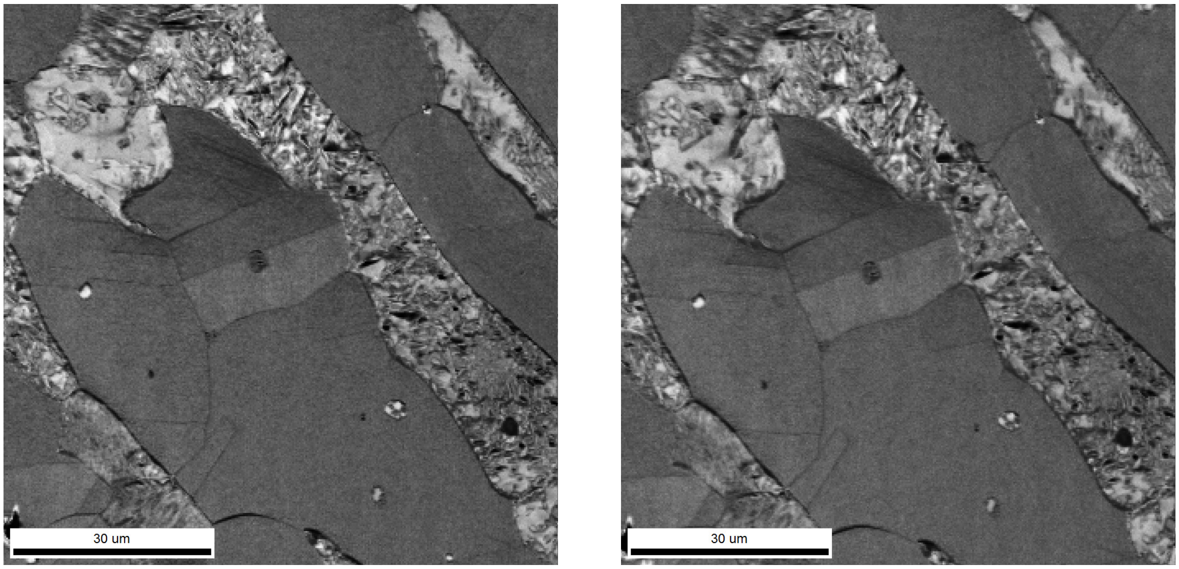

(a) IQ map acquired 250 min after heating

(b) IQ map acquired 280 min after heating

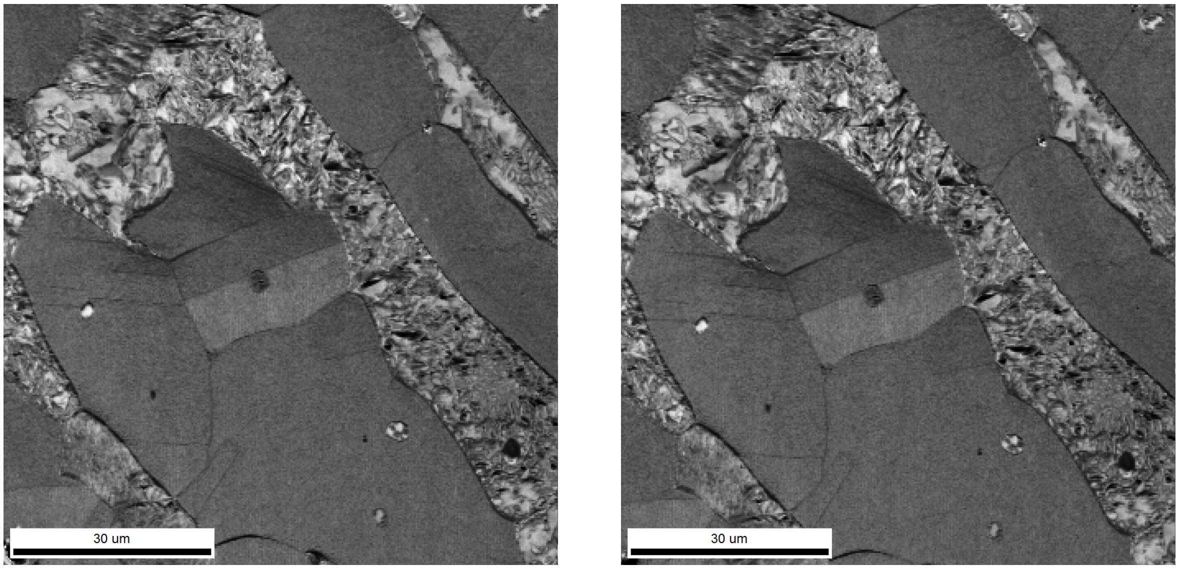

(c) IQ map acquired 310 min after heating

(d) IQ map acquired 340 min after heating

Figure E.46: IQ maps from Experiment 7: Temperature set at 750°CC in oven

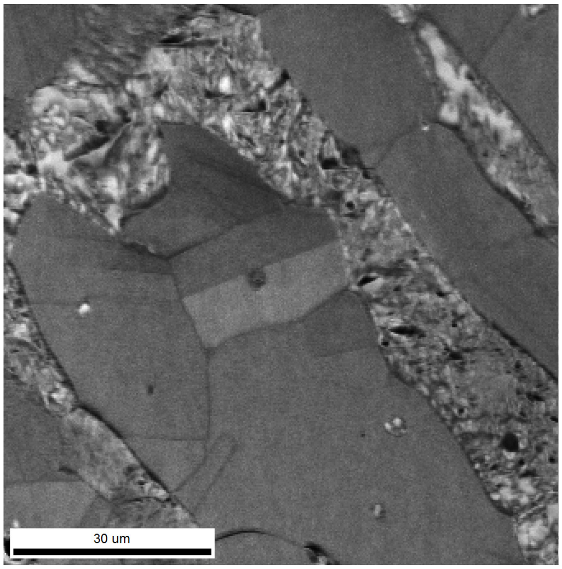

(a) IQ map acquired 370 min after heating

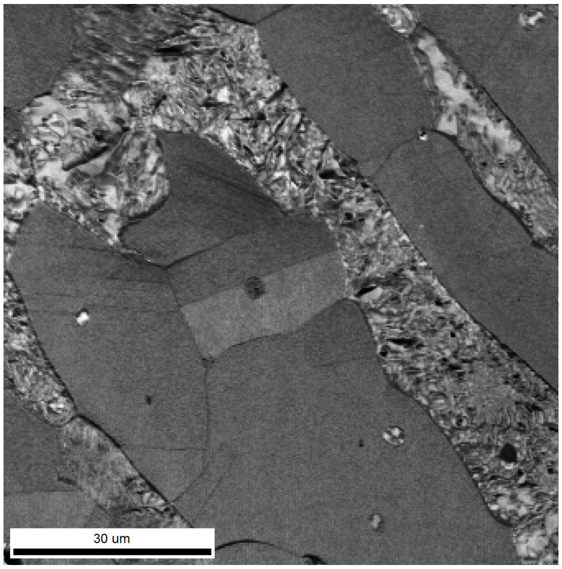

(b) IQ map acquired 400 min after heating

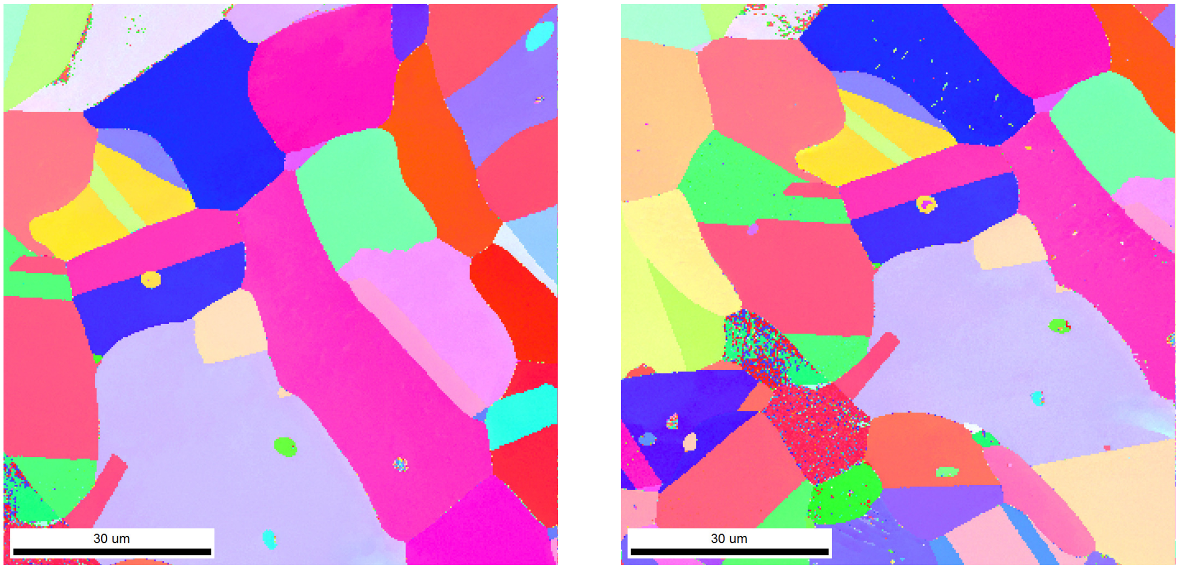

(a) IPF map acquired 10 min after heating (b) IPF map acquired 40 min after heating

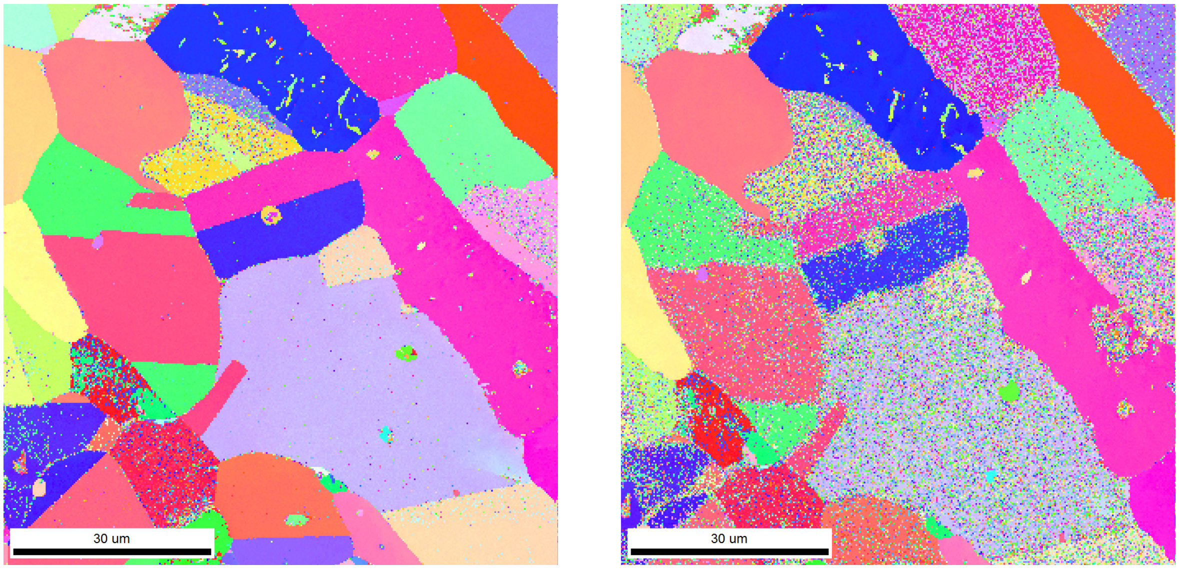

(c) IPF map acquired 70 min after heating (d) IPF map acquired 100 min after heating

Figure E.47: IPF maps from Experiment 7: Temperature set at 750 °C in oven

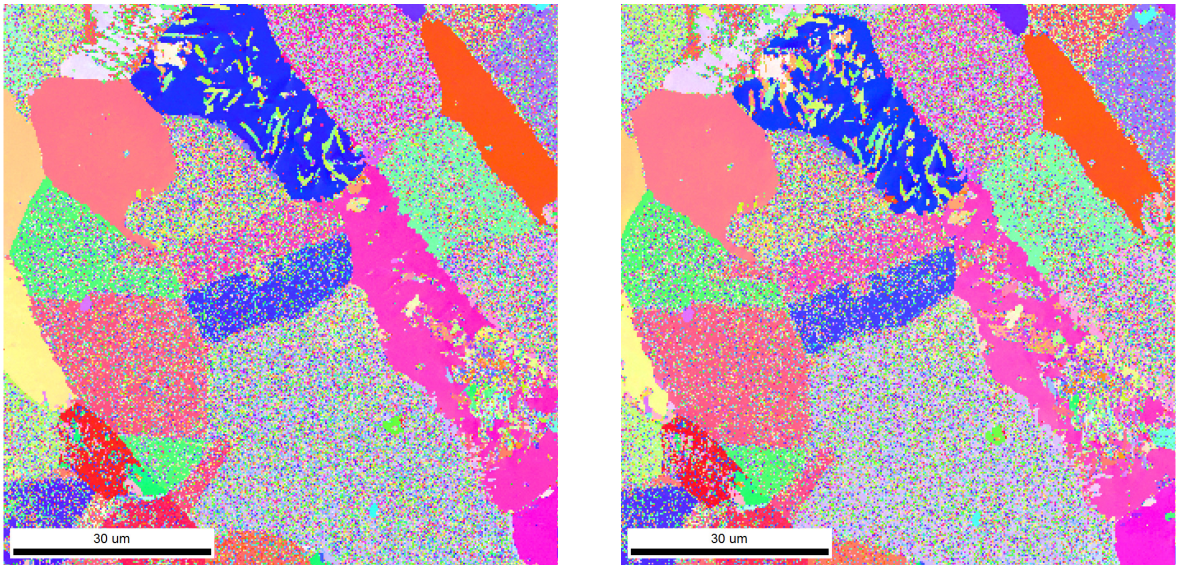

(a) IPF map acquired 130 min after heating

(b) IPF map acquired 160 min after heating

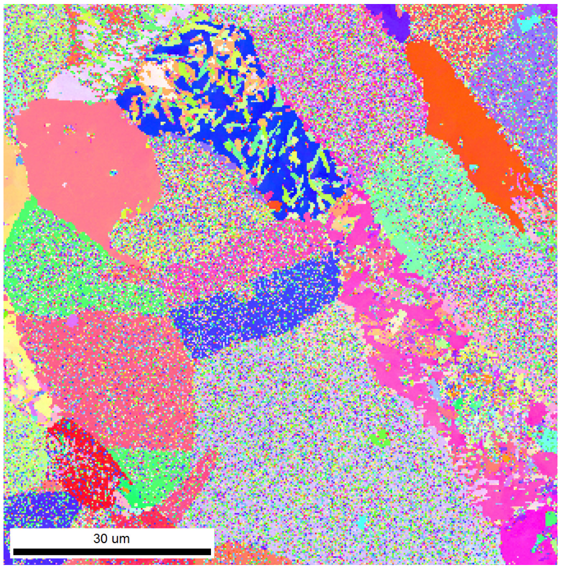

(c) IPF map acquired 190 min after heating

Figure E.48: IPF maps from Experiment 7: Temperature set at 750 °C in oven

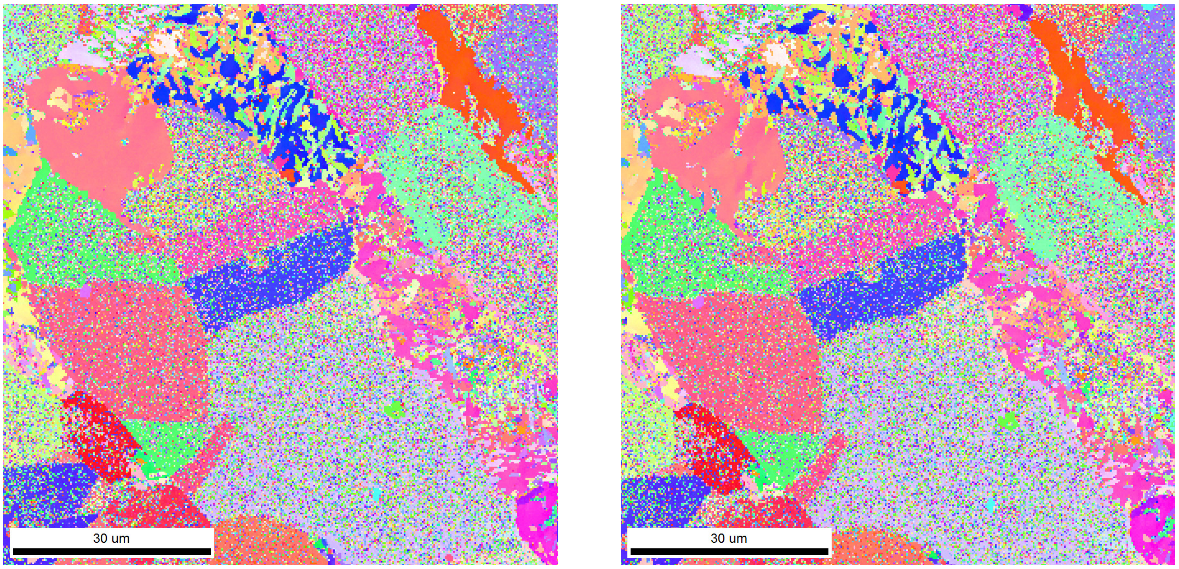

(a) IPF map acquired 250 min after heating (b) IPF map acquired 280 min after heating

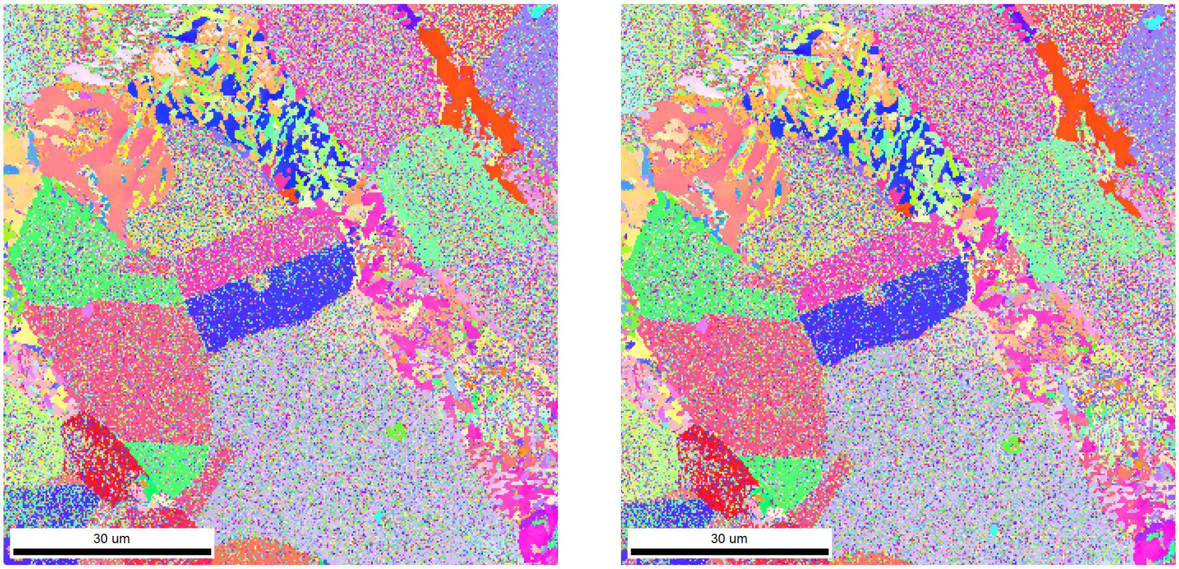

(c) IPF map acquired 310 min after heating (d) IPF map acquired 340 min after heating

Figure E.49: IPF maps from Experiment 7: Temperature set at 750 °C in oven

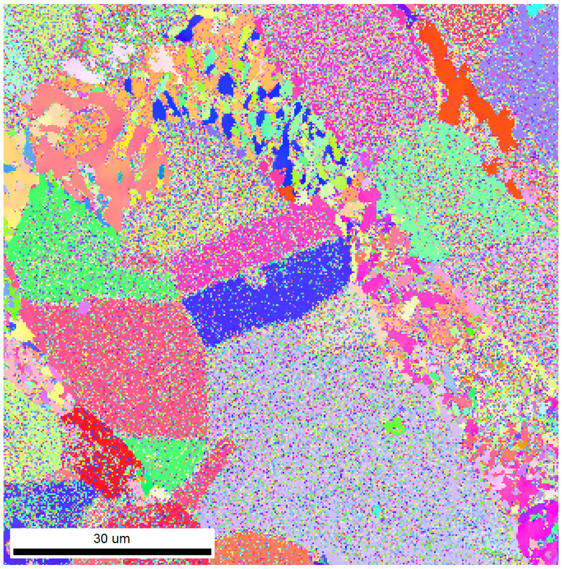

(a) IPF map acquired 370 min after heating

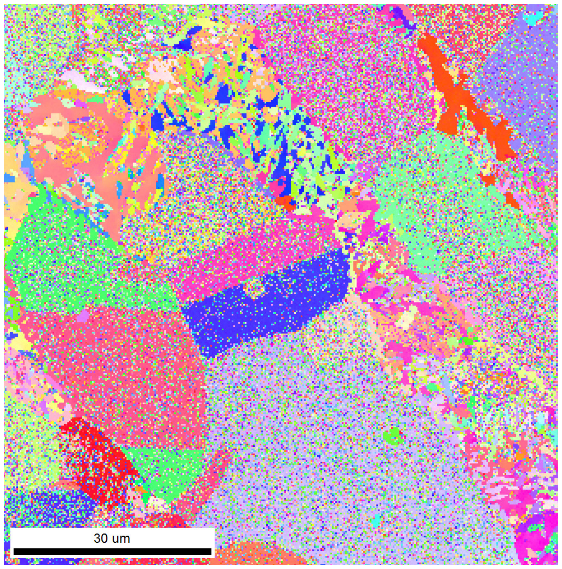

(b) IPF map acquired 400 min after heating

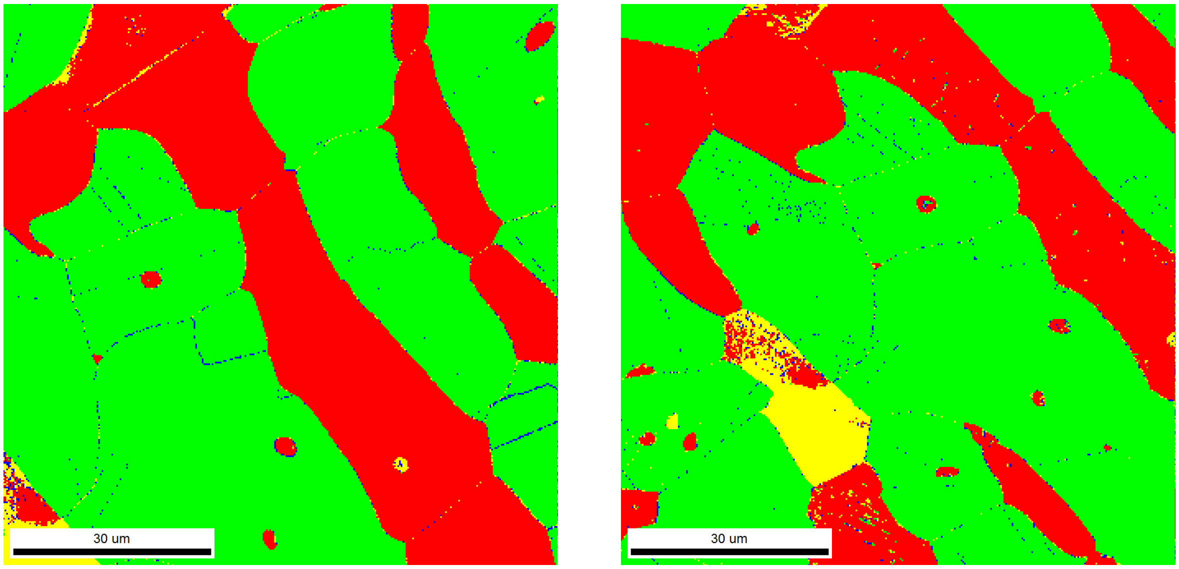

(a) Phase map acquired 10 min after heating (b) Phase map acquired 40 min after heating

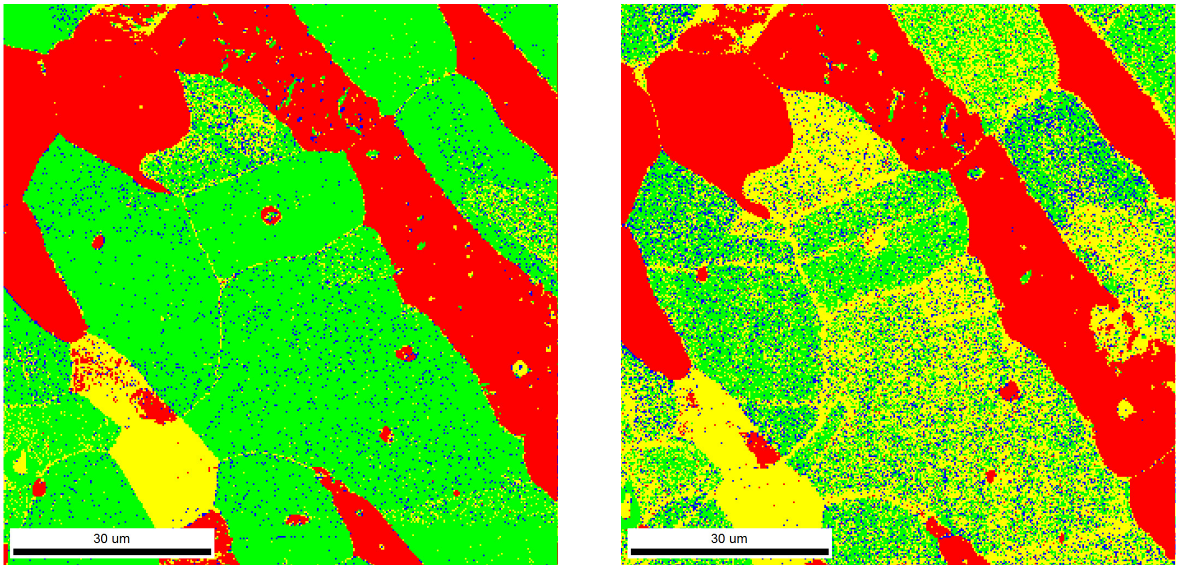

(c) Phase map acquired 70 min after heating (d) Phase map acquired 100 min after heating

Figure E.50: Phase maps from Experiment 7: Temperature set at 750 °C in oven

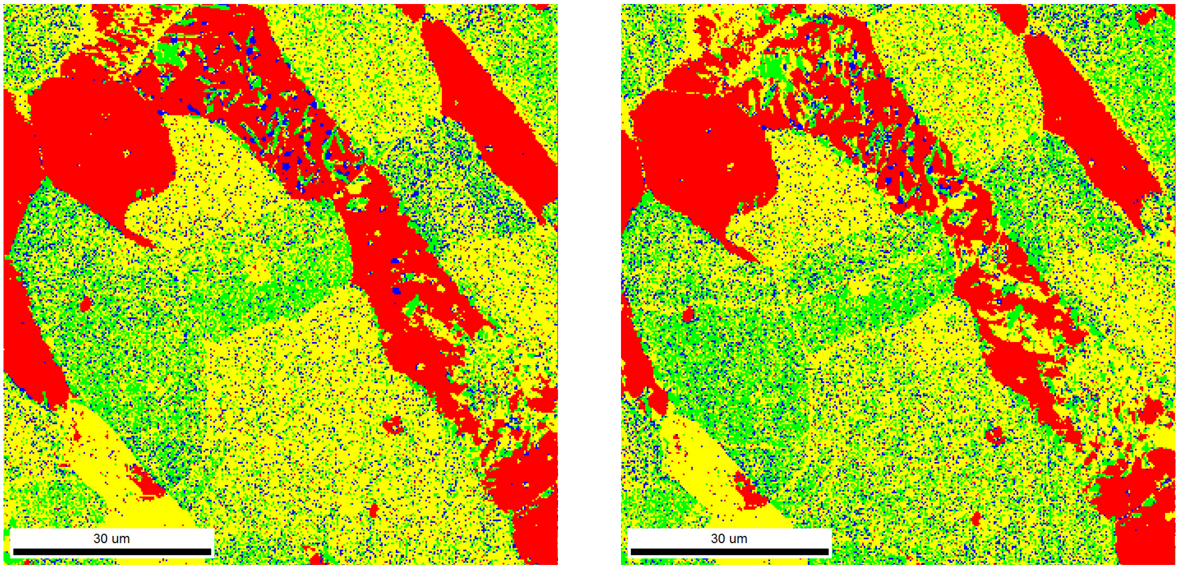

(a) Phase map acquired 130 min after heating (b) Phase map acquired 160 min after heating

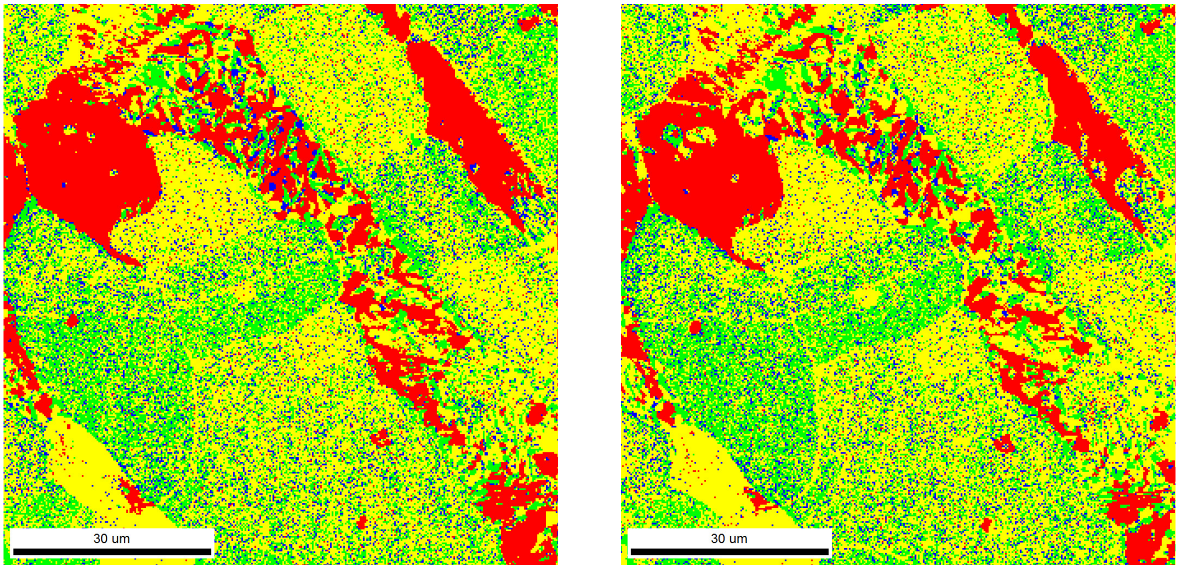

(c) Phase map acquired 190 min after heating (d) Phase map acquired 220 min after heating

Figure E.51: Phase maps from Experiment 7: Temperature set at 750 °C in oven

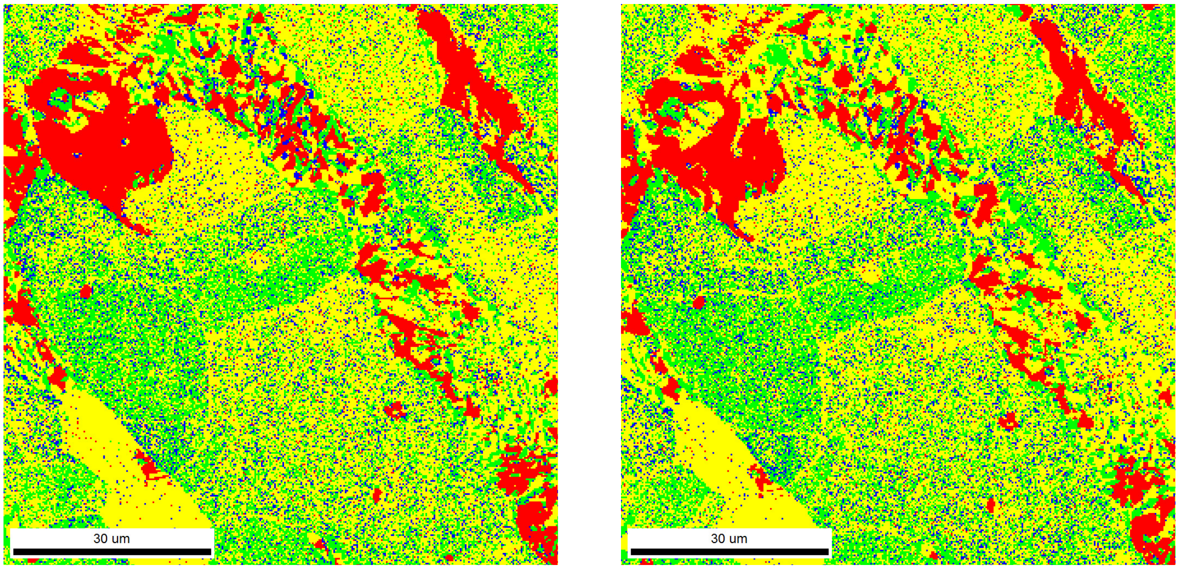

(a) Phase map acquired 250 min after heating (b) Phase map acquired 280 min after heating

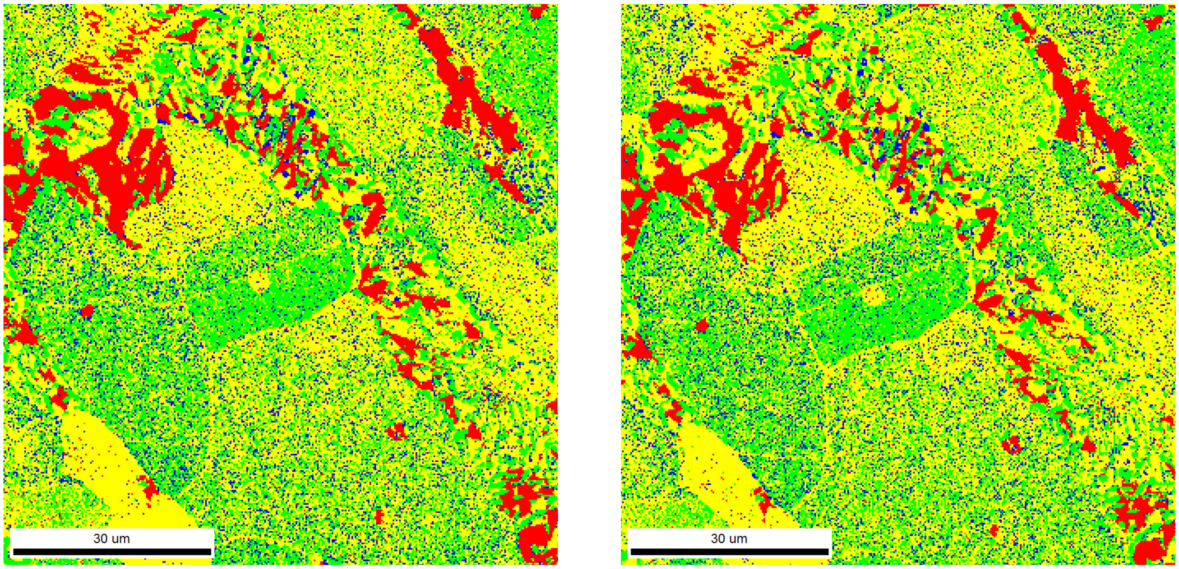

(c) Phase map acquired 310 min after heating (d) Phase map acquired 340 min after heating

Figure E.52: Phase maps from Experiment 7: Temperature set at 750 °C in oven

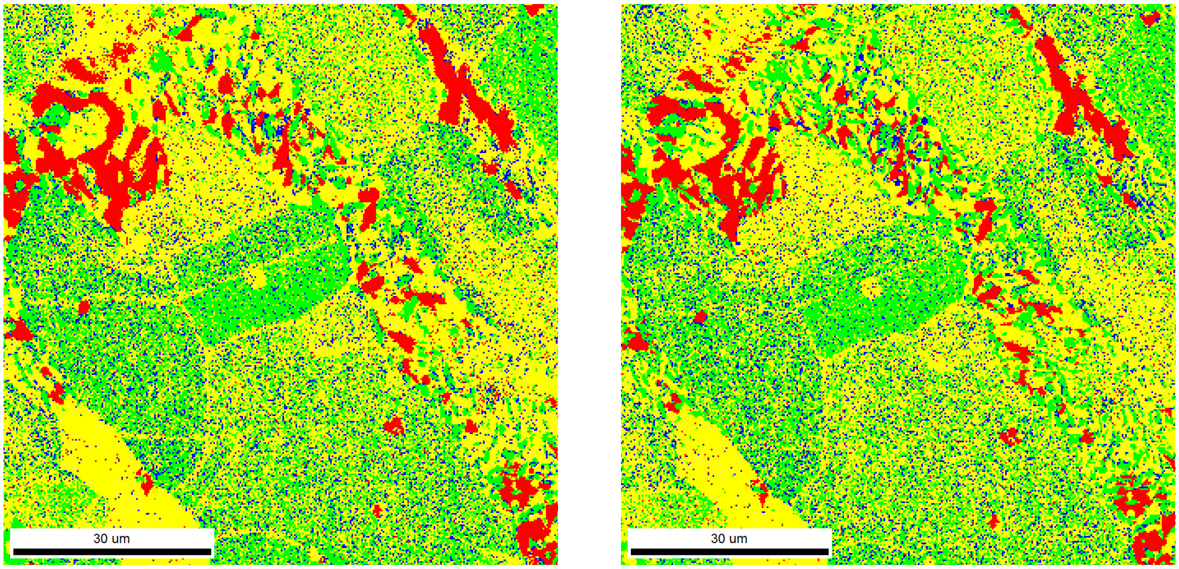

(a) Phase map acquired 370 min after heating (b) Phase map acquired 400 min after heating

Figure E.53: Phase maps from Experiment 7: Temperature set at 750 °C in oven